Photothermoacoustic effect in solids with piezoelectric detection

D. A. Andrusenko and I. Ya. Kucherov

Taras Shevchenko Kiev University, 252017 Kiev, Ukraine

The photothermoacoustic effect in solids with piezoelectric signal detection is investigated theoretically and experimentally. Analytical expressions are found for the amplitude and phase shift of the photothermoacoustic signal as a function of the thicknesses of the sample and piezoelectric transducer, the modulation frequency, and the material constants of the structure. A method is proposed for detecting the signal using a compound piezoelectric transducer. It is shown for a bilayer piezoelectric transducer that the reduced Young's modulus and the thermal diffusion coefficient of the experimental object can be found from the amplitude–frequency and phase–frequency curves. © *1999 American Institute of Physics.* [S1063-7842(99)00112-9]

The photothermoacoustic method has been increasingly used in recent years to study matter in various aggregate states.[1–3] This method is based on the use of heat waves as carriers of information about the properties of the material. Heat waves are generated by irradiating a material with modulated light, which is absorbed and heats the material with a variable temperature. Various methods are used to detect the heat waves. Acoustic methods are the most widely used, and the piezoelectric transducer method is the most sensitive of these.[1] A characteristic feature of this method is that the signal detected with a piezoelectric transducer is a function of the geometry of the sample–transducer system. In its general form this is a very complicated problem. For this reason, it has been solved for the simplest cases:[4,5] in Ref. 4 — in the quasistatic approximation neglecting the effect of the transducer on the generation of acoustic waves in the sample–transducer system; in Ref. 5 — for the case of relatively high modulation frequency, so that the wavelength of the acoustic waves is comparable to the dimensions of the sample–transducer system. In the overwhelming majority of photothermoacoustic investigations low modulation frequencies, so that the wavelength of the acoustic waves is much greater than the characteristic dimensions of the experimental system, are most promising. In this case the ratio of the linear dimensions of the sample–transducer system, as shown in Ref. 6, should play a fundamental role in the formation of the photothermoacoustic (PA) signal. For this reason, it seems to us to be very important to study the photothermoacoustic effect in solids with piezoelectric detection, where the dimensions of the experimental structure are much smaller than the wavelength of the acoustic waves (quasistatic approximation), taking account of the influence of the piezoelectric transducer. In the present work the theory of the PA effect in a layered sample–piezoelectric transducer structure is studied and experimental investigations are performed on certain materials.

Let us consider a sample–piezoelectric transducer structure in the form of a thin bilayer plate. The geometry of the problem is shown in Fig. 1. The sample *1* is an isotropic solid of thickness h_1, the piezoelectric transducer *2* is a 6-mm class piezoelectric with thickness h_2, and we shall assume its elastic constants to be isotropic. The polar axis of the piezoelectric is perpendicular to the basal surfaces of the plate (it is the Z axis). The sample surface ($Z=0$) is uniformly irradiated with amplitude-modulated light

$$P = \frac{P_0}{2}(1+\cos \omega t), \tag{1}$$

where P_0 is the intensity of the incident light and ω is the angular frequency of modulation of the light.

We shall consider media which strongly absorb light, $\alpha h_1 \gg 1$ (α is the optical absorption coefficient of the sample material). In addition, we shall assume that at the lowest light modulation frequency the thermal diffusion length l_t is smaller than the sample thickness h_1 (the heat wave does not reach the piezoelectric transducer). As a result of thermal expansion, the temperature field of the heat wave produces thermoelastic stresses. Only the elastic stresses T_{11} and T_{22} will be nonzero. Their variable components are given by[7]

$$T_{11} = T_{22} = E_\Pi(a - bz - \alpha_T\Theta), \tag{2}$$

where $E_\Pi = E/(1-\sigma)$ is the reduced Young's modulus, E and σ are, respectively, Young's modulus and the Poisson
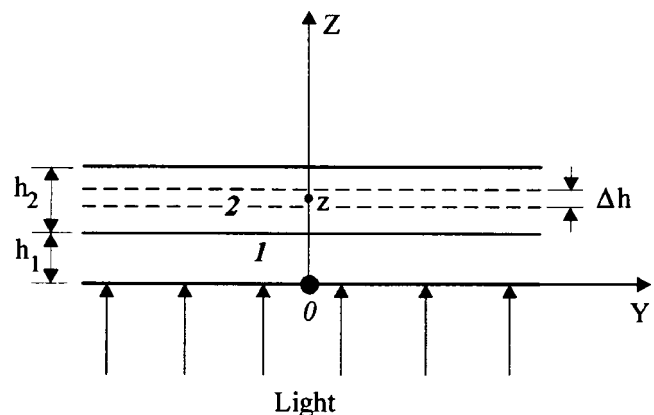

FIG. 1. Geometry of the problem.

ratio of the sample (piezoelectric transducer), α_T is the linear thermal expansion coefficient of the sample, and Θ is the variable temperature of the sample.

For the conditions indicated above, the temperature distribution over the sample thickness in our case will be[1]

$$\Theta = \Theta_0 e^{-\gamma z}, \tag{3}$$

where

$$\gamma = \frac{1+i}{l_t}, \quad l_t = \sqrt{\frac{2\chi_1}{C_1\rho_1\omega}};$$

C_1, ρ_1, and χ_1 are, respectively, the specific heat, density, and thermal conductivity of the sample, $\Theta_0 = gP_0/2\chi_1\gamma$, and g is a coefficient that determines the fraction of the light energy incident on the sample that is converted into heat.

The constants a and b in Eq. (2) are found from the boundary conditions expressing the fact that the total forces and the total moment of the acting stresses vanish:[7]

$$\int_0^h T_{11}dz = 0, \quad \int_0^h T_{11}z\,dz = 0; \quad h = h_1 + h_2. \tag{4}$$

Substituting expression (2) into Eq. (4), using Eq. (3), and neglecting the quantity $e^{-\gamma h_1}$ compared to unity (the heat wave almost completely decays over a distance equal to 2/3 of the wavelength), we obtain

$$a = \frac{\alpha_T\Theta_0\eta\left(Z_p - \dfrac{1}{\gamma h}\right)}{\gamma h[1+(\eta-1)H_1](Z_p - Z_u)};$$

$$b = \frac{\alpha_T\Theta_0\eta\left(Z_u - \dfrac{1}{\gamma h}\right)}{\gamma h^2[1+(\eta-1)H_1](Z_p - Z_u)Z_u}; \tag{5}$$

$$Z_p = \frac{2}{3}\frac{1+(\eta-1)H_1^3}{1+(\eta-1)H_1^2}; \quad Z_u = \frac{1}{2}\frac{1+(\eta-1)H_1^2}{1+(\eta-1)H_1};$$

$$\eta = \frac{E_{\Pi1}}{E_{\Pi2}}; \quad H_1 = \frac{h_1}{h}. \tag{6}$$

Here the indices 1 and 2 refer to the sample and the piezoelectric transducer, respectively. Let us calculate the potential difference $\hat{U}$ across a layer of thickness Δh and coordinate z in the piezoelectric transducer (Fig. 1)

$$\hat{U} = -\int_{z-\frac{\Delta h}{2}}^{z+\frac{\Delta h}{2}} E_z\,dz, \tag{7}$$

where E_z is the electric field produced in the piezoelectric by the thermoelastic stresses T_{11} and T_{22}.

The electric displacement D_z in the piezoelectric is

$$D_z = 2d_{31}T_{11} + \varepsilon_{33}E_z. \tag{8}$$

Since there are no external electric fields, the electric displacement outside the piezoelectric is zero. Then, as a result of the continuity of the normal component of the electric displacement, we find from Eq. (8) with the use of Eq. (2)

$$E_z = -\frac{2d_{31}E_{\Pi2}}{\varepsilon_{33}}(a - bz). \tag{9}$$

Equation (9) takes account of the fact that the heat wave does not reach the piezoelectric transducer, and therefore $\Theta = 0$ in the transducer. Integrating Eq. (7), using expressions (9) and (5), we find

$$\hat{U} = U_m\frac{(Z-Z_p)Z_u\gamma h - (Z-Z_u)}{2Z_u(\gamma h)^3}\Delta H;$$

$$U_m = \frac{2\alpha_T gP_0 d_{31}E_{\Pi1}h^2}{\varepsilon_{33}\chi_1[1+(\eta-1)H_1](Z_u - Z_p)};$$

$$Z = \frac{z}{h}; \quad \Delta H = \frac{\Delta h}{h}. \tag{10}$$

From Eq. (10) we find the amplitude U and the phase shift φ of the PA signal

$$U = U_m\frac{Z-Z_p}{F^{3/2}}\Delta H\sqrt{n^2 + (n - \sqrt{F})^2}, \tag{11}$$

$$\tan\varphi = 1 - \frac{\sqrt{F}}{n}; \quad n = \frac{Z-Z_u}{2Z_u(Z-Z_p)}, \tag{12}$$

where $F = (\pi h^2/D_T)f$ is the dimensionless frequency, $f = \omega/2\pi$ is the frequency, and $D_T = \chi_1/c_1\rho_1$ is the thermal diffusivity (thermal diffusion coefficient) of the sample.

Expressions (11) and (12) make it possible to determine the optimal ratios of the thicknesses h_1 and h_2 for specific materials of the structure depending on what one wishes to obtain: a larger PA signal amplitude or a larger change in phase of the signal. Let us analyze the expressions for U and φ for certain conditions. It is evident from Eqs. (11) and (12) that the amplitude and phase of the PA signal depend in a complicated manner on the frequency ($\sqrt{F}$), the parameters of the sample and the piezoelectric transducer (U_m, Z_u, Z_p), and the coordinates (Z) of the center of the piezoelectric layer from which the signal is extracted. Here it is important that the phase shift does not depend on the thickness of the layer from which the signal is extracted, but rather it is determined for a specific experimental structure only by the coordinate of the center of this layer and by the frequency.

Let us analyze the dependence of the phase shift φ of the PA signal on the frequency F for various values of the parameters of the structure. It is evident from Eq. (12) that if the coordinate Z of the piezoelectric transducer layer from which the signal is extracted is Z_p ($Z = Z_p$, $n = \infty$), then the phase shift is independent of the frequency and is $\varphi = \pi/4$. If $Z = Z_u$ ($n = 0$), then the phase shift $\varphi = -(\pi/2)$ likewise is frequency-independent. If $Z_u < Z < Z_p$, then the parameter $n < 0$, and the phase shift increases in magnitude with frequency from $\varphi = \pi/4$ to $\varphi = \pi/2$. However, if Z is greater than Z_u and Z_p, then the parameter $n > 0$, and the phase shift varies monotonically with increasing frequency from $\varphi = \pi/4$ to $\varphi = -(\pi/2)$. It is also interesting that $\tan\varphi$ is a linear function of $\sqrt{F}$. Here the characteristic point is the point where the phase shift vanishes. This occurs at frequency $f = f_0$ satisfying the condition

$$\sqrt{\frac{\pi h^2}{D_T}}\,f_0 = n. \tag{13}$$

Having determined the experimental frequency f_0 for known elastic constants of the structure (z_u and z_p) from Eq. (13), the thermal diffusion coefficient D_T of the sample can be found directly and then, for known c_1 and ρ_1, the thermal conductivity χ can be determined.

Let us analyze the frequency dependence of the amplitude of the PA signal for various values of the coordinate of the piezoelectric transducer layer from which the signal is extracted. For $Z=Z_u$ ($n=0$) the amplitude of the PA signal is inversely proportional to the frequency, as one can see from Eq. (11). However, if $Z=Z_p$, then $U\sim F^{-3/2}$. In a structure for which $n\gg1$, $U\sim F^{-3/2}$ also holds at low frequencies, for which $n\gg\sqrt{F}$. As the frequency increases, when $\sqrt{F}$ becomes much greater than n, the dependence $U(F)$ becomes $U\sim F^{-1}$.

In principle, certain parameters of the sample can be determined from the amplitude–frequency $U(F)$ and phase–frequency $\varphi(F)$ dependences of the PA signal according to Eqs. (11) and (12). However, since U and φ depend on a large number of parameters of the sample and the piezoelectric transducer and since the effect of the reactive parameters of the system is superposed on the measurement results, it is difficult to determine the sample parameters from these dependences. For this purpose, it is better to use a multilayer piezoelectric transducer made of the same material, so as to be able to measure the potential difference independently on each layer. We shall analyze the possibilities of such a structure for the example of a bilayer transducer with equal layer thicknesses $h_2/2$. The coordinate of the first transducer layer from the sample will be $Z_1=(1+3H_1)/4$, and the coordinate of the second one will be $Z_2=(3+H_1)/4$. The amplitude ratio U_1/U_2 and the phase difference $\varphi_1-\varphi_2$ of the PA signals extracted from these layers of the piezoelectric transducer will be

$$\frac{U_1}{U_2} = \frac{Z_1-Z_p}{Z_2-Z_p}\sqrt{\frac{n_1^2+(n_1-\sqrt{F})^2}{n_2^2+(n_2-\sqrt{F})^2}}, \tag{14}$$

$$\tan(\varphi_1-\varphi_2) = \frac{n_1-n_2}{2n_1n_2/\sqrt{F}+\sqrt{F}-(n_1+n_2)}, \tag{15}$$

where n_1 and n_2 are the values of the parameter n for the first and second layers, respectively, of the piezoelectric transducer.

As one can see from Eq. (14), the ratio (U_1/U_2) approaches, as frequency increases, a constant $(U_1/U_2)_\Pi$ given by

$$(U_1/U_2)_\Pi = \frac{Z_1-Z_p}{Z_2-Z_p}. \tag{16}$$

The second feature of the frequency dependence of (U_1/U_2) is the presence of extrema (maxima and minima). They occur for $\sqrt{F_e}$ given by

$$\sqrt{F_e} = (n_1+n_2) \pm \sqrt{n_1^2+n_2^2}. \tag{17}$$

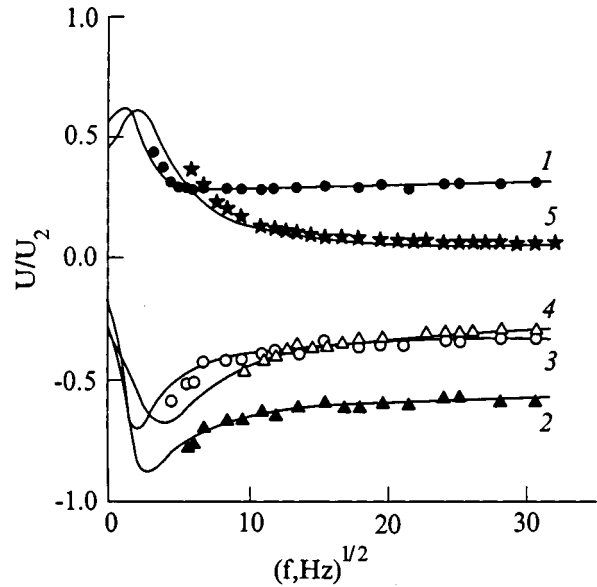Figure 2 (solid curves) shows (U_1/U_2) versus the fre-

FIG. 2. Curves of the ratio U_1/U_2 of the amplitudes of the signals extracted from different layers of the piezoelectric transducer versus the frequency $f^{1/2}$. *1* — steel, *2,3* — Pb, *4,5* — Zn, mm: *1* — 1.46, *2* — 1.51, *3* — 1.81, *4* — 1.13, *5* — 1.64.

quency $\sqrt{f}$ for U-8 steel, lead, and zinc, as calculated using Eq. (14). These curves illustrate the features noted above. Negative values of (U_1/U_2) signify that the signals extracted from different layers of the piezoelectric transducer are in antiphase.

Estimates show that for reasonable thicknesses of the sample and piezoelectric transducer (of the order of 1 mm each) the frequency dependence of (U_1/U_2) becomes essentially constant at frequencies above several hundreds of Hz, which is easily achievable experimentally. Having measured (U_1/U_2) in this manner and knowing the thicknesses of the sample and piezoelectric transducer layers, from Eq. (16) we find Z_p. Using the known elastic parameters of the transducer, we determine from the expression for Z_p (6) the reduced Young's modulus E_Π of the sample material.

As is evident from Eq. (15), the quantity $\varphi_1-\varphi_2\equiv\Delta\varphi$ depends on the frequency in a complicated manner. At low frequencies $\Delta\varphi$ approaches zero. At higher frequencies $\Delta\varphi$ can change quite strongly (from 0 to π) as a function of the geometric parameters n_1 and n_2 of the structure. The parameters n_1 and n_2 for a given sample material and the same piezoelectric transducer can be changed by varying the thickness of the sample (H_1). Figure 3 (lines) shows as an example the curves of $\Delta\varphi$ versus the frequency ($1/\sqrt{f}$), which are calculated using Eq. (15) for relatively high frequencies for structures consisting of a Zn sample and PZT piezoelectric transducer (TsTS-19) with different relative thicknesses of the sample. It is evident that for certain sample thicknesses a maximum is observed on the curves of $|\Delta\varphi|$ versus frequency. It occurs at

$$F=2n_1n_2. \tag{18}$$

We note that the maximum in the curves of $\Delta\varphi$ versus the frequency is observed at values of H_1 for which $n_{1,2}$
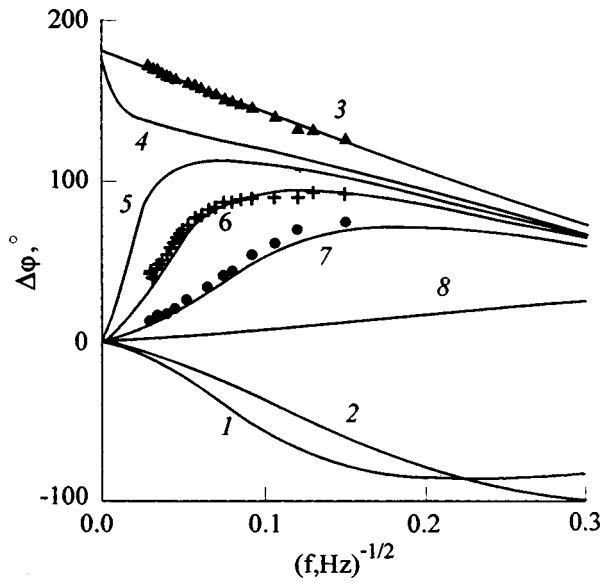
FIG. 3. Curves of the phase difference $\Delta\varphi$ of signals extracted from two layers of the piezoelectric transducer versus the frequency $f^{-1/2}$ for Zn with H_1: *1* — 0.1, *2* — 0.3, *3* — 0.48, *4* — 0.55, *5* — 0.56, *6* — 0.58, *7* — 0.6, *8* — 0.7.

FIG. 4. Curves of the phase difference $\Delta\varphi$ of signals extracted from two layers of a piezoelectric transducer versus the frequency $f^{-1/2}$ for Pb (*1,2*) and U-8 steel (*3, 4*), mm: *1* — 1.51. *2* — 1.81, *3* — 0.7, *4* — 1.46.

> 0. The frequencies at which $|\Delta\varphi| = \pi/2$ are also special points on the curves of $\Delta\varphi$ versus the frequency. These points occur at

$$(\sqrt{F})_{1,2} = \frac{1}{2}(n_1 + n_2 \pm \sqrt{n_1^2 + n_2^2 - 6n_1 n_2}). \qquad (19)$$

We note another feature of the dependence of $\Delta\varphi$ on F. For structure parameters $n_{1,2}$ somewhat greater than 1, at frequencies for which $\sqrt{F} \gg 2n_1 n_2$ as one can see from Eq. (15),

$$\tan(\Delta\varphi) \cong \frac{n_1 - n_2}{\sqrt{F}}. \qquad (20)$$

In this frequency range $\tan(\Delta\varphi)$ is a linear function of $1/\sqrt{F}$. Each of these features of the frequency dependence of the phase difference of the signals extracted from two parts of the piezoelectric transducer makes it possible to determine the thermal diffusion coefficient D_T of the material, if the structure parameters $n_{1,2}$ are known. Thus, the above-noted features of the photothermoacoustic effect in solids with the PA signal detected with a bilayer piezoelectric transducer make it possible to determine at least the reduced Young's modulus and the thermal diffusion coefficient of materials.

The experimental investigations were performed on U-8 steel, zinc, and lead samples. The piezoelectric transducer consisted of two layers of PZT piezoceramic (TsTS-19), each 0.6 mm thick. The elastic constants of the piezoelectric transducer was measured by the method described in Ref. 8, and they were found to be $E = 6 \times 10^{10}$ N/M^2 and $\sigma = 0.42$. These values were used in the calculations. The experimental samples and piezoelectric transducer consisted of plane-parallel disks of the same diameter, equal to 15 mm. Two U-8 steel and lead (Pb) samples and three zinc (Zn) samples were prepared. The sample thicknesses were: U-8 — h_1
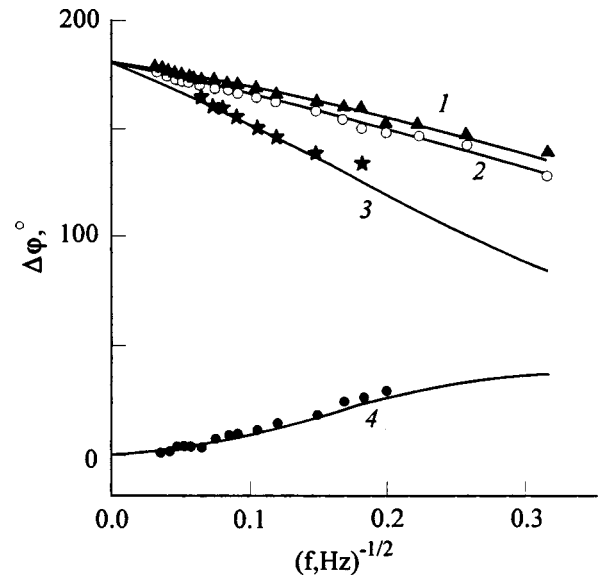
$= 0.7$, 1.46 mm; Pb — $h_1 = 1.51$, 1.81 mm; Zn — $h_1 = 1.13$, 1.64, 1.79 mm. The samples were irradiated with modulated radiation from an LG-38 laser ($\lambda = 0.6328$ μm). Modulation was performed with a mechanical chopper. The surface of the samples was illuminated uniformly. For this, the laser beam was expanded. The investigations were performed in the frequency range 30–1000 Hz. The frequency dependences of the amplitude and phase shift of the PA signal extracted from each layer of the piezoelectric transducer separately were measured.

The experimental results for certain samples are presented in Figs. 2–5 (symbols). The ratios $(U_1/U_2)_{\Pi}$ for each of the samples were determined from the experimental
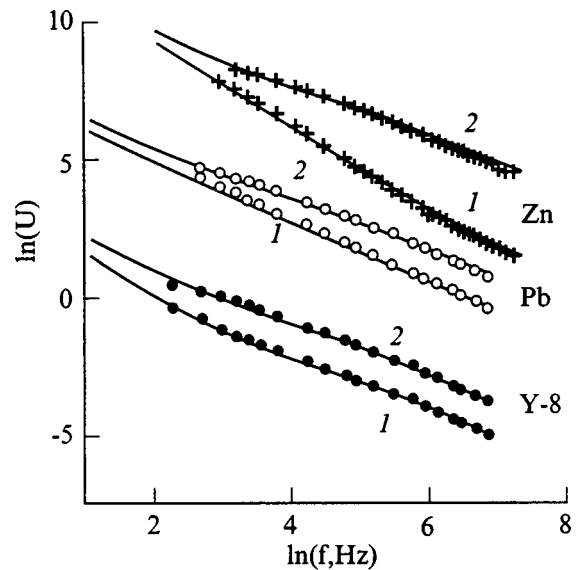

FIG. 5. Amplitudes (ln U) of signals extracted from individual layers of the piezoelectric transducer versus frequency (ln f) for Pb ($h_1 = 1.81$ mm), Zn ($h_1 = 1.64$ mm), and U-8 steel ($h_1 = 1.46$ mm).

data presented in Fig. 2, and they were used to determine the reduced Young's moduli of the experimental materials using the scheme described above. The following values were obtained for the reduced Young's modulus. For U-8 steel: $E_\Pi = 27 \times 10^{10}$ N/M^2 [$(26–33) \times 10^{10}$ N/M^2], for Pb: $E_\Pi = 3.4 \times 10^{10}$ N/M^2 [$(1.3–4.0) \times 10^{10}$ N/M^2], for Zn: $E_\Pi = 10.6 \times 10^{10}$ N/M^2 [$(11–12) \times 10^{10}$ N/M^2]. The values in brackets are the values calculated for E_Π from handbook data.[9,10]

These values of E_Π were then used to determine the thermal diffusion coefficient D_T. The coefficient D_T was determined from the experimental frequency dependences of $\Delta\varphi$ presented in Figs. 3 and 4: either using the approximate formula (20) at relatively high frequencies or using Eq. (19) at frequencies for which $\Delta\varphi = \pi/2$. The following values were obtained. For U-8: $D_T = 13.9 \times 10^{-6}$ M^2/s [13.7×10^{-6} M^2/s]; for Pb: $D_T = 25.6 \times 10^{-6}$ M^2/s [23.8×10^{-6} M^2/s]; for Zn: $D_T = 40.5 \times 10^{-6}$ M^2/s [$(36.8–41.9) \times 10^{-6}$ M^2/s]. The values of D_T calculated from the handbook data[9,10] are presented in brackets. It is seen that the values of E_Π and D_T found from investigations of the photothermal acoustic effect agree well with published data. The experimental values of E_Π and D_T obtained were used for all theoretically computed dependences presented in Figs. 2–5 (solid lines).

Figure 5 shows a log–log plot of the theoretical (curves), computed [using Eq. (11)], and experimental (symbols) frequency (f) dependences of the amplitude U of the PA signals (in relative units), extracted from separate layers of the piezoelectric transducer (*1* and *2*, respectively), for certain samples of U-8 steel, Pb, and Zn. The experimental data were ''tied in'' to the theoretical data using the curves *1* at the points with frequency $f = 460$ Hz.

Comparing the experimental results obtained in this work and the theoretical calculations shows that they are in good agreement with one another.

In summary, in this work the photothermoacoustic effect in solids with piezoelectric detection of the heat waves has been investigated theoretically and experimentally. Analysis of the theoretical dependences for the amplitude and phase shift of the PA signal showed that they depend strongly on the ratio of the thicknesses of the sample and piezoelectric transducer. The PA signal was detected using a compound piezoelectric transducer. It was shown that when the PA signal is detected with a bilayer piezoelectric transducer, the reduced Young's modulus and the heat diffusion coefficient of the sample can be determined from the amplitude–frequency and phase–frequency dependences of the PA signal. The experiment was performed on U-8 steel, lead, and zinc samples. Good agreement was obtained between the experimental results and theoretical calculations and the published data.

[1] A. Rozencwaig, *Photoacoustics and Photoacoustic Spectroscopy* (Wiley, New York, 1980), 310 pp.

[2] V. P. Zharov and V. S. Letokhov, *Laser Optoacoustic Spectroscopy* [in Russian], Nauka, Moscow (1984), 320 pp.

[3] V. É. Gusev and A. A. Karabutov, *Laser Optoacoustics* [in Russian], Nauka, Moscow, (1991), 304 pp.

[4] W. Jachson and N. M. Amer, Appl. Phys. **51**, 3343 (1980).

[5] Yu. V. Gulyaev, A. I. Morozov, and V. Yu. Raevskiĭ, Akust. Zh. **31**, 469 (1985).

[6] D. A. Andrusenko and I. Ya. Kucherov, Zh. Tekh. Fiz. **68**, 75 (1998) [Tech. Phys. **43**, 67 (1998)].

[7] A. D. Kovalenko, *Thermoelasticity* [in Russian], Vishcha Shkola, Kiev (1975), 216 pp.

[8] *Materials for Piezoceramics. Computational Methods* [in Russian], Soviet State Standards Commission (1980), 30 pp.

[9] G. Kaye and T. Laby, *Tables of Physical and Chemical Constants* [Longman, New York, 1986; Fizmatgiz, Moscow, 1962, 248 pp.].

[10] I. K. Kikoin, *Tables of Physical Quantities* [in Russian], Atomizdat, Moscow (1976), 1008 pp.

Translated by M. E. Alferieff

Investigation of the aerodynamic properties and flow field around hypervelocity objects in a ballistic test range

P. I. Kovalev, A. N. Mikhalev, A. B. Podlaskin, S. G. Tomson, and V. A. Shiryaev

A. F. Ioffe Physicotechnical Institute, Russian Academy of Sciences, 194021 St. Petersburg, Russia

S. A. Isaev

Academy of Civil Aviation, St. Petersburg, Russia

The equipment of a ballistic test range for research on hypersonic motion and flow around typical models of explosion-propelled projectiles. A method for obtaining instantaneous interferograms of the flow around an object and a procedure for calculating the radial density distributions from measurements made on them are briefly set forth. The values of the aerodynamic drag at zero angle of attack are obtained for three models in trajectory experiments, and a comparative assessment of their stability is made. The principles for performing numerical aerodynamic calculations of hypervelocity flow around objects typically having a compound shape are formulated. © *1999 American Institute of Physics.*
[S1063-7842(99)00212-3]

INTRODUCTION

Research on the hypersonic motion of objects with aspect ratios $L/D=2-4$ in the atmosphere at Mach numbers $M=3-8$ is of relevance both for the analysis of the gasdynamic flow field around objects and for determination of the aerodynamic coefficients for objects with novel shapes. On a ballistic test range the aerodynamic coefficients are found from data obtained by analyzing trajectory measurements. An important problem in a comprehensive investigation is to find an aerodynamic shape that is stable in flight and possesses moderate drag. Here one must take into account the geometry of the elements of actual explosion-propelled projectiles. One must find an optimum between acceptable static stability of the element and low aerodynamic drag, which must be small if the flight range is to be increased beyond 1000 diameters. A projectile shape with adequate static stability and with the lowest attainable drag was worked out experimentally and numerically in Ref. 1 with allowance for the properties of real explosion-propelled projectiles.

Hypervelocity projectiles with a blunt nose and a stabilizing fin have a complicated aerodynamic flow field at supersonic speeds. For the shapes considered here, the flow field around the object typically contains shock waves, rarefaction and compression regions, separation zones, and shear layers. At Mach numbers $M=3-7$ the flow in the boundary layers of the models is turbulent for Reynolds numbers $Re_{\infty D}=10^6$. In view of the hypervelocity nature of the objects, a simplified combined mathematical procedure is used for numerical calculations of the aerodynamic parameters.

BALLISTIC EXPERIMENT AND METHOD OF SABOT SEPARATION

Substantial technical difficulties arise in ballistic investigations of the aerodynamic coefficients of elements of hyper-velocity objects. Because the typical object in our study was teardrop-shaped and equipped with a stabilizing fin in back (Fig. 1), it was necessary to make a shaped sabot to hold the models in the barrel during firing. To make the models as stable as possible in flight, they were made with a weighted nose piece. To achieve Mach numbers $M=5-7$, the models had to be shot at velocities of 2000–2300 m/s. The powder gun was equipped with a reinforced breech piece, in which the gunpowder can burn at high pressure (forcing). Using this breech piece, we reached velocities ~ 1900 m/s (50 g projectile) without forcing the combustion of the gunpowder.

After construction of the ballistic model and preparation of a trajectory experiment, the next major problem is the construction of a sabot. The sabot, which protects the model from damage during acceleration in the barrel, either must not distort the rectilinear motion of the model as it separates from the sabot or else it must impart prescribed oscillations to the model.

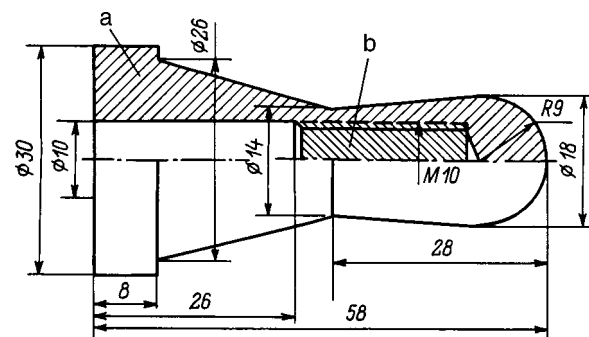We developed a new method for imparting an angular

FIG. 1. Sketch of the construction of an explosion-propelled projectile with head diameter half the base diameter: a — body of a composite material, b — brass insert.

velocity (oscillations) to a model fired from a barrel.[2] An impulse acts on the model in a transverse direction while the model is still in the sabot. According to the diagram in Fig. 2, in the separation process, the sabot imparts an impulse of transverse oscillations to the model, which has been accelerated in the axial direction. The apparatus for imparting angular momentum to the projectile is shown in Fig. 2. Here the following are shown: the barrel *a*, a static magnetic field generator *b* mounted on the barrel, and the accelerated object *c* placed inside the sabot *d*. An induction circuit *e* and an electric detonator *f*, which form a closed circuit, are placed in the sabot. A recess *g* in the sabot *d* is cut in the axial direction. The positions *A*, *B*, and *C* indicate the position of the accelerated body and the sabot in the initial position (*A*), during flight through the magnetic field (*B*), and at separation from the sabot (*C*).

The apparatus functions as follows. The sabot and model acquire a longitudinal acceleration in the barrel. Leaving the barrel, the assembly of the model in the sabot enters a magnetic field generated by the inductor *b*. A current proportional to the gradient of the magnetic field intensity is induced in a small closed circuit (coil) in the back part of the sabot. The induced current triggers the electric detonator. The triggering of the detonator ejects the detonator from the sabot, imparting an impulse to the latter. The model in a slit sabot acquires an impulse of angular rotation when it separates from the sabot. The value of the angular impulse depends on the distance between the centers of mass of the model–sabot assembly and the detonator, on the energy required to trigger the detonator, and on the cut in the sabot. The angular momentum imparted to the body can be varied over a substantial range by varying the depth of the longitudinal cut.

In view of the complexity of the shapes of typical explosion-propelled projectiles, the method described above must be used for trajectory experiments in a prescribed range of angles of attack. In setting these angles for explosion-propelled models, it is essential to be able to impart to them a controlled impulse in a direction normal to the trajectory (variation of the total amplitude of the oscillations). In addition, it is desirable to estimate the magnitude of the admissible perturbing impulse arising during the formation of a real explosion-propelled object, such that the projectile remains within the limits of stability. This will be observed when the angle of attack corresponding to instability is

reached. By following this procedure one can check the acceptable asymmetry of the impulse propelling the projectile in the sense of imparting stable transverse oscillations. The description of the method given in Ref. 2 contains the formulas required to estimate the impulse perturbing the body. The effect of the asymmetry of a real explosion-propelled object on the motion of the object can be checked qualitatively. If the angular oscillations of an asymmetric model are qualitatively similar to the observed oscillations of an aerodynamically symmetric stable model, this level of asymmetry is taken as admissible.

INTERFEROMETRIC INVESTIGATION OF THE FLOW FIELD

Using the experience in interferometric investigations of supersonic separated flows, we used an interferometer to study the characteristic features of the flow field around hypervelocity elements.[3] After interpreting the axisymmetric interferograms, we analyzed the radial density distributions in a lateral section of the model above the stabilizing fin and behind the bottom of the model (Fig. 3).

There exists an optical scheme for a shearing grating interferometer modified for double-frame photography.[4] We used single-channel photography without separating the light into two beams at the entrance and exit of the apparatus. In so doing it was possible to use less sensitive photographic film and to place a more compact diffuser into the illumination part, which increased the quality of the interferograms.

To interpret the density field of the flow around our objects, taking account of the construction of the interferometer, we chose a reference field which consisted of ~ 60 straight equidistant fringes perpendicular to the trajectory. The working field in the direction of flight was ~ 200 mm. A prescribed phase of flow in the field of the apparatus was recorded by means of an autonomous, laser-controlled synchronizer. We note some details of the analysis of the interferograms which are associated with the conditions in an ordinary ballistic experiment. We used the method of Ref. 5 to obtain the density distributions. We had to enumerate the fringes at a transition through shock waves because of the sharp break in the fringes and the impossibility of tracing fringes.

Using the algorithm described in Ref. 5, first we established the number of a fringe behind the bow wave. Then, the same algorithm was used to establish a correspondence
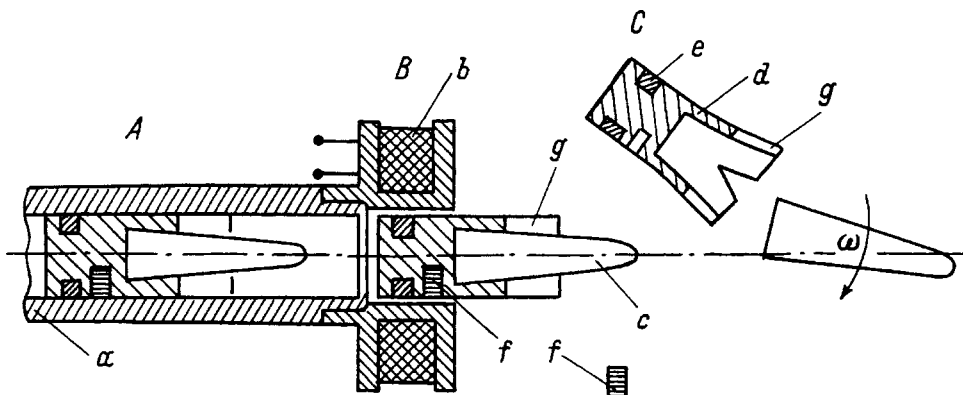

FIG. 2. Scheme of apparatus for imparting oscillations to the model in the pitch plane: phase *A* — sabot together with the model exits the barrel; phase *B* — sabot together with the model crosses a magnetic inductor *b*; phase *C* — the model exits the barrel and obtains an impulse for angular oscillations (the detonator imparts an impulse to the sabot).
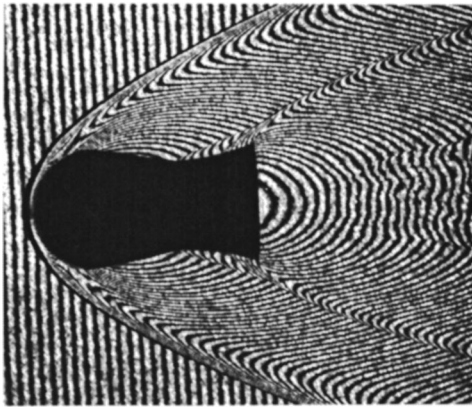
FIG. 3. Interferogram of flow around a teardrop-shaped explosion-propelled model. The interferogram was recorded at laboratory pressure and temperature and Mach number 4.28. The optical arrangement of the interferometer and the auxiliary devices are described in Ref. 4.
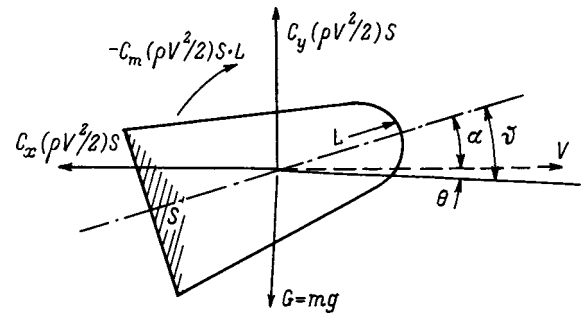

FIG. 4. Diagram of the forces and moment acting on the model undergoing planar oscillatory motion in a coordinate system tied to the model.

on the inner wave. By comparing the results of the identification of the fringes in neighboring sections we were able to to check the reliability of the enumeration of the fringes. Next, the Schardin zone method in its simplest formulation was used to interpret the density distributions. The section investigated was divided into ring-shaped zones. The width of the zones was assumed to be proportional to the bunching of the fringes. The density of zones was higher in the regions of rapid radial variation of the density and vice versa. This approach to separation into ring-shaped zones decreased the approximation error.

Just as in Schardin's work,[6] the refractive index (gas density) was assumed to be constant in each zone. The refractive index in the outer zone was calculated at the first step. The result was used to calculate the refractive index in the next zone, and so on. The gas density was related to the refractive index by the linear Gladstone–Dale relation with a constant depending on the molecular composition of the working gas. The density profiles established for the explosion-propelled models will be demonstrated in the discussion of the results at the end of this paper.

ANALYSIS OF TRAJECTORY DATA

Because of the large diversity of shapes and flight conditions of explosion-propelled projectiles, at the first step of the experimental investigation it is desirable to use a simplified approach to the analysis of the data from the trajectory investigation. The basic equations of the longitudinal and transverse accelerations of the center of gravity of the model under the action of aerodynamic forces and the equation of the angular oscillation (the angle of pitching) have the form[7]

$$\ddot{X} = -(C_x \cos \Theta + C_y \sin \Theta)(\rho S/2m)V^2,$$

$$\ddot{Y} = (C_y \cos \Theta - C_x \sin \Theta)(\rho S/2m)V^2,$$

$$\ddot{\theta} = -C_m(\rho S/2m)r^{-2}LV^2. \tag{1}$$

Let us consider Fig. 4, where, just as in Eqs. (1), C_x, C_y, and C_m are the static aerodynamic coefficients, m is the mass of the model, S is the area of the midsection, ρ is the air

density, V is the velocity, α is the angle of attack, θ is the pitch angle, Θ is the angle of inclination of the trajectory, r is the transverse radius of gyration, X and Y are the coordinates of the center of gravity of the model, t is the time, and an overdot signifies differentiation with respect to time.

Introducing, as is usually done, the ballistic coefficient $k = \rho S/2m$ and the coefficient of the radius of gyration $b = L/r^2$, we can rewrite the system (1) in a different form. First, it is helpful to make the following assumptions in the trajectory measurements. They follow from the initial conditions of the experiment and physical considerations concerning the ratios of the longitudinal and transverse accelerations. We produced oscillations of our models in the vertical plane XY (Fig. 4) $V^2 \sim (\dot{X})^2$, $\dot{Y}^2 \ll \dot{X}^2$, and $\ddot{Y} \ll \ddot{X}$. Then the simplified system of equations — the dynamical equations of planar motion of the center of gravity and oscillations under the action of the aerodynamic moment — assume the form

$$\ddot{X} = -kC_x(\dot{X})^2, \quad \ddot{Y} = kC_y(\dot{X})^2, \quad \ddot{\theta} = -kbC_m(\dot{X})^2. \tag{2}$$

Under these assumptions each coefficient C_x, C_y, and C_m can be determined from its equation independently.

Direct double differentiation of the tabulated functions $X(t)$, $Y(t)$, and $\theta(t)$ constructed from data obtained from measurements performed on the photographs leads to large errors in the computed values of C_x, C_y, and C_m if appropriate measures to smooth the initial data are not taken.[7]

The aerodynamic coefficients $C_x(t)$, $C_y(t)$, and $C_m(t)$ are obtained in the course of the numerical solution of Eqs. (2). Since the dependence of the angle $\theta(t)$, actually the angle of attack, is known, taking account of physical considerations concerning the behavior of $C_x(\alpha)$, $C_y(\alpha)$, and $C_m(\alpha)$ the corresponding polynomial dependences of these coefficients can be constructed by comparing the tables. As a rule, a biquadratic dependence on the angle of attack is used for $C_x(\alpha)$, which is an even function, and polynomials with a cubic term are used for $C_y(\alpha)$ and $C_m(\alpha)$, which are odd functions. We note that for large angles of attack the functions $C_x(\alpha)$, $C_y(\alpha)$, and $C_m(\alpha)$ are found less reliably because of their nonlinearity.

PRINCIPLES OF NUMERICAL SIMULATION

Because of the complicated composite shapes typical of explosion-propelled projectiles, numerical simulations char-
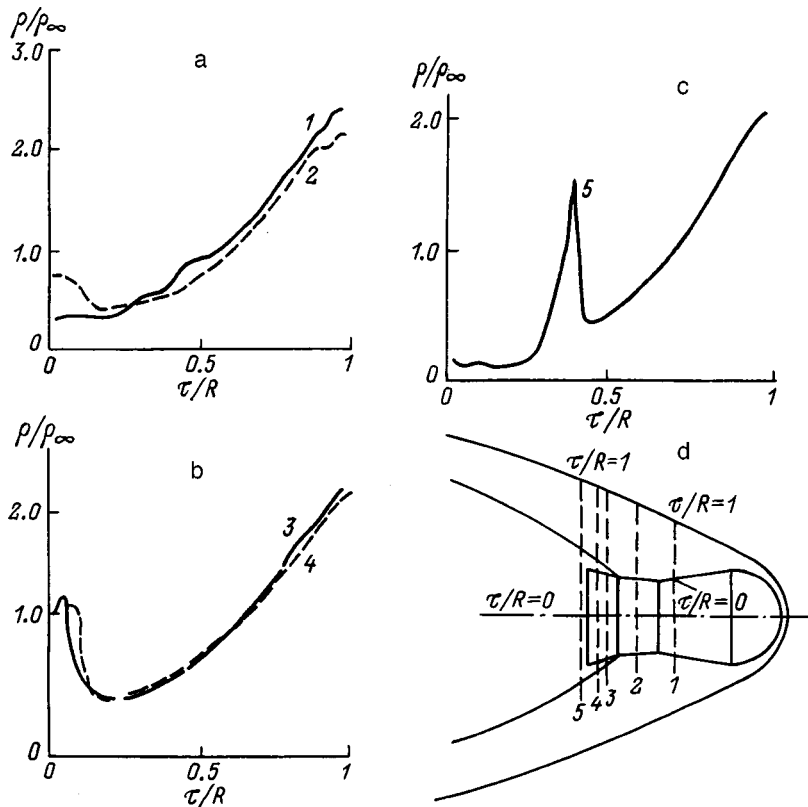
FIG. 5. Radial density profiles in sections of an explosion-propelled model (teardrop shape; Fig. 3): a — in sections above the lateral surface in front of the jump from the stabilizing fin, b — in sections above the stabilizing fin, c — in the section of the bottom region, d — axial section of the model with the positions of the analyzed sections shown.

acteristically yield more information on the thermodynamic parameters of the flow around them than do experimental investigations. Numerical simulation certainly permits detailed variation of the gasdynamic similarity criteria, primarily the geometry of the components and the Mach numbers. We know of an entire hierarchy of mathematical models of different levels of complexity, which has to do with the dimension of the problem and the reproducibility of the hypersonic features of flow in application to the indicated bodies.[3]

A numerical calculation of the three-dimensional flow around compound shapes of bodies which are typical for explosion-propelled objects was developed on the basis of a simplified mathematical procedure. It includes combining the well-known Newtonian approach and a method for calculating a potential flow. The procedure uses the experimental data. This very simple mathematical model makes it possible to estimate the aerodynamic coefficients of an axisymmetric body (as well as bodies deviating from symmetry) moving with moderate angles of attack. The corresponding numerical procedure was inserted in the subroutine describing the plano-oscillatory motion of a body along a trajectory. This made it possible to compare with experimental data.

The computational procedure developed was checked by comparing with ballistic experimental data and the results of test calculations. A comparison was performed along the contour of the bow shock wave and other waves near the model. The aerodynamic drag established in tunnel and ballistic experiments was compared with the computed value of this parameter. Satisfactory agreement was found for all parameters compared.

EXPERIMENTAL RESULTS

The brief discussion of methods for investigating the flow around and motion of hypervelocity objects (explosion-propelled projectiles) gives a basis for demonstrating a number of typical results concerning the flow parameters and the aerodynamic characteristics. The data were obtained for objects with $L/D = 1.8$–2, differing by the shape of the generatrix of the body and by the aspect ratio. All models had an axisymmetric shape, and the center of gravity was shifted toward the nose by construction (Fig. 1). Figure 5 shows the radial density profiles around a teardrop-shaped projectiles. The distributions are characteristic for supersonic flow around a bluff body. The density profiles in front of the fin (1–5) in Fig. 5 show the appearance of a stand-off shock. The density profiles above the fin show a strong density jump in the stabilizing shock wave. The last plot (Fig. 5c) demonstrates the density distribution in a transverse section of the bottom region. The plot contains a strong density jump on the radius where the section meets the inner shock wave.

Let us summarize the experimental results concerning the aerodynamic characteristics.

1. A teardrop-shaped projectile with a diameter of the head part close to the fin and $L/D = 1.83$ showed a low margin of stability. The center of gravity of the model was shifted by construction to $x_{c.g}/L = 0.45$ from the nose piece. To make the body more stable, a conical stabilizer must be placed farther from the center of gravity of the projectile for any ratio L/D of the latter (Fig. 3). The aerodynamic drag of the model was $C_x = 0.97$ in the range of angles $a = 0 - 4°$.
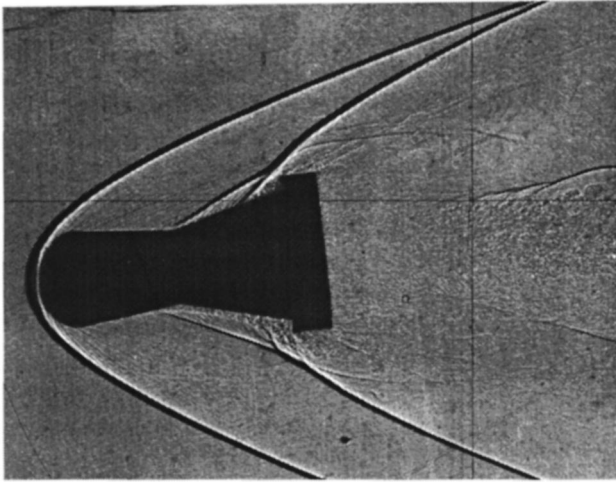
FIG. 6. Direct shadow pattern of an explosion-propelled model in flight with Mach number 4.08. In flight the model is stabilized mainly by the presence of the conical fin and by a shift of the center of gravity toward the nose (Fig. 1).

This is 7% higher than for a sphere under the same conditions because of the nonzero angles of attack of the model. The Mach number was 4.35.

2. A compound conical model of a projectile with a thinner nose piece had a lower aerodynamic drag. The center of gravity was located at a distance $x_{c.g}/L = 0.68$ from the nose piece. Thus, the margin of stability was small, and the model had a small ballistic coefficient and, correspondingly, large spatial deviations in flight. The drag for angles of attack $a = 0 - 2°$ was $C_x = 0.60$. The Mach number was 4.7.

3. The center of gravity of a model with a compound shape with a spherical blunt nose with diameter half that of the fin, an inverted cone, and an expanded conical stabilizer, is located at $x_{c.g}/L = 0.63$. The step near the bottom section, whose diameter was 13% greater than that of the cone, had an additional stabilizing effect (Fig. 6).

The drag for average oscillations of the angle of attack near 2° was $C_x = 0.57$. The Mach number was 4.08. The data obtained for this model with $L/D = 1.93$ show that among the shapes investigated it is the best one with respect to both the aerodynamic drag and the longitudinal stability at moderate angles of attack. The data presented are collected together in Table I.

CONCLUSIONS

The main region of analysis of the density field of our objects are the separation zone, formed above the lateral surface in front and behind the fin, and the bottom region. The density distributions near and above the stabilizing fin are

important for understanding the process stabilizing the flight of an explosion-propelled projectile. Estimating the density jump in the wave from the fin quantitatively, the investigator determines whether or not the angle of and the arrangement of the fin are adequate for obtaining the required restoring force. Low values of the bottom density (pressure) for explosion-propelled models are characteristic for any conical shapes at Mach numbers 4–5.

It is impossible to perform a numerical calculation of the flow around a model in a simplified formulation without knowing the boundaries and sizes of the separated formations and the corresponding shock-wave structure. In turn, the experimental values of the average density (proportional to the pressure) around and near the body serve as a check of the validity of the assumptions made in the calculations.

It is helpful to present a brief conclusion about the aerodynamics of three shapes of explosion-propelled projectiles. The teardrop-shaped model, studied in greatest detail, characteristically has a low margin of stability (with a large shift of the center of gravity toward the nose) and an impressive aerodynamic resistance $C_x \sim 1$. For a model with a head part with a smaller diameter and with an extended stabilizer, the drag was $C_x = 0.60$. However, the stability was low because the center of gravity was not located near the nose. An explosion-propelled model with a step on the fin in front of the bottom with $x_{c.g}/L = 0.63$ showed simultaneously good stabilizing properties and acceptable drag. This made this shape the best among the models investigated.

It is of interest to check (in order to optimize the projectiles) the effect of replacing the fin by a slotted star-shaped fin on the stability and drag. How will this effect the density profiles behind it? Because the effective surface area is smaller, the total contribution of a slotted fin to the wave resistance will be smaller. The bottom pressure should be higher and the bottom resistance correspondingly lower than for a solid fin. This is due to the air flow through the slots. However, a star-shaped stabilizer gives rise to the danger of sharp wave configurations appearing. Their effect on aerodynamics is not obvious. Analysis of the wave structure of a star-shaped stabilizer using the experimentally obtained optical pictures is helpful for developing an effective engineering method for calculating the flow around a projectile.

TABLE I.

Model No.	Mach number M	Aspect ratio L/D	Centering $x_{c.g}/L$	Angle of attack α, deg	Drag
1	4.35	1.83	0.45	0–4	0.97
2	4.70	1.77	0.68	0–2	0.60
3	4.08	1.93	0.63	0–2	0.57

[1] D. Warken and H. Schilling, Report Ernst-Mach Institute, No. 1/86 (Freiburg, Germany, 1986).

[2] S. M. Dvirnyĭ, P. I. Kovalev, and S. G. Tomson, Preprint No. 1509 [in Russian], A. F. Ioffe Physicotechnical Institute, St. Petersburg (1991), 22 pp.

[3] S. A. Isaev, A. Ju. Mitin, A. N. Mikhalev *et al.*, in *Proceedings of the International Conference on the Methods of Aerophysical Research*, Novosibirsk, 1992, pp. 63–66.

[4] I. M. Dementjev, I. A. Kamalov, and P. I. Kovalev, Opt. Lett. **19**, 316 (1987).

[5] N. P. Mende and Yu. E. Shtengel', Preprint No. 1564 [in Russian], A. F. Ioffe Physicotechnical Institute, St. Petersburg (1991), 25 pp.

[6] H. Schardin, Ergeb. Exakten. Naturwiss. **20**, 303 (1942).

[7] I. A. Belov, I. M. Dement'ev, S. A. Isaev *et al.*, Preprint No. 1033, A. F. Ioffe Physicotechnical Institute, St. Petersburg (1986).

Translated by M. E. Alferieff

Some effects of the electrostatic interaction of water drops in the atmosphere

B. A. Saranin

V. G. Korolenko Glazov State Pedagogical Institute, 427600 Glazov, Russia

The electric field at the surface of two conducting spherical charged particles and their interaction force are calculated. It is shown that as particles carrying like charge approach each other, the force changes sign and becomes attractive. The case where the charge on each particle varies as the square of its radius is an exception (repulsion at any distance between the particles). Self-similar asymptotic solutions for the interaction force and energy are found for particles of identical size. For a pair of charged water drops falling simultaneously in the atmosphere, a numerical simulation shows that a drop formed by coalescence of the pair may be subject to the Rayleigh instability. © *1999 American Institute of Physics.*
[S1063-7842(99)00312-8]

INTRODUCTION

The interaction of water drops in the atmosphere has a decisive effect in the formation of precipitation, thunderstorms, and other atmospheric phenomena. A comprehensive study of this interaction is therefore appropriate. The well-known phenomena involving drops include, for example, electrification, coalescence, fragmentation, and corona discharges. It is important to know the role of particular factors in the development of a phenomenon. It is obvious that the electric field at the surface of drops and the electric forces acting on the drops are important factors that influence the course of the processes involving drops. Therefore it is necessary to develop efficient methods for calculating these parameters to a high degree of accuracy.

In the often cited paper by Davis[1] (see also Refs. 2–4) a method was proposed and implemented for calculating the electric fields at the surfaces of two spherical charged particles in a uniform external field and the electrical interaction force between them. The computational method in Ref. 1 is quite cumbersome and the results are hard to reproduce. In the present paper a simpler method is proposed for calculating the electric fields and interaction force without taking the external field into account.

DERIVATION OF RELATIONS FOR CALCULATING THE ELECTRIC FIELD AND INTERACTION FORCE

Let us consider two conducting spheres with radii R_1 and R_2, separated by a distance l and possessing charges q_1 and q_2. As a result of electrostatic induction, the charge of the first sphere creates in the second sphere an electric image Q_{11}, which in turn is a source of a secondary image q_{12} in the first sphere (Fig. 1). Thus the electric field at the point A is produced by an infinite number of charges — the image charges formed in the two spheres. If only the first sphere is charged, then the field at point A can be represented in the form

$$E_{A1} = k\left(\sum_{n=1}^{\infty} \frac{q_{1n}}{r_{1n}^2} - \sum_{n=1}^{\infty} \frac{Q_{1n}}{R_{1n}^2} \right), \quad k = 1/4\pi\varepsilon_0. \tag{1}$$

Using the results of Ref. 5, we can write

$$q_{1n} = q_1 \frac{\gamma \sinh \beta}{\sinh n\beta[\gamma + \sinh(n-1)\beta/\sinh n\beta]},$$

$$Q_{1n} = -q_1 \frac{\gamma \sinh \beta}{r(1+\gamma)\sinh n\beta},$$

$$r_{1n} = \frac{1}{1+\gamma} - r + \frac{r\gamma}{\gamma + \sinh(n-1)\beta/\sinh n\beta}, \tag{2}$$

$$R_{1n} = r - \frac{1}{1+\gamma} - \frac{r\gamma[\gamma + \sinh(n-1)\beta/\sinh n\beta]}{1+\gamma^2 + 2\gamma\cosh\beta}. \tag{3}$$

Here $r = l/(R_1 + R_2)$, $\gamma = R_2/R_1$, and the parameter β is related with the distance between the centers of the spheres as

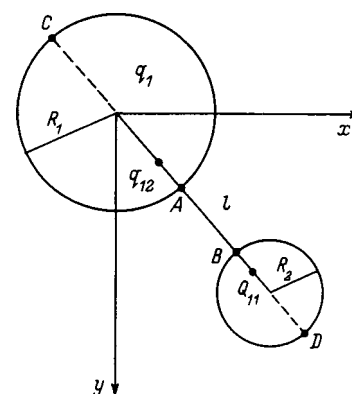$$\cosh\beta = \frac{r^2(1+\gamma)^2 - (1+\gamma^2)}{2\gamma}. \tag{4}$$

FIG. 1. Relative arrangement of charged drops and the coordinate system.

Now let the first sphere be uncharged, $q_1 = 0$, and the let the second sphere carry a charge q_2. Then we have, similarly, for the electric field at point A

$$E_{A2} = k\left(-\sum_{n=1}^{\infty} \frac{q_{2n}}{r_{2n}^2} + \sum_{n=1}^{\infty} \frac{Q_{2n}}{R_{2n}^2}\right), \qquad (5)$$

$$q_{2n} = q_2 \frac{\sinh \beta}{\sinh n\beta[1 + \gamma + \sinh(n-1)\beta/\sinh n\beta]},$$

$$Q_{2n} = -q_2 \frac{\sinh \beta}{r(1+\gamma)\sinh n\beta}, \qquad (6)$$

$$r_{2n} = -\frac{1}{1+\gamma} + \frac{r}{1 + \gamma \sinh(n-1)\beta/\sinh n\beta},$$

$$R_{2n} = \frac{1}{1+\gamma} - \frac{r[1 + \gamma \sinh(n-1)\beta/\sinh n\beta}{1 + \gamma^2 + 2\gamma \cosh \beta}. \qquad (7)$$

If both spheres possess nonzero charge, the field at point A is

$$E_A = E_{A1} + E_{A2} = \frac{kq_1}{R_1^2} K_1. \qquad (8)$$

The field at point B (Fig. 1) can be calculated using the same formulas as at point A but with the substitutions $\alpha \to 1/\alpha$ ($\alpha \equiv q_2/q_1$), $\gamma \to 1/\gamma$ and, correspondingly, it is given by

$$E_B = \frac{kq_2}{R_2^2} K_2. \qquad (9)$$

The quantities K_1 and K_2 defined in this manner are essentially the enhancement factors of the self-field of each sphere.

To find the force acting on each sphere, we first write their interaction energy in the form[6]

$$W = \frac{1}{2}(q_1^2 s_{11} + 2q_1 q_2 s_{12} + q_2^2 s_{22}).$$

Here s_{11}, s_{12}, and s_{22} are potential coefficients. However, it is more convenient to use capacitance coefficients, since the expressions for them are well known. Then, the interaction energy in dimensionless form will be

$$W = \frac{(1+\gamma)}{2\alpha}\left[\frac{\alpha^2 c_{11} - 2\alpha c_{12} + c_{22}}{c_{11}c_{22} - c_{12}^2}\right]. \qquad (10)$$

The energy is expressed in units of $k|q_1 q_2|/(R_1 + R_2)$, and the capacitance coefficients are expressed in units of R_1/k. The expressions for c_{11}, c_{12}, and c_{22} in the units chosen can be written as[6]

$$c_{11} = \gamma \sinh \beta \sum_{n=1}^{\infty} [\gamma \sinh n\beta + \sinh(n-1)\beta]^{-1},$$

$$c_{12} = -\frac{\gamma \sinh \beta}{r(1+\gamma)} \sum_{n=1}^{\infty} (\sinh n\beta)^{-1},$$

$$c_{22} = \gamma \sinh \beta \sum_{n=1}^{\infty} [\sinh n\beta + \gamma \sinh(n-1)\beta]^{-1}. \qquad (11)$$

An expression for the force can be obtained by differentiating Eq. (10) with respect to the distance l between the centers of the spheres. In the units $k|q_1 q_2|/(R_1 + R_2)^2$ it can be represented as

$$F_r = -\frac{\partial W}{\partial r} = -\frac{r(1+\gamma)^3}{2\alpha\gamma \sinh \beta} \oint (c_{ik}, c_{ik}'); \quad i, k = 1, 2. \qquad (12)$$

Here $\oint$ denotes the derivative with respect to β of the expression appearing in brackets in Eq. (10). The derivatives of the capacitance coefficients with respect to β, (c_{ik}'), appearing in $\oint$ can likewise be easily obtained. Like $\oint$, they are too complicated to be written out here.

The dimensionless force and the enhancement factors of the field at the surface of each sphere were calculated on a computer using the formulas derived above. For this, all terms in the sums were expressed in terms of the parameter $z = e^{-\beta}$ [once again, β is determined by relation (4)]. The calculation of the sums was terminated when the parameter z reached machine zero, i.e., 10^{-38} in standard precision, while the calculations done to check the results were performed in the double precision, down to 10^{-80}.

COMPUTATIONAL RESULTS FOR THE ELECTRIC FIELDS AND FORCE

Two cases of the interaction of charged conducting spheres of different sizes are often encountered in theory and practice, and these were examined in greatest detail: a) spheres with equal potentials relative to infinity, and b) spheres with charges that vary as the square of their radii. The case of spheres with equal potentials relative to infinity means that $q_1/q_2 = R_2/R_1$, i.e., $\alpha = \gamma$. This case can occur if, before approaching each other, the spheres are charged from the same voltage source or the potentials are equalized by a corona current. Then, as expected, the field enhancement factors at points A and B (Fig. 2, curve *1*) increase monotonically from 0 to 1 as the distance between the centers of the spheres increases from 1 to ∞ [here and below distances are given in units of $(R_1 + R_2)$]. The field enhancement factor for the larger sphere approaches 1 somewhat more rapidly than that for the smaller sphere.

The situation is much more complicated for the interaction force. For $\alpha = \gamma \neq 1$ the force at close distances between the spheres is attractive and grows without bound as the spheres approach one another. As the spheres move apart, the force changes sign and becomes repulsive, reaches a maximum, and then starts to decrease, and as the distance between the spheres increases further, the field starts to fall off nearly according to the Coulomb law. A typical plot of the force as a function of distance between the centers of the spheres for $\alpha = \gamma = 4.3$ is shown in Fig. 3 (curve *3*); curve *4* corresponds to a point charge and a sphere with $\alpha = 1$; curve *1* corresponds to the Coulomb law. The coordinates of the
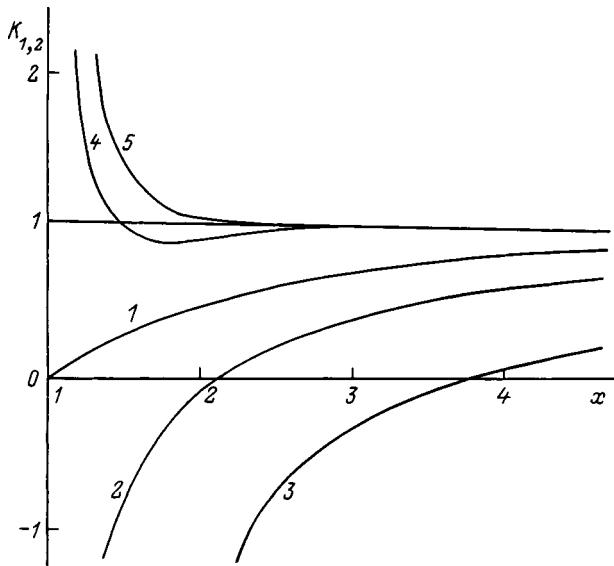
FIG. 2. Enhancement factors for the field at the surface of the particles (at points A and B) versus the dimensionless distance between their centers: $1 — \alpha = \gamma$; $2,4 — \alpha = \gamma^2$, $\gamma = 2$; $3,5 — \alpha = \gamma^2$, $\gamma = 4$. The top curves correspond to the larger particle.

zero and maximum of the force vary as a function of the quantity $\gamma(\alpha)$ in the ranges $1 \leqslant r_0 \leqslant 1.08$ and $r_0 \leqslant r_m \leqslant 1.27$, respectively.

The case of identical spheres $R_1 = R_2$ or $\alpha = \gamma = 1$ is of special interest. In this case, the problems of the field and the interaction force between the spheres become self-similar. Specifically, a calculation of the repulsive force between the spheres as a function of the distance between their centers gives the curve 2 in Fig. 3, and at close distances between the spheres we have the asymptotic solution $F_r = 0.615 F_K$, where F_K is the force calculated in the Coulomb approximation, i.e., for the case where the charges of the spheres are
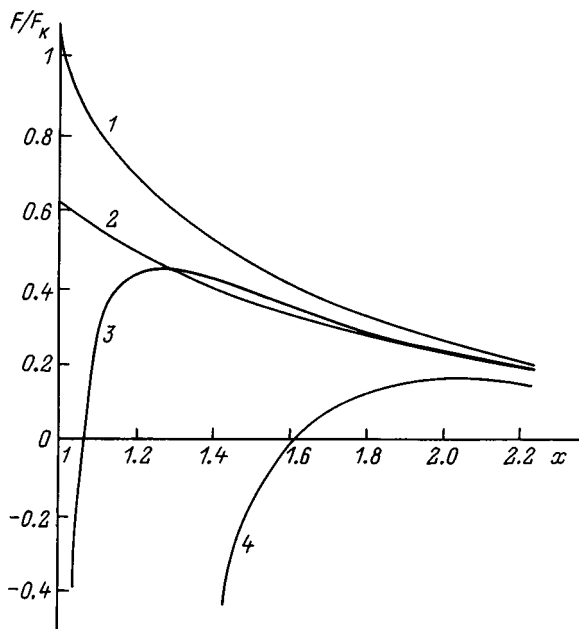

FIG. 3. Curves of the dimensionless force acting on a particle versus the dimensionless distance between their centers.

assumed to be concentrated at their centers. The corresponding asymptotic solution for the energy gives $W = 0.885 W_K$.

If the charges of these spheres have different signs, $\alpha = -\gamma = -1$, then as the spheres approach one another, their interaction force increases without bound according to the asymptotic law

$$F_r = -\frac{4 F_K}{S(\ln(2/s) + 1)^2}, \quad S = r - 1, \tag{13}$$

which is established using the Euler–Maclaurin summation formula

$$\sum_{n=1}^{\infty} f(n) = \int_1^{\infty} f(t)dt + \frac{1}{2}\left(f(1) + f(\infty)\right)$$

and then expanding the result in a Taylor series in $\beta \ll 1$. The interaction energy remains finite and approaches $2 W_K$ as the spheres approach each other. A numerical calculation of the field at point A (B) showed that in the present case the behavior of the field at the indicated point as a function of the distance between spheres is described quite well (with an error not exceeding 1%) for any $S > 0$ ($r > 1$) by Pick's approximate formula[7]

$$E = \frac{1}{S}(1 + 2S + \sqrt{(1 + 2S)^2 + 8}). \tag{14}$$

We shall now discuss the computational results for the case where the ratio of the charges on the spheres equals the square of the ratio of their radii, i.e., $\alpha = \gamma^2$. This case can occur in practice if the charges of the spheres arise as a result of their inductive charging in an external electric field. As is well known,[2] in this case the limiting charge on a sphere of radius R is

$$q = c_a E_0 R^2,$$

where c_a is a constant factor that depends on the specific charging mechanism and E_0 is the external field.

In this case, in contrast to the first, the question of the interaction force between the spheres can be answered unexpectedly easily: It is repulsive for all distances between the spheres. For small $\gamma \lesssim 3$ the repulsive force is close, even quantitatively, to the repulsive force for $\alpha = \gamma = 1$. However, as γ and α increase, the repulsive force approaches the Coulomb limit, i.e., for $\alpha = \gamma^2$ a plot of the dependence of the force on the distance between the centers of the spheres always falls between curves 1 and 2 in Fig. 3.

The field enhancement factors in the case $\alpha = \gamma^2$ behave as follows. At close distances between the spheres the field becomes stronger, so that the electric fields at the surface of each sphere grow without bound as the spheres come closer to one another. In the process, the field at the surface of the smaller sphere (at point B in Fig. 1) is directed into the sphere (for definiteness, we shall assume that both spheres are positively charged), i.e., it is negative, if the spheres are located sufficiently close to one another. The corresponding plots of the field enhancement factors as a function of the distance between the centers of the spheres are shown in Fig. 2: curve 2 ($\gamma = 2$, $\alpha = 4$) and curve 3 ($\gamma = 4$, $\alpha = 16$). The field at the surface of the larger sphere (at point A in Fig. 1)

is always directed away from it (curves *4* and *5* in Fig. 2, which also correspond to $\gamma=2$ and 4). It is evident that as γ decreases to 1, the curves of the field enhancement factors as a function of the distance between the spheres approach the function $E(r)$ for the case $\alpha=\gamma=1$.

We note that Davis[1] solved the more general problem of determining the field at points *A* and *B* (Fig. 1) and the interaction force between the spheres. However, the results of the numerical calculations of the electric fields and forces in Ref. 1 are valid only qualitatively. For example, in the absence of an external field, for $\alpha=1$, $\gamma=1$, and $r=1.005$, according to Ref. 1 the dimensionless electric field at points *A* and *B* has the value $E_A=56.06$, which is almost four times smaller than the value calculated in the present work using Eqs. (1)–(8) or Pick's formula (14): $E_A=200.7$. Large discrepancies also remain for other not-too-large distances between the spheres. These unsatisfactory results[1] are probably due to the insufficient accuracy of calculations of the sums of the series (in Ref. 1 summation was terminated if the magnitude of the terms in the series dropped below 0.1, while in the present work the summation was terminated below 10^{-38}).

INTERACTION OF CHARGED DROPS

Using the results obtained above, we shall now examine certain nonstandard effects due to the interaction of charged drops in the atmosphere. Specifically, the attractive force arising as a result of the interaction of drops with like charge can promote coalescence of the drops, as a result of which the radius and charge of a drop increase. Let us assume that before coalescing, both drops satisfy the Rayleigh stability condition

$$Q_i^2 \equiv \frac{kq_i^2}{16\pi\alpha_S R_i^3} < 1, \quad i=1,2,$$

where α_S is the surface tension of the drops.

Then there arises the question of whether the drop formed is Rayleigh-stable or falls in the parameter range where the spherical drop formed is in unstable equilibrium. To answer this question we write the Rayleigh parameter for the drop formed as

$$Q^2 = \frac{k(q_1+q_2)^2}{16\pi\alpha_S(R_1^3+R_2^3)} = Q_1^2 \frac{(1+\alpha)^2}{1+\gamma^3}.$$

Then the stability condition for the initial drops and the instability condition of the resulting drop form the following system of inequalities:

$$Q_1^2 \frac{(1+\alpha)^2}{1+\gamma^3} \geq 1, \quad \frac{Q_1^2\alpha^2}{\gamma^3} < 1, \quad Q_1 < 1. \quad (15)$$

As was shown above, in the general case the field at the surface of the drops increases strongly as the drops approach each other, and this can result either in a Taylor instability of the drops[8,9] or a corona or spark discharge. The discharge equalizes the potentials of the drops. But, for equal potentials, the fields on the near surfaces of the drops decrease as the drops approach each other, making the Taylor instability
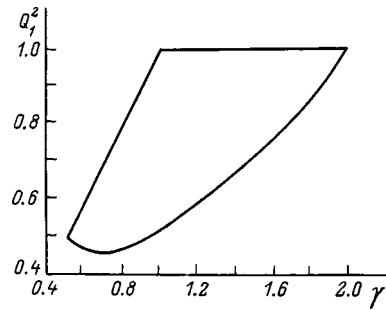

FIG. 4. The parameter region in which the equilibrium of the drop formed by the coalescence of two smaller drops is Rayleigh unstable.

and the discharge unlikely. For this reason the case of equal drop potentials $\alpha=\gamma$ is of interest for answering the question posed. Setting $\alpha=\gamma$ in Eq. (15), we obtain the inequalities

$$\frac{Q_1^2(1+\gamma)}{1-\gamma+\gamma^2} \geq 1, \quad Q_1^2 < \gamma, \quad Q_1^2 < 1. \quad (16)$$

Satisfying this system, we shall find the following limits for the ranges of variation of the parameters where the Rayleigh instability condition holds for the drop formed:

$$0.46 \leq Q_1^2 < 1; \quad 0.5 < \gamma < 2. \quad (17)$$

This parameter region is shown in Fig. 4.

To assess the possibility of the coalescence and instability of drops under atmospheric conditions, let us examine the free fall of two nearly spherical drops. We write the equations of motion of the drops, assuming that initially the drops are quite close to each other and possess a negligibly low velocity relative to the air, and then they are set into free fall. In this formulation of the problem, when the drop velocities are low, the drag due to the air can be neglected, and only gravity and electric forces need be taken into account. Then we have the following equations of motion, written in dimensionless form, for the centers of mass of the drops:

$$\frac{d^2\mathbf{r}_i}{dt^2} = \mathbf{j} \pm f_q \frac{\mathbf{r}_1-\mathbf{r}_2}{r}, \quad r=|\mathbf{r}_1-\mathbf{r}_2|; \quad i=1,2, \quad (18)$$

$\mathbf{j}$ is a unit vector directed vertically downwards. Here the unit of length is the same as before, the unit of time is $[t]=\sqrt{(R_1+R_2)/g}$, and the quantity f_q is

$$f_q = \frac{3kq_1q_2}{4\pi\rho g(R_1+R_2)^2 R_1^3} f(r),$$

where f was calculated according to Eq. (12).

In the numerical integration of Eq. (18) in the x,y plane, the initial velocities of the drops were assumed to be 0, and their arrangement was varied.

The possibility that a charged drop is unstable in an external electric field (produced by a neighboring drop) was assessed according to the dimensionless number[8,9]

$$\mathrm{Ne} = \frac{kq^2}{16\pi\alpha_S R^3} + b\frac{\varepsilon_0 E_S^2 R}{4}, \quad (19)$$

where E_S is the external field at the surface of the drop.

The second term in this expression is responsible for the Taylor instability at $q=0$, which in a uniform field occurs if[8]

$$\frac{\varepsilon_0 E_0^2 R^2}{4\alpha_S} \geqslant 0.052, \qquad (20)$$

where E_0 is the external field at a large distance from the drop.

At the onset of instability the drop is a prolate ellipsoid with a ratio of semiaxes $\varkappa = 1.0$. Therefore the field at the surface of a drop (at the tip of the ellipsoid) is[10]

$$E_S = \frac{E_0}{n_x(\varkappa)},$$

$$n_x = \frac{1-e^2}{2e^3}(\tanh^{-1} e - 2e), \quad e = \frac{1}{\varkappa}\sqrt{1-\varkappa^2}. \qquad (21)$$

Calculations of n_x with $\varkappa = 1.9$ give $1/n_x = 5.45$. Then we have instead of Eq. (20) the condition

$$\frac{\varepsilon_0 E_S^2 R}{4\alpha_S} \geqslant 1.54.$$

Therefore the coefficient b in Eq. (19) can be taken as $b = 1/1.54$. Then the possibility of instability of the surface of the drops as they approach one another can be assessed according to the condition $\text{Ne} \geqslant 1$.[9] The value of the parameter Ne was calculated at the points A, B, C, and D (Fig. 1) in the course of a numerical calculation of the coordinates of the falling drops.

The numerical simulation of two simultaneously falling drops showed that there does indeed exist a range of parameters where the condition $\text{Ne} < 1$ is satisfied as the drops approach one another, the drops coalesce, and after coalescence the Rayleigh instability condition holds for the drop formed. Specifically, this is valid for drops with radii 0.2 and 0.18 mm and charges 0.04 and 0.36 nC.

Therefore the possible results of the interaction of a pair of drops with like charge in the atmosphere could be that the drops fly apart or coalesce with Rayleigh instability followed by fragmentation of the resulting drop occurring. We note that qualitatively all these interaction scenarios have been observed experimentally.[4]

It is also of interest to examine the process of oppositely charged drops approaching one another in order to determine which of two competing processes predominates: spark breakdown between the drops or development of a Taylor instability of their surface (it is assumed that the charges of the drops satisfy the Rayleigh stability condition). We note that this question is a subject of discussion.[11] For this, in the course of the numerical calculation of the coordinates of drops with the same radii ($\gamma = 1$) but opposite sign of the charge ($\alpha = -1$), the field at point A (B) and the parameter Ne responsible for the Taylor instability were calculated in the falling regime. To judge the possibility of breakdown the computed value of the electric field was compared with the spark-breakdown field, which was calculated as a function of the radius of the drops according to the formula[12]

$$E_* = 27.2\left(1 + \frac{0.54}{\sqrt{R}}\right) \text{ kV/cm},$$

where R is the radius of the drops in cm and E_* is the breakdown field in kV/cm.

This formula is valid for $0.27 \leqslant S \leqslant 1$. The numerical experiments showed that as drops approach one another, for most of the drop spectrum, the Taylor-instability condition $\text{Ne} \geqslant 1$ is satisfied before the spark-breakdown condition. However, for relatively large drops ($R \gtrsim 1$ mm) cases were observed in which the condition $\text{Ne} < 1$ was satisfied for $E_A > E_*$. For example, for drops with $R_1 = R_2 = 1$ mm and $q_2 = -q_1 = 0.4$ nC for $r = 1.75$ the condition $E_A > E_*$ ($E_* = 75$ kV/cm) started to hold when $\text{Ne} = 0.7$. Considering the approximate character of the investigation and the fact that Ne is close to 1, it can be assumed that spark breakdown between drops, if it is possible at all, is very unlikely, and the dominant effect is Taylor instability of the drops.

CONCLUSIONS

The analytical and numerical investigations established the following.

1. The calculations of the electric field in the gap between two charged conducting spheres showed that in the general case of spheres with different radii and like charges, as the spheres approach one another the field increases substantially, and it changes sign on the surface of the smaller sphere. The case of spheres with the same potentials is an exception: In this case the field decreases to 0 invariantly as the spheres approach one another.

2. Calculations of the interaction force showed that in the general case of spheres with like charge and different radii, as the spheres approach one another, the force changes sign, becoming increasing with respect to the modulus of the attractive force. The case where the charges of the spheres vary as the squares of their radii is an exception: In this case the force decreases invariantly with increasing distance between the spheres, remaining attractive.

3. In the self-similar case of spheres with equal radii and charges of equal modulus, the asymptotic solutions for the interaction force and energy were found numerically and analytically. Specifically, it was established that when spheres with like charge almost touch one another, the real interaction force is about 62% of the force calculated in the Coulomb approximation (when the charges are assumed to lie at the centers of the spheres), and the energy is $\sim 89\%$.

4. It was shown that when two spherical, Rayleigh-stable liquid drops carrying like charge coalesce, the resulting drop can be Rayleigh-unstable. The parameter range where this effect is possible was found.

5. Two simultaneously falling charged drops in the atmosphere were simulated numerically. The possible results of the falling and interaction were: 1) the drops fly apart, 2) drops with like and unlike charge coalesce, 3) drops with like charge coalesce and the resulting drop is Rayleigh-unstable, and 4) for large drops with unlike charge a Taylor instability of their surface predominates over spark breakdown between them.

[1] M. H. Davis, Q. J. Mech. Appl. Math. **17**, 499 (1964).

[2] V. M. Muchnik and B. E. Fishman, *Electrification of Coarsely Dispersed Aerosols in the Atmosphere* [in Russian], Gidrometeoizdat, Leningrad (1982), 207 pp.

[3] V. M. Kim, Tr. Inst. Éksp. Meteor. (Gidrometeoizdat, Moscow) **48**(138), 29 (1989).

[4] H. T. Ochs and R. R. Czys, Nature (London) **327**, 606 (1987).

[5] M. V. Mirolyubov *et al.*, *Methods for Calculating Electrostatic Fields* [in Russian], Vysshaya Shkola, Moscow (1963), 415 pp.

[6] W. R. Smythe, *Static and Dynamic Electricity*, 2nd edition [McGraw-Hill, New York (1950); Inostr. Lit., Moscow (1954), 604 pp.].

[7] V. A. Govorkov, *Electric and Magnetic Fields* [Énergiya, Moscow (1968), 487 pp.].

[8] A. I. Grigor'ev and S. O. Shiryaeva, Izv. Ross. Akad. Nauk Mekh. Zhidk. Gaza, No. 3, 3 (1994).

[9] E. I. Mukhina and A. I. Grigor'ev, Zh. Tekh. Fiz. **60**(9), 25 (1990) [Sov. Phys. Tech. Phys. **35**, 1015 (1990)].

[10] L. D. Landau and E. M. Lifshitz, *Electrodynamics of Continuous Media* [Pergamon Press, New York; Nauka, Moscow (1982), 620 pp.].

[11] V. M. Muchnik, *Physics of Thunderstorms* [Gidrometeoizdat, Leningrad (1974), 351 pp.].

[12] G. I. Skanavi, *Physics of Dielectrics* (*Strong Fields*) [Gostekhizdat, Moscow (1949), p. 174].

Translated by M. E. Alferieff

Formation of a shock wave in aerogel irradiated with a high-current pulsed electron beam

B. A. Demidov, V. P. Efremov, M. V. Ivkin, I. A. Ivonin, V. A. Petrov, and V. E. Fortov

Kurchatov Institute Russian Science Center, 123182 Moscow, Russia
(Submitted September 11, 1998)
Zh. Tekh. Fiz. **69**, 18–25 (December 1999)

The propagation of pressure jumps excited by a high-current pulsed electron beam in SiO_2 aerogels with density ranging from 0.025 to 0.25 g/cm^3 is investigated using a laser differential interferometer and optical methods. Spallation on the back side of the aerogel targets is observed and the velocity of the spallation fragments is measured. The expansion velocity of the aerogel in the direction of the electron beam is determined. The parameters of the shock adiabat are established in a wide range of aerogel porosities. The depth of the energy-deposition zone of the electron beam is determined experimentally as a function of the aerogel density in the range from 0.015 to 0.25 g/cm^3. A model describing highly porous materials which reflects the fractal properties of highly porous aerogels is developed on the basis of the experimental data. Numerical calculations of the observed phenomena are performed. © *1999 American Institute of Physics.* [S1063-7842(99)00412-2]

INTRODUCTION

The process proposed in Ref. 1 for the shock compression of porous bodies makes it possible to obtain more complete information about the thermodynamic properties of matter and to investigate the equation of state of matter in a region of the phase diagram that is not accessible by shock loading of a continuous body. In Ref. 2 the results of investigations of shock compression of porous metals are described and a number of theoretical conclusions about the equation of state of porous materials are drawn. A model of a porous material is also presented in Ref. 3, where shock adiabats of a porous material which depend on the degree of porosity are presented. In Ref. 4 experimental results on the power-law dependence of the sound velocity on the porosity in highly porous metals are presented. This can be described using a fractal model with universal exponents that depend on the structure of the materials.[5,6]

SiO_2 aerogels are a unique porous material. They consist of transparent, fine-pore, dielectrics with cluster structure, low density, and small charge number Z. The high transparency of the aerogels makes it possible to investigate experimentally, using optical methods, the process of dynamic compression of porous substances irradiated with a relativistic pulsed electron beam. Interest in aerogels as a new class of materials has increased strongly in the last few years in connection with improvements in the technology for fabricating aerogels[7] and new possible applications, for example, as radiators for Cherenkov counters.[8] The thermodynamics of weakly ionized plasma produced by shock compression has been studied using an SiO_2 aerogel.[9] In optics aerogels are used to perform spectroscopic investigations of complex organic molecules embedded in an aerogel matrix.[10]

In Refs. 11 and 12 an FÉR-7 slit-scan streak camera is used to investigate the dynamics of the interaction of a high-current electron beam with SiO_2 aerogels with different den-

sities (0.03, 0.14, 0.36 g/cm^3) and porosities. The dynamical characteristics of aerogels in the energy-deposition zone of a powerful electron beam are determined. A model describing highly porous materials is developed on the basis of the information obtained about the unloading of aerogels in the energy-deposition zone of the electron beam and measured energy-deposition profiles. A corresponding nonlinear self-consistent equation of state reflecting the thermodynamic characteristics of aerogels with porosity varying by a factor of 10 is obtained. The percolation exponent $\gamma = 1.7$ for a softened aerogel in the energy-deposition zone of an electron beam is found. This value corresponds to the low yield point.[6]

The objective of the present work, in contrast to Refs. 11 and 12, is to investigate the thermodynamic parameters of aerogels with density $\rho = 0.025 - 0.25$ g/cm^3 outside the energy-deposition zone of a high-current pulsed electron beam by measuring the parameters of a shock wave excited by an electron beam in aerogel targets.

Spallation phenomena are also studied and the velocity of the spallation fragments of the aerogel are determined under various experimental conditions. The depth of the energy-deposition zone of an electron beam is measured in a wide range of aerogel densities (from 0.015 to 0.25 g/cm^3). A consistent model of the equation of state of aerogels that correctly describes the new experimental observations is constructed on the basis of the experimental data obtained, which includes measurements of the expansion velocity of the aerogels and the depth of the energy-deposition zone of the electron beam. To obtain maximum information in one irradiation of an aerogel, an experimental arrangement close to that proposed in Ref. 12 but differing by the addition of a laser differential interferometer, used in Ref. 13, was chosen. Using the laser interferometer, the arrival time of the shock wave, excited by the electron beam, at the back side of the
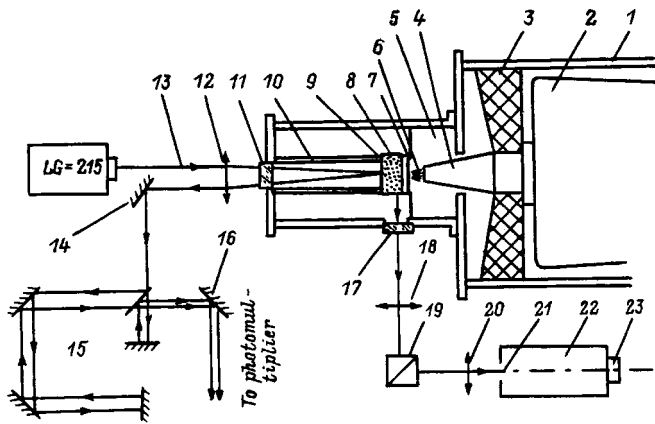
FIG. 1. Diagram of the experiment.

aerogel target was determined to a high degree of accuracy.

In individual cases the laser interferometer made it possible to measure directly the velocity of the back surface of the target.

DESCRIPTION OF THE EXPERIMENT

The experimental arrangement for production of a shock wave in an aerogel irradiated with a high-current pulsed electron beam (electron energy $U_0 = 290$ keV, current $I = 13 - 15$ kA, current duration at half-height $\tau = 150$ ns, electron beam diameter $d = 12$ mm) is displayed in Fig. 1. The exit part of the Kal'mar accelerator,[14] including the case *1*, an exit transformer *2*, a dielectric spacer diaphragm *3*, and a cathode *4*, was connected with a vacuum chamber *5*. The electron beam *6* passed through a 10-μm thick aluminum foil *7* and struck the experimental aerogel sample *8*. A 10-μm thick aluminum foil *9* was glued to the back surface of the aerogel. A lens *12* directed the beam from an LGN-215 laser *13* through a transparent vacuum window *11* onto the central part of the foil *9*, whence it was reflected, and the mirror *14* directed the beam onto the laser differential interferometer *15*. The interference period of the LDI corresponds to 26 m/s. A metal tube *10* with a 16-mm outer diameter protected the laser interferometer from a parasitic light flash, arising when the electron beam interacts with the aerogel and striking the interferometer mirror, that can distort the indications of the interferometer. In addition, the tube *10* also functioned as an acoustic decoupler, ensuring that the arrival time of the shock wave at the back surface of the aerogel sample is measured correctly. The laser beams reflected from the mirror *16* struck the photocathode of a FÉU-84 photomultiplier, the signal from which was detected with an S1-75 oscillograph.

The light flash due to the interaction of the electron beam with the aerogel passed through a transparent vacuum side window *17* and a lens *18* and struck a prismatic device *19*, which rotated the image of the energy-deposition zone of the electron beam by 90° in the horizontal and vertical planes. A lens *20* focused the image on the vertical entrance slit *21* of an FÉR-7 streak camera, which ensured high linearity of light transmission from the aerogel *22*. Sweeps of 0.75, 2.5, 7.5, and 25 μs/cm with a 0.1-mm entrance slit

were used in the experiments. A photoattachment *23* recorded the image from the exit screen of the FÉR-7 streak camera. Aerogel samples with density 0.015, 0.020, 0.025, 0.16, and 0.25 g/cm³, thicknesses ranging from 5 to 34 mm, and dimensions larger than 25×25 mm, right up to 5×500 mm, were investigated. The aerogel samples were of high quality and had good transparency (the pore size in the aerogel was less than the wavelength of the light) and polished walls.

The vacuum gap between the aluminum foil *7* and the aerogel sample *8* was 5 mm for aerogels with different density. In some experiments, to determine the depth of the energy-deposition zone more accurately, the aerogel samples were placed flush against the aluminum foil *7*. The system of lenses *18* and *20* gave an optical reduction such that the image of the aerogel sample and of the vacuum gap between the aerogel and the aluminum foil fit completely in the vertical direction, with room to spare, on the 10-mm high entrance slit of the FÉR-7 streak camera. The optical spatial resolution, which was checked using a test object placed in the region of the aerogel, made it possible to determine the depth of the energy-deposition zone with better than 10% accuracy.

The time-of-flight method was used to determine the velocity of the spalled particles. A tube *10* was moved along the axis of the apparatus away from the aerogel sample to a fixed distance (5–50 mm). The aluminum foil *9* was transferred to the back side of the aerogel target onto the end face of the tube *10*. The moment when the aluminum foil reached the spalled aerogel fragments was recorded with the laser interferometer *15*.

The experimental arrangement was changed for measurements of the propagation velocity of a purely shock disturbance in a low-density aerogel ($\rho = 0.025$ g/cm³), in which the depth of the energy-deposition zone of the electron beam is comparable to the dimensions of the aerogel sample. A $34 \times 50 \times 50$ mm aerogel target was placed on a 60 mm in diameter and 3 mm thick aluminum disk, which served as the anode of the accelerator. A 10-μm thick aluminum foil was glued to the back side of the target. When the electron beam struck the aluminum anode, a pressure jump appeared in the anode and reached the aerogel sample in a time $\tau < 1.0$ μs and propagated in the sample. The arrival time of the pressure jump at the back surface of the target and the velocity of the back surface were determined using the interferometer *15*.

EXPERIMENTAL RESULTS

Figure 2 shows a series of streak photographs, differing by the FÉR-7 sweep rate and illustrating the dynamics of the interaction of the electron beam with the aerogel and the propagation of the radiation front into the aerogel. All streak photographs are for irradiation of a $\rho = 0.25$ g/cm³ aerogel by an electron beam ($I = 15$ kA, $U_0 = 290$ keV). The dashed line marks the thickness of the aerogel. The vertical arrows indicate the arrival time of the shock wave at the back surface of the aerogel, measured with an interferometer. In all streak photographs ($A - C$), with the exception of the photo-
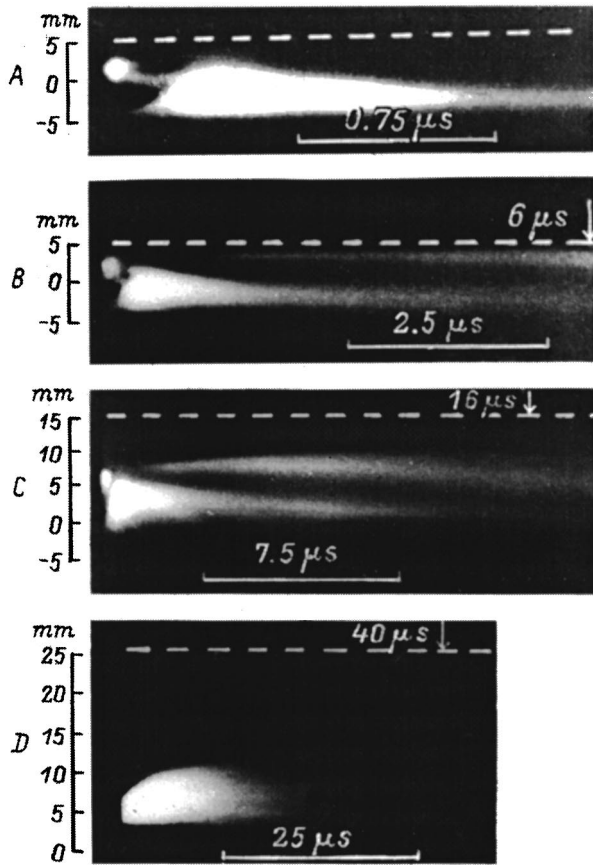
FIG. 2. Streak photographs of the interaction of an electron beam with an aerogel.

FIG. 3. Arrival time of a shock wave at the free surface as a function of the thickness of the aerogel sample.

graph D in Fig. 2, the gap between the aluminum anode foil and the aerogel is 5 mm. For the photograph D in Fig. 2 this gap is zero. It is evident from Fig. 2 that the depth of the energy-deposition zone of the electron beam in a $\rho=0.25$ g/cm^3 aerogel is 3 mm.

Streak photographs obtained with different FÉR-7 scan duration make it possible to determine more accurately the expansion velocity of the aerosol toward the electron beam, the expansion velocity of the anode aluminum foil, and the propagation velocity of the radiation front into the aerogel. Analysis of the streak photographs 2A and 2B shows that the expansion velocity of the aerogel toward the electron beam is 5.75 km/s, and the expansion velocity of the aluminum foil is 10–12 km/s. The streak photograph in Fig. 2C shows that the propagation velocity of the radiation front into the aerogel is $\leqslant 500$ m/s.

Analysis of similar streak photographs obtained for aerogels with other densities and the same irradiation parameters showed that the depth of the energy deposition zone is 17 and 4 mm for 0.025 and 0.16 g/cm^3 aerogels, and the expansion velocity of the aerogel toward the electron beam is 2.5 and 4.5 km/s, respectively. For 0.015 and 0.020 g/cm^3 the depth of the energy-deposition zone increased up to 22 and 19 mm.

The dependence of the arrival time of the shock wave at the back surface of the aerogel sample on the thickness of the sample is shown in Fig. 3. Here the crosses and circles rep-
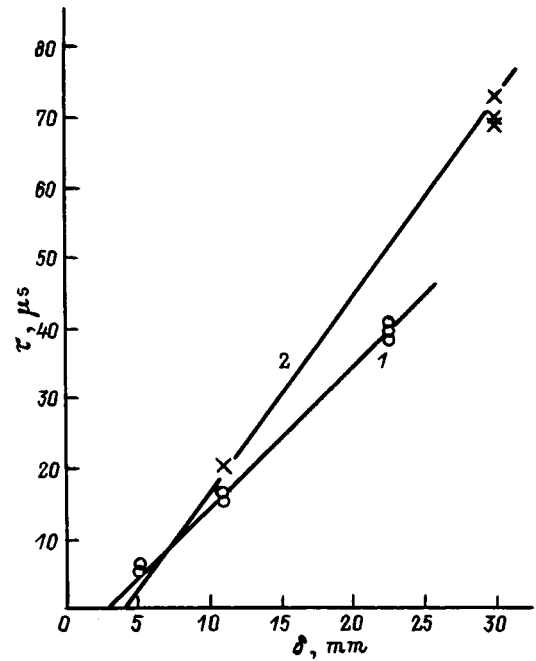
resent the experimental results for 0.16 and 0.25 g/cm^3 aerogels, respectively. Ths slope angle of the straight lines drawn through the experimental points make it possible to estimate the average propagation velocity of the shock front in aerogels with different density for the same electron-beam parameters. As one can see from Fig. 2, these velocities are 350 and 500 m/s for 0.16 and 0.25 g/cm^3 aerogels (curves 2 and 1, respectively).

As noted above, the propagation velocity of the pressure jump in a low-density aerogel was determined by a different method. Figure 4 shows interferograms characterizing the propagation of a pressure jump in a 34-mm thick 0.025 g/cm^3 aerogel in different operating regimes of the accelerator. In the first case (Fig. 4A) the electron beam ($I=15$ kA, $U_0=290$ keV) produced a bulge (spallation) on the back surface of the anode disk, to which the aerogel sample was secured, and spallation on the back surface of the aerogel. In the second case (Fig. 4B) ($I=13$ kA, $U_0=290$ keV) no such
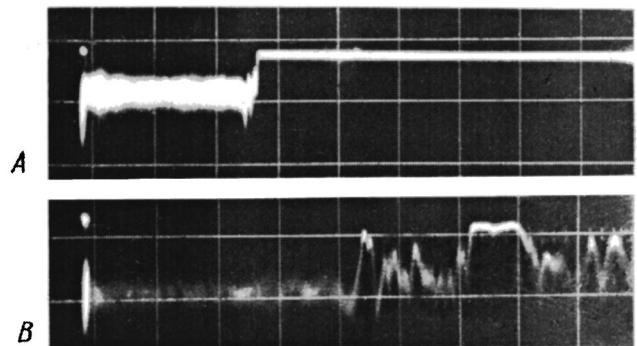

FIG. 4. Interferograms illustrating the propagation of a shock wave in the aerogel (100 μs per division). Shock wave excitation regime: A — strong, B — weak.
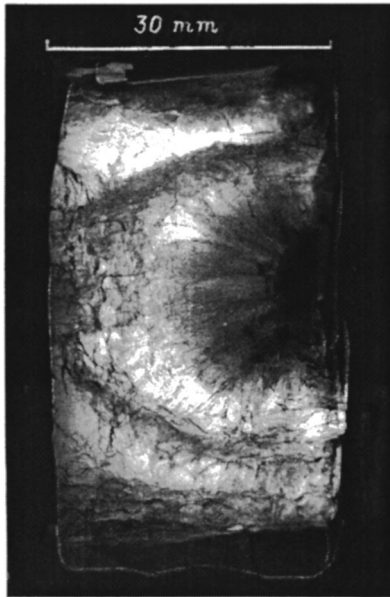
FIG. 5. Aerogel sample after the action of the electron beam.

FIG. 6. Velocity of the spallation fragments as a function of the thickness of the aerogel sample.

bulge was observed. As one can see from Fig. 4, in the first case the interference signal appeared in 270 μs, which corresponds to a propagation velocity of the pressure jump $V = 125$ m/s. This velocity is much lower, 85 m/s, in the second case. It follows from the interferograms in Fig. 4B that the velocity of the back surface of the aerogel is 78 m/s.

The shock waves excited by the electron beam produce the spallation phenomena observed in the experiment. Spalls with a depth of 4 mm were recorded in 22.5 mm thick aerogels ($\rho = 0.15$ g/cm^3). Figure 5 shows an aerogel sample ($\rho = 0.16$ g/cm^3) irradiated with an electron beam ($I = 15$ kA, $U_0 = 290$ keV). The aerogel sample is located in a special holder, which prevented the sample from falling apart after interacting with the beam. The aerogel is 30 mm thick. It is evident from Fig. 5 that the electron beam forms an approximately 4-mm deep crater.

The maximum velocity of the spallation fragments depends strongly on the thickness of the aerogel sample. Figure 6 shows such a dependence for $\rho = 0.16$ g/cm^3 aerogel. As the aerogel thickness increases, the spalled fragments increase in size, forming classical spalled "plates" moving with low velocities. Thin aerogel samples, whose thickness is comparable to or less than the depth of the energy-deposition zone of the electron beam, fly apart with velocities of the order of the expansion velocity of aerogels toward the electron beam. For a 20-mm thick $\rho = 0.025$ g/cm^3 aerogel this velocity is 1.2 km/s. The spallation fragments are much smaller than 1 mm.

DISCUSSION OF THE EXPERIMENTAL RESULTS

The measured depths of the energy-deposition zone of an electron beam ($U_0 = 290$ keV), equal to 3, 4, 17, 19, and 22 mm in aerogels with densities 0.25, 0.16, 0.025, 0.020, and 0.015 g/cm^3, respectively, confirm the results of Ref. 12. In Ref. 12 it was noted that for aerogel densities $\rho < 0.2$ g/cm^3 the effect of a volume electric charge must be taken
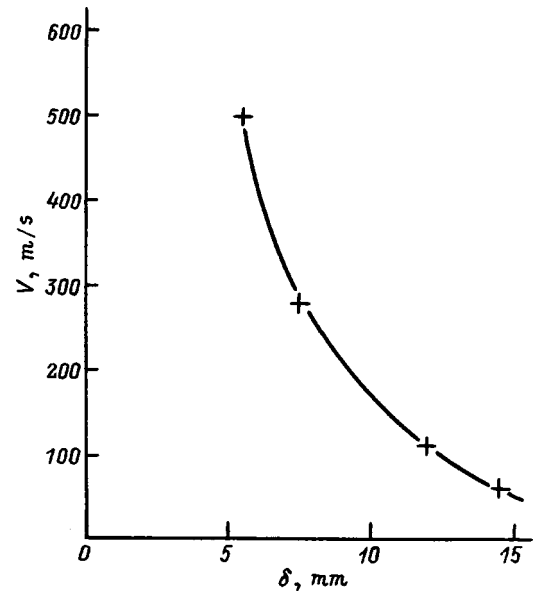
into account. The electric potential in the energy-deposition zone in this case becomes comparable to the initial energy of the electrons in the beam, decreasing the depth of the energy-deposition zone. Indeed, a 17-mm depth of the energy-deposition zone in $\rho = 0.025$ g/cm^3 aerogel is much less than the classical depth, which is 30 mm. For a $\rho = 0.015$ g/cm^3 aerogel this difference is even greater. The initial displacement of the radiation front into the aerogel (with velocity $U \simeq 500$ m/s) as the aerogel undergoes unloading after irradiation seems to occur with mass velocity, since the excited electrons giving rise to the radiation cannot leave the energy-deposition zone. Subsequently, the radiation intensity decreases, which results in a visual stopping of the motion of the radiation front through the aerogel.

The measured expansion velocities of aerogels toward the electron beam are higher than the velocities obtained previously in the experiments of Ref. 12. This is explained by the fact that in the present experiments a more powerful electron beam with the parameters to $I = 15$ kA, $U_0 = 290$ keV than in Ref. 12, where $I = 10$ kA, $U_0 = 270$ keV, was used.

The back-side spall thickness in $\rho = 0.25$ g/cm^3 aerogel, equal to 4 mm, agrees quite well with the depth of the energy-deposition zone. This is consistent with generally accepted ideas.

The effect of a shock wave on a 0.16 g/cm^3 aerogel is illustrated well in Fig. 5, where it is evident that at least two successive back-side spalls, producing mainline cracks, have occurred. The depth of the first spall corresponds to half the energy-deposition zone (or the first appearance of negative normal stresses). The depth of the second spall is of the order of the depth of the energy-deposition zone, attesting to the smallness of the spallation stresses.

The isobar of the tangential stresses (boundary of the turbidity zone), forming a cup-shaped curve, is clearly seen in Fig. 5. Outside this boundary the tangential stresses did not exceed the yield point and the material remained trans-

parent. Tangential shears, accompanied by the formation of cracks greater in size than the wavelength of visible light, which caused the aerogel to become turbid, occurred inside the boundary. The decrease in the transverse size of the turbidity zone toward the back side of the aerogel, is explained by the lateral unloading of the aerogel and by the damping of the shock wave as it propagates into the material.

It is interesting to note that even though the shock front cannot be resolved in the interferograms in Fig. 4 for the slow scan chosen, the velocity of the back surface can still be measured because of the slowness of the decay of the amplitude of the shock wave after the passage of the front.

NUMERICAL SIMULATION

To determine the dynamical characteristics of aerogels and to compare with experiments, we performed numerical calculations of the interaction of an electron beam from the Kal'nar accelerator with aerogels, excitation of a pressure pulse in an aerogel, formation and propagation of a shock wave, as well as spallation phenomena.

Strong electric fields arise in an aerogel when it absorbs an electron beam. These fields result in breakdown of the aerogel and leakage of charge out of the interior volume to the surface of the energy-deposition zone. These electric fields can strongly distort the energy-deposition profile of the electrons.[14] To determine correctly the effect of these fields on the formation of the energy-deposition zone, it is necessary to take account of the high-energy conductivity[15] of dielectrics, which appears when electronic radiation is absorbed.

The high-energy conductivity in wide-gap dielectrics is due to the fact that when an electron cools down to the energy of the band gap, the energy losses decrease sharply (by a factor of 1000) because subsequent excitation of electrons from the band gap into the conduction band is impossible. The main cooling channel for electrons with such energies is interaction with optical phonons and with thermalized electrons.[15] In strong electric fields, the heating of the electrons must be taken into account, and with compensation of the heating and energy losses breakdown due to high-energy electrons occurs. The magnitude of this breakdown field is determined mainly by the energy of the optical electrons and, as a rule, is several orders of magnitude[12,15] less than the standard value of the breakdown voltage of thermalized electrons.

As the electrons cool down further (to less than the energy of optical phonons), the interaction of the electrons with acoustic phonons and traps — lattice defects and impurities — becomes substantial. The energy losses once again increase. For this reason, the contribution of these electrons to the production of conductivity was neglected in our calculations.

The specific energy deposition of the electron beam as a function of the Lagrangian absorption depth and the irradiation time was calculated in the diffusion approximation[16] taking account of the quasistationary generation of electric fields as well as the real current and voltage oscillograms of the Kal'mar accelerator and the dependence of the range of

TABLE I. Depth of the energy-deposition of the electron beam with the electron energy and current density amplitudes $U_0 = 290$ keV and $j = 15$ kA/cm², respectively.

Aerogel density ρ, g/cm²	Electron penetration depth R, mm		
	experiment	calculation	calculation without electrification
0.25	3	3	3
0.16	4	4.5	5
0.025	17	17	30
0.02	19	18	38
0.115	22	20	51

electrons as a function of their energy, taken from Ref. 17.

The experimental results of the present work made it possible to refine the numerical estimate made in Ref. 12 of the breakdown electric field E_{br} of high-energy electrons, which characterizes the band structure of the aerogel. Thus, the best agreement with the experimental results obtains with $E_{br} = 70-80$ kV/cm for aerogels with density $\rho = 0.015 - 0.03$ g/cm² (Table I).

A predictor–corrector Lagrangian method with second-order accuracy[18] and monotonization was used for numerical simulation of the passage of pressure pulses through matter. The system of equations of hydrodynamics was solved numerically taking account of elastoplastic deformations. The system was closed with the Mie–Grüneisen differential equations of state $P(\rho, Q, \Pi)$ of a porous medium with self-consistent variation of the Grüneisen coefficient $\langle \Gamma \rangle$ and the bulk modulus $\langle K \rangle$ as a function of the porosity Π[5,6,11] and with Mies' yield condition.[9] A power-law, percolation-classical model of the coupling of dynamical characteristics of an aerogel with the characteristics of its foundation (fused quartz[19]) was used:

$$\{\langle K \rangle, \langle \Gamma \rangle, \langle \sigma \rangle, \langle Y \rangle,\} = \{K_i, \Gamma_i, \sigma_i, Y_i\}\beta^\gamma,$$

$$\beta \equiv \frac{\langle \rho \rangle}{\rho_i}, \quad \Pi \equiv \frac{1-\beta}{\beta}, \tag{1}$$

where K, Γ, σ, Y, and ρ are, respectively, the bulk modulus, the Grüneisen coefficient, the spallation stress, the yield point, and the density; the brackets refer to a porous aerogel; and the index i refers to the base.

In our experiments the internal energy of the aerogels (i.e., the specific energy deposition minus the work performed by the pressure forces) was of the order of the heat of sublimation of its base. For this reason, in the calculations the system of equations was supplemented by the differential equation of state of the gas phase.

The dependence of the thermodynamic coefficient $\langle \Gamma \rangle = \Gamma_i \beta^\gamma$ in Eq. (1) follows from the general formula for the Grüneisen coefficient of heterogeneous materials[20]

$$\langle \Gamma \rangle = \mu_m \frac{\Gamma_m Q_m}{K_m} \frac{\langle K \rangle}{\mu_j Q_j}, \tag{2}$$

where summation over repeated indices m and j is implied.

Actually, a porous material can be regarded as a particular case of a heterogeneous material consisting of a base and

TABLE II. Unloading of a shock-loaded aerogel (impact of an Al plate irradiated by an electron beam with current density amplitude j_0).

Current density amplitude j_0, kA/cm^2	Pulse emergence time τ, μs		Velocity of back side V_T, m/s	
	experiment	calculation	experiment	calculation
13 (weak regime)	400	360	78	60
15 (strong regime)	270	310	⋯	90

pores. In our case the weight fraction of the quartz base is $\mu_i = 1$, which immediately leads to the desired dependence.

The percolation coefficient γ depends on many factors, primarily on the type of interaction of the atoms.[5,6] Thus, for an isotropic interaction, manifested as a small shear modulus, $\gamma = 1.7$. For a central interaction with the maximum possible shear modulus $\langle G \rangle = 3/4 \langle K \rangle$, the coefficient $\gamma = 4.4$. In Ref. 6 crossover from an isotropic to a central interaction was investigated and it was shown that the percolation coefficient remains in the range 1.7–4.4.

It should be noted that the percolation coefficient γ is the only free parameter in the model under study. All other coefficients refer to the base of the porous material and, as a rule, are known. In our case, the parameters for fused quartz were used in the numerical experiments.[19] Since the shear modulus approaches zero as the temperature increases to the softening temperature, it is natural to take in the energy-deposition zone of a powerful electron beam a percolation coefficient $\gamma = 1.7$, corresponding to the isotropic interaction model. Indeed, numerical experiments showed best agreement with experimental results precisely for this choice.[1] But, heating was negligible behind the shock front which exited from the energy-deposition zone — only several tens of degrees and γ was different from 1.7.

A linear temperature dependence of the coefficient γ was chosen in the calculation. The best agreement with the experimental results was obtained with $\gamma_0 \approx 3.2$ for heated aerogel. Thus, in experiments on the generation of a pressure pulse in $\rho = 0.025$ g/cm^3 aerogel using irradiation of an aluminum plate placed flush against the aerogel (weak shock excitation regime, Fig. 4B), the pressure pulse propagated

only through the unheated aerogel. For $\gamma_0 = 3.2$ the average computed propagation velocity $\langle D \rangle$ of the shock front through a 34 mm thick aerogel was 95 m/s, and the maximum velocity of the back surface was $V_T = 60$ m/s, which is close to the experimental results (Table II). It is interesting to note that, even though the shock front is not resolved with the chosen slow sweep of the experimental interferogram, the velocity of the back surface still can be recorded because of the slowness of the decay of the shock amplitude after the passage of the front. This arose because the stiffness of Al is sharply different from that of the aerogel.

The same sharp difference of the dynamical characteristics of an aerogel arises between the irradiated and unirradiated parts of an aerogel in experiments on its direct irradiation. This is due to the change in the exponent γ. In the heated energy-deposition zone $\gamma = 1.7$, and the elastic moduli and sound velocity are much higher than in the unheated zone with $\gamma_3 = 3.2$. This has the effect that the expansion velocity V_0 of the aerogel from the irradiated surface is also higher than the velocity V_T from the back surface. The computational results for these expansion velocities and the shock propagation time τ in aerogels irradiated in a regime with voltage amplitude $U_0 = 290$ eV and current density $j_0 = 15$ kA/cm^2 are presented in Table III. Comparing the computational and experimental results in this table shows that the self-consistent model presented above for the equation of state of highly porous materials is well-applicable in a wide range of porosities. The results presented in Tables II and III also show that the computational model is suitable for describing aerogels under various conditions and with different load intensities.

CONCLUSIONS

The excitation of shock waves in SiO$_2$ aerogels with various densities ranging from 0.025 to 0.25 g/cm^3 by a high-current electron beam was investigated using optical methods and laser interferometry. The evolution of the radiation from the energy-deposition zone and the expansion of the aerogel toward the electron beam were studied. The velocities of shock waves in aerogels with different densities and the velocities of the spallation fragments were measured. A model of the equation of state of fine-pore materials, tak-

TABLE III. Unloading of an aerogel irradiated with an electron beam with electron energy and current density amplitudes $U_0 = 290$ keV and $j_0 = 15$ kA/cm^2, respectively.

Aerogel density ρ, g/cm^3	Target thickness l, mm	Pulse emergence time τ, μs		Velocity of back side V_T, m/s		Velocity of irradiated side V_C, km/s	
		experiment	calculation	experiment	calculation	experiment	calculation
0.25	5	5−6	6	⋯	200		
	11	15−16	18	⋯	150	5.75	4
	22.5	38−40	38	⋯	130		
0.16	5.5	⋯	4	500	300		
	7.5	⋯	10	240	250		
	11−12	20	20	120	150	4.5	3
	14.6		27	80	130		
	30	69−72	70	⋯	80		
0.025	20	⋯	10	1200	1200	2.5	2.5*

*The value is indicated at time $\tau = 10$ μs after irradiation starts.

ing into account self-consistently the change in the porosity under compression, was proposed on the basis of these results. In this model of a porous material the elastic and shear moduli and the Grüneisen coefficient are power-law functions of the porosity. This is a reflection of the cluster structure of the porous material.

The following differences from the conventional models (for example, Ya. B. Zel'dovich's model[3]) are a consequence of this self-consistency. In the model proposed there is no uncertainty in the choice of the initial compression of highly porous aerogels (in the model of Ref. 3 the pores completely collapse even under a negligible load). The parameters (pressure, density, porosity) of the point at which the type of shock adiabat changes (from normal to anomalous) are determined self-consistently. In addition, in the proposed model much greater heating of the material than in the model of Ref. 3 occurs behind the shock front; this is a consequence of the impossibility of strong compression and complete collapse of the pores. This second difference was substantial even in the asymptotic limit of a strong load. The estimates made showed that the numerical value of the percolation coefficient of the proposed model (the exponent in the dependence of the elastic modulus on the porosity) is in agreement with its theoretical value 1.7 (provided that there are no shear stresses), while in the unheated aerogel $\gamma = 3.2$.

[1] L. V. Al'tshuler, K. K. Krupenikov, B. N. Ledenev *et al.*, Zh. Éksp. Teor. Fiz. **34**, 874 (1958) [Sov. Phys. JETP **7**, 606 (1958)].

[2] S. B. Kormer, A. I. Funtikov, V. D. Urlin *et al.*, Zh. Éksp. Teor. Fiz. **42**, 686 (1962) [Sov. Phys. JETP **15**, 477 (1962)].

[3] F. B. Zel'dovich and Yu. P. Raĭzer, *Physics of Shock Waves and High-Temperature Hydrodynamic Phenomena*, Vols. 1 and 2, transl. of 1st Russian edition [Academic Press, New York, 1966, 1967; 2nd ed., Nauka, Moscow, 1966].

[4] Yu. A. Krysanov and S. A. Novikov, Prikl. Mekh. Tekh. Fiz. No. 6, 57 (1988).

[5] I. M. Sokolov, Usp. Fiz. Nauk **150**, 221 (1986) [Sov. Phys. Usp. **29**, 924 (1986)].

[6] S. Feng and P. N. Sen, Phys. Rev. Lett. **52**, 216 (1984).

[7] V. E. Fortov, A. S. Filimonov, V. K. Gryaznov *et al.*, in *Proceedings of the International Conference on the Physics of Strong Coupled Plasmas*, edited by W. D. Kraft and M. Langes (World Scientific Publishers, Singapore, 1996), pp. 317–321.

[8] V. A. Aksenov *et al.*, in *Proceedings of the International Symposium on Position Detectors in High Energy Physics* (Dubna, 1988), D1. 13-88-172, pp. 313–314.

[9] V. Ya. Ternovoĭ, V. K. Gryaznov, D. N. Nikolaev *et al.*, in *Abstracts of the 11th International Conference on the Equations of State of Matter* [in Russian], Nal'chik (1996), p. 5.

[10] S. A. Bagnich, V. N. Bogomolov, D. A. Kudryukov *et al.*, Fiz. Tverd. Tela (St. Petersburg) **37**, 2879 (1995) [Phys. Solid State **37**, 1642 (1995)].

[11] B. A. Demidov, V. P. Efremov, I. A. Ivonin *et al.*, Zh. Tekh. Fiz. **67**(11), 26 (1977) [Sov. Phys. Tech. Phys. **42**, 1264 (1997)].

[12] B. A. Demidov, V. P. Efremov, I. A. Ivonin *et al.*, Zh. Tekh. Fiz. **68**(10), 112 (1998) [Sov. Phys. Tech. Phys. **43**, 1239 (1998)].

[13] B. A. Demidov, M. V. Ivkin, V. A. Petrov *et al.*, At. Énerg. **46**(2), 100 (1979).

[14] A. F. Akkerman, Yu. I. Nikitushev, and V. A. Botvin, *Monte Carlo Solution of the Problem of Transport of Fast Electrons in Matter* [in Russian], Nauka, Alma-Ata (1972), 163 pp.

[15] D. I. Vaĭsburd (ed.), *High-Energy Electronics of Solids* [in Russian], Novosibirsk (1982), 227 pp.

[16] K. Kanaya and S. Okadama, J. Phys. D **5**, 43 (1972).

[17] V. F. Baranov, *Electron Dosimetry* [in Russian], Atomizdat, Moscow (1974), 229 pp.

[18] A. B. Bushman, G. I. Kanel', A. L. Ni, and F. E. Fortov, *Thermal Physics and Dynamics of Intense Pulsed Interactions* [in Russian], Chernogolovka (1988), 199 pp.

[19] I. S. Grigor'ev and E. Z. Meĭlikhov (eds.), *Handbook of Physical Quantities* [in Russian], Énergoatmoizdat, Moscow (1991), 1232 pp.

[20] B. A. Demidov, V. P. Efremov, I. A. Ivonin *et al.*, Preprint No. 5419/11 [in Russian], Kurchatov Institute of Atomic Energy, Moscow (1991), 33 pp.

Translated by M. E. Alferieff

Dispersing of a charged drop in an electrostatic field

A. N. Zharov, S. O. Shiryaeva, and A. I. Grigor'ev

P. G. Demedov Yaroslavl State University, 150000 Yaroslavl, Russia

The characteristics of the breakup of a charged drop in a uniform electrostatic field are calculated on the basis of Onsager's principle of minimum dissipation of energy in nonequilibrium processes. The ranges of the physical parameters where daughter droplets are emitted from two tips and from one tip of an unstable parent drop and when emission is completely absent are found. The dimensionless radii, charges, and specific charges of the daughter droplets are determined. © *1999 American Institute of Physics.* [S1063-7842(99)00512-7]

INTRODUCTION

Dispersing of charged drops in an external electrostatic field is of interest for various applications in technical physics, scientific instrument building, geophysics, and chemical technology (see, for example, Ref. 1 and the literature cited therein). At present the breakup of a charged drop, which is unstable with respect to its own charge,[2] and an uncharged drop in a strong electrostatic field and unstable with respect to the polarization charge,[3,4] has been investigated quite completely experimentally and theoretically. In both of these situations the distribution of the surface charge of a drop is symmetric with respect to the equatorial plane perpendicular to the symmetry axis of a spheroid. For the problem of the breakup of a charged drop in a uniform external electrostatic field, the symmetry in the charge distribution over the surface of the drop is lost. The daughter droplets, detaching from the opposite tips of an unstable parent drop, will now have different sizes and charges. The momentum carried off by the daughter droplets emitted from opposite tips of the parent drop will be different and, therefore, the parent drop will move in the direction of the external electric field, as observed experimentally.[5,6]

The problem of calculating the characteristics of the breakup of a charged drop in a uniform external electrostatic field has almost not been studied theoretically. The present paper fills this lacuna.

1. Let a spherical drop of radius R with surface tension σ, density ρ, permittivity ε, electrical conductivity λ, and charge Q be placed in a uniform electrostatic field with intensity **E**. The drop extends along **E** into a figure close to a spheroid with eccentricity e.[7] For sufficiently large electric charge Q or field **E** or both at the same time, the drop can suffer an instability with respect to the intrinsic surface and polarization charges.

The characteristic equalization time due to the conductivity of the electric potential of a drop undergoing capillary oscillations is determined by the Maxwellian relaxation time $\tau_q = \varepsilon/(4\pi\lambda)$. The characteristic growth time of an instability of a drop with respect to the surface charge is determined by the relation $\tau_u = [\rho R^3/\sigma\{1 - W^2 - w^2/(16\pi)\}]^{1/2}$ (Ref. 8). In these expressions $w^2 = E^2 R/(\varepsilon\sigma)$ is the Taylor parameter,

characterizing the stability of a drop with respect to the polarization charge, and $W^2 = Q^2/(16\pi\sigma\varepsilon R^3)$ is the Rayleigh parameter, characterizing stability of a drop with respect to the electric charge.

If λ is small and the characteristic instability growth time τ_u is much shorter than the characteristic equalization time τ_q of the electric potential, $\tau_u \ll \tau_q$, then in the course of an instability the drop can be assumed to be nonconducting and the charge to be frozen in the surface. When such a drop becomes unstable with respect to the surface charge, it breaks up into two equal daughter droplets, carrying identical charges.[9] However, if λ is so large that the characteristic instability time τ_q of a drop with respect to the charge is much longer than the equalization time τ_u of the electric potential of the surface of the drop, $\tau_q \ll \tau_u$, then the drop can be assumed to be ideally conducting. In the analysis given below, this situation will be analyzed in greater detail.

2. When a drop becomes unstable as a function of the charge Q and external electric field **E**, highly dispersed, strongly charged, daughter droplets are shed from one or both tips of the drop. We shall assume that after detaching from the parent drop each daughter droplet moves in the time before emission of the next droplet to a large distance away from the parent drop and the electrostatic field of its charge does not influence the characteristics of the next droplet emitted from the same tip.

Let us consider the detachment of the nth droplet from one of the tips of the drop, which for definiteness we shall call the first tip, and of the lth droplet from the second tip. We shall also take account of the fact that up to the running moment in time $n-1$ emissions of daughter droplets from the first tip of the parent drop and $l-1$ emissions from the second tip have occurred. As a result of the emission, the parent drop emits daughter droplets with charges $q_{ij} \ll (Q + ER^2)$ and radii $r_{ij} \ll R$ (the first index enumerates the tips of the parent drop: $i=1$ for the droplet moving in the direction of **E** after emission; $i=2$ for the droplet moving in the direction opposite to **E**; the second index j indicates the number of the droplet in the emission process). We shall assume that the emission time of a daughter droplet is of the order of the period of the capillary oscillations of its fundamental mode, $\sim (r_{ij})^{3/2}$. Therefore, in the time period during

which one large daughter droplet is shed from the second tip, k small droplets are shed from the first tip (where k is the integer part of the ratio $(r_{2l}/r_{1n})^{3/2}$). The daughter droplets in the total electric field near the parent drop (we shall assume the field to be quasiuniform on characteristic spatial scales comparable with the sizes of the daughter droplets) are prolate spheroids with eccentricities e_{ij},[2,7] which will be determined below in an iterative procedure.

We shall assume that the dispersal process occurs at constant temperature. Then, since the total charge and mass of the liquid phase are constant (we neglect the possible effect of evaporation and condensation of the liquid), it is not difficult to find the change in the potential energy of the system as a result of the next emission of a daughter droplet from a tip of the parent drop as[10]

$$\Delta U_{ij} = 4\pi\sigma(R_{ij}^2 A(e) - R_{ij-1}^2 A(e) + r_{ij}^2 A(e_{ij})) + q_{ij}^2 \frac{B(e_{ij})}{2r_{ij}}$$

$$+ \frac{B(e)}{2R_{ij}} \left[Q - \sum_{j=1}^{n-1} q_{1j} - \sum_{j=1}^{l-1} q_{2i} \right]^2 - q_{ij} \frac{B(e)}{R_{ij}}$$

$$\times \left[Q - \sum_{j=1}^{n-1} q_{1j} - \sum_{j=1}^{l-1} q_{2j} \right] - \frac{B(e)}{2R_{ij-1}}$$

$$\times \left[Q - \sum_{j=1}^{n-1} q_{1j} - \sum_{j=1}^{l-1} q_{2j} \right]^2 + q_{ij} \frac{K(\nu_{ij})}{R_{ij}}$$

$$\times \left[Q - \sum_{j=1}^{n-1} q_{1j} - \sum_{j=1}^{l-1} q_{2j} \right] + (-1)^{i+1} E R_{ij} q_{ij} \Omega(\nu_{ij});$$

$$A(e_{ij}) = \frac{1}{2} \left((1 - e_{ij}^2)^{1/2} + \frac{\sin^{-1} e_{ij}}{e_{ij}} \right) (1 - e_{ej}^2)^{-1/6};$$

$$B(e_{ij}) = \frac{(1 - e_{ij}^2)^{1/3}}{e_{ij}} \tanh^{-1}(e_{ij});$$

$$K(\nu_{ij}) = \frac{(1 - e^2)^{1/3}}{e} \tanh^{-1}\left(\frac{e}{\nu_{ij}} \right); \quad \nu_{ij} = \left(1 + \frac{\xi_{ij}}{a^2} \right)^{1/2};$$

$$\Omega(\nu_{ij}) = \frac{e(\nu_{ij} - 1) - \nu_{ij} \tanh^{-1}[e(\nu_{ij} - 1)(\nu_{ij} - e^2)^{-1}]}{(1 - e^2)^{1/3}(\tanh^{-1} e - e)};$$

$$n(i) = \begin{cases} n, & \text{if } i = 1, \\ l, & \text{if } i = 2; \end{cases}$$

$$R_{ij} = \left(R^3 - r_{ij}^3 - \sum_{j=1}^{n-1} r_{1j}^3 - \sum_{j=1}^{l-1} r_{2j}^3 \right)^{1/3}; \tag{1}$$

α is the major semiaxis of the parent drop; ν_{ij} is the distance between the centers of the parent and daughter droplets, measured in units of the major semiaxes of the parent drop; ξ_{ij} are the spheroidal coordinates of the daughter droplets at the moment they are shed from the parent drop.

The first term in Eq. (1) characterizes the change in the surface energy of the system; the second term characterizes the intrinsic electrostatic energy of the daughter droplet; the third and fourth terms characterize the intrinsic electrostatic energy of the parent drop after an emission; the fifth term is

the intrinsic electrostatic energy of the parent drop before an emission; the sixth term is the electrostatic interaction energy between the charge of the daughter droplet and the intrinsic charge of the parent drop; the seventh term is the interaction energy between the daughter droplet and the polarization charge of the parent drop.

Emission of daughter droplets will continue until the Coulomb force detaching the daughter droplet is greater than the Laplacian force $2\pi\sigma r_{ij}^*$ holding it back (r_{ij}^* is the radius of the neck connecting the daughter droplet and the parent drop). Assuming that the intensity of the field at the point of detachment is determined by the field of the parent drop, we obtain the condition for the detachment of daughter droplets from different tips of the parent drop:

$$\frac{\alpha_{ij} X_{ij}(1 - e_{ij}^2)^{1/6}}{8} \leq Y_{ij} \left(\frac{w}{(16\pi)^{1/2}} + W \right)^2 \left\{ \left[\frac{W}{w(16\pi)^{-1/2} + W} \right. \right.$$

$$\left. - \sum_{j=1}^{n-1} Y_{1j} - \sum_{j=1}^{l-1} Y_{2j} \right] \frac{C(\nu_{ij})}{H_{ij}^2} + (-1)^{i+1}$$

$$\left. \times \frac{w}{w(16\pi)^{-1/2} + W} T(\nu_{ij}) \right\};$$

$$T(\nu_{ij}) = 1 - \frac{\tanh^{-1}(e\nu_{ij}^{-1}) - e\nu_{ij}(\nu_{ij}^2 - e^2)^{-1}}{\tanh^{-1}(e) - e};$$

$$C(\nu_{ij}) = \frac{(1 - e^2)^{2/3}}{(\nu_{ij}^2 - e^2)};$$

$$H_{ij} = \left(1 - X_{ij}^3 - \sum_{j=1}^{n-1} X_{1j}^3 - \sum_{j=1}^{l-1} X_{2j}^3 \right)^{1/3};$$

$$\alpha_{ij} = \frac{r_{ij}^*}{b_{ij}}; \quad Y_{ij} = \frac{q_{ij}}{(Q + ER^2)}; \quad X_{ij} = \frac{r_{ij}}{R}; \tag{2}$$

X_{ij} and Y_{ij} are the dimensionless radii and charges of the daughter droplets, b_{ij} are the minor semiaxes of the daughter droplets; the first and second terms in braces characterize the intensity of the electric field produced by the intrinsic and polarization charges of the parent drop near the daughter droplet.

We require that, on the basis of Onsager's principle of minimum dissipation of energy in nonequilibrium processes, the change in the potential energy be an extremum, i.e., $\partial(\Delta U_{ij})/\partial q_{ij} = 0$ and $\partial(\Delta U_{ij})/\partial r_{ij} = 0$.[10] This gives in addition to the two equations (2) four equations for the six unknowns X_{1j}, Y_{1j}, ν_{1j}, X_{2j}, Y_{2j}, and ν_{2j}:

$$Y_{ij} \frac{B(e_{ij})}{X_{ij}} + \left[\frac{W}{w(16\pi)^{-1/2} + W} - \sum_{j=1}^{n-1} Y_{1j} - \sum_{j=1}^{l-1} Y_{2j} \right]$$

$$\times \frac{[K(\nu_{ij}) - B(e)]}{H_{ij}} + (-1)^{i+1} \frac{w}{w(16\pi)^{-1/2} + W}$$
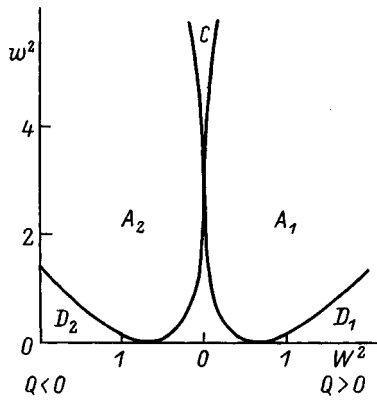
$$\times H_{ij} \Omega(\nu_{ij}) = 0; \tag{3}$$

FIG. 1. Boundaries of the regions of values of the parameters W^2 and w^2 where the laws of emission of the daughter droplets are different ($e^2 = 0.7$, $\alpha_1 = \alpha_2 = 0.9$).

$$H_{ij}\frac{\partial H_{ij}}{\partial X_{ij}}A(e) + X_{ij}A(e_{ij}) - \left(\frac{w}{(16\pi)^{1/2}} + W\right)^2 Y_{ij}^2 \frac{B(e_{ij})}{X_{ij}^2}$$

$$+ \left(\frac{w}{(16\pi)^{1/2}} + W\right)\left[\frac{W}{w(16\pi)^{-1/2} + W} - \sum_{j=1}^{n-1} Y_{1j}\right.$$

$$\left. - \sum_{j=1}^{l-1} Y_{2j}\right]\frac{B(e)}{H_{ij}^2}\frac{\partial H_{ij}}{\partial X_{ij}}\left\{Y_{ij} - \left[\frac{W}{w(16\pi)^{-1/2} + W}\right.\right.$$

$$\left.\left. - \sum_{j=1}^{n-1} Y_{1j} - \sum_{j=1}^{l-1} Y_{2j}\right]\right\} - 2\left(\frac{w}{(16\pi)^{1/2}} + W\right)^2$$

$$\times \frac{Y_{ij}K(\nu_{ij})}{H_{ij}^2}\frac{\partial H_{ij}}{\partial X_{ij}}\left[\frac{W}{w(16\pi)^{-1/2} + W} - \sum_{j=1}^{n-1} Y_{1j}\right.$$

$$\left. - \sum_{j=1}^{l-1} Y_{2j}\right] - (-1)^{i+1}\frac{2w}{(16\pi)^{1/2}}\left(\frac{w}{(16\pi)^{1/2}} + W\right)$$

$$\times \frac{\partial H_{ij}}{\partial X_{ij}}\Omega(\nu_{ij})Y_{ij} = 0. \tag{4}$$

3. In the numerical analysis of the system (2)–(4), the parameter α_{ij} was assumed to be the same for droplets detached from the first and second tips and independent of the number of a droplet in the emission process, i.e., $\alpha_1 = \alpha_2 = 0.9$.[2]

Six characteristic regions of existence of solutions of the system of equations (2)–(4) can be identified in the parameter plane (W^2, w^2) for fixed values of other physical quantities. These regions are presented in Fig. 1.

Emission in the region A_1 occurs only from the first tip of the parent drop. In the region A_2 emission occurs only from the second tip. In the region B the initial drop is stable. In the regions C, D_1, and D_2 emission occurs from both emission protuberances. In the regions D_1 and D_2 the parent drop emits daughter drops with the same sign from both tips. In the region C the daughter droplets emitted from the opposite tips have different signs. The boundaries of the regions presented were obtained as follows.

The parameters $w^2 < 2.59$ and W^2 were chosen from the region A_1 where solutions for daughter droplets, detached from the second tip of the parent drop do not exist. Solutions of the system of three equations for the first tip in the first emission, i.e., X_{II}, Y_{II}, ν_{II}, were sought, keeping the Rayleigh parameter fixed and decreasing the Taylor parameter. At a certain finite value of the Taylor parameter the solutions of the system (2)–(4) vanished, i.e., we reached the boundary of the region. Thus, in the range of W^2 from 0 to 0.6 a curve $w^2(W^2)$ separating the regions A_1 and B was obtained. Next, the parameters $w^2 > 2.59$ and W^2 were chosen from the region C. The solutions of the system (2)–(4) for the first and second tips of the parent drop in the first emission, i.e., X_{11}, Y_{11}, ν_{11}, X_{21}, Y_{21}, and ν_{21}, were sought. Once again the Rayleigh parameter was held fixed and the Taylor parameter was decreased. At a certain value of the Taylor parameter the solutions X_{21}, Y_{21}, and ν_{21} vanished. Thus, a function $w^2(W^2)$ separating the regions C and A_1 was obtained in the range of W^2 from 0 to 0.255. Next, the parameters $W^2 \geqslant 0.6$ and w^2 were chosen from the region D_1. The solutions of the system (2)–(4) for the first and second tips of the parent drop in the first emission event, i.e., X_{11}, Y_{11}, ν_{11}, X_{21}, Y_{21}, and ν_{21}, were found. The Rayleigh parameter was held fixed and the Taylor parameter was increased. At a certain value of the Taylor parameter the solutions X_{21}, Y_{21}, ν_{21} vanished. Finally, a function $w^2(W^2)$ separating the regions D_1 and A_1 was determined in the range of W^2 from 0.6 to 2.

All regions for $Q < 0$ were obtained by mapping the regions calculated for $Q > 0$. This was done because when Q is replaced by $-Q$ in the equations of the system (2)–(4) the equations describing the solutions for X_{1j}, Y_{1j}, ν_{1j} transform into the equations determining X_{2j}, Y_{2j}, ν_{2j}, and vice versa.

4a. Let the initial values of the parameters W^2 and w^2 lie in the region A_1 or A_2. Then emission occurs only from a single emission protuberance: for $Q > 0$ — from the first one and for $Q < 0$ — from the second one. In addition, dispersal in the regions A_1 and A_2 occurs in a similar manner, with the exception of the fact that in the region A_1 the daughter droplets have positive charges and in the region A_2 they have negative charges. In the emission process the Rayleigh parameter for a drop decreases more rapidly than the Taylor parameter, and in the (W^2, w^2) diagram a drop can reach the boundary of the A_1 (or A_2) region. The direction of the subsequent realization of the process leading to the breakup of the parent drop depends on the value of the Taylor parameter. If $w^2 < 2.59$, then a drop in the plane (W^2, w^2) falls into the region B and emission stops completely. If $w^2 > 2.59$, then the drop falls into the region C and emission occurs from both emission protuberances. The computational results for $W^2 = 0.4$, $w^2 = 0.4$ are presented in Fig. 2.

4b. If the initial values of the parameters W^2 and w^2 lie in the region D_1 or D_2, then emission occurs from both emission protuberances. The charges of the daughter droplets shed from the first and second tips have the same sign but different magnitudes. In the emission process the Rayleigh parameter decreases and the drop moves from the region D_1 into the region A_1 (or from the region D_2 into the region
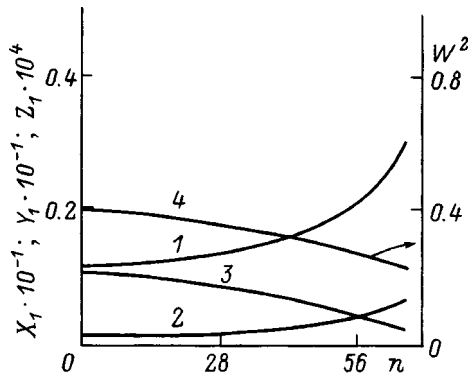
FIG. 2. Dimensionless quantities as a function of the order number n of a droplet: *1* — radii X_1; *2* — charges Y_1; *3* — specific charges Z_1 for daughter droplets emitted from the first tip of the parent drop; *4* — Rayleigh parameter for a parent drop. Initial values: $w^2 = 0.4$, $W^2 = 0.4$, $Q > 0$, $e^2 = 0.7$, $\alpha_1 = 0.9$.
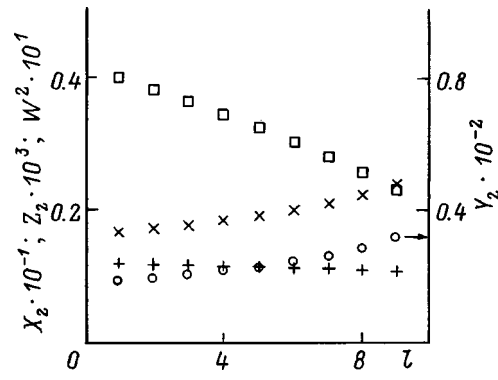

FIG. 4. Dimensionless quantities as a function of the order number l of the daughter droplet: $\times$ — radii X_2; $\bigcirc$ — charges Y_2, $\square$ — specific charges Z_2 for daughter droplets emitted from the second tip of the parent drop; $+$ — Rayleigh parameter for the parent drop. Initial values: $w^2 = 0.18$, $W^2 = 1.2$, $Q > 0$, $e^2 = 0.7$, $\alpha_2 = 0.9$.

A_2), after which the process described in paragraph **4a** occurs. The situation with the initial values of the parameters W^2 and w^2 from region D_1 is illustrated in Figs. 3 and 4 for the initial values of $W^2 = 1.2$, $w^2 = 0.18$. In the detachment time from the first to ninth daughter droplets from the second tip, 8, 8, 9, 9, 9, 10, 10, 11, and 12 droplets are shed, respectively, from the first tip. Then in the plane (W^2, w^2) the drops fall into the region A_1 and emission continues only from the first tip of the parent drop. Then in the plane (W^2, w^2) the drop moves into the region B and emission stops.

4c. If the initial values of the parameters W^2 and w^2 lie in the region C, emission occurs from both emission protuberances, and the charges of the daughter droplets detached from the first and second tips of the parent drop have different signs and magnitudes. The results of the numerical calculations with $W^2 = 0.0025$ and $w^2 = 2.7$ from the region C are illustrated in Figs. 5 and 6. At the start of the emission process, in the time that one daughter droplet detaches from the second tip, three droplets detach from the first tip. Then, in the time one daughter droplet detaches from the second tip, two or three daughter droplets detach from the first tip. In addition, in the time two droplets detach from the first tip and one detaches from the second tip the Rayleigh parameter increases, and in the time three droplets detach from the first

tip and one detaches from the second tip the Rayleigh parameter decreases. This process corresponds to the first plateau in Figs. 5 and 6. Next, after the Taylor parameter has decreased somewhat, the charges of the daughter droplets increase and a moment arrives when with two droplets detached from the first tip and one from the second tip the Rayleigh parameter decreases. This corresponds to the second decrease of the Rayleigh parameter. In time one droplet detaches from the second tip, one or two droplets detach from the first tip. In addition, in the time one droplet detaches from the second and first tips the Rayleigh parameter increases, and in the time two droplets detach from the first and one detaches from the second tip the Rayleigh parameter decreases. This process corresponds to the second plateau in Figs. 5 and 6. As the Taylor parameter decreases further, the charges increase and then, when one droplet detaches from the first and second tips the Rayleigh parameter decreases and reaches zero. Then in the plane (W^2, w^2) the drop falls into the region B and emission stops.

In concluding this section we note that the accumulation of excess surface charge by an unstable drop terminates in the form of the emission of a series of highly dispersed, strongly charged droplets, as illustrated in Figs. 2–6, when the parent drop in the range of values of the parameters (W^2, w^2) falls into the region W in Fig. 1. In Figs. 3–6 it is
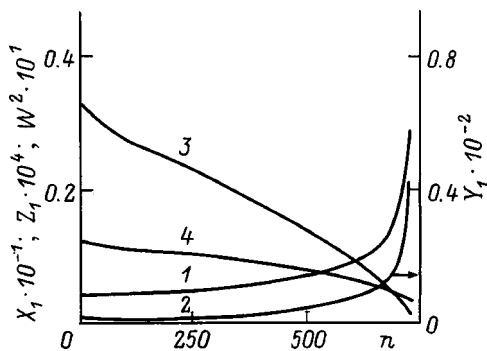

FIG. 3. Same as Fig. 2 for the initial values $w^2 = 0.18$, $W^2 = 1.2$, $Q > 0$, $e^2 = 0.7$, $\alpha_1 = 0.9$.
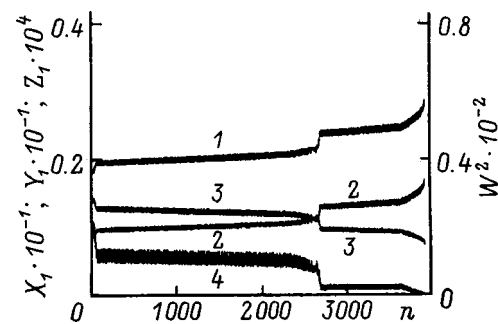

FIG. 5. Same as Fig. 2 with initial values $w^2 = 2.7$, $W^2 = 0.0025$, $Q > 0$, $e^2 = 0.7$, $\alpha_1 = 0.9$.
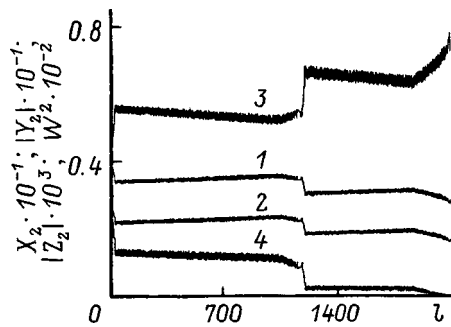
FIG. 6. Dimensionless quantities as a function of the order parameter l: *1* — radii X_2; *2* — absolute charges $|Y_2|$; *3* — absolute specific charges $|Z_2|$ for daughter droplets emitted from the second tip of the parent drop; *4* — Rayleigh parameter for the parent drop. Initial values: $w^2 = 2.7$, $W^2 = 0.0025$, $Q > 0$, $e^2 = 0.7$, $\alpha_1 = 0.9$.

CONCLUSIONS

Depending on the external electrostatic field **E** and the magnitude and sign of the intrinsic charge Q of an electrically conducting drop, the drop becomes unstable with respect to the superposition of the intrinsic and induced surface electric charge under different conditions with the emission of daughter droplets only from one tip of the drop parallel or antiparallel to **E** or from both tips. In the latter case the sizes and charges of the daughter droplets emitted from different tips of the parent drop are different, as a result of which the parent drop moves on account of the reactive effect. The emission regimes can change continuously as a drop breaks up.

interesting that the sizes, charges, and number of daughter droplets emitted by the parent drop under different conditions differ from one another substantially. This difference was previously noted by comparing two very simple situations: breakup of a strongly charged drop which is unstable with respect to its own charge and breakup of an uncharged drop, which is unstable with respect to the induced charge, in a strong external electrostatic field.[4]

The small-scale structure of the curves in Figs. 5 and 6 is due to the fact that the charges of the daughter droplets emitted from opposite tips of the parent drop differ in sign and magnitude. This results in oscillations of the residual intrinsic charge of the drop and therefore oscillations of the characteristics of the emitted daughter droplets.

[1] A. I. Grigor'ev and S. O. Shiryaeva, Izv. Ross. Akad. Nauk, Mekh. Zhidk. Gaza, No. 3, 3 (1994).
[2] A. I. Grigor'ev and S. O. Shiryaeva, Zh. Tekh. Fiz. **61**(3), 19 (1991) [Sov. Phys. Tech. Phys. **36**, 258 (1991)].
[3] A. I. Grigor'ev and S. O. Shiryaeva, J. Phys. D **23**, 1361 (1990).
[4] S. O. Shiryaeva and A. I. Grigor'ev, Pis'ma Zh. Tekh. Fiz. **19**(18), 87 (1993) [Tech. Phys. Lett. **19**(9), 600 (1993)].
[5] M. N. Beǐtuganov, Meteorol. Gidrol., No. 9, 42 (1989).
[6] T. Mochizuki, T. Mori, and N. Kaji, AIChE. J. **36**, 1039 (1990).
[7] A. I. Grigor'ev, S. O. Shiryaeva, and E. I. Belavina, Zh. Tekh. Fiz. **59**(6), 27 (1989) [Sov. Phys. Tech. Phys. **34**, 602 (1989)].
[8] S. O. Shiryaeva and A. I. Grigor'ev, Zh. Tekh. Fiz. **64**(3), 1 (1994) [Tech. Phys. **39**, 229 (1994)].
[9] V. A. Koromyslov, A. I. Grigor'ev, and S. O. Shiryaeva, Zh. Tekh. Fiz. **68**(8), 31 (1998) [Tech. Phys. **43**, 904 (1998)].
[10] S. O. Shiryaeva and A. I. Grigor'ev, Zh. Tekh. Fiz. **65**(2), 11 (1995) [Tech. Phys. **40**, 122 (1995)].

Translated by M. E. Alferieff

Hysteresis in the presence of electron–cyclotron resonance

A. B. Petrin

High-Temperature Institute, Russian Academy of Sciences, 127412 Moscow, Russia

A method of determining the nonlinear interaction of microwaves with a magnetoactive low-pressure plasma is presented. It is shown by solving simultaneously the problems of the propagation of electromagnetic waves, the balance of charged particles, and the energy balance that near a critical value of the constant magnetic induction the character of the interaction of the wave and the plasma changes substantially: For magnetic fields above the critical field a much stronger interaction is observed, for which the penetration depth of the incident wave into the plasma increases. An investigation of the strong interaction regime showed the existence of hysteresis, which is accompanied by an abrupt transition from one standing-wave mode in plasma to another. It is shown that virtually complete absorption of the wave is possible. © *1999 American Institute of Physics.* [S1063-7842(99)00612-1]

INTRODUCTION

The study of the nonlinear microwave–plasma interaction is of great importance for the problem of maintaining an electron-cyclotron plasma, used in ion sources which components of setups for depositing thin films and etching films during the fabrication of microcircuits. Methods for simulating rf discharges[1–3] are not suitable for investigating microwave discharges because of the characteristic features of such discharges, which are determined by the higher frequency of the electromagnetic fields. In addition, the quasistatic approximation for the electromagnetic problem, including the Poisson equation for the electric potential in the plasma, also is not suitable for modeling a microwave discharge.

Although the differential equations determining the propagation of electromagnetic waves in a magnetoactive plasma are well known,[4,5] in a complex geometry problems arise with the boundary conditions for the electromagnetic fields because of the open nature of the problem for microwaves. A well-known method of integral equations has been developed for such open problems of scattering of electromagnetic waves.[6,7]

In Refs. 8–12 integral-equation methods were used to describe the propagation of microwaves in a magnetoactive plasma. It was shown that it is important to take account of the change in the electrical parameters of the plasma caused by the wave, and these methods were combined with methods for investigating rf discharges. In the present paper these investigations are elaborated and refined.

FORMULATION OF THE PROBLEM

We consider first the solution of the electrodynamic problem of the propagation of an electromagnetic wave with circular frequency ω in a space filled with dielectric bodies and plasma. We shall assume the complex permittivity tensors of the dielectric bodies $\boldsymbol{\varepsilon}^d(\mathbf{r})$ and plasma $\boldsymbol{\varepsilon}^p(\mathbf{r},t)$ to be known. We shall consider the dielectric bodies to be nonuni-

form isotropic dielectric bodies,[6,7] and the plasma to be a nonuniform anisotropic dielectric body. The fields are assumed to have a complex representation with time dependence $e^{j\omega t}$. An explicit time dependence of $\boldsymbol{\varepsilon}^p(\mathbf{r},t)$ exists only in the nonstationary case because of the time dependence of the electron density in plasma. It is assumed that the characteristic time in which the plasma density varies is much longer than the characteristic time required to establish a distribution of the electromagnetic field. For this reason, to find the electromagnetic field it can be assumed that $\boldsymbol{\varepsilon}^p(\mathbf{r},t)$ (and the fields, potentials, and currents) is determined by the instantaneous electron density in the plasma, while the distribution of the electromagnetic field at the moment in time considered is the same as in the stationary case.

For a stationary plasma distribution the complex permittivity tensor of the plasma does not depend explicitly on the time.

a) *Derivation of a three-dimensional integrodifferential equation of the electromagnetic problem.* Let V be the volume of the dielectric bodies and plasma under study, and let $\mathbf{E}^i$ be the electric field of the incident wave. We represent the electromagnetic field in the plasma as a sum of the field of the incident wave and the scattered field due to the volume polarization current with density $\mathbf{J}$, which can be calculated at the points of the dielectric bodies and at the points of the plasma according to the formulas

$$\mathbf{J}(\mathbf{r},t)=j\omega[\boldsymbol{\varepsilon}^d(\mathbf{r})-\boldsymbol{\varepsilon}^0]\cdot\mathbf{E}(\mathbf{r},t), \tag{1}$$

$$\mathbf{J}(\mathbf{r},t)=j\omega[\boldsymbol{\varepsilon}^p(\mathbf{r},t)-\boldsymbol{\varepsilon}^0]\cdot\mathbf{E}(\mathbf{r},t) \tag{2}$$

in the dielectric and plasma, respectively. Here $\boldsymbol{\varepsilon}^0$ is the vacuum permittivity tensor, equal to the product of the vacuum permittivity ε_0 and the unit matrix. Then

$$\mathbf{E}(\mathbf{r},t)=\mathbf{E}^i(\mathbf{r})+\mathbf{E}^s(\mathbf{r},t), \tag{3}$$

where

$$\mathbf{E}^s(\mathbf{r},t)=-j\omega\mathbf{A}(\mathbf{r},t)-\nabla\varphi(\mathbf{r},t), \tag{4}$$

$$\mathbf{A}(\mathbf{r},t)=\frac{\mu_0}{4\pi}\int_V \mathbf{J}(\mathbf{r}',t)\frac{e^{-jk|\mathbf{r}-\mathbf{r}'|}}{|\mathbf{r}-\mathbf{r}'|}dv', \tag{5}$$

$$\varphi(\mathbf{r},t)=\frac{1}{4\pi\varepsilon_0}\int_V \rho(\mathbf{r}',t)\frac{e^{-jk|\mathbf{r}-\mathbf{r}'|}}{|\mathbf{r}-\mathbf{r}'|}dv', \tag{6}$$

where $k=\omega\sqrt{\mu_0\varepsilon_0}=2\pi/\lambda$ and λ is the wavelength in vacuum.

The electric charge density is related with the polarization current density in Eqs. (1)–(6) by the relation

$$\nabla\cdot\mathbf{J}(\mathbf{r},t)=-j\omega\rho(\mathbf{r},t). \tag{7}$$

The equations (1) and (2) with expressions (3)–(7) substituted into them form an integrodifferential equation for the polarization current density $\mathbf{J}$

$$\mathbf{J}(\mathbf{r},t)-\boldsymbol{\sigma}(\mathbf{r},t)\cdot\left(-j\omega\mathbf{A}+\frac{c^2}{j\omega}\nabla(\nabla\cdot\mathbf{A})\right)=\boldsymbol{\sigma}(\mathbf{r},t)\cdot\mathbf{E}^i(\mathbf{r}), \tag{8}$$

where the conductivity tensor $\boldsymbol{\sigma}(\mathbf{r},t)=j\omega[\boldsymbol{\varepsilon}(\mathbf{r},t)-\boldsymbol{\varepsilon}^0]$ has been introduced, and $\boldsymbol{\varepsilon}(\mathbf{r},t)$ is the tensor $\boldsymbol{\varepsilon}^d(\mathbf{r})$ if the point at which Eq. (8) is written lies in the dielectric bodies and the tensor $\boldsymbol{\varepsilon}^p(\mathbf{r},t)$ if the point indicated lies in a region occupied by the plasma, and the vector potential $\mathbf{A}$ is determined in terms of $\mathbf{J}$ by expression (5).

Solving Eq. (8) we find the polarization current density $\mathbf{J}$, and substituting the distribution obtained into Eqs. (1) and (2) and solving these equations we find the electric field distribution $\mathbf{E}$ in the plasma and in the dielectric bodies. Then we can find the average volume density of the Joule losses from the formula

$$w(\mathbf{r},t)=\frac{1}{2}\mathrm{Re}(\mathbf{J}\cdot\mathbf{E}^*). \tag{9}$$

In Eqs. (1)–(9) the explicit dependence of the complex amplitude of the polarization current density, the vector and scalar potentials, and the complex amplitude of the electric field is determined by the slow time dependence of the plasma density. For this reason, at each moment in time these quantities are related with one another by the same equations by which they were related for constant plasma parameters, equal to their instantaneous values.

If a metal screen, which we assume to be flat and infinite, is introduced into the system of dielectric bodies and plasma under study, the integrodifferential equation of the problem changes somewhat. In Eq. (8) $\mathbf{E}^i$ should be interpreted as the sum of the fields of the incident wave from the external (with respect to the system) currents and the incident wave reflected from the metal screen, and the vector potential is given by the expression

$$\mathbf{A}(\mathbf{r},t)=\frac{\mu_0}{4\pi}\int_V \mathbf{J}(\mathbf{r}',t)\frac{e^{-jk|\mathbf{r}-\mathbf{r}'|}}{|\mathbf{r}-\mathbf{r}'|}dv'$$

$$+\frac{\mu_0}{4\pi}\int_{V_{\mathrm{refl}}} \mathbf{J}_{\mathrm{refl}}(\mathbf{r}'',t)\frac{e^{-jk|\mathbf{r}-\mathbf{r}''|}}{|\mathbf{r}-\mathbf{r}''|}dv'', \tag{10}$$

where V_{refl} is the volume occupied by the reflected polarization currents $\mathbf{J}_{\mathrm{refl}}$ and arranged mirror-symmetrically with respect to the metal screen.

If the polarization current at some point of the dielectric or plasma is $\mathbf{J}$, then at a mirror-image point with respect to the metal screen the reflected current $\mathbf{J}_{\mathrm{refl}}$ equals in modulus the initial current, and the direction is such that the initial and reflected currents together produce a zero tangential electric field on the metal sheet.

b) *Conductivity and permittivity tensors.* We orient the $0Z$ axis of the coordinate system parallel to the magnetic induction vector $\mathbf{B}$. In this system the permittivity tensor of the magnetoactive plasma is well known.[7] Then the conductivity tensor can be represented in the form

$$\boldsymbol{\sigma}^p(\mathbf{r},t)=\begin{bmatrix} \sigma_1 & -\sigma_2 & 0 \\ \sigma_2 & \sigma_1 & 0 \\ 0 & 0 & \sigma_3 \end{bmatrix}, \tag{11}$$

where

$$\sigma_1=j\varepsilon_0\frac{\omega_p^2\cdot(\omega-j\nu_c)}{\omega_c^2-(\omega-j\nu_c)^2}; \quad \sigma_2=\varepsilon_0\frac{\omega_p^2\cdot\omega_c}{\omega_c^2-(\omega-j\nu_c)^2};$$

$$\sigma_3=-j\varepsilon_0\frac{\omega_p^2}{(\omega-j\nu_c)};$$

$\omega_c=eB/m$ is the cyclotron frequency;

$$\omega_p=\left(\frac{n(\mathbf{r},t)e^2}{\varepsilon_0 m}\right)^{\frac{1}{2}}$$

is the plasma frequency; m is the electron mass; e is the elementary charge; ν_c is the average electron collision frequency; $n(\mathbf{r},t)$ is the electron density; the permittivity tensor of the plasma is related with the conductivity tensor as $\boldsymbol{\varepsilon}^p(\mathbf{r},t)=\boldsymbol{\varepsilon}^0+\boldsymbol{\sigma}^p(\mathbf{r},t)/j\omega$.

The permittivity tensor of a nonuniform isotropic dielectric can be found much more simply. Let the relative complex permittivity be described by the function $\varepsilon^{\mathrm{rel}}(\mathbf{r})$. Then the permittivity and conductivity tensors will have the form $\boldsymbol{\varepsilon}^d(\mathbf{r})=\varepsilon^{\mathrm{rel}}(\mathbf{r})\boldsymbol{\varepsilon}^0$ and $\boldsymbol{\sigma}^d(\mathbf{r},t)=j\omega(\boldsymbol{\varepsilon}^d(\mathbf{r})-\boldsymbol{\varepsilon}^0)$.

c) *Electron balance in the plasma.* The equation of electron balance in the general case can be written as

$$\frac{\partial n}{\partial t}=k_i n N_b-k_{\mathrm{rec}}n^2-k_{\mathrm{att}}nN_b+(\nabla\cdot(\mathbf{D}\cdot\nabla n)), \tag{12}$$

where n is the electron density, k_i is the ionization constant, k_{rec} is the recombination constant, k_{att} is the attachment constant, N_b is the neutral gas density, and $\mathbf{D}$ is the electron diffusion tensor (in the presence of a magnetic field anisotropic diffusion changes from nonambipolar to ambipolar).

For an electron–cyclotron plasma, used as an ion source, the degree of ionization of the plasma is low (approximately 10^{-4}), and for this reason the influence of recombination on the indicated process can often be neglected. Moreover, in the present work we shall consider for definiteness an argon plasma, where attachment can be neglected. Thus, the number of electrons changes mainly as a result of diffusion and ionization.

The ionization coefficient is determined by the average electron energy ε_{el}. For example, the function $k_i = k_i(\varepsilon_{el})$ for argon can be represented as[3]

$k_i = k_i(\varepsilon_{el})$

$$= \begin{cases} 0, & \text{if } \varepsilon_{el} \leq 5.3, \\ 8.7 \times 10^{-15}(\varepsilon_{el} - 5.3)\exp[-4.9/\sqrt{\varepsilon_{el} - 5.3}], & \text{if } \varepsilon_{el} > 5.3, \end{cases}$$

where k_i is expressed in $m^3 \cdot s^{-1}$ and ε_{el} in eV.

For this reason, to determine the source term in the electron balance equation it is necessary to solve the problem of the energy balance of an electron gas.

d) *Energy balance equations for an electron gas.* The permittivity tensor of a magnetoactive plasma can be obtained from the equation of motion of an ''average electron.'' This equation can be obtained from the moments of the Boltzmann equation (Ref. 13, pp. 179–181): $m\ddot{\mathbf{r}} = e\mathbf{E} - e(\mathbf{v} \times \mathbf{B}) + \mathbf{F}_f$, where $\mathbf{F}_f = -m\nu_c\mathbf{v}$ is the effective friction force acting on an electron, ν_c is the average electron collision frequency, and $\mathbf{v}$ is the electron velocity. This force arises as a result of the loss of momentum in collisions of electrons with neutral atoms.

On the average, in a collision an electron loses momentum of directed motion, and the energy of directed motion is converted into random thermal motion of the electron gas and also into excitation and ionization. For this reason, the electron temperature increases to values where all of the wave energy transferred to the plasma electrons will be transferred to the plasma boundaries as a result of heat conduction of the electron gas, and a certain amount of energy will be converted into energy of excited and ionized atoms. We can write the energy balance equation in the form

$$\frac{\partial w_e}{\partial t} = \left(\nabla \cdot \left(\frac{5}{3}\varepsilon_{el}\mathbf{D} \cdot \nabla n \right) \right) + \left(\nabla \cdot \left(\frac{2}{3}\mathbf{k} \cdot \nabla \varepsilon_{el} \right) \right)$$
$$+ w(\mathbf{r},t) - \nu(\mathbf{r},t) - u(\mathbf{r},t), \qquad (13)$$

where $w_e = n\varepsilon_{el} = (3/2)k_b n T_e$ is the volume energy density of the electron gas, ε_{el} is the average energy of one electron, k_b is Boltzmann's constant, n is the electron density, T_e is the electron temperature, $w(\mathbf{r},t)$ is the volume power density of Joule losses, $\nu(\mathbf{r},t) = q_i(\mathbf{r},t) \cdot \varepsilon_{ion}$ are inelastic power losses per unit volume as a result of ionization, q_i is the ionization rate per unit volume, ε_{ion} is the ionization energy of the neutrals, $u(\mathbf{r},t)$ are the inelastic power losses per unit volume due to excitation and elastic power losses due to elastic electron–neutrals and electron–ion collisions, $\mathbf{k}$ is the thermal conductivity tensor of the electron gas (in the isotropic case it can be represented by the scalar $k = (3/2)k_b n D_e$), D_e is the scalar electron diffusion coefficient, and $\mathbf{D}$ is the ambipolar diffusion coefficient tensor.

The power losses arising per unit volume as a result of the excitation of atoms and molecules in a low-pressure plasma are much less than the power losses due to ionization and heat conduction. Power losses due to elastic electron–neutral and electron–ion collisions are small compared with inelastic losses. For this reason, in the present work the term $u(\mathbf{r},t)$ was assumed to be negligibly small.
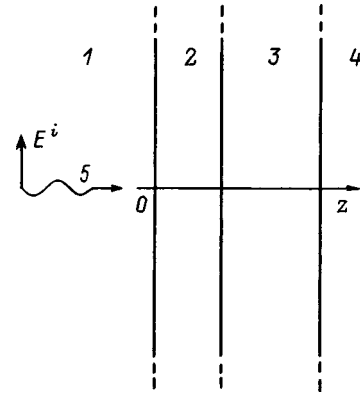

FIG. 1. Geometry of the problem: *1* — free space, *2* — dielectric, *3* — plasma, *4* — metal, *5* — incident wave.

We note that the introduction of the electron temperature here does not imply the use of a Maxwellian distribution. Even for a distribution function different from the Maxwellian function, the expression $\varepsilon_{el} = (3/2)k_B T_e$ is used for the electron thermal energy only because the term ''electron temperature'' is used in experimental investigations, for example, in measurements using a Langmuir probe. In the present work T_e is simply 2/3 of the average electron energy.

e) *Method for determining the stationary distribution of the plasma electrons.* The stationary electron density distribution arising after a discharge is established was determined in the present work by the method of successive approximations. In the proposed method, the approximate nonstationary problem was studied and the limit of its solutions as time approaches infinity was found. This limit is the desired solution of the stationary problem.[12]

The approximate nonstationary problem differed from the exact problem in that the diffusion coefficient tensor was assumed to be the same as the ambipolar diffusion tensor, i.e., it was assumed that diffusion is ambipolar immediately after a discharge starts. Starting with the background distribution of the electron density and electron temperature, a sufficient number of iterations was performed with a sufficiently small time step, the desired solution of the stationary problem was obtained, and the stationary electron density, the electron temperature distribution, and the corresponding electromagnetic field in the plasma were found. These distributions are solutions of the stationary problem.

SOLUTION OF THE ONE-DIMENSIONAL PROBLEM

Let us consider the planar problem, whose geometry is shown in Fig. 1. Let an electromagnetic plane wave be incident in a direction along the normal from the dielectric side onto a flat plasma layer separated from free space by a dielectric layer and a metal screen. Free space can be filled with air at atmospheric pressure. Plasma will not exist at such a pressure, and the wave will propagate here as if in free space. We orient the *OZ* axis of the coordinate system perpendicular to the layer under study in the direction of the metal screen, and we locate the origin of the coordinates on the front surface of the dielectric layer. Then the polarization current density and the ac electric fields will have only com-

ponents perpendicular to the OZ axis, and they will depend only on the coordinate z. This greatly simplifies the equations of the electrodynamic, particle balance, and energy balance problems.

The planar electrodynamic problem for the stationary case was solved numerically by the method of pointwise collocation at points uniformly placed on a $[0,L]$ segment of the OZ axis, where L is the total width of the dielectric layer and the plasma layer. The polarization current density was approximated by a functional cosine series.

The particle and energy balance problems in the method of successive approximations were solved by the Galerkin method with the density approximated by sinusoidal basis functions for the electron density and electron temperature. Such basis equations correspond to zero boundary conditions. The basis functions, i.e., the sine functions, were chosen as the weighting functions. The electron diffusion coefficient was assumed to be constant and equal to the ambipolar diffusion coefficient.

COMPUTATIONAL RESULTS

The calculations were performed for an argon plasma layer with thickness $L=6$ cm. This thickness was chosen so that the maximum of the standing wave formed by the incident wave and the wave reflected from the metal screen would lie in the rarefied plasma approximately at the center of the plasma layer. This promotes stable ignition of the discharge. The thickness of the dielectric layer separating the plasma from free space was chosen to be $L_d=4$ cm.

The transport coefficients and parameters for the discharge in argon were calculated according to the formulas[3,13,14]

$$\mu_e \cdot p = 30.0\,(\mathrm{m^2/(V\cdot s)})\,\mathrm{Torr};$$

$$\mu_i \cdot p = 0.14\,(\mathrm{m^2/(V\cdot s)})\,\mathrm{Torr};$$

$$D_e \cdot p = 120.0\,(\mathrm{m^2/s})\,\mathrm{Torr};$$

$$D_i \cdot p = 4.0\times10^{-3}\,(\mathrm{m^2/s})\,\mathrm{Torr};$$

$$D_a = (\mu_i D_e + \mu_e D_i)/(\mu_i + \mu_e);$$

$$\nu_c\,[1/s] = 5.3\times10^9 \cdot p\,[\mathrm{Torr}];$$

$$k_{\mathrm{rec}} = 10^{-14}\,\mathrm{m^3/s},$$

where μ_e and μ_i are the mobilities and D_e and D_i the diffusion coefficients of the electrons and ions, D_a is the ambipolar diffusion coefficient, and ν_c is the electron–neutral collision frequency.

A discharge at pressure $p=25$ mTorr was investigated. The frequency of the electromagnetic wave was 2.45 GHz. The intensity of the wave incident on the plasma was taken to be $I=1.5\times10^4$ W/m^2. The permittivity of the dielectric layer was assumed to be $\varepsilon^{\mathrm{el}}(\mathbf{r})=5$.

It was found that an incident wave with right-handed circular polarization interacts strongly with the plasma.[10,12] Since the literature contains two directly opposite definitions of right-handed circular polarization, in the present work the polarization is considered to be right-handed when the electric field vector of the wave rotates clockwise looking in the
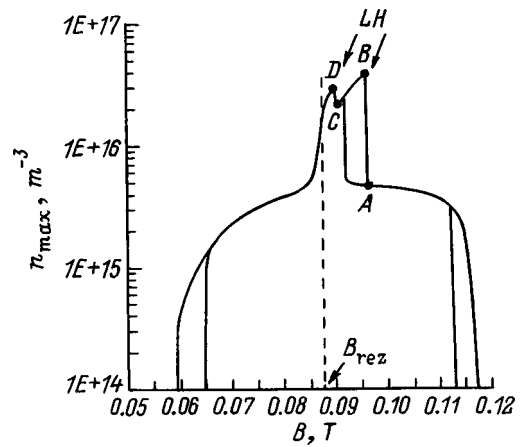

FIG. 2. Maximum of the electron density in the plasma versus the constant magnetic induction (LH — hysteresis loop).

direction of propagation of the wave. The electric field of the right-polarized wave with the frequency of the wave equal to the cyclotron frequency accelerates electrons constantly, giving rise to electron-cyclotron resonance.

Figure 2 shows the dependence of the maximum electron density in the plasma on the magnetic induction B in the region of electron–cyclotron resonance with the incident wave having right-handed circular polarization. A wave with left-handed circular polarization produces a plasma with electron density many orders of magnitude lower and therefore was not studied. It is evident from Fig. 2 that the strong interaction is observed only near values of B equal to $B_{\mathrm{cr}}=8.752\times10^{-2}$ T. This field corresponds to the electron-cyclotron frequency, equal to the frequency of the incident microwave ($f=2.45$ GHz). However, Fig. 2 shows that the maximum of the interaction is observed for $B>B_{\mathrm{cr}}$. Hysteresis of the resonance curve indicates a complicated nonlinear interaction of the electromagnetic wave with the plasma. Two hysteresis loops are clearly seen.

Figure 3 shows the absorption coefficient of the plasma for an electromagnetic field of the incident wave as a function of the magnetic induction. It is evident that the character
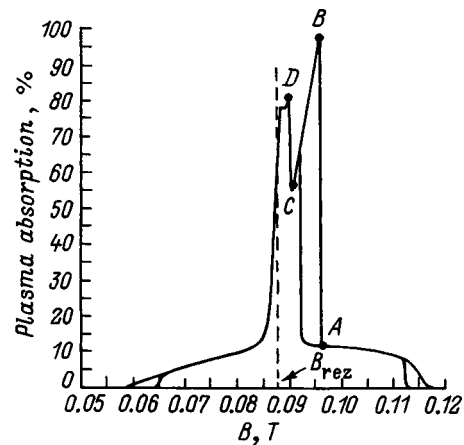

FIG. 3. Absorption coefficient of the plasma versus the constant magnetic induction.
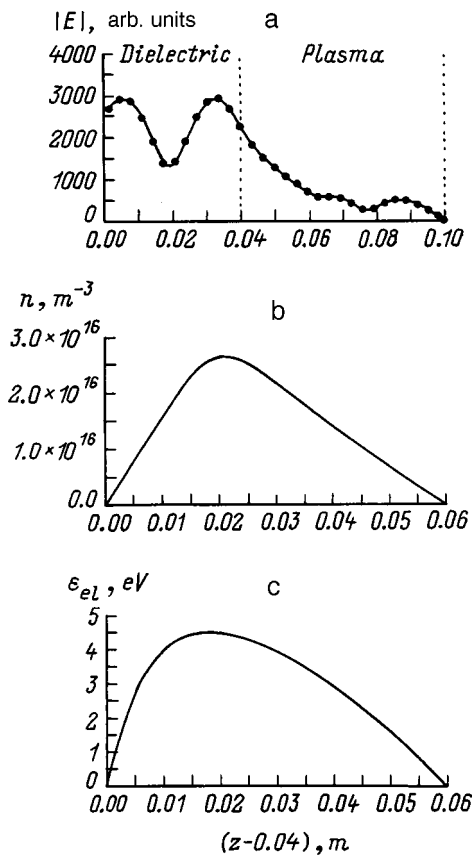
FIG. 4. Distribution of the modulus of the electric field of the wave (a), the electron density (b), and the electron temperature (c) along the z axis with $B = 0.089$ T, $I = 15000$ W/m^2.
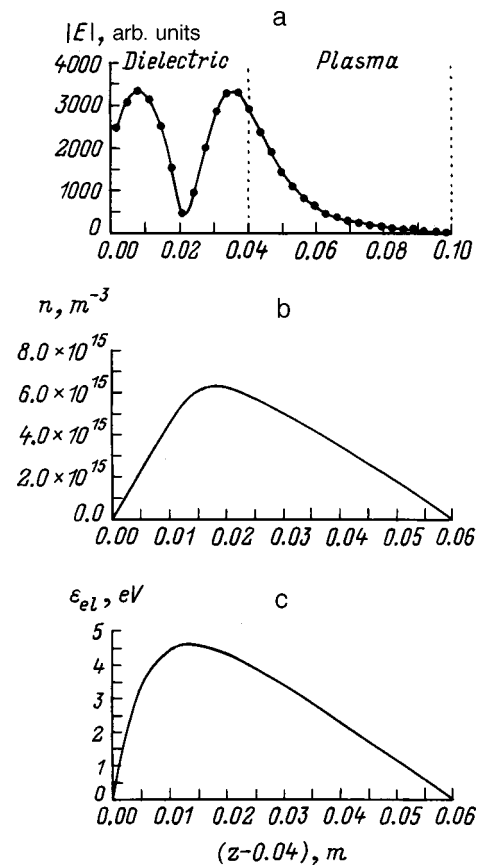

FIG. 5. Same as Fig. 4 with $B = 0.086$ T.

of the resonance is qualitatively the same as the dependence shown in Fig. 2.

We now call attention to the different behavior of the curves shown in Figs. 2 and 3 for B above and below B_{cr}. The character of the right-hand parts of the curves indicates interference. It can be inferred that a wave which has passed into the plasma interferes with the wave reflected from the metal screen. Then, the absence of irregularity of the curves to the left of B_{cr} indicates that interference vanishes. This can occur only if the wave reflected from the metal screen vanishes or substantially decreases. Therefore the wave can be expected to decay exponentially for $B < B_{cr}$ and an interference pattern can be expected for $B > B_{cr}$.

As the calculations showed, such a pattern is indeed observed. Figure 4a shows the distribution of the modulus of the electric field in the dielectric layer and in the plasma. Such a distribution of the electric field in the plasma is typical for interference of two decaying waves propagating toward one another. The wave propagating from the left is the incident wave which has passed into the plasma and the wave propagating from the right is the wave reflected from the metal screen. The distribution of the electron density and electron temperature (Figs. 4b and 4c) reaches a maximum at a point close to the center of the plasma layer, shifted somewhat toward the front edge of the plasma layer.

The curves of the modulus of the electric field of the electromagnetic wave in the plasma, the electron density,

and the electron temperature for magnetic induction less than the critical value are different. It is evident from Fig. 5 that, in contrast to the preceding case, the field decays exponentially in the plasma, and the density distribution is more asymmetric. Electrons are created in a thin layer where the field penetrates into the plasma, giving rise to the asymmetry of the density distribution.

The differences of the distributions shown in Figs. 4 and 5 can be explained by the following two factors. The first one is the change in phase of the coefficients of the conductivity tensor as the magnetic induction passes through B_{cr}. For $B < B_{cr}$, the incident electromagnetic field generates currents that in turn generate electromagnetic fields that decrease (on account of destructive interference) the transmitted field. A phenomenon similar to the spin effect occurs. However, if $B > B_{cr}$, then the phase of the currents changes by approximately $180°$ and interference of the incident electromagnetic wave and the fields due to the currents arises. This interference is already an almost in-phase superposition of the fields. The field in the plasma in this case decays not as a result of the quenching, destructive interference, but rather as a result of the absorption of the wave by the plasma. The electromagnetic field penetrates deep into the plasma, giving rise to a high electron density.

Second, for $B < B_{cr}$ electrons are produced only in a thin layer near the surface. A high gradient in the direction from the left edge of the plasma and a strong leftward electron flux out of the plasma arise, which strongly decreases the average
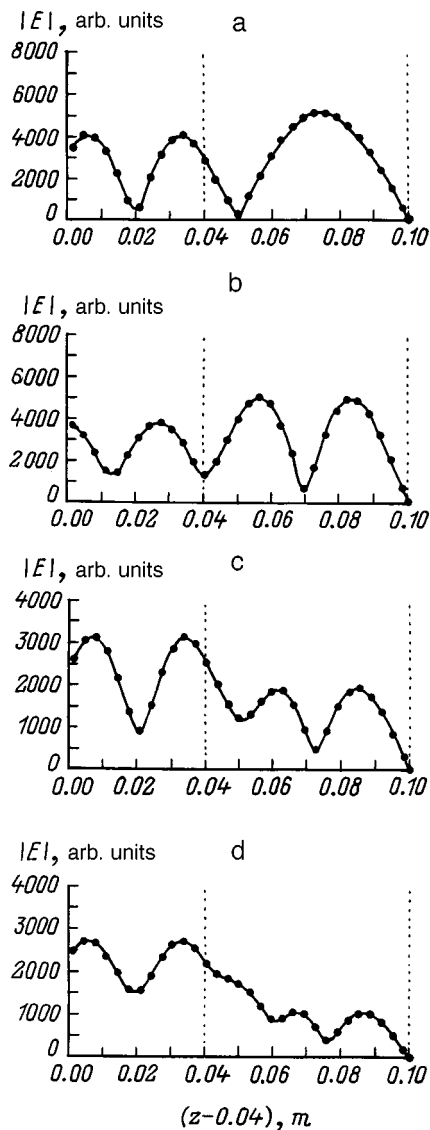
FIG. 6. Distribution of the modulus of the electric field of the wave along the z axis. B, T: a — 0.09650 (point A); b — 0.09575 (point B); c — 0.09075 (point C); d — 0.08975 (point D) for $0 < (z - 0.04) \leqslant 0.04$ — dielectric, $0.04 \leqslant (z - 0.04) \leqslant 0.1$ — plasma.

wave in the plasma changed abruptly, which is what led to the abrupt change in the distribution of the Joule power. Thus the transition of one mode of a standing wave to another occurs abruptly with a delay — hysteresis arises.

For the smaller hysteresis loop, the transition from the point C to the point D is also accompanied by a change in the number of modes of the standing wave in the plasma. Figures 6c and 6d show the distribution of the modulus of the electric field in the plasma and the insulator for the points C and D, respectively. However, in this case the standing wave is not as sharp, which is what results in the small jump in the parameters. Apparently, even smaller hysteresis loops exist for even smaller values of B. Here the standing wave is so weakly expressed against the damping background that the hysteresis loops are no longer noticeable.

CONCLUSIONS

A method for determining the nonlinear interaction of a microwave and a magnetoactive plasma was presented. By solving simultaneously the problems of propagation, balance of charged particles, and energy balance, it was shown that near the critical constant magnetic induction the character of the wave–plasma interaction changes substantially: A much stronger interaction, in which the penetration depth of the incident wave into the plasma increases, is observed for magnetic fields above the critical value. Investigation of the strong interaction regime showed hysteresis due to a delayed abrupt transition from one standing-wave mode in the plasma into another. It was shown that a regime with virtually complete absorption of the wave is possible.

[1] M. Meyyappan, J. Appl. Phys. **69**, 8047 (1991).

[2] M. Meyyappan and T. R. Govindan, J. Appl. Phys. **74**, 2250 (1993).

[3] J. D. P. Passchier and W. J. Goedheer, J. Appl. Phys. **74**, 3744 (1993).

[4] V. L. Ginzburg, *The Propagation of Electromagnetic Waves in Plasmas*, 2nd ed. [Pergamon Press, Oxford, 1972; Nauka, Moscow, 1967].

[5] V. L. Ginzburg, *Theoretical Physics and Astrophysics: A Selection of Key Problems* [Pergamon Press, Oxford, 1985; Nauka, Moscow, 1981].

[6] D. H. Schaubert, D. R. Wilton, and A. W. Glisson, IEEE Trans. Antennas Propag. **AP-32**, 77 (1984).

[7] D. H. Schaubert and P. M. Beaney, IEEE Trans. Antennas Propag. **AP-34**, 587 (1986).

[8] A. B. Petrin, Deposited in VINITI, No. 1039 [in Russian], Moscow (1996).

[9] A. B. Petrin, Deposited in VINITI, No. 1329 [in Russian], Moscow (1996).

[10] A. B. Petrin, Deposited in VINITI, No. 1988 [in Russian], Moscow (1996).

[11] A. B. Petrin, Deposited in VINITI, No. 3062 [in Russian], Moscow (1996).

[12] A. B. Petrin, IEEE Trans. Plasma Sci. **PS-26**, 150 (1998).

[13] Yu. P. Raĭzer, *Physics of Gas Discharges* [in Russian], Nauka, Moscow, 1987.

[14] G. Francis, *Ionization Phenomena in Gases* (Butterworths, London, 1960), Chap. 2.

electron density in the plasma and shifts the maximum of the electron density distribution to the left of the center of the plasma layer. For $B > B_{cr}$ the electromagnetic field of the wave penetrates deep into the plasma and such a phenomenon does not occur.

Finally, it is necessary to understand the reason for the hysteresis of the dependences studied above. Let us consider the large hysteresis loop and the points A and B (Figs. 2 and 3) near the right-hand jump of the loop.

The distributions of the modulus of the electric field at the points A and B are shown in Figs. 6a and b, respectively. One can see how the number of maxima of the standing

Translated by M. E. Alferieff

Yet another contribution to the question of the stabilization of an extended glow discharge in a transverse gas flow

I. A. Ivanchenko

Institute of Theoretical and Applied Mechanics, Siberian Branch of the Russian Academy of Sciences, 630090 Novosibirsk, Russia
(Submitted May 27, 1998; resubmitted April 9, 1999)
Zh. Tekh. Fiz. **69**, 38–41 (December 1999)

The instability of a discharge in a transverse gas flow is studied experimentally. It is shown that the characteristics of the source influence the stability. © *1999 American Institute of Physics.* [S1063-7842(99)00712-6]

INTRODUCTION

A glow discharge in a transverse gas flow is used in CO_2 lasers. High lasing densities — about 5 kW per meter of electrode[1] — are obtained based on such a discharge using relatively simple electrode systems and moderate gas flow velocities (up to 60–70 m/s).

Substantial progress has been made in the technology of gas discharges. Nonetheless the mechanisms of instability (a transition of the discharge from diffuse to contracted form) are still not completely understood. The results from modern theoretical models of instability do not agree with the experimentally observed regularities of the phenomena. Thus it follows from theoretical works that, as a rule, an increase of the gas velocity v should result in a higher maximum specific energy input W^* (the energy at which a transition of the discharge from the diffuse into the contracted form occurs). But, in experiments with increasing v, an increase of W^* is observed first, followed by saturation and then a decrease (see, for example, Ref. 2).

The answer to the traditional question of the effect of the characteristics of the supply circuit on the stability of the discharge[3,4] in application to discharges in a gas flow has not yet been found from the scientific standpoint. Theoretical works on this subject are based on the result of investigations of the static current–voltage characteristics of a discharge and its parts. The dynamic characteristics are not used in calculations, since virtually no experimental work has been done.

In the present paper the results of investigations of the static and dynamic current–voltage characteristics and the stability of an extended glow discharge in a transverse gas flow are presented.

DESCRIPTION OF THE EXPERIMENTAL APPARATUS

Eleven LOK lasers (Pluton) were used as experimental setups.[5] The electric-discharge setups of the lasers were not identical. They differed by their structural characteristics, such as the arrangement of the cathode relative to the channel walls, the structural connections of the electrodes with the components of the setup, the characteristics of the flux, and the characteristics of the source and power supply circuit for the discharge. For this reason, the contraction probabili-

ties of a discharge in the setups were substantially different, and the transition rates into a contracted form differed by a factor of 10–100.

One variant of an electric discharge setup is presented in Fig. 1. It shows a transverse section and one variant of the discharge power supply circuit. The arrow indicates the direction of flow of the laser gas mixture. An extended tubular cathode *1* and a flat anode *2* are oriented in a direction transverse to the gas flow. The electrodes are 0.86–1.1 m long. The electrodes are connected through a ballast resistor or directly to the power supply based on an inductive-capacitive converter. A tight parametric coupling and negative feedback on current are used in the source. Fluctuations of the grid voltage and slow variations of the load current are compen-
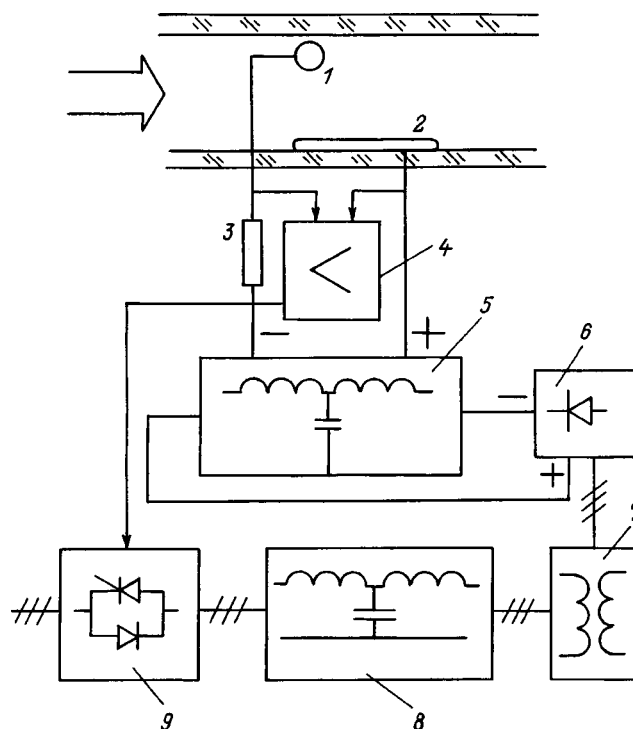

FIG. 1. Scheme of the electric discharge setup based on inductive–capacitive converter: *1* — cathode, *2* — anode, *3* — resistor, *4* — feedback on current, *5* — filter, *6* — rectifier, *7* — transformer, *8* — inductive–capacitive converter, *9* — transistor voltage regulator for controlling the discharge current.

sated by negative feedback. The other variants of the electric-discharge setup differed by the power sources — they used power sources with a nonstiff external characteristic and negative feedback with respect to current. In all cases low frequencies were used to convert ac into dc current. The characteristic parameters of the discharge were as follows: $v_0 = 30–60$ m/s is the velocity of the gas flow at the front edge of the gas-discharge channel, $U = 1300–2000$ V is the voltage across the discharge gap, and $I = 10–20$ A is the discharge current.

ELECTROOPTIC CHARACTERISTICS OF THE DISCHARGE

The electrical and optical characteristics of transverse discharges are presented in detail in Refs. 6–9. The fundamental property of such discharges is that a Faraday space occupies a substantial portion of their volume. This space is manifested in a gas mixture and in the components of the mixture. From the standpoint of the creation and annihilation of charged particles this property can be formulated as follows: A discharge is locally non-self-sustained in a substantial portion of the volume; plasma forms as a result of ambipolar drift of charged particles from the near-electrode regions.[10,11]

ON THE INSTABILITY

The transition of a discharge from a diffuse to a contracted form appears inevitably if its parameters exceed certain limiting values. This situation is not considered in the present work. There are many construction-related and technological aspects of the occurrence of this transition. In addition, it can occur at values of the parameters below the maximum values; this is the situation studied in the present work. If the discharge changes into a contracted form at a rate of $\leq 1\ h^{-1}$, then we shall consider it to be unstable.

A transition of the discharge into a contracted form was detected according to a change in the current and voltage on the electrodes.
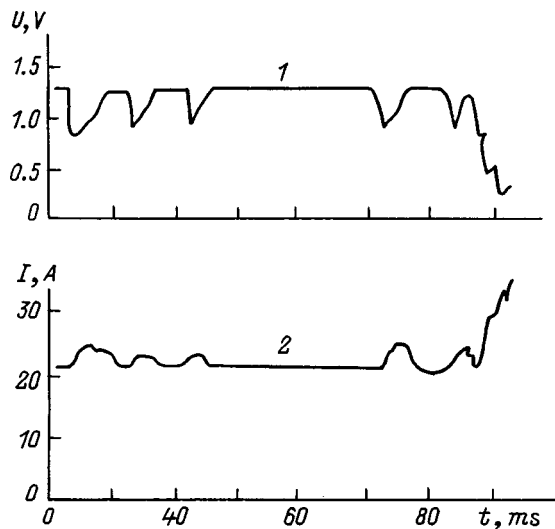

FIG. 2. Contraction development process: *1, 2* — pulsations of the discharge voltage and current, respectively.
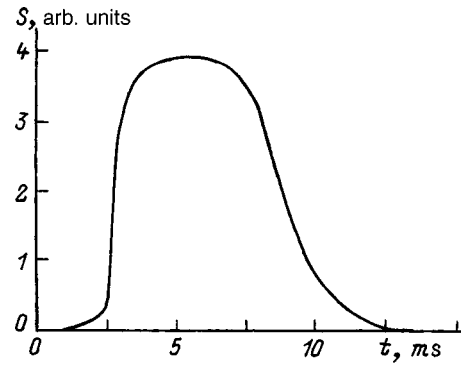

FIG. 3. Contraction development process. Pulsations of emission brightness.

The experiments showed that the contraction could be associated with the anode and cathode. Sometimes situations arose where two discharges were observed to exist: a contracted discharge and an uncontracted extended diffuse discharge. In either case the characteristic dimensions of the channel in which contraction developed did not exceed about 1 cm. This is about 1% of the length of the entire gas-discharge channel. For this reason, its external electrical circuit can be treated as an equivalent resistance consisting of two parallel circuits: the discharge circuit and the power supply circuit for the discharge.[12]

The experimental investigations of discharges with the same configuration on different lasers showed that for the same nominal laser operating regimes the probabilities of a transition of the discharge from a diffuse into a contracted form can differ by two orders of magnitude. No reasons were found for contraction, except factors associated with accumulation of adsorbed substances on the electrodes and the properties of the electric circuits of the discharge. It was always possible to eliminate effects associated with the accumulation of adsorbed substances on the electrodes by special technological methods, in particular, by conditioning the electrodes, in a time of about 10 h and longer.

The temporal development of the contraction of a glow discharge can be judged according to the current and voltage pulsations (Fig. 2) or pulsations of the emission brightness of the discharge (Figs. 3 and 4). The voltage was measured directly on the electrodes, and the current was measured in the power supply circuit for the discharge. The pulsations of the emission brightness were measured using photocells turned directed toward the volume element where contrac-
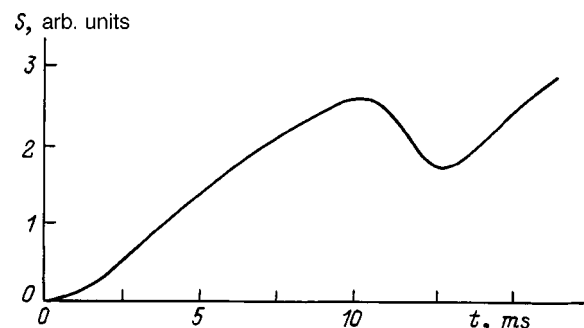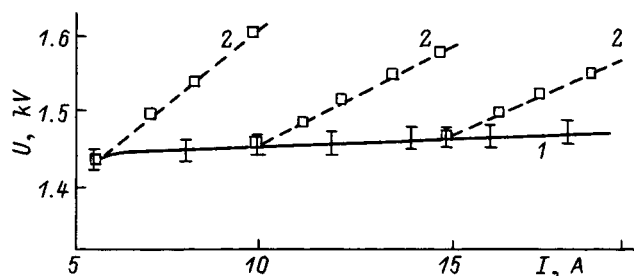

FIG. 4. Same as in Fig. 3.

FIG. 5. Static *1* and dynamic *2* discharge characteristics $U(I)$.

tion was assumed to arise. As a rule, ''contraction precursors'' — a series of pulses ranging in duration from 1 to 10 ms — appear. The process can convert at any stage or it can be extended and terminate by a transition of a diffuse into a contracted discharge.

CURRENT–VOLTAGE CHARACTERISTICS OF A DISCHARGE

The static current–voltage characteristics of the discharge, i.e., the functions $U(I)$, were measured under the condition that the rate of change of I satisfies $\partial I/\partial T \leqslant 2$ A/s. For the experimental conditions, this means that in 1 s the magnitude of the current changes by no more than approximately 20%. The dynamic characteristics $U(I)$ presented correspond to the condition where the rate of change of the current satisfies $\partial I/\partial T > 100$ A/s.

Typical static and dynamic characteristics $U(I)$ of the discharge are presented in Fig. 5. The dynamic characteristics $U(I)$ were found by comparing oscillograms of the pulsations of I and U. Pulsations of I up to 50% in magnitude and about 10^{-2} s in duration were produced using a source of pulsating voltage in the power supply circuit of the discharge. Under the experimental conditions, the differential static resistance of the discharge was $-5 \ \Omega \leqslant (\partial U/\partial I)_{st} \leqslant 15 \Omega$. In contrast to the static resistance, the dynamic differential resistance was positive: $(\partial U/\partial I)_{dyn} = 15 - 80 \ \Omega$.

EFFECT OF THE CIRCUIT AND SOURCE CHARACTERISTICS ON THE DISCHARGE STABILITY

In practice, it is difficult to perform experiments with low rates of transition of a discharge into the contracted form, where the transition rate is 1 h or less. For this reason, conditions were created so that the transition rate of a discharge into the contracted form was higher, $0.3 - 0.1 \, \text{min}^{-1}$. A control check was made for low contraction probability of a discharge.

A prolonged (tens of hours without a transition into a contracted form) discharge could be obtained if the characteristics of its power supply are determined by active and inductive elements. In setups where the electrodes were connected directly to an inductive–capacitive filter (i.e., not through a ballast resistor), the discharge was unreliable. Specifically, connecting to the electrodes of an $L-C$ circuit with a capacitance of about $10 \, \mu$F introduced sharp destabilizing effects — the contraction probability of the discharge increased by a factor of $10-100$. In principle this should have

been expected from analysis of the $U(I)$ characteristics. However, an unexpected fact was that in this case sometimes a relatively prolonged (duration of about 1 h) discharge could occur.

Two sources were connected alternately to the same load: a) a source based on an inductive–capacitive converter with tight feedback on current with ac to dc current conversion with frequency 50 Hz; b) a source with negative feedback on current with ac to dc current conversion with frequency 50 Hz, and an output source resistance of 12 Ω. In the experiments no difference could be observed in the transition rates of the discharge into a contracted form.

A source with negative feedback on current with an output resistance of about 12 Ω was connected to the electrodes through a 30 Ω resistor or directly. No effect of the resistor on the transition rate of the discharge into a contracted form was observed.

An inductance ranging from 0 to 1 H was introduced into the power supply circuit for the discharge. Now effect of the inductance on the transition rate of the discharge into the contracted form was observed.

The effect of current pulsations on the frequency of contractions of the discharge was studied. Current pulsations were either specially introduced by using a source of pulsating voltage or they were produced by using special schemes for rectifying the current. In the experiments, the pulsation frequency varied in the range 50–300 Hz, and the amplitude of the pulsations was 1–50%. No effect of the pulsations on the transition rate of the discharge into a contracted form was observed.

In the adjusted electric discharge setups a discharge operated for 70 h without a transition into a contracted form. This limit is due to termination of the investigations.

CONCLUSIONS

It follows from the results obtained that: a) a discharge cannot be regarded as being autonomous from the standpoint of stability, i.e., stability is an aggregate property of the discharge and its power supply circuit, including the power source; b) the stability of a discharge must be studied taking into account its static and dynamic characteristics $U(I)$.

It was shown that a stable discharge can be realized by using current sources with a soft external $U(I)$ characteristic, and with slow feedback on current, i.e., at low frequencies (50 Hz) of ac to dc current conversion.

[1] V. L. Volkov, A. A. Denisenko, S. I. Zakrevskiĭ *et al.*, Kvantovaya Élektron. (Moscow) **16**, 2234 (1989) [Sov. J. Quantum Electron. **19**(11), 1437 (1989)].

[2] A. I. Ivanchenko, V. V. Krasheninnikov, A. G. Ponomarenko, and A. A. Shepelenko, in *Application of Lasers in the National Economy* [in Russian], Nauka, Moscow (1986), pp. 53–62.

[3] C. E. Jernndo, C. Y. Rowe, and D. J. Swift-Hook, J. Phys. D **8**, L179 (1975).

[4] K. G. Emeleus, Int. J. Electron. **142**, 105 (1977).

[5] V. K. Golov, A. I. Ivanchenko, V. V. Krasheninnikov *et al.*, Izv. SO AN SSSR Ser. Tekh. **10**(2), 87 (1986).

[6] C. C. Vorontsov, A. I. Ivanchenko, V. V. Krasheninnikov *et al.*, Zh. Tekh. Fiz. **47**, 2287 (1977) [Sov. Phys. Tech. Phys. **22**, 1323 (1977)].

[7] A. I. Ivanchenko and A. A. Shepelenko, Zh. Tekh. Fiz. **51**, 2043 (1981) [Sov. Phys. Tech. Phys. **26**, 1191 (1981)].

[8] V. I. Kuprenyuk, S. I. Kliment'ev, N. V. Marusyak *et al.*, Opt.-Mekh. Promst., No. 2, 8 (1984) [Sov. J. Opt. Technol. **51**(2), 71 (1984)].

[9] J. Bergman, E. Ose, and W. Triebel, Exp. Tech. Phys. (Berlin) **34**, 17 (1986).

[10] Yu. S. Akishev, F. N. Vysikaĭlo, and V. V. Ponomarenko, Teplofiz. Vys. Temp. **18**, 266 (1980).

[11] E. P. Velikhov and S. V. Pashkin, Usp. Fiz. Nauk **137**(1), 117 (1982) [Sov. Phys. Usp. **25**, 340 (1982)].

[12] A. I. Ivanchenko, R. I. Soloukhin *et al.*, *Gas Lasers* [in Russian], Nauka, Novosibirsk (1977), pp. 112–134.

Production of fullerenes in gas discharge plasmas. II. Dynamics of reactions between charged and neutral carbon clusters

N. I. Alekseev and G. A. Dyuzhev

A. F. Ioffe Physicotechnical Institute, Russian Academy of Sciences, 194021 St. Petersburg, Russia
(Submitted September 3, 1998)
Zh. Tekh. Fiz. **69**, 42–47 (December 1999)

The formation of fullerene structures in the presence of an electric charge on the carbon clusters is studied. It is shown that the effect of plasma as a carbon source on the dynamics of the change in carbon clusters reduces exclusively to the formation of the initial conditions for efflux of a plasma jet from the interelectrode gap. © *1999 American Institute of Physics.*
[S1063-7842(99)00812-0]

The effect of plasma on fullerene formation processes is described quite clearly in Ref. 1. The crux of the results obtained reduces to the fact that for a given carbon mass flow rate, the fullerene yield can be substantially different for different methods of organizing a discharge.

It is obvious that it is exceedingly difficult to analyze the processes occurring in a high-current arc, which include fullerene synthesis as a component. Such an analysis must take account of the erosion of the electrodes, plasma-forming processes in the interelectrode gap filled with a buffer gas, extraction of the gas jet into the surrounding space, and reactions between the carbon clusters in this jet.

Gas flow in a high-current arc is determined by thermal processes and by the intrinsic magnetic field. An approximate calculation of the gas-transport velocity v_0 in the arc, performed in Ref. 2, gives $v_0 = 151.2 \cdot (I/r_0)(T/P_{He})^{1/2}$. Accordingly, for arc current $I = 100$ A, arc channel radius $r_0 = 0.3$ cm, gas temperature $T = 0.3$ eV, and buffer gas (helium) pressure $P_{He} = 100$ Torr, v_0 is estimated to be $v_0 = 2 \times 10^3$ cm/s. The Reynolds number reaches at least several tens and admits the existence of flow only in the form of a turbulent jet. Striking the electrodes, such a jet turns and flows out of the gap. To a first approximation, the efflux velocity can be set equal to v_0. For reasonable values of the gas temperature $T = 0.3 - 1$ eV the velocity v_0 is always an order of magnitude lower than the sound velocity.

To examine the intertransformations of carbon clusters in such a jet, one must know, as a minimum, the characteristic values of the initial parameters at the gap edge at $r = r_0$, i.e., the density N_1 of atoms, the gas temperature T, the velocity v_0, and the effective initial thickness d_0 of the jet (the thickness d_0 different from the gap width d needs to be introduced because the efflux of helium with the jet requires influx of helium into the gap along the electrodes and the position of the point where the radial velocity changes sign must be set self-consistently). As will be seen below, this set of initial data enters in the dimensionless parameters in the balance equations for carbon clusters of different types and determines the evolution of these clusters.

The dependence of the enumerated parameters on the external conditions (current, voltage on the gap, and pressure P_{He}) is unknown, with the exception of the dependence for the carbon mass flow rate, i.e., for $n_0 v_0 d$ (where n_0 is the total concentration of all possible carbon clusters). It is extremely difficult to perform a theoretical calculation of the stationary state. For this reason, in the present work it was assumed that the initial parameters of the jet were formed in some manner and emphasis was placed on the effect of the plasma component of the jet on the dynamics of the carbon clusters.

This effect can be as follows. The cross sections of the mono- and bimolecular reactions into which clusters enter depend strongly on whether or not the clusters carry a charge; the turbulent transport coefficients determining the residence time of the clusters in the temperature range that is most effective for fullerene formation can differ from the corresponding values for neutral clusters; the spectrum formed and the fullerene yield can depend on the distribution of clusters at the exit of the interelectrode gap, i.e., on the proportion in which the elements C_2, C, C_2^+, and C^+ are present; if the carbon and buffer-gas concentrations are of the same order of magnitude, and the degree of ionization of the plasma sufficiently high, then the energy transfer to it from the hotter electronic component can influence the coarse of the change in gas temperature.

The qualitative picture of the interaction and intertransformations of clusters that is incorporated in the calculation was as follows. A definite sequence of configurations occurs in the formation of both neutral and charged clusters: atoms → molecules → chains → rings → multiring systems → fullerenes,[3] i.e., the topologies of the charged and neutral clusters are identical.

At each stage the difference of the ionic clusters from neutral clusters results in the reaction being speeded up or slowed down. For example, the interaction of a charged chain with a neutral chain can be considered, to a first approximation, to be the interaction ion → dipole, i.e., an attraction. For this reason, the effective barrier E_1 to coagulation should decrease. If E_1 for the coagulation of two atoms, estimated in Ref. 4 to be 0.5 eV, for the interaction of a C^+ ion → C atom decreases to zero, then the reaction rate should approximately triple. On the other hand, the curling

of a charged chain into a ring is inhibited, since the approaching ends of the chains inevitably carry charge of the same sign.

The direct contribution of C^+ ions which exist near the source should not strongly affect the fullerene yield, though the growth rate of charge clusters in the course of coagulation reactions is several times higher. This is due, in the first place, to the fact that the degree of ionization of carbon under the conditions of a large quantity of buffer gas, apparently, is not so high; in the second place, under the conditions of a decreasing electron temperature, charged clusters should intensively recombine.

Even though the final result can be predicted, the proposed computational estimate is helpful at least because it makes it possible to determine the real boundaries of the influence of a plasma on the fullerene formation process.

PARAMETERS OF THE PLASMA INSIDE A FAN-SHAPED RADIAL-SLIT SOURCE OF A TURBULENT JET

In Refs. 5 and 6, where a jet consisting of neutral atoms was investigated, no information was required on the source of the jet, except for the carbon mass flow rate. In the case of plasma, as initial conditions at the boundary of the source it is necessary to set, besides the gas temperature and the carbon concentration, the electron temperature T_e and the concentration of the charged component. For now, there is clearly not enough experimental information for calculating the energy balance in an arc. For this reason, in the present work the electron temperature T_e in the source, the gas temperature T, and the carbon mass flow rate were prescribed. The velocity of all components at the exit of the gap was assumed to be the same and equal to v_0.

The concentration of various plasma components was found from the balance equations. It was assumed that under the conditions of high T_e and T, C atoms, C^+ ions, and small quantities of C_2 molecules and C_2^+ ions are present in the interelectrode gap. The following reactions were taken into account in the calculation: formation of C_2 molecules: $C+C \rightarrow C_2$, and C_2^+ molecules: $C+C^+ \rightarrow C_2^+$, and the reverse spontaneous decay reactions of these molecules; collisional ionization–recombination for C and C^+; dissociative recombination $C_2+e \rightarrow C+C^*$, where C^* is an excited carbon atom.

The cross section σ_0 for the formation of C_2 molecules from two atoms, just as in Ref. 4, was assumed to be $\sigma_0 = \sigma_A \cdot \exp(-E_1/T)$, where $\sigma_A = 5.3 \times 10^{-16}$ cm^2 in a wide range of buffer-gas pressures.[1] The cross section of the atom–ion reaction was given in a similar form as $\sigma_0^+ = \sigma_A \times t^1$. The exponential factor t^1 was varied. In our calculations it was assumed that $t^1 = 1$.

The rate constants for the reverse process of spontaneous decomposition of the molecules were assumed to be

$$\beta_2 = B_2 \exp(-E_2/T), \quad \beta_2^+ = B_2^+ \exp(-E_2^+/T),$$

where E_2 and E_2^+ were the minimum energies of the potential curves for C_2 and C_2^+; the values $E_2 = E_2^+ = 6$ eV were used in the calculation.
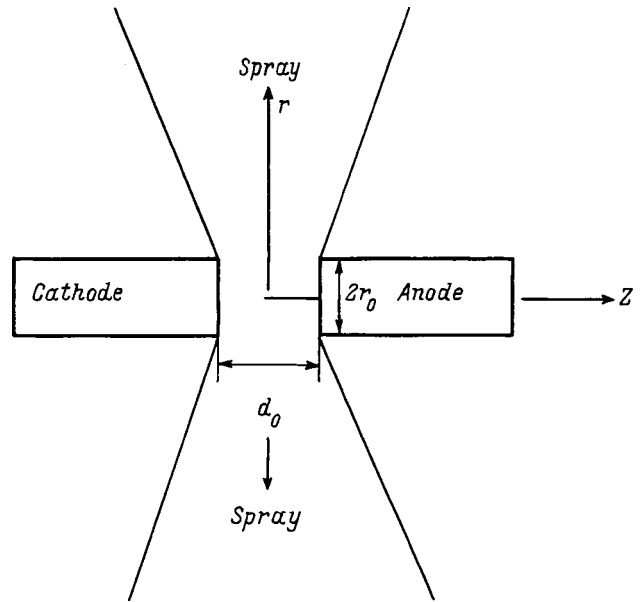

FIG. 1. Geometry of the discharge gap and the radial–slit jet flowing out of the gap.

The dissociative recombination constant K_{diss} for carbon molecules are not available in the existing literature, but it does not differ much for various gases. Specifically, for nitrogen and oxygen at 1 eV $K_{\text{diss}} \approx 2 \times 10^{-8}$ cm^{-3}/s, and it has a similar temperature dependence. The same dependence was also taken for carbon.

The reverse associative ionization process $C+C^* \rightarrow C_2^+ + e$ should also be included in the balance of C atoms and C_0^+ molecules together the dissociative recombination, but reliable information about the rate of such a reaction could not be found either for carbon or for nitrogen and oxygen. On the other hand, the coagulation reaction $C+C \rightarrow C_2$ with the formation of a neutral C_2 molecule has a very large cross section. Against the background of such a reaction, the loss of atoms due to associative ionization can be taken as negligible for the balance of atoms, and the inflow of C_2^+ ions is negligible compared with the result of the reaction $C+C^+ \rightarrow C_2^+$.

A calculation of the rate of step ionization–recombination in collisions $\Gamma_i = \beta_i N_1 n_e - \alpha n_e^3$, as far as we know, has never been performed for carbon. For this reason, just as in the case of dissociative recombination, we used the nitrogen data.[7] In accordance with these data, for gas concentration N_1 at the level $N_1 = 10^{15} - 10^{16}$ cm^{-3} and temperature $T_e = 1.2 - 1.4$ eV, the ionization constant β_i is $\beta_i = 10^{-12} - 10^{-13}$ cm^{-3}/s, and the recombination rate αn_e^3 is much lower than the ionization rate.

We shall assume that the arc burns in a plane-parallel cathode–anode gap with circular electrodes with radius r_0 and symmetry axis passing through their centers (Z axis in Fig. 1).

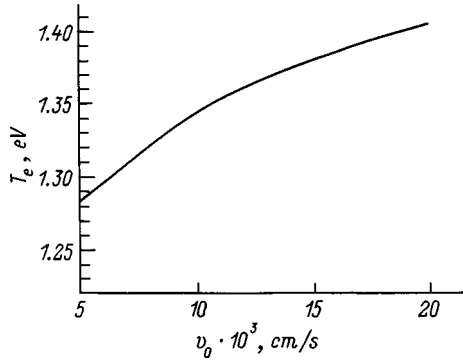The balance equations for the components C, C^+, C_2, and C_2^+ were written as follows:

FIG. 2. The minimum temperature T_e versus the jet velocity v_0 at the gap edge ($T = 0.4$ eV).

FIG. 3. Concentration of the ions C^+ (*1–3*) and C_2^+ (*1′–3′*) versus T_e. $P_C = 20$ torr; $v_0 = 5 \times 10^3$ (*1, 1′*), 10^4 (*2, 2′*), 2×10^4 cm/s (*3, 3′*).

$$-\Gamma_i + R - N_1\eta + \beta_2^+ N_2^+ + 2\beta_2 N_2 - \alpha_0^+ N_1 N_1^+$$
$$- 2\alpha_0 N_1^+ N_1^+ + 2n_e K_{\text{diss}} N_2^+ = 0,$$

$$\Gamma_i - N_1^+ \eta + \beta_2^+ N_2^+ - \alpha_0^+ N_1^+ N_1 = 0,$$

$$-N_2 \eta - \beta_2 N_2 + \alpha_0^+ N_1^2 = 0,$$

$$-N_2^+ \eta - \beta_2^+ N_2^+ + \alpha_0^+ N_1^+ N_1 - n_e K_{\text{diss}} N_2^+ = 0, \quad (1)$$

where $n_e = N_1^+ + N_2^+$ is the electron density; α_0 and α_0^+ are atom–atom and atom–ion coagulation constants; $\alpha_0 = v_T \sigma_0$, $\alpha_0^+ = v_T \sigma_0^+$, v_T is the thermal velocity of C_2 molecules; R is the source of carbon vapor per unit volume of the discharge gap; $\eta = 2v_0/r_0$.

To solve the system (1) it is convenient to give the concentration N_1 and find the source strength for the experimental value of the carbon flow rate. Then, taking account of the condition $N_2^+ \ll N_1^+$, we have

$$N_1^+ = [N_1(\beta_2^+\beta_i + \eta(\beta_i - \alpha_0^+)) - \eta(\beta_2^+ + \eta)]$$
$$\times [\eta - N_1(\beta_i - \alpha_0^+)]^{-1},$$

$$N_2^+ = \alpha_0^+ N_1^+ N_1 / (\eta + \beta_2^+ + n_e K_{\text{diss}}). \quad (2)$$

The requirement $N_2^+ > 0$ and the balance of C^+ ions give the condition

$$\beta_i < \alpha_0^+ + \eta/N_1, \quad (3)$$

which can be regarded as an upper limit on the electron temperature T_e.

On the other hand, the simultaneous solution of the equations for C^+ and C_2^+ together with the condition $N_1^+ > 0$ gives a lower limit on T_e,

$$\beta_i > \eta[\alpha_0^+ + (\eta + \beta_2^+)/N_1]/(\beta_2^+ + \eta). \quad (4)$$

The dependence of the minimum temperature T_e on the velocity v_0 with a fixed carbon pressure $P_C = 20$ Torr is presented in Fig. 2. Figure 3 shows the concentrations of the ions C^+ and C_2^+ as a function of T_e for several velocities v_0. All curves shown in the figure are drawn for electron temperatures approximately corresponding to the maximum degree of ionization of the plasma.
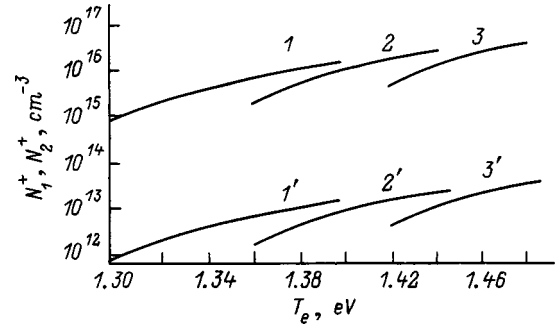
CALCULATION OF THE CHANGE IN THE PARAMETERS OF THE PLASMA AND GAS IN A JET

As noted previously, reactions leading to intertransformations of clusters outside the discharge gap proceed under the conditions of a subsonic turbulent jet. Existing theories of such a jet make it possible to determine its parameters only if the concentration of one component, considered to be the impurity, is low. Then the gas temperature and the total concentration of the impurity (carbon) are determined by linear equations of turbulent transport and are described by simple analytical solutions. The reactions leading to intertransformations of carbon clusters are studied against the background of these solutions.

We used the simplest variant of the turbulent theory — Prandtl's theory,[8] which makes it possible to obtain the radial–axial dependences of the total impurity concentration and temperature of the gas on the basis of boundary-layer equations and self-similarity hypotheses for the solutions, i.e., the possibility of writing the solution for any quantity $\Re(r,z)$ in the form $\Re = \Re(r)f(z)/r$. Let us write out the solutions.

The radial velocity is $v_r = v_r^m dF/d\psi$, where $v_r^m = v_0 \Theta_v/x$ is the gas velocity in the symmetry plane of the jet and $x = r/r_0$; $\psi = z/ar$; $\Theta_v = 1.2 \cdot (d_0/2ar_0)^{1/2}$; a is a universal experimental constant in the turbulent theory, equal to approximately 0.12; F is a universal function which is calculated numerically. The transverse velocity is $v_z = a v_r^m(\psi dF/d\psi - F(\psi))$. The total impurity concentration is $n = n_m(v/v_r^m)^{\text{Sc}}$, where $n_m = n_0 \Theta_n/x$; $\Theta_n = 1.2 \times (d_0/2ar_0)$; Sc is the empirically determined turbulent Schmidt number. For a radial–slit geometry of the problem, the best agreement with experiment is obtained with Sc = 0.8. The temperature difference between the gas inside and outside the jet is $\delta T = \delta T_m(v/v_r^m)^{P_r}$, where $\delta T_m = \delta T_0 \Theta_T/x$, $\Theta_T = 1.2(d_0/2ar_0)$, and P_r is the turbulent Prandtl number.

The dynamics of carbon clusters was described by a system of continuity equations averaged over the transverse coordinate z within the jet. Just as in Refs. 5 and 6, we did not use the solution of the two-dimensional problem, since the constants of all reactions described on the right-hand side of the equations are nonlinear functions of the temperatures and concentrations, and the self-similarity hypothesis most likely does not hold for different impurity components.

To include new components in the analysis, as compared with the components which were studied in the interelectrode gap of the arc, specifically, neutrals and charged chains and rings, it is necessary to include the additional reactions $C + C_2 \rightarrow C_3$, $C + C_2^+ \rightarrow C_3^+$, $C^+ + C_2 \rightarrow C_3^+$ — coagulation of carbon atoms and ions with C_2 molecules; $C_2 + C_2 \rightarrow C_4$, $C_2^+ + C_2 \rightarrow C_4^+$ — coagulation of charged and neutral C_2 molecules; $C_m + C_n \rightarrow C_{m+n}$, $C_m + C_n^+ \rightarrow C_{m+n}^+$ — coagulation of chains of different sizes; $C_n \rightarrow R_n$ — curling of a chain into a ring; $C_n^+ + e \rightarrow C_{n-1} + C$ — dissociative recombination of charged chains.

The constants for these reactions were chosen as follows. The cross sections σ_{mk} for the coagulation of neutral chains were calculated in Ref. 4. Just as in Ref. 4, we assumed that σ_{mk} are proportional to the exponential factor $t^0 = \exp(-E_1/T)$, which is a common factor for all collisions of clusters up to chains, inclusively. It was assumed that the cross sections for the coagulation of neutral and charged clusters are determined by the same weighting factors as neutral clusters, and the exponential factor $t^1(T)$ can be varied. For the results presented below, it is simply 1, but for generality it is retained in the balance equations.

We were not able to find any experimental data on the dissociative-recombination rates of charged chains C_n^+ and even on the possible channels for such a reaction. For this reason, it was assumed that in the course of recombination the chain length decreases by 1, and the reaction constant is the same as for recombination of a C_2^+ chain. This idea is based on the fact that the most weakly bound atom in a chain should be the endmost atom.

As an illustration, we shall write out on this basis the balance equations for C atoms and charged chains C_n^+.

Atoms

$$dv_1/dx + v_1/x = Ax \left[-\Gamma_i/\alpha_A v_T - \xi_{11} v_1(2v t^0 + v_1^+ t^+) \right.$$

$$-\xi_{12} v_1(v_2 t^0 + v_2^+ t^+)$$

$$\left. -v_1 \sum_{c=3} \xi_{1c}(\gamma_c^+ t_c^+ \gamma_c t^0) \right]$$

$$+ (1/\sigma_A v_T n_0) \left[(2\beta_2 v_2 + \beta_2^+ v_2) \right.$$

$$\left. + (v_e K_{\text{diss}}/\sigma_A v_T) \left(2v_2^+ + \sum_{c=3} \gamma_c^+ \right) \right]. \quad (5)$$

Neutral chains of length c

$$d\gamma_c/dx + \gamma_c/x = Ax \left[-\xi_{1c}(v_1 t^0 + v_1^+ t^0) \gamma_c \right.$$

$$+ \xi_{1,c-1}(v_1 t^0 \gamma_{c-1} + v_1 t^+ \gamma_{c-1}^+)$$

$$+ \xi_{2,2-c}(v_2 t^0 \gamma_{c-2} + v_2^+ t^0 \gamma_{c-2}^+)$$

$$-\xi_{2,c}(v_2 t^0 + v_2^+ t^+) + \sum_d \xi_{d,c-d}(\gamma_d t^0$$

$$+ \gamma_d^+ t^+) \gamma_{c-d} - \gamma_c \sum_d \xi_{d,c}(t^0 \gamma_d + t^+ \gamma_d^+)$$

$$-\gamma_c^2 \xi_{c,c} t^0 + K_{\text{diss}} \gamma_{c+1}^+/\sigma_A v_T \Big]$$

$$-w_0 r_0 x \gamma_c/v_0 \Theta_v, \quad (6)$$

where $A = \sigma_a r_0 n_0 v_T \Theta_n/\Theta_v V_0$; $\xi_{m,k} = ((m+k)/mk)^{1/2}$; v_1, v_1^+, γ_c, and γ_c^+ are the concentrations of the atoms, C^+ ions, and neutral and charged chains scaled to n_0; w_c is the probability of a chain curling into a ring.

The initial equation for determining the temperature decrease law was the energy balance equation for a partially ionized plasma in the form[9]

$$\text{div}((5/2)n v_{T_e} - n\chi \nabla T_e) = -n v \nabla \varphi - E_i \Gamma_i$$

$$- n v_T(3/2) N_{\text{He}}(T_e - T)$$

$$\times (m/M_{\text{He}}) \sigma_{e-\text{He}}, \quad (7)$$

where $n\chi = k = n v_{T_e}/\sigma_{e-\text{He}} N_{\text{He}}$ is the electron thermal conductivity due to collisions with helium atoms; φ is the plasma potential; $\sigma_{e-\text{He}} = 5 \times 10^{-16}$ cm^2 is the cross section for elastic scattering of electron by helium.[10]

Following the general scheme for constructing turbulent solutions,[8] this equation must be averaged and time-averages of the type $\langle \delta v \delta T_e \rangle$, and so on, must be given. Thus, the average $\langle \delta v \delta T_e \rangle$ should be set equal to $\langle \delta v \delta T_e \rangle = (l_u 2/Pr_{T_e})|\partial v_z/\partial z|\partial T_e/\partial z$, where l_u is the characteristic mixing length for the velocity. Unfortunately, nothing reliable is known about empirical constants of the type Pr_{T_e}, and in addition there are no arguments in favor of the self-similarity hypothesis being valid for T_e. For this reason, since the large electron energy losses in collisions with a buffer gas are large, the turbulent losses in Eq. (7) were neglected. The temperature curve obtained in this manner can be assumed to be an upper limit.

After substituting into Eq. (7) the value of $\nabla \varphi$ derived from the equation of motion of electrons in the form

$$n_e v = -\mu[-n\nabla \varphi + T_e \nabla n_e + n_e \nabla T_e(1 + k_e T)]$$

(where μ is the electron mobility), and taking account of the balance of the number of electrons in the form $\text{div}(n_e v) = \Gamma_i$, we obtain

$$2n_e(v \nabla T_e) - \chi \cdot \text{div}(n_e \nabla T_e)$$

$$= n_e v^2/\mu + \Gamma_i \cdot (-E_i - 3T_e/2) - G, \quad (8)$$

where $G = n_e v_{T_e} \cdot (3/2) \cdot N_{\text{He}} \cdot (T_e - T)(m/M_{\text{He}}) \cdot \sigma_{e-\text{He}}$.

Let us estimate the role of the different terms on the right-hand side of the equation. The ratio $\Gamma_i E_i/G$ is 0.05 for $N_c/N_{\text{He}} = 1/5$ and cross section $\sigma_{\text{ion}} = 10^{-12}$ cm^2 (which corresponds to the temperature $T_e = 1.3$ eV); the ratio $n_e v^2 \mu_{-1}/G \approx (T_e/(T_e - T)) \cdot (v/v_{T_e})^2 \cdot (m/M_{\text{He}})^{-1}$ is also much less than 1. Therefore the term G, describing energy transfer from electrons to buffer-gas atoms predominates.

On the left-hand side of the equation the ratio of the energy fluxes transported together with the jet and due to heat conduction is $v_0 T_e/k dT_e/dx \sim L/300 r_0 \ll 1$ for $v_0 = 2$

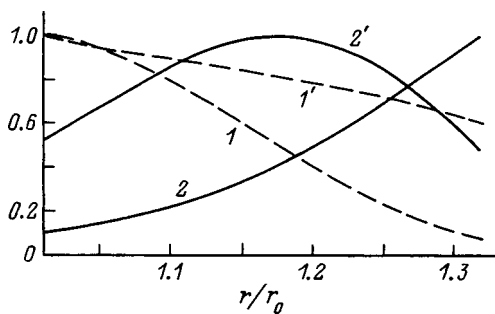FIG. 4. Radial distributions of the concentrations of the ions C^+ (*1*), molecular ions C_2^+ (*2*), atoms C (*1'*), and molecules C_2 (*2'*). $P_C = 20$ Torr, $P_{He} = 200$ Torr, $T = 0.4$ eV, $T_e = 1.42$ eV, $v_0 = 2 \times 10^4$ cm/s, $N_1 = 4.2 \times 10^{16}$ cm^{-3}, $N_1^+ = 3.82 \times 10^{15}$ cm^{-3}, $N_2^+(1) = 3.31 \times 10^{12}$ cm^{-3}.

FIG. 5. Radial distributions of the concentrations of charged chains C_3^+ (*1*), C_6^+ (*2*) and neutral chains C_3 (*1'*), C_6 (*2'*). The computational parameters correspond to Fig. 4.

$\times 10^3$ cm/s, where L is the characteristic decay scale of the temperature T_e. Therefore, in contrast to a supersonic jet, energy transport due to heat conduction dominates on the left-hand side and the equation acquires the form

$$(r^{-1} + n_e^{-1} dn_e/dx) dT_e/dx + d^2 T_e/dx^2$$
$$= (9/4)(r_0 N_{He} \sigma_{e-He})^2 (T_e - T)(m/M_{He}). \quad (9)$$

To solve the second-order differential equation it is necessary to know the derivative dT_e/dx at the boundary of the source, which is determined by the energy balance, which we do not know. For this reason, we proceed as follows: we neglect $n_e^{-1} dn_e/dx$ compared with 1 and, using the dependence $T \sim 1/x$, we write the solution of the equation in the form

$$T_e = (T_e^{(0)} - T_0) K_0(\lambda^{1/2} x)/K_0 \lambda^{1/2} + T_0/x, \quad (10)$$

where $\lambda = (9/4) \cdot (r_0 N_{He} \sigma_{e-He})^2 (m/M_{He})$; $T_e^{(0)} = T_e(x=1)$, $T_0 = T(x=1)$.

The second term in Eq. (10) is a particular solution of the inhomogeneous equation, and the first term is the general solution of the homogeneous equation. The factor in front of the modified Bessel function $K_0(\lambda^{1/2} x)$ is chosen on the basis of the boundary condition $T_e = T_e^{(0)}$ at $x=1$.

COMPUTATIONAL RESULTS AND DISCUSSION

The radial distributions of the concentration of C atoms, C^+ ions, C^2 molecules, and C_2^+ ions, in arbitrary units, are presented in Fig. 4. The concentration values presented are normalized to their maximum value in the interval $(1, x)$. It is evident that the concentration of molecular ions increases much more rapidly than that of the neutral molecules C_2, but it then drops off much more rapidly. This is due to not only intensive recombination but also annihilation of C_2^+ ions as a result of which merging with other clusters.

The same regularities also appear for C_2^+ chains, even though, in contrast to neutral chains, their annihilation channel via curling into a ring is essentially closed. The concentration of C_2^+ chains (Fig. 5, curve *2*) decreases to zero, while the concentration of neutral chains of the same size has still not reached a maximum. Therefore, under the conditions presented in Fig. 5, the plasma essentially does not spread further than 0.5 radii of the discharge gap.
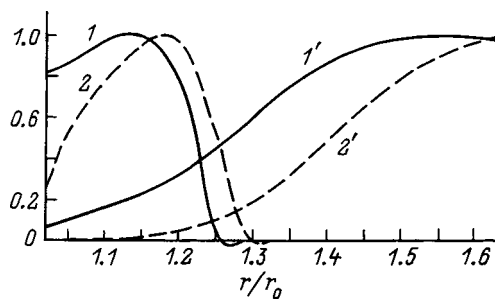
An analysis of a very wide range of conditions (velocity from 2×10^3 to 2×10^4 cm/s and carbon atom density at the jet entrance from 5×10^{15} to 5×10^{16} cm^{-3}) shows that in the optimal case plasma should not propagate further than $(0.5 - 1) r_0$. The concentration of neutral chains at the moment when there are no longer any charged clusters present is approximately proportional to the total concentration of charged and neutral monomers at the jet entrance, i.e., information about the degree of ionization of the initial plasma remains almost forgotten. Thus, the effect of plasma as a carbon source on the dynamics of the variation of carbon clusters reduces exclusively to the formation of initial conditions for efflux of the jet from the gap, i.e., the initial velocity, temperature, and concentration.

[1])In reality, for helium pressures of 100–200 Torr the formation of a dimer C_2 is a zero-barrier three-particle association process with the participation of a helium atom. The cross section of the process is more accurately expressed as $\sigma_0 = R_3 \cdot N_{He}/v_T$ with the constant K_3, where N_{He} is the helium concentration and v_1 is the thermal velocity.

[1] D. Afanas'ev, I. Blinov, and A. Bogdanov, Zh. Tekh. Fiz. **64**(10), 76 (1994) [Tech. Phys. **39**, 1017 (1994)].
[2] S. Ramakrishnan, A. Stokes, and J. Lowke, J. Phys. D **11**, 2267 (1978).
[3] J. M. Hunter, J. L. Fye, and M. F. Jarrold, J. Chem. Phys. **3**, 1785 (1993).
[4] V. A. Schwiegert, A. L. Alexandrov, Y. N. Morokov, and V. I. Bedanov, Chem. Phys. Lett. **235**, 221 (1995).
[5] G. A. Nerushtev and G. I. Sukhinin, Pis'ma Zh. Tekh. Fiz. **21**(13), 50 (1995) [Tech. Phys. Lett. **21**(7), 514 (1995)].
[6] A. V. Krestinin, A. P. Moravskiĭ, and P. A. Tesner, Khim. Fiz. **17**(9), 70 (1998).
[7] A. V. Potapov, L. E. Tsvetkova, V. I. Antropov, and G. I. Volkova, Opt. Spektrosk. **43**(3), 112 (1977) [Opt. Spectrosc. **43**, 243 (1977)].
[8] G. N. Abramovich, *The Theory of Turbulent Jets* [in Russian], Nauka, Moscow (1984), 560 pp.
[9] B. Ya. Moĭzhes and G. E. Pikus (Eds.), *Thermionic Converters and Low-Temperature Plasmas* [in Russian], Moscow (1973), 480 pp.
[10] L. M. Biberman, V. S. Vorob'ev, and I. T. Yakubov, *Kinetics of Nonequilibrium Low-Temperature Plasmas* [Consultants Bureau, New York (1987); Nauka, Moscow (1982), 375 pp.].

Translated by M. E. Alferieff

Production of fullerenes in an arc discharge in the presence of hydrogen and oxygen

D. V. Afanas'ev, A. A. Bogdanov, G. A. Dyuzhev, V. I. Karataev, and A. A. Kruglikov

A. F. Ioffe Physicotechnical Institute, Russian Academy of Sciences, 194021 St. Petersburg, Russia

D. Deininger

Institute of Innovational Technologies, Keten, Germany

The production of fullerenes in an arc with graphite electrodes in mixtures of helium with oxygen and hydrogen as well as in pure oxygen and hydrogen is investigated. The radiation spectra of the arc and the mass spectra of the soot obtained in the arc are recorded; the content of fullerenes in the soot is determined. It is shown that fullerenes are formed in appreciable quantities ($\sim 1\%$) even in pure hydrogen. © *1999 American Institute of Physics.*
[S1063-7842(99)00912-5]

Quite a long time has now passed since the discovery of fullerenes, but the enigma of the effective formation of fullerene molecules in an arc discharge remains largely unsolved. In this situation, information about fullerene synthesis in an arc under strongly suboptimal conditions could be helpful. The objective of the present work is to study the effect of hydrogen and oxygen on fullerene formation in an arc discharge.

EXPERIMENT

Arc discharges were studied in a 180-mm in diameter water-cooled vacuum chamber. Vertically arranged graphite electrodes with diameter $d_{el} = 6$ mm were secured to mobile water-cooled holders, which were introduced into the chamber through end flanges using Wilson seals. The volume of the chamber was $16l$. Prior to a discharge, the chamber was evacuated to pressure below 0.1 torr and flushed with helium. Next, the experimental gases and mixtures were introduced into the chamber. The chamber contained observation windows for extracting the discharge radiation. Radiation in the range 360–700 mm was detected with an MDR-23 monochromator and a photomultiplier or on photographic film using an ISP-51 spectrograph (with a glass prism).

A short focal length lens and a Dove prism were used for photographing the spectrum. This made it possible to record the discharge radiation from regions located at different radial distances along the axis of the discharge. With an 8–10 mm high slit, radiation from an approximately 40 mm in diameter discharge region could be recorded.

The soot was collected from the chamber walls after the discharge. A weighed amount of soot (50 mg) was mixed with toluene (25 cm^3), after which the components of soot dissolved in the toluene were extracted. The absorption spectra of the solutions obtained were recorded with a spectrophotometer in the range 300–600 nm. Mass spectra of the volatile components of the soot were obtained for a number of regimes using a mass-reflectron type time-of-flight mass spectrometer. Vapors of the experimental mixture were introduced into the ionization chamber of the mass reflectron by heating microquantities of soot in a furnace.

RESULTS

a) *Helium + hydrogen mixture.* As a rule, regimes with helium pressure 70 Torr and current 80 A were investigated. The hydrogen addition ranged from 0.1 to 30 Torr. Some discharges were conducted in a pure-hydrogen atmosphere at 20 and 70 Torr pressures.

Detection of the atomic hydrogen line H$_\alpha$ (656.28 nm) during the discharge showed that the intensity of the radiation in this line decreases, and the radiation completely vanishes after a time τ_H. The dependence of τ_H on the initial helium pressure is shown in Fig. 1. The vanishing of hydrogen from the chamber is seen especially clearly in experiments with a discharge in pure hydrogen. The pressure in such a discharge drops smoothly to zero (Fig. 2). Comparing Figs. 1 and 2 shows that helium strongly slows down the escape of hydrogen. It is evident that hydrogen, combining with carbon vapors, forms diverse hydrocarbons, which settle onto the chamber walls together with the soot. This was confirmed by the mass spectra of soot obtained in such discharges. They consist of many peaks in the range up to 400–500 u with periodicity 14 and 20 u. In this region the maximum peaks were recorded at 152, 178, 202, 226, and 252 u. The position of these peaks is identical to the previously observed peaks of polyaromatic hydrocarbons (PAHs) under conditions of laser vaporization of graphite in an argon–hydrogen mixture.[1] The total amount of such PAHs in soot does not exceed 1% even for a discharge in pure hydrogen.

In the regimes investigated the erosion rate of the anode was ≈ 3 mg/s, while the average rate of hydrogen ''burnup'' is an order of magnitude of lower. Since the ratio of carbon and hydrogen in the PAHs is approximately 2:1, and the mass spectrometry shows a very small quantity of hydrogenated fullerenes $C_{60}H_x$, where $x < 3$, most of the hydrogen is
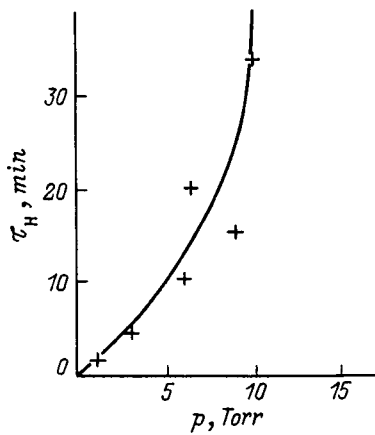
FIG. 1. Dependence of the time τ_H at which the H_α line vanishes on the initial pressure with $p_{He} = 70$ Torr and $I = 80$ A.

FIG. 3. Absorption coefficient of a toluene solution of soot extract as a function of wavelength. $I = 80$ A; p_{He}, Torr: *1–3* — 70; *4, 5* — 0; p_{H_2}, Torr: *1* — 0; *2, 3* — 1.5; *4* — 70; *5* — 20; τ_d, min: *2* — 30; *3* — 10; *4, 5* — 20.

therefore a constituent of the nonvolatile components of soot with very large mass.

In contrast to previous work[1,2] it was found, using mass spectroscopy, that fullerenes form in small quantities even in discharges burning in a pure-hydrogen atmosphere.

The fullerene content α in soot increases as the admixture of hydrogen in the mixture decreases and as the burn time τ_d of the discharge increases. It is obvious that for $\tau_d \gg \tau_H$ the fullerene content α should be essentially equal to the value $\alpha = 14\%$ for a discharge in pure helium. This was confirmed by mass spectra and measurements of α performed with the aid of the absorption spectra of the solutions.

It should be noted that for such regimes the absorption spectra (Fig. 3) can differ from the standard spectra of fullerene solutions, since all soluble hydrocarbons formed in the discharge pass from the soot into the solution. Especially large differences are seen for discharges in pure hydrogen (curves *4* and *5*), where only a feature in the form of a step on a smoothly growing absorption curve remained from the strong maximum of fullerene absorption at $\lambda = 335$ nm. It is obvious that these differences decrease as hydrogen pressure decreases and τ_d increases.

Although the standard method of determining α from the absorption of the solutions is inapplicable here, it was
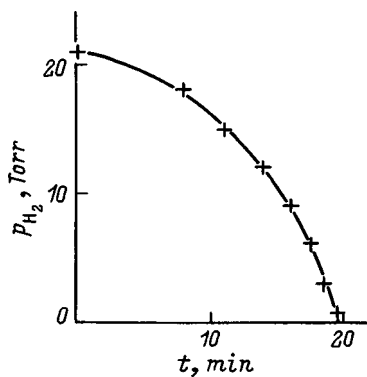

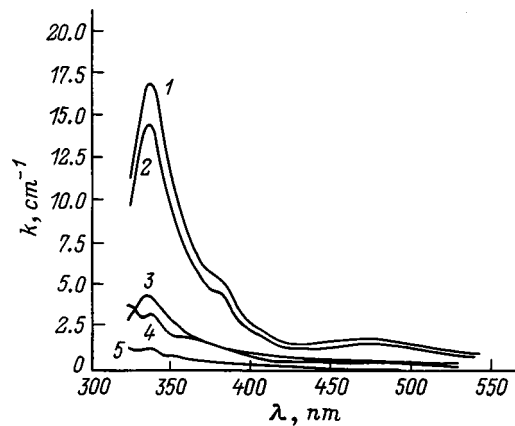FIG. 2. Variation of the pressure in a discharge in pure hydrogen with $I = 80$ A.

shown using the mass-spectroscopic method that the fullerene contents in regimes corresponding to the curves *2*, *3*, and *5* in Fig. 3 are in the ratio 10:5:1. Despite such a large difference in the absolute values of α, the relative content of the fullerenes C_{60} and C_{70} in these three regimes is very close and equals 84:16. In all regimes the soot also contains higher fullerenes (up to C_{84}) in a total amount of 3–5%.

When interpreting the results of the detection of the discharge radiation, it should be kept in mind that only the intensities of the atomic or molecular lines averaged over oscillations in the space of the current channel can be determined from the spectra obtained on photographic film exposed for several seconds.

Only strong molecular bands of the Swan system of the C_2 molecule and the violet system of the CN molecule as well as the atomic lines of HeI and CI were recorded in the spectrum of the discharge in pure helium.[3,4] The radiation of the atomic lines in the interelectrode gap intensifies toward the cathode, and the molecular bands intensify toward the anode. In the radial direction, the radiation of the atomic lines is concentrated in a quite narrow channel with diameter $1-1.5 d_{el}$. The atomic lines fix in the arc a region of maximum temperatures, which coincides with the current channel. The molecular bands are also emitted in the far periphery of the discharge (in the region 40 mm and greater). In some photographs the luminance of the molecular bands has two maxima located directly on both sides of the region where the radiation of the atomic lines is observed.

When hydrogen is added, the Balmer series of the hydrogen atom, whose lines are emitted only within the current channel, appear in the spectrum. The number of these lines increases with the hydrogen partial pressure in the mixture. At $p = 9$ Torr three lines from H_α (656.28 nm) to H_γ (434.05 nm) are seen, and in the discharge in pure hydrogen at $p = 70$ Torr five lines up to H_ε (397.00 nm) can be seen. A molecular band of the radical CH (314.2 nm) appears in the spectrum. It is very weak even with the addition of 30 Torr hydrogen to 40 Torr helium. Judging from the blackening on the photographic film, its integrated intensity is several orders of magnitude lower than the total intensity in all
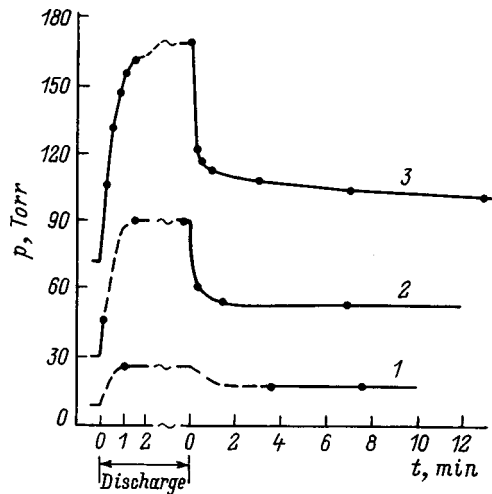
FIG. 4. Total pressure in the chamber as a function of time during and after the discharge. p_{O_2}, Torr: *1* — 9.0, *2* — 30.0, *3* — 31.5; p_{He}, Torr: *1, 2* — 0; *3* — 39.6; τ_d, min: *1, 3* — 50; *2* — 16.

FIG. 5. Fullerene content α in soot versus the initial oxygen pressure in the chamber with $p_{He} = 70$ Torr and $I = 80$ A.

bands of the molecules C_2 and CN. The rotational structure of the very weak molecular band CH 388.90–387.13 nm is also seen in the spectrum of a discharge in pure hydrogen ($p = 70$ Torr). In contrast to the 314.2 nm band, this band is tinted red and does not have such a strongly expressed "head." In the radial direction, the luminescence of the CH band terminates before that of the C_2 and CN bands.

b) *Helium + oxygen mixture.* In this case, just as in hydrogen, regimes with helium pressure 70 Torr and current 80 A were investigated. The addition of oxygen to helium ranged from 0.3 to 30 Torr. Discharges in pure oxygen were also conducted (p from 10 to 300 Torr).

Information about the behavior of oxygen can be obtained by analyzing the time dependence of the total pressure in the chamber during and after the discharge (Fig. 4). The pressure was measured with a deformation vacuum meter to within 0.5 Torr.

When the discharge was switched on, the pressure started to increase and reached a stationary value in 1–2 min. After the discharge ended, the electrons, the fittings, and the gas in the chamber cooled down and the pressure decreased, reaching the final value p_k after several minutes. It turned out that in all regimes investigated the difference of p_k and the initial helium pressure is, to within 5–10%, twice the initial oxygen pressure. Such a pressure increase can be explained only by the formation of two stable carbon monoxide molecules CO from each oxygen molecule O_2 in the discharge. An estimate of the minimum bonding time of oxygen with an average anode erosion rate of 3 mg/s gives 1 min, which correlates well with the experimental variation of the pressure at the start of the discharge.

The absorption spectra of the toluene extracts of soot, which was obtained from discharges in a helium + oxygen mixture and in pure oxygen, have essentially the same form as the spectra of the extract from a discharge in pure helium. This shows that such extracts contain only fullerenes, and the C_{60} and C_{70} ratio is essentially independent of the amount of oxygen added. This was confirmed by the mass spectrum of
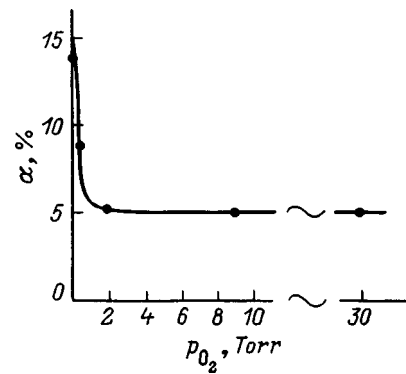
soot obtained from the discharge in the mixture $p(He) = 70$ Torr, $p(O_2) = 9$ Torr. Only groups of peaks corresponding to the fullerenes C_{60} and C_{70} in the ratio 84:16 were observed in this mass spectrum. The $C_{60}O$ peak is absent in the mass spectrum. Therefore, under these conditions, the method of the optical absorption of the extracts can be used to determine the fullerene content α in the soot.

Figure 5 shows α as a function of the oxygen pressure in a helium–oxygen mixture. It is evident that when only 1 Torr oxygen is introduced, α drops by almost a factor of 3 from 14 to 5%, and it then remains essentially unchanged as $p(O_2)$ increases to 30 Torr.

Figure 6 shows α as a function of $p(O_2)$ for discharges in pure oxygen. Fullerenes form, and by no means in small quantities, even in pure oxygen (more accurately, as shown above, in carbon monoxide). As the oxygen pressure decreases, α is observed to decrease, as is also characteristic for other buffer gases (He, Ar, Ne, and their mixtures[4,5]). The maximum value of α in oxygen is $\sim 2.3\%$. This value is close to the value of α which we obtained in Ar and Ne.[4]

Emission of a strong line of atomic oxygen OI $\lambda = 777.19$ nm, which showed little change over a quite long period of time, was detected in the spectrum of a discharge in pure oxygen and mixtures of oxygen with helium. For example, with the addition of 1.5 Torr oxygen the OI line decreased in intensity after the discharge burned for 30 min. With the addition of 10 Torr oxygen no appreciable decrease
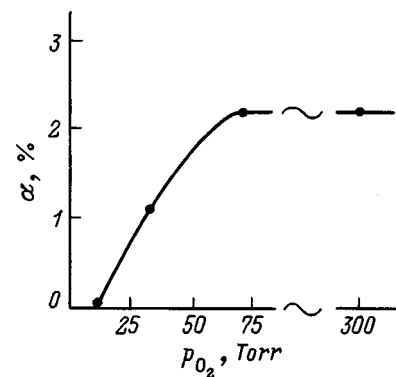

FIG. 6. Fullerene content α in soot versus the initial oxygen pressure in the chamber for discharges in pure oxygen with $I = 80$ A.

of emission was detected after the discharge burned for 50 min. With the addition of 10 Torr oxygen to helium (70 Torr) the atomic lines HeI and CI virtually vanished. The molecular bands became sharper, and a larger number of bands was recorded. In addition, sequences of bands of C_2 molecules can be seen: 619.1 nm (from the Swan system) and 361.7 nm (from the Deslandres–d'Azambuja system); CN molecules: 460.6 nm. The CO and O_2 molecules, which have strong molecular bands in the entire optical range, were not represented at all in the spectrum.

CONCLUSIONS

Of course, it is very difficult to give a detailed description of the kinetics of the system helium + hydrogen, but plausible conjectures can be made which would take account of the experimental facts presented above and at least shed some light on the situation. In the arc channel, hydrogen and carbon are in an atomic state. Away from the channel, as the gas temperature decreases, at first small, purely carbon molecules are formed, since the energy of the C–C bond is much higher than that of C–H. At distances from the arc channel where hydrogen starts to bind successfully with carbon, most of the carbon is now combined into molecules with 10 atoms on the average. Apparently, hydrogen is incorporated into a growing molecule so as to prevent further transformation of the molecule into fullerene and PAHs with mass up to 400–500 u. This is why the fullerene formation is ineffective ($\alpha \leqslant 1\%$) as long as hydrogen is present in the chamber.

The growing carbon molecules with hydrogen inclusions serve as nuclei of particles of soot, together with which hydrogen settles on the walls. After hydrogen leaves the chamber, the fullerene formation efficiency is finally restored to a level characteristic for a discharge in pure helium. For this reason, in the production of fullerenes in a nonflow-through system, even comparatively large admixtures of hydrogen to helium 1–2 Torr have virtually no effect on the fullerene yield. This result also pertains to other hydrocarbon contaminants in helium.

In contrast to hydrogen, oxygen reacts rapidly with carbon vapors, since only one carbon atom is required to bind one oxygen atom. The reaction rate is limited in the regimes investigated only by carbon vapor inflow (anode erosion). Carbon monoxide CO forms in this reaction, and it remains inside the chamber throughout the entire time of the discharge, raising the pressure. However, the presence of O_2 and CO molecules is not manifested at all in the emission spectrum of the discharge and in the mass spectrum of soot. Nonetheless, the introduction of oxygen into the discharge decreases the fullerene yield to 5%. It can be inferred that outside the arc channel recombination of C and O atoms and the CO molecules formed, which can be regarded as a molecular buffer gas, change the temperature distribution of the gas, which, undoubtedly, should effect the fullerene formation process.

[1] M. S. De Vries, K. Reihs, and H. R. Wendt, Geochim. Cosmochim. Acta **57**, 933 (1993).
[2] I. Tai, K. Inukai, and T. Osaki, Chem. Phys. Lett. **224**, 118 (1994).
[3] D. V. Afanas'ev, A. A. Bogdanov, and G. A. Dyuzhev, Mol. Mater. **7**, 93 (1996).
[4] D. V. Afanas'ev, A. A. Bogdanov, and G. A. Dyuzhev, Zh. Tekh. Fiz. **67**(2), 125 (1997) [Tech. Phys. **42**, 234 (1997)].
[5] D. V. Afanas'ev, A. A. Bogdanov, and G. A. Dyuzhev, Zh. Tekh. Fiz. **64**(10), 76 (1994) [Tech. Phys. **39**, 1017 (1994)].

Translated by M. E. Alferieff

Effect of multiple ion reflections on the structure of an ion-sound shock wave

I. R. Smirnovskiĭ

Scientific–Research Institute of Radio Physics, St. Petersburg State University, 198904 St. Petersburg, Russia
(Submitted November 14, 1997; resubmitted July 13, 1999)
Zh. Tekh. Fiz. **69**, 52–56 (December 1999)

It is shown that multiple ion reflection, arising as a result of collisional dissipation, from a shock front can produce an ion-sound shock wave with an arbitrarily large Mach number. For an exponentially small number of reflected ions, the ion-sound shock wave ''degenerates'' into a collisionless quasishock wave. The comparative role of viscosity and sound dispersion with different initial nonisothermality of the plasma is discussed. © *1999 American Institute of Physics.* [S1063-7842(99)01012-0]

An ion-sound shock wave as an asymptotic form of initial disturbances in a nonisothermal collisionless plasma has been investigated in Ref. 1. The possibility of a stationary structure forming is based on the dispersion properties of ion sound. Specifically, the stabilization of a wave profile can be explained by the ''competition'' between the nonlinearity and dispersion effects on a spatial scale of the order of the Debye radius D.

In a collisionless plasma, a wave with constant propagation velocity $c > V$ ($V = \sqrt{T_e/m_i}$ is the speed of ion sound, T is the temperature, m is the mass, and the indices i and e refer to ions and electrons) is a ''quasishock'' wave[2] if the ion temperature T_i is different from zero. For absolutely cold ions ($T_i = 0$) a quasishock wave degenerates into a soliton, the plasma state being the same in front and behind the soliton. For $T_i \neq 0$ reflection of some ions from the potential barrier destroys the symmetry, and the form of the wave becomes similar in form to a shock wave. This behavior occurs even though irreversible dissipation processes are forbidden (the collision integral in the kinetic equation is zero). A quasishock wave is not completely stationary: It includes a ''foot,'' formed by the reflected ions, that ''runs away'' from the front.

A characteristic feature of a quasishock wave is the existence of a critical Mach number M_{**}, bounding the region of formation of laminar disturbances ''from above'' with respect to intensity $M = c/V$.[3–5] In Ref. 3 it was found that $M_{**} < M_0$, i.e., that M_{**} is even smaller than the critical Mach number M_0 ($M_0 \approx 1.6$)[1] for a soliton. In Refs. 4 and 5 it was shown that taking account the ''running away'' foot extends out this region right up to $M_{**} \approx 1.82$ for $\beta = 0$ ($\beta = 2T_i/T_e$ is the degree of nonisothermality of the plasma) and up to a certain value $M_*(\beta)$, where $M_* < M_{**}$, for finite β. In Ref. 5 it was concluded that laminar ion-sound shock waves do not exist for $M > M_{**}$.

Let us see if energy dissipation of the reflected ions influences the structure of the shock wave. Such an effect is possible if the ion braking time is much shorter than the lifetime of the wave. In that case the reflected particles again reach the front, thereby increasing the efficiency of the dissipation mechanism. Fast ions excite a longitudinal polariza-

tion electric field, which brakes the ions and accelerates electrons.[2] Collisional relaxation of the electrons increases the electron temperature. Energy transfer from ions to electrons is characterized by two time scales: the braking time τ_d of a fast ion and the decay time τ_l of the oscillations. For a two-temperature plasma τ_d can be estimated as follows:[2]

$$\tau_d (2\sqrt{2}/3\sqrt{\pi})\tau\sqrt{m_e/m_i}(v/V)^3,$$
$$v \approx 2c \geq V, \ T_e \gg T_i, \tag{1}$$

where $\tau = l_e m_i/(v_{T_e} m_e)$ is the characteristic equalization time of the electron and ion temperatures, v is the velocity of a reflected ion in a stationary coordinate system, v_T is the thermal velocity, and l is the mean free path length.

For $T_e \gg T_i$ and sufficiently frequent electron collisions, τ_l can be estimated as[2]

$$\tau_l = \sqrt{m_i/m_e}\,\omega_s^{-1}(k)\sqrt{8/\pi}$$
$$\ll \nu_{ii}^{-1}\sqrt{m_i/m_e} = \tau(T_i/T_e)^{3/2}, \tag{2}$$

where ω_s and k are the frequency and wave number of ion sound and ν_{ii} is the ion–ion collision frequency.

Ion scattering by equilibrium fluctuations of the electric field is neglected in Eq. (1), since the corresponding contribution is of the order of m_e/m_i.[2] The ''noise'' level does not increase materially on the foot, since the ion-sound spectrum is nondecaying, and the effect of anisotropic instability, discussed in Ref. 1, is substantial only in a quite rarefied plasma.

The electron heating time is determined by the greater of the times τ_d and τ_l, but in any case it is less than the equalization time of the electron and ion temperatures. Thus the reflected ions are scattered by electrons. This conclusion agrees with the result of Ref. 6, explaining the well-known fact that electron heating predominates in thermonuclear set-ups. As a result, a stationary shock structure, in which dissipation is due to multiple reflections of ions and ion scattering by electrons, can form.

Collisions give rise to high-frequency ion viscosity, in turn giving rise to damping of ion-sound waves in the linear approximation.[7] Viscosity is also capable of producing an

ion-sound wavefront structure. This has been shown on the basis of a gas-dynamic description.[8] However, it is known[2] that for strong shock waves a strict proof of this requires a kinetic approach. Ion-sound waves decay and disperse. It is of interest to make a comparative estimate of the influence of these effects on the structure of a shock jump in plasma. For this, we shall employ the gas-dynamic equations for the electron and ion components, taking account of ion viscosity. We shall determine the condition under which viscous damping of small disturbances behind a shock front remain small right up to scales $L \sim D$. The condition for the term containing the viscosity to be small compared with the inertial term in the equation of motion gives

$$D \gg (v_{T_i}/c) l_i. \tag{3}$$

For a strongly ionized plasma (viscosity is due to ion–ion collisions), we have from Eq. (3)

$$T_e/T_i \gg (v_{T_i}/c)^2 \Lambda^{-2} g^{-3}(9/4), \tag{4}$$

where Λ is the Coulomb logarithm ($\Lambda \sim 10-20$), $g = e^2 n_i^{1/3}/T_i \ll 1$ is the plasma parameter, e is the absolute value of the electron charge, and n is the electron density.

If the neutral component is sufficiently dense, viscosity is determined by ion–neutral collisions.[9] Then the inequality (3) gives

$$T_e/T_i \gg (v_{T_i}/c)^2 (n_i/N_e)^2 g a^{-2} n_i^{-2/3}, \tag{5}$$

where a is the molecular radius and the index n marks the density of the neutral component.

Thus, even without viscosity a shock front can be stabilized as a result of the dispersion of ion sound. In the plasma of a gas discharge ($g \leqslant 10^{-2}$) this occurs for virtually any intensity of the shock wave. Dispersion can be strong only for sufficiently intense waves $v_{T_i}/c < 10^{-3}$ in the upper ionosphere ($g \leqslant 10^{-4}$).

Let us now consider an isotropic, two-temperature, strongly ionized plasma with a Maxwellian distributions of the particles and singly charged ions. On a scale of the lesser of l_i a plasma is described by the Vlasov equations for ions and electrons. Here the formulation of problem corresponds to Ref. 5. The ions are assumed to be sufficiently ''cold'' and the electrons sufficiently ''hot'' so that

$$v_{T_i} \ll c \ll v_{T_e}. \tag{6}$$

In this case the particle distribution functions depend on the Cartesian coordinate r and the time t implicitly via the self-consistent electric field potential $\varphi(r,t)$ (we are considering one-dimensional plane waves). The inequalities (6) make it possible to integrate the electron distribution function and obtain a Boltzman distribution for the electron density scaled to the unperturbed value for $\varphi=0$: $N_e = \exp(\Phi)$, where $\Phi \equiv e\varphi/T_e$.

For ions a boundary condition is given on the foot—a quasihorizontal section of the shock profile. The ion distribution function has a double-hump form, corresponding to ion fluxes incident on the front and reflected from the front.

The structure of the jump in the fields, which is due to the spatial separation of the charge on a scale D, is described by an equation for the electric field potential[5]

$$(d\Phi/d\xi)^2 = -2U(\Phi), \tag{7}$$

$$-U(\Phi)$$

$$= \exp(\Phi) + N_f \left(\int_{\sqrt{2(\Phi-\Phi_f)}}^{\sqrt{2(\Phi_A-\Phi_f)}} F(W) W \sqrt{W^2-2(\Phi-\Phi_f)} dW \right.$$

$$\left. + \int_{\sqrt{2(\Phi-\Phi_f)}}^{\infty} F(W) W \sqrt{W^2-2(\Phi-\Phi_f)} dW \right) + C, \quad \xi < 0,$$

$$-U(\Phi) = \exp(\Phi) + N_f \int_{\sqrt{2(\Phi_A-\Phi_f)}}^{\infty} F(W)$$

$$\times W \sqrt{W^2-2(\Phi-\Phi_f)} dW + C, \quad \xi \geqslant 0.$$

$$F(W) = \exp-(-(W-M_f)^2/\beta)/\sqrt{\pi\beta},$$

$$W = \sqrt{v^2/V^2 + 2(\Phi-\Phi_f)},$$

$$C = -N_f(M_f^2+\beta/2) - \exp(\Phi_f) - N_f \int_0^{\sqrt{2(\Phi_A-\Phi_f)}} F(W) W^2 dW.$$

Here $\xi = -(r-ct)/D$, $\beta = 2T_{i0}/T_e$, and v is the particle velocity. The index 0 is used to denote fields in the unperturbed plasma, Φ_A is the value of the potential at the maximum for $\xi=0$. The coordinate system moves together with the wave and it is arranged so that $\xi < 0$ ahead of the shock front. The index f marks values of the fields on the foot, $v_f > 0$ is the velocity of the ion flux incident on the front, $M_f = v_f/V$ is the Mach number, and N_f is the ion density in the incident flux scaled to the unperturbed value for $\Phi=0$.

The spatial scale of variation of T_e, due to the electronic heat conduction, can be estimated as[10]

$$\Delta = (v_{Te}/c) l_e. \tag{8}$$

We neglect the variation in the ion temperature ahead of the shock front: $T_i \approx T_{i0}$. The characteristic length l_d of the foot is determined by the relaxation length of the ion momentum. From Eq. (1) we find $l_d = 8 l_e (c/V)^4$.

Thus, we obtain the following inequality for the spatial scales: $l_d \ll \Delta$. This makes it possible to represent the front of the foot as an isothermal jump. The equations of conservation of the particle fluxes, momentum, and energy give the desired boundary relations between the unperturbed state of the plasma and the state on the foot,

$$M = M_f(N_f - N_r),$$

$$M^2 + \beta(\beta_0^{-1} + 1/2) = (1 + M_f^2 + \beta/2)(N_f + N_r),$$

$$M^2/2 + \beta/\beta_0 = M_f^2/2 + \Phi_f + 1, \tag{9}$$

where

$$N_r = N_f \int_0^{\sqrt{2(\Phi_A-\Phi_f)}} F(W) dW$$

is the density of reflected ions on the foot, $N_r + N_f = \exp(\Phi_f)$ is the condition of quasineutrality of the plasma on the foot, and $\beta_0 = 2T_{i0}/T_{e0}$ is the initial degree of nonisothermality.

The first two inequalities in Eq. (9) relate the fluxes on the foot and the unperturbed fluxes in front of the heated zone, and the last inequality is obtained from the condition that the energy flux is continuous at a transition from the state directly in front of an isothermal jump to a state on the foot.

Our problem (7) and (9) differs from that of Ref. 5 only with respect to the boundary condition: At infinity the plasma velocity in the laboratory coordinate system is zero.

On the scale of long mean-free path lengths of the particles the shock wave is a discontinuity on which the field satisfies the Hugoniot relations

$$N_1 M_1 = M_0,$$

$$N_f(T_1/T_0 + M_1^2) = M_0^2 + 1,$$

$$(T_1/T_0)\bar{\gamma}/(\bar{\gamma}-1) + M_1^2/2 = M_0^2/2 + \bar{\gamma}/(\bar{\gamma}-1),$$

$$T_1 \equiv T_{e1} + T_{i1}, \quad T_0 \equiv T_{e0} + T_{i0}, \tag{10}$$

where $M_0 = c/V_0$, $V_0 = \sqrt{T_0/m_i}$ is the isothermal sound velocity in the undisturbed plasma, $\bar{\gamma}$ is the effective ratio of specific heats, and the index 1 marks the fields behind the shock front.

Here it is assumed that small long-wavelength disturbances propagate with phase velocity $\bar{V} \equiv V\sqrt{\bar{\gamma}}$, $\bar{\gamma} > 1$. This is due to the characteristics of heat conduction in a plasma.[9] From Eq. (10) we obtain for the temperature ratio the expression

$$T_1/T_0 = (\bar{\gamma}+1)^{-2}M_0^{-2}[2M_0^2 - \bar{\gamma}+1]$$
$$\times [M_0^2(\bar{\gamma}-1) + 2\bar{\gamma}], \tag{11}$$

which, in contrast to the well-known relation,[11] contains the Mach number, equal to the ratio of the velocity c of the wave to the isothermal sound velocity. The left-hand side of Eq. (1) is 1 for $M_0^2 = \bar{\gamma}$.

Thus, the structure of a nonviscous ion-sound shock wave is determined by the solution of Eq. (7), which is continuous at the point of the maximum of $\Phi(\xi)$ at $\xi = 0$ and satisfies the boundary relations (9) and (10) with

$$T_e + T_{i0} = T_1. \tag{12}$$

The particular case $\beta = 0$ and $T_{e0} = T_{i0}$ was investigated in Ref. 12 on the basis of equations for the fluxes neglecting the structure of the front.

The following conditions are necessary for the existence of the required solution of Eq. (7). There exist Φ_A, Φ_f, and Φ_- such that

$$U(\Phi_A), U(\Phi_f) = 0 \text{ for } \xi \le 0,$$

$$U(\Phi_A), U(\Phi_-) = 0 \text{ for } \xi > 0,$$

$$N_{iA} \ge N_{eA}, \tag{13}$$

where

$$N_{iA} = N_f \int_{\sqrt{2(\Phi_A - \Phi_f)}}^{\infty} F(W) \frac{W dW}{\sqrt{W^2 - 2(\Phi_A - \Phi_f)}},$$

$$N_{eA} = \exp(\Phi_A)$$

are the electron and ion densities at $\xi = 0$.

The relations (9) determine the unknown values of M, M_f, and Φ_f. Therefore, near a jump T_e is unknown a priori. Its value is determined by the scattering of the reflected-ion flux by electrons.

Figures 1(a)–1(d) show the parameters of a nonviscous ion-sound shock wave as a function of its intensity M_0 with various values of the initial nonisothermality; $\langle \Phi \rangle$ is the "average" value of the oscillating potential behind the shock front, the solution of the equation

$$dU(\Phi)/d\Phi = 0 \text{ for } \xi > 0. \tag{14}$$

A calculation of the structure of such a shock wave for an equilibrium strongly and weakly ionized equilibrium plasma is contained in Ref. 13.

The quasishock disturbance of a collisionless plasma investigated in Refs. 4 and 5 is not an ion-sound shock wave in the strict sense of the term. Conversion of energy into internal energy of the gas does not occur in a quasishock jump and the entropy does not increase there. It can be stated that the "dissipation" region is located at infinity.

The fact that the region of dissipation of the flux of reflected ions is located at a finite distance away from the front results in the possibility of multiple reflection of the particles. In each reflection an ion takes energy from the wave and transfers it to the plasma. Thus, any ion ultimately can overcome the potential barrier and end up behind the front. This situation resembles the one occurring for a magnetosonic shock wave propagating across a magnetic field. In this case the reflected ions return by "twisting" of the trajectory in the magnetic field.[1] Both cases (collisionless ion–sound and magnetosound) become similar, if the action of the magnetic field at times $t < \omega_{H_i}^{-1}$ (ω_{H_i} is the ion gyrofrequency) is neglected.[5] The fundamental possibility of any particle passing from a state ahead of the front to a state behind the front is due to the presence of dissipation in the shock layer. In a collisionless magnetosonic shock wave, at times $t > \omega_{H_i}^{-1}$ the accelerated particles lose energy to radiation. In our case the reflected ions are scattered by electrons.

As a result of multiple reflection of ions, a laminar shock wave can have an arbitrarily high intensity M_0, and a critical Mach number M_{**} does not exist.

A strong shock wave forms for any initial nonisothermality, even in an equilibrium plasma ($T_{e0} = T_{i0}$), where low-amplitude ion-sound waves are strongly absorbed. This is possible because of the increase in the electron temperature in front of the shock wave in a region with a spatial scale of the order of Δ.

The inequality (3) bounds "from below" the region of existence of a nonviscous shock wave. Let it hold for arbitrarily weak shock waves. For strong initial nonisothermality, in the region $M_0 \sim 1$ the number of reflected ions N_r becomes exponentially small. The parameters of the wave approach the corresponding values for a collisionless qua-
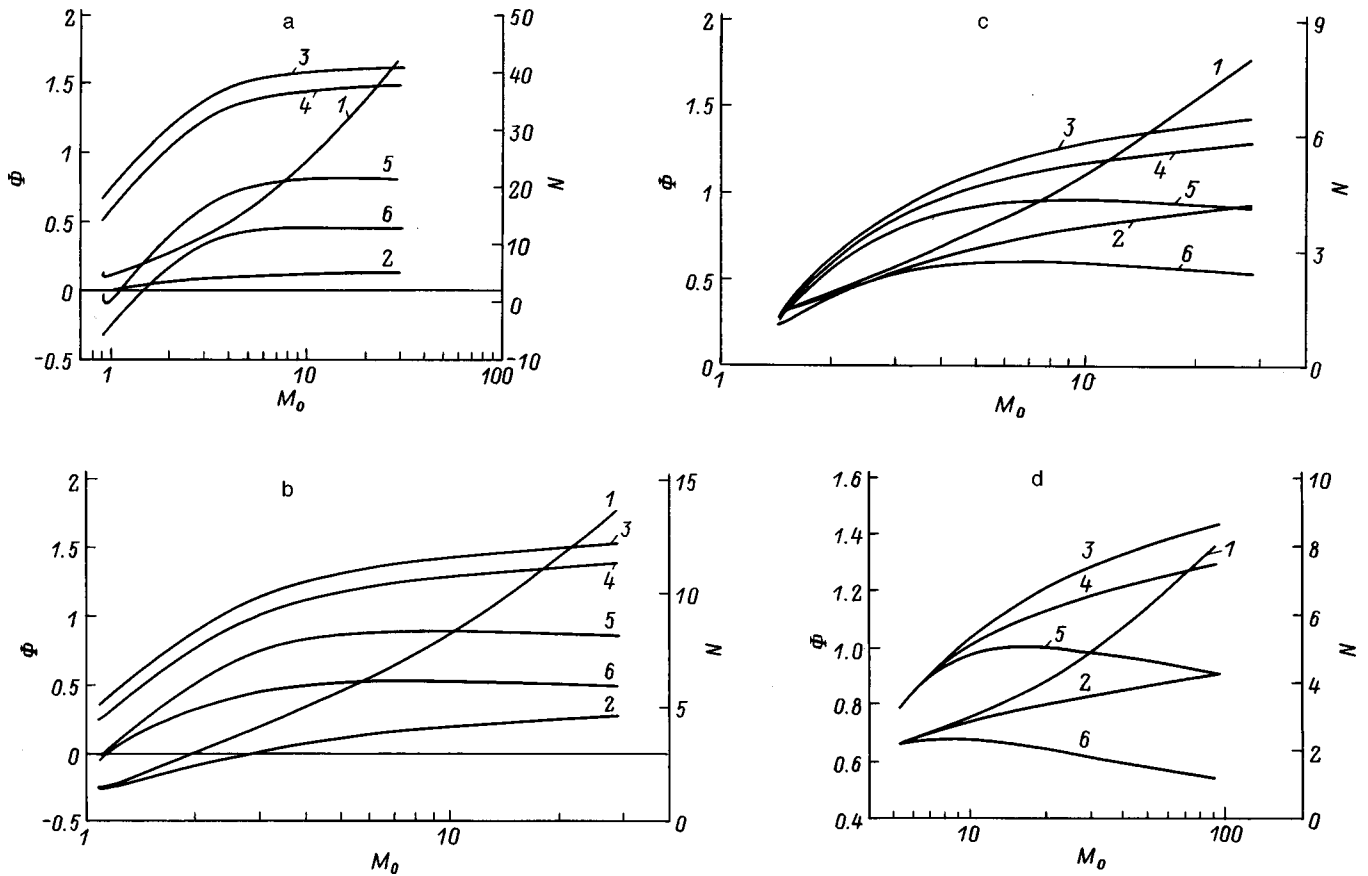
FIG. 1. N_{iA} (*1*), N_{eA} (*2*), Φ_A (*3*), $\langle\Phi\rangle$ (*4*), Φ_- (*5*), Φ_f (*6*) versus M_0. β_0: a—10^{-4}, b—10^{-2}, c—0.1, d—2.

sishock wave.[3] This is explained by the negligibly small influence of the dissipation of energy of the reflected flux as $N_r \to 0$.

A different branch of the solution of the system of Eqs. (9) and (13), on which $T_e < T_{e0}$ and $\Phi_f < 0$, exists in the region $\beta_0 < 10^{-2}$, $M_0 \sim 1$. Figure 2 shows the computed behavior of $\Phi_f(M_0)$ near the point $\Phi_f = 0$ for $\beta_0 = 10^{-4}$. For some value M_0^+ the solution abruptly jumps from one branch to the other. The jump-like character of this transition is not noticeable on the scale of Figs. 1a and 1b (curve *6*). Actually, the curve $\Phi_f(M_0)$ cannot intersect the abscissa at the point $M_0 = M_0^+$. Indeed, substituting $\Phi_f = 0$, $\beta = \beta_0$ into Eq. (9) we obtain $N_r = 0$, which can occur only for $\Phi_A = 0$.
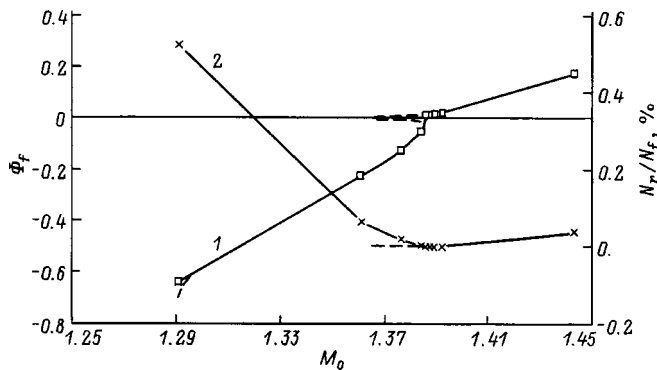

FIG. 2. Behavior of the curves $\Phi_f(M_0)$ (*1*) and $N_r(M_0)$ (*2*) near $\Phi_f = 0$ for $\beta_0 = 10^{-4}$.

Therefore, for $M_0 < M_0^+$ there are three solutions for Eqs. (9) and (13). Two of them are approximately symmetric with respect to the abscissa, differing from it by an exponentially small quantity. The third solution has finite values $\Phi_f < 0$ and $N_r \neq 0$. Both branches emanate from the same point, where $\Phi_A = 0$, $M_0 = 1$. The probable behavior of the branches is shown in Fig. 2 (dashed lines).

If the relations (10) were exact, it would follow from them that a compression shock wave is possible only if

$$M_0^2 > \bar{\gamma} > 1. \tag{15}$$

However, a solution for the structure of the shock wave also exists under the weaker condition $M_0 > 1$. Actually, the relations (10) are approximate. They neglect the radiation fluxes and the more ''subtle'' relaxation processes occurring in a two-temperature plasma. For this reason, the free parameter $\bar{\gamma}$ does not have a clear physical meaning, and for Eqs. (10) and (12) to be satisfied formally, $\bar{\gamma} = \bar{\gamma}(\beta_0, M_0^2)$ must be a slow function of its arguments. Nonetheless, a calculation showed approximately 5% agreement for Eq. (12) with $\bar{\gamma} = 5/3$. This shows that the internal energy of the plasma in the relaxation zone behind the front remains approximately constant and the required heating of the ions is accomplished primarily as a result of heat transfer between the components of the plasma.

The equality (12) also holds, to the same degree of accuracy, for a shock wave with $T_e < T_{e0}$. Such a wave can evolve provided that there exist relaxation processes due to

scattering of the reflected ions, which occur with decreasing T_e. For example, secondary electrons with lower energy can form as a result of charge trasnfer on the ions. Experimental observations of the radiation from the gas in a ahead of the shock front confirms such a phenomenon indirectly.[14]

For small initial nonisothermality ($\beta_0 \geqslant 0.1$), there appears a characteristic Mach number $M_-(\beta_0)$ below which a nonviscous shock wave is not formed. This is clearly seen in Fig. 1(d) for the case of an initially equilibrium plasma $\beta_0 = 2$, where $M_- \approx 7$. It is obvious that ion viscosity determines the structure of the shock for $M_0 < M_-$.

With the exception of the case $M_0 = M_-$ in an equilibrium plasma, where the wave profile is monotonic, a nonviscous ion-sound shock front has an oscillatory structure.

In summary, on account of multiple reflection of ions, the required level of dissipation in the front of an ion-sound shock wave obtains at much lower particle densities in the reflected flux than in a quasishock wave.[5] As a result, for a laminar ion-sound shock wave a critical Mach number at which the number of reflected ions becomes equal to the number of incident ions (the critical Mach number is approximately 1.82 according to Ref. 5) does not exist. An ion-sound shock wave forms as a result of the presence of irreversible dissipative processes associated with particle collisions, and it has a strictly stationary shock profile, which is the asymptote of an arbitrary initial disturbance.

I thank V. A. Pavlov for his attention to this work and for valuable remarks.

[1] R. Z. Sagdeev, in *Reviews of Plasma Physics*, Vol. 4, edited by M. A. Leontovich [Consultants Bureau, New York, 1966, pp. 23–91; Atomizdat, Moscow, 1964, No. 4, pp. 4–83].

[2] *Plasma Electrodynamics*, edited by A. I. Akhiezer [Pergamon Press, Oxford, 1975; Nauka, Moscow, 1974].

[3] S. G. Alikhanov, V. G. Belan, G. N. Kichigan, and P. Z. Chebotaev, Zh. Éksp. Teor. Fiz. **60**, 982 (1971) [Sov. Phys. JETP **33**, 532 (1971)].

[4] D. W. Forlund and J. P. Freiberg, Phys. Rev. Lett. **27**, 1189 (1971).

[5] V. M. Bardakov, A. G. Morozov, and I. G. Shukhman, Fiz. Plazmy **1**(6), 955 (1975) [Sov. J. Plasma Phys. **1**, 521 (1975)].

[6] D. V. Sivukhin, in *Reviews of Plasma Physics*, Vol. 4, edited by M. A. Leontovich (Consultants Bureau, New York, 1966, pp. 93–241; Atomizdat, Moscow, 1964, No. 4, pp. 84–161].

[7] A. F. Aleksandrov, L. S. Bogdankevich, and A. A. Rukhadze, *Principles of Plasma Electrodynamics* (Vysshaya shkola, Moscow, 1987).

[8] V. A. Pavlov, Fiz. Plazma **22**(2), 182 (1996) [Plasma Phys. Rep. **22**, 167 (1996)].

[9] B. N. Gershman, L. M. Erkhumov, and Yu. Ya. Yashin, *Wave Phenomena in the Ionosphere and Cosmic Plasma* (Nauka, Moscow, 1984).

[10] A. L. Velikovich and M. A. Liberman, *The Physics of Shock Waves in Gases and Plasma* (Nauka, Moscow, 1987).

[11] L. D. Landau and E. M. Lifshitz, *Fluid Mechanics* [Pergamon Press, New York; Nauka, Moscow, 1987].

[12] V. G. Ledenev, Prikl. Mekh. Tekh. Fiz. **30**(2), 17 (1990).

[13] I. R. Smirnovskiĭ Prikl. Mekh. Tekh. Fiz. **39**(3), 14 (1998).

[14] C. Covault, Aviation Week and Space Technology **135**(18), 18 (1991).

Transition states in the melting of germanium in dynamic and quasistatic regimes

L. A. Bityutskaya and E. S. Mashkina

Voronezh State University, 394693 Voronezh, Russia

The conditions under which transition states arise and exist during the melting of germanium are identified by digital differential-thermal analysis. The pre- and postmelting cooperative effects arising under real conditions in dynamic and quasistatic regimes are nonequilibrium phase transitions and can be characterized by a system of thermodynamic parameters. Instability of the thermodynamic parameters of the transition states is observed in quasistatic regimes as a result of dynamic instability. The system of parameters introduced characterizes the formation of a special phase state — pre- and postmelting mesophases. © *1999 American Institute of Physics.* [S1063-7842(99)01112-5]

The existence of transition regions during melting was indicated in Refs. 1 and 2. However, transition states during melting have been little studied, and as a rule they are a spin-off of investigations of the melting process. Data are often obtained by extrapolation with the temperature approaching the melting point T_m, and thermodynamic parameters describing the regions and the conditions of existence of transition regions are lacking.

The experimental data are contradictory. On the one hand, they show a dynamic structure of premelting phases,[3] a change in symmetry with the appearance of icosahedral structures which are uncharacteristic for a crystal state,[4] a change in the coordination number, a hierarchy of structures in the melt,[5] temperature oscillations in the premelting region,[6] a change in the photoacoustic response,[7] and so on. On the other hand, they also show a monotonic increase of the specific heat and other thermodynamic parameters. This inconsistency is removed if the experimental data obtained in thermostatic, quasistatic, and dynamic regimes are separated. Instabilities are observed in the dynamic and quasistatic regimes, and monotonic variations are observed in thermostatic regimes. The theory also contains two concepts: a monotonic nonlinear variation of the properties, as a result of vacancy formation,[8] and the appearance of correlated states.[9] Thus, the experimental and theoretical prerequisites exist for treating transition states as dissipative. The microscopic description of the melting of clusters has shown that collective processes play a fundamental role. The melting of clusters is interpreted as a phase transition occurring in a certain temperature range.[10]

In our works[11–14] it has been shown that the melting of crystal substances with different types of chemical bonds in dynamic heating regimes with heating rates $v = 5$ and 10 K/m is accompanied by the appearance of excited regions pre- and postmelting and is characterized by a system of nonequilibrium thermodynamic parameters. In Ref. 15 the premelting and melting thermodynamic parameters of ionic KCl crystals were shown to be unstable in the quasistatic regimes of heating at rates $v \leqslant 1$ K/m.

1. PROCEDURE

A digital method of measurement and processing of differential-thermal analysis (DTA) signals was developed to investigate transition states during melting of crystal substances.[16] The controllable record length and the transmission band of the dc amplifier made it possible to determine the conditions under which transition states can be identified on the DTA melting curves in dynamic and quasistatic regimes.

Different scales of the measured characteristics are characteristic for the observed transition states and the proper melting effect. During endothermal melting the maximum deviation of the baseline is 10° on average, whereas for a transition effect the maximum deviation of the baseline for the same batch is 1° on average (Fig. 1). For this reason, we introduce different scales for the detection and display of the effects — macro- and micro-, just as for macro- and microphase diagrams.

The DTA methodology for studying first-order phase transitions such as melting was formulated as a reversible jump. Accordingly, to increase the resolving power, which is determined by the width of the peak, the mass of the experimental object was decreased and the rate of heating (cooling) was increased.

As the mass decreases, the area of the pre- and postmelting effects decreases and vanishes for batches of the order of several mg, which are used in standard DTA methods.[17] The mass for which transition states are not observed can be taken as the critical mass m_c. As the mass increases, the area of the transition effect decreases, and exothermicity remains. It should be noted especially that, in contrast to the classical linear mass dependence[18] of the area of the effect, the mass dependence of the area of the transition effect is nonlinear (Fig. 2).

In our experiments, we used 2-g batches. This gave good resolution and allowed the optimal representation of the data. The experiments were performed in standard graphitized Stepanov quartz vessels, evacuated to 10^{-4} Torr, and Pt–
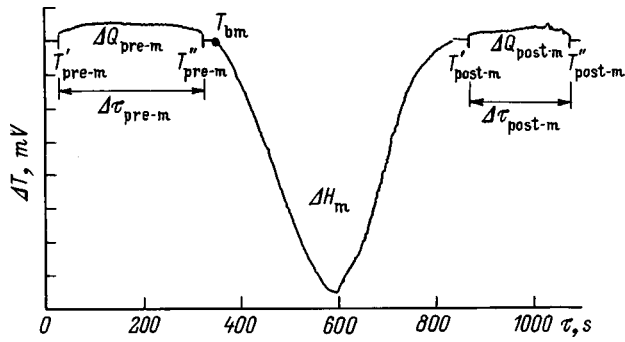
FIG. 1. DTA curve of melting of germanium in the dynamic regime. The heating rate is $v=5$ K/m with a fixed mass of matter 2 g; scale ΔT — 1:0.02.

Pt/Rh (10%) thermocouples were used as the sensing elements.

To make sure the data are reliable, the transition states during melting of Ge were investigated on 10 samples under identical experimental conditions. Each sample was first melted and then three heating–cooling cycles were conducted. The investigations were performed in the dynamic ($v=5,10$ K/m) and in the quasistatic ($v=1$ K/m) regimes. To determine the effect of the initial conditions (prehistory of the sample) on the transition state during melting, heating was performed in two regimes: 1) from room temperature to 1250 K and 2) from 1000 to 1250 K.

2. EXPERIMENTAL PART

A typical DTA curve of premelting of Ge with a heating rate of 5 K/min is displayed in Fig. 3a. Together with premelting, for the same heating rate a postmelting effect (Fig. 3b), which has the same manifestation as the premelting effect, is observed. At the critical value of the controlling parameter — the temperature — and for a fixed mass of the matter and heating rate, a heat pulse with a finite time base is generated.

The amount of heat released during pre- and postmelting was estimated relative to the main effect and was determined as the modulus of the ratio of the areas P_1 and P_3 of the pre-
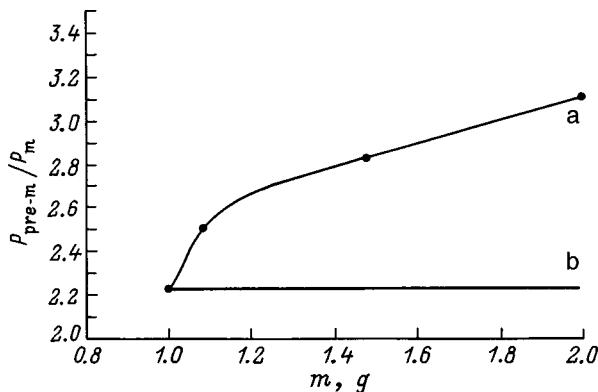

FIG. 2. Reduced area of the premelting effect during the melting of Ge versus the mass: a — experimental curve, b — ''classic'' curve. The experiments were performed under identical conditions in vessels of the same shape.
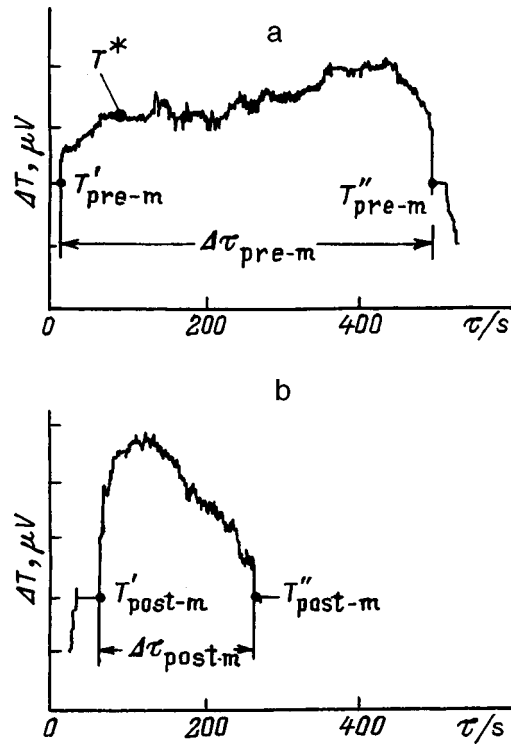

FIG. 3. DTA curves of transition states during the melting of Ge ($v=5$ K/m): a — premelting (T^* — isothermal holding temperature), b — postmelting; scale ΔT — 1:5.

and postmelting effects to the area P_2 of the main effect. The area of the DTA peak for the pre- and postmelting effects was calculated by the trapezoidal rule. Then the areas were scaled to unit mass.

The presence of macroscopic low-frequency thermal fluctuations in the pre- and postmelting pulses is characteristic.

To study the stability of the excited state of the observed effects, isothermal holdings under conditions allowing for the appearance of premelting were performed in the dynamic regimes. The DTA curve of isothermal holding of premelting of Ge at temperature $T^*=1173$ K is shown in Fig. 4; the holding time was 35 min. Compared with the polythermal DTA curve, the fluctuations amplitudes are larger, and the total amplitude of the thermal oscillations becomes comparable to the magnitude of the premelting effect itself. A weak
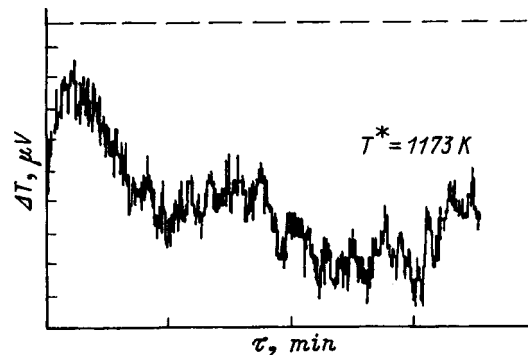

FIG. 4. DTA curve for isothermal holding of premelting of Ge.

TABLE I. Parameters of transient processes during melting of Ge.

v, K/min	Premelting				Postmelting			
	T'_{pre-m}, K	T''_{pre-m}, K	$\Delta\tau_{pre-m}$, c	ΔQ_{pre-m}	T'_{post-m}, K	T''_{post-m}, K	$\Delta\tau_{post-m}$, c	ΔQ_{post-m}
5	1157.9	1206.1	509	0.079	1256.5	1298.1	230	0.063
10	1139.4	1204.3	436	0.15	1248.9	1301.0	212	0.051

additional periodicity arises. The prolonged presence of the excited state is striking. Isothermality of the fluctuations was investigated by the method of digital spectral analysis with data processing by a special program employing the Walsh periodogram method. A linear frequency dependence, known as flicker noise, of the spectral power density in double-logarithmic coordinates was obtained for the fluctuation process.[19]

Thus, the observed pre- and postmelting effects show indications of thermodynamically nonequilibrium phenomena. The characteristic features of the observed effects are that the recorded heat pulses of the pre- and postmelting phenomena are integral characteristics of the process and reflect changes occurring in the system as a whole in the entire volume of the matter. The stationary excited states arising in the interior volume of the matter at the pre- and postmelting stages have sharp thermal boundaries on the poly- and isothermal DTA curves in the dynamic and quasistatic regimes. These states can be characterized by a system of experimentally observed, nonequilibrium, thermodynamic parameters that depend on the mass of the matter, temperature, heating rate, dimensions, and time — J: T'_{pre-m}, T''_{pre-m} — temperatures of the onset and termination of the premelting effect; T'_{post-m}, T''_{post-m} — temperatures of the onset and termination of the postmelting effect; $\Delta\tau_{pre-m}$, $\Delta\tau_{post-m}$ — durations of the pre- and postmelting heat pulses; ΔQ_{pre-m}, ΔQ_{post-m} — heat of pre- and postmelting, respectively.

Let us examine the pre- and postmelting parameters of Ge in various dynamic regimes. The typical values of the

parameters of the pre- and posttransition states in Ge with heating rates of 5 and 10 K/min are presented in Table I. The heats of pre- and postmelting are given in arbitrary units, which are the modulus of the ratio of the area of the transition effect to the area of the main melting effect.

As the heating rate increases to 10 K/min, the character of the processes remains unchanged. Only the kinetics of energy release changes.

By quasistatic regime we mean the conditions approaching close to equilibrium with continuous heating rates $v \leqslant 1$ K/min. According to classical models, in this range a monotonic variation of the parameters accompanied by an increase in enthalpy should occur. This is due to the increase in the specific heat, associated with the anharmonicity of lattice vibrations at high temperatures. In the experiment monotonic behavior is obtained by performing coarse measurements, by averaging the data, and with prolonged isothermal holdings at the measured points. This approach is due to general belief whereby a first-order phase transition is interpreted as a jump in the absence of transition regions.

Transition states, just like the nonequilibrium state of matter in a first-order phase transition, also remain in quasistatic regimes with continuous heating. As the heating rate decreases from 5 to 1 K/min, in the quasistatic regime the impulse of premelting of Ge transforms from a stable into a ''noise'' circle and the temperature–time interval increases. The onset temperature T'_{pre-m} of premelting with $v \leqslant 1$ K/min is 40 K lower than T'_{pre-m} with $v = 10$ K/min and 60 K lower than T'_{pre-m} with $v = 5$ K/min (Fig. 5).

In the quasistatic regime, for premelting of Ge the parameters of the transition states, such as T'_{pre-m}, T''_{pre-m}, and $\Delta\tau_{pre-m}$ become unstable. The instability of T'_{pre-m} is observed as an anomalous variance $\sigma(T'_{pre-m})$ of this parameter compared with dynamic regimes in a single heating–cooling cycle. The variance was calculated for ten points for each heating rate (Table II).

But, for covalent Ge crystals, in contrast to KCl,[15] a separation of the regions of instability of the premelting parameters is not observed for the heating regimes 1 and 2 (Fig. 6). The interval of instability of T'_{pre-m} is 65 K. For Ge, the melting onset temperature T_{bm} is a stable parameter for heating rates of 1–10 K/min.
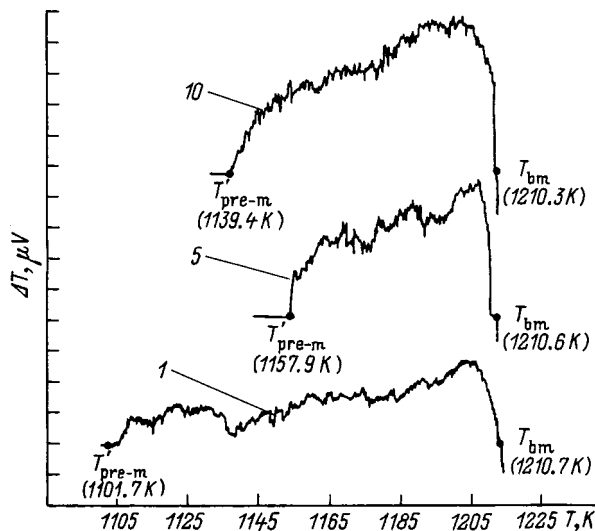

FIG. 5. DTA curves of premelting of Ge in dynamic and quasistatic regimes. Scale ΔT — 1:2; the numbers on the curves are the values of v in K/min.

TABLE II.

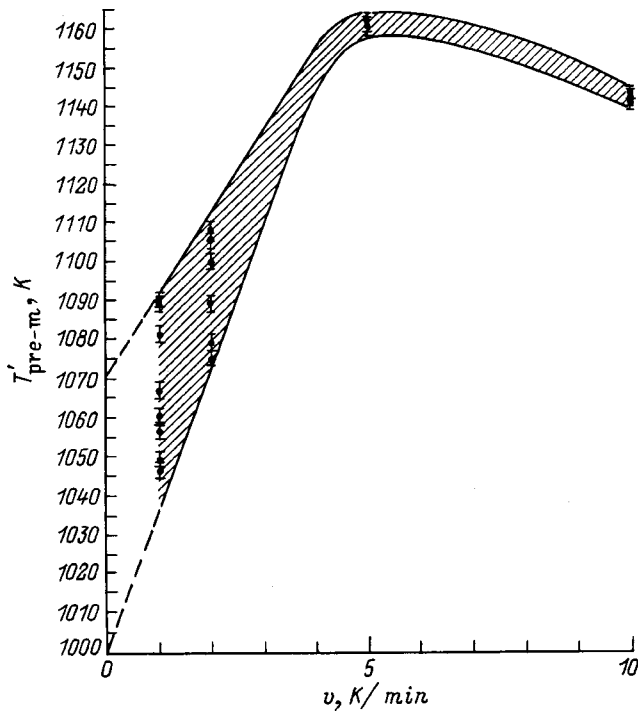| Heating rate, K/min	Variance $\sigma(T'_{pre-m})$, K
1	208.2
5	0.34
10	0.25

FIG. 6. $T'_{\text{pre-m}}$ for Ge versus the heating rate.

The quasistatic regime can be characterized by additional parameters reflecting the instability of the system and manifested as an anomalous variance: the corridor $\delta T'_{\text{pre-m}}$ of instability of $T'_{\text{pre-m}}$, the corridor $\delta T''_{\text{pre-m}}$ of instability of $T''_{\text{pre-m}}$, and the corridor δT_{bm} of instability of the melting onset temperature.

3. RESULTS AND DISCUSSION

Our experimental results show that many stationary and nonstationary states with sharp fixed values of the parameters of the regions of existence correspond to various kinetic regimes of melting of germanium. Such states correspond to nonlinear dynamic processes, and on the basis of all distinguishing indicators (exothermality, fluctuation nature, abruptness, irreversibility, nonequilibrium nature) can be classified as nonequilibrium phase transitions.[20] In our case, a nonequilibrium state is reached as a result of the anharmonicity of the crystal lattice at the premelting stage due to a sharp increase in the vacancy density.

In an elaboration of Frenkel's idea of cooperativeness, Yu. L. Khait[9] proposed a phenomenological description of the accumulation of energy by an atom as a result of directed energy flow from the environment, i.e., from the atomic subsystem. Although Khait does not indicate a specific mechanism for the anomalous burst of energy, instability is evidently easily predicted. The vacancy density, which is $\sim 10^{-2}$ per atom,[8] increases near the melting temperature, and it should radically change the phonon spectrum. An investigation of the Raman scattering spectra in NaOH as $T \to T_{\text{m}}$ showed a sharp decrease in the intensity of phonon vibrations, while close to T_{m} phonons are virtually not observed.[21]

According to Khait, the cooperativeness at the premelting stage is due to correlation in the phonon subsystem, which results ultimately in the formation of clusters. For our data, the Frenkel'–Khait correlation model is a limiting quasistatic case with continuous heating at a rate $v \sim 1$ K/min. At these heating rates premelting is characterized by an extended temperature–time interval, the presence of "noise" circles, and sensitivity of the parameters of the transition states to the initial experimental conditions. This state can be regarded as a system with weak correlation. As the heating rate increases to 5.10 K/min, the "noisy" cycle transforms into long-time heat pulses, i.e., strongly correlated states arise, leading to the formation of clusters in the entire volume of the crystal.

Using the Frenkel'–Khait approximation we estimated the sizes of the clusters formed at the premelting stage. The inverse Khait problem was solved — determination of the cluster sizes according to the magnitude of the premelting temperature interval $\delta T_{\text{pre-m}} = T''_{\text{pre-m}} - T'_{\text{pre-m}}$ on the basis of our experimental data. The diameter d of the clusters was determined in terms of the characteristic correlation length A_i with an experimentally fixed premelting temperature interval $\delta T_{\text{pre-m}}$:

$$A_i = \sqrt[3]{\frac{T_m^2}{\delta T_{\text{pre-m}}^2 \, z \, (T'_{\text{pre-m}})}}, \quad d = A_i a,$$

where z is the specific heat per degree of freedom and a is the lattice constant.

For Ge the cluster diameter is $\sim 21.2 - 27.5$ Å with a premelting temperature range 50–65 K.

The computational data for clusters of premelting phases are approximate, since the Khait model does not take account of the dynamic dependence of the parameters $J + f(m, v, x, \tau)$ and the energetics of the processes, but they are fundamental, since they show the appearance of a special phase state in solids — premelting mesophases.

[1] A. Ubbelohde, *The Molten State of Matter* [Wiley, New York, 1978; Mir, Moscow, 1982].

[2] Ya. I. Frenkel', *Kinetic Theory of Liquids* [Clarendon Press, Oxford, 1946; Leningrad, 1975].

[3] N. N. Panova, L. A. Zhukova, and S. I. Popel', Rasplavy, No. 6, 15 (1991).

[4] L. A. Zhukova, V. P. Manov, S. I. Popel', and N. I. Razikova, Rasplavy, No. 5, 15 (1992).

[5] Yu. G. Poltavtsev, *The Structure of Semiconductor Melts* (Metallurgiya, Moscow, 1984).

[6] K. Hiroaki, J. Phys. Soc. Jpn. **8**, 2784 (1983).

[7] S. Kojima, Jpn. J. Appl. Phys. **28**, 228 (1989).

[8] A. I. Karasevskiĭ, R. E. Kris, and É. V. Panov, Rasplavy, No. 5, 51 (1992).

[9] Yu. L. Khait, Phys. Status Solidi B **131**, K19 (1985).

[10] R. E. Kunz and R. S. Berry, Phys. Rev. E **49**, 1895 (1994).

[11] L. A. Bityutskaya and E. S. Mashkina, Pis'ma Zh. Tekh. Fiz. **21**(18), 8 (1995) [Tech. Phys. Lett. **21**, 728 (1995)].

[12] L. A. Bityutskaya and E. S. Mashkina, Pis'ma Zh. Tekh. Fiz. **21**(18), 85 (1995) [Tech. Phys. Lett. **21**, 720 (1995)].

[13] L. A. Bityutskaya and E. S. Mashkina, Pis'ma Zh. Tekh. Fiz. **21**(20), 30 (1995) [Tech. Phys. Lett. **21**, 828 (1995)].

[14] L. A. Bityutskaya and E. S. Mashkina, Pis'ma Zh. Tekh. Fiz. **21**(24), 90 (1995) [Tech. Phys. Lett. **21**, 1032 (1995)].

[15] L. A. Bityutskaya and E. S. Mashkina, Pis'ma Zh. Tekh. Fiz. **22**(21), 1 (1996) [Tech. Phys. Lett. **22**, 863 (1996)].

[16] L. A. Bityutskaya, D. V. Kitin, N. Yu. Khukhryanskiĭ, and G. V. Byadorova, Zav. lab., No. 4, 53 (1990).

[17] G. O. Piloyan, *Introduction to the Theory of Heat Analysis* (Nauka, Moscow, 1964).

[18] W. W. Wendlandt, *Thermal Methods of Analysis*, 2nd edition [Wiley, New York, 1974; Mir, Moscow, 1978].

[19] L. A. Bityutskaya and G. V. Seleznev, Pis'ma Zh. Tekh. Fiz. **24**(14), 24 (1998) [Tech. Phys. Lett. **24**, 551 (1998)].

[20] G. Nicolis and I. Prigogine, *Exploring Complexity* [W. H. Freeman, New York, 1989; Mir, Moscow, 1990].

[21] I. D. Zakir'yalova, A. P. Khaĭmenov, V. A. Khokhlov, and V. A. Kochedykov, Rasplavy, No. 3, 45 (1977).

Translated by M. E. Alferieff

Layered structure of epitaxial yttrium iron garnet films

S. I. Yushchuk

L'vov State University, 290646 L'vov, Ukraine
(Submitted October 19, 1998)
Zh. Tekh. Fiz. **69**, 62–64 (December 1999)

The layered structure of yttrium iron garnet films, ranging in thickness from 0.7 to 4.1 μm, grown epitaxially on single-crystal gallium–gadolinium garnet substrates, was investigated by x-ray spectral microanalysis. The ferrite films were chemically etched layer by layer in a mixture of orthophosphoric and sulfuric acids at $T = 353 - 423$ K. It was established that the chemical composition of the films varies over the thickness because of the nonuniform distribution of gadolinium, gallium, lead, and platinum ions; the film–substrate transitional layer and the surface layer of the film differ most greatly with respect to the composition and magnetic properties. It was shown that the thickness of the transitional layers and their negative effect on the magnetic characteristics of ferrite films decrease appreciably if at the time of immersion of the substrate and pulling of epitaxial structure out of the fluxed solution the substrate holder together with a special mixer rotate at a rate of 50 rpm and the pulling velocity is 20 cm/min. © *1999 American Institute of Physics.* [S1063-7842(99)01212-X]

Single-crystal yttrium iron garnet (YIG) films with uniform parameters over the area and minimal magnetic losses are required for use in microwave devices operating on surface magnetostatic waves. The basic parameters of ferrite films are the saturation magnetization $4\pi M_s$, the magnetic anisotropy field H_a, the width ΔH of the ferromagnetic resonance (FMR) line, and the thickness h of the ferrite layer. The saturation magnetization and the magnetic anisotropy field determine the frequency range and the width of the FMR line determines the magnetic losses of a microwave device. For thin ferrite films, the effect of the film–substrate (F–S) and the surface layer of the film at the film–air (F–A) boundary on the basic parameters becomes important.

In the present work, the layer structure of YIG films ranging in thickness from 0.7 to 4.1 μm was investigated by x-ray spectral electron-probe microanalysis. The films were grown on single-crystal gallium–gadolinium garnet (GGG) substrates with (111) orientation by liquid-phase epitaxy (LPE) from a supersaturated fluxed solution of the ferrite charge and a PbO–B$_2$O$_3$ solvent.

To investigate the thicknesses of the transitional layers and their influence on the magnetic properties of epitaxial structures (ESs) the ferrite films were chemically etched layer by layer in a mixture of concentrated orthophosphoric and sulfuric acids in the temperature range 353–423 K. The etching velocity was 0.05–0.2 μm/min. After each etching the thickness of the ferrite film, the saturation magnetization, and the width of the FMR line were measured. The parameters $4\pi M_s$ and ΔH were measured by the methods of Refs. 1–3, and the film thickness was measured by the interference method.[4]

When the GGG substrates are immersed in a super-cooled fluxed solution of ferrite-forming oxides, the surface of the substrate is additionally etched by the corrosive components of the solvent. As a result, the boundary diffusion layer of the melt near the substrate becomes enriched with Gd^{3+} and Ga^{3+} ions. The number of these ions depends on the degree of supercooling of the melt.

During LPE lead oxide evaporates from the surface of the melt. As a result, the ratio of the components of the

TABLE I.

Film No.		Thicknesses and magnetic parameters of YIG films during the etching process						
1	h, μm	4.1	3.2	2.4	1.5	0.8	0.5	0.2
	ΔH, Oe	0.90	0.83	0.80	0.64	0.73	1.40	2.11
	$4\pi M_s$, G	1780	1780	1700	1710	1650	1600	1470
2	h, μm	3.8	3.0	2.2	1.4	0.7	0.6	0.4
	ΔH, Oe	0.80	0.85	0.71	0.47	0.7	1.34	1.92
	$4\pi M_s$, G	1740	1710	1680	1590	1530	1460	1390
3	h, μm	3.7	2.8	1.9	1.2	0.6	0.4	0.3
	ΔH, Oe	1.10	1.00	0.86	0.78	0.93	1.38	2.14
	$4\pi M_s$, G	1780	1780	1700	1720	1670	1580	1510

solvent changes in the direction of a larger quantity of boron oxides. The excess boron oxide promotes further dissolution of the substrate. The Gd^{3+} and Ga^{3+} ions enter into the growing epitaxial YIG film, and the Gd^{3+} ions replace the Y^{3+} ions in dodecahedra, while the Ga^{3+} ions replace primarily the tetrahedral Fe^{3+} ions. The substitution of the non-magnetic Ga^{3+} ions for Fe^{3+} ions in tetrahedra decreases the magnetization of the iron garnet film. The Gd^{3+} ions contribute to the broadening of the FMR line through an ionic relaxation mechanism.[5]

High-temperature solid-phase diffusion of cations between the $Y_3Fe_5O_{12}$ film and the $Gd_3Ga_5O_{12}$ substrate also promotes the appearance and thickening of the F–S transitional layer.[6] The effect of this factor can be decreased by lowering the growth temperature of the films. But as the growth temperature decreases, i.e., the degree of supercooling of the fluxed solution increases, the entry of Pb^{2+} ions into the ferrite film increases.

The Pb^{2+} ions, having a larger ionic radius (1.49 Å), occupy dodecahedral positions in YIG, displacing Y^{3+} ions ($r = 1.06$ Å) from them, and the Y^{3+} ions enter octahedra.[7] The partial filling of octahedral positions by nonmagnetic Y^{3+} ions results in a higher magnetization compared with pure YIG, for which $4\pi M_s = 1750$ G.

A film–air (F–A) transitional layer is formed as a result of the diffusion layer of the fluxed solution bounding the substrate becoming depleted of ferrite-forming components and the resulting increase in the number of Pb^{2+} ions entering the structure of the ferrite film from the solvent. When divalent lead ions enter the YIG film, the electric neutrality of the film is destroyed, which is accompanied by the appearance of Fe^{4+} ions in tetrahedral positions and Pb^{4+} and Fe^{2+} ions in octahedral positions of the garnet.[8,9] It is known that these ions increase the width of the FMR line.[9]

Table I contains the values of $4\pi M_s$, ΔH, and the thickness h of YIG films after each etching of the films in the mixture of acids. It is evident from the table that a ferrite film possesses a layered structure which is formed during the growth process. These layers possess different thicknesses and they are characterized by lower or greater magnetization and much larger values of the parameter ΔH as compared with YIG. For example, the films 1 and 3 had a magnetization of 1780 G. After two etchings their magnetization decreased to 1700 G. Therefore the higher magnetization of these films was due to the F–A surface layers, which contain an especially large number of lead ions.

To decrease the concentration of Gd^{3+} and Ga^{3+} ions in the diffusion layer near the substrate, it is necessary to decrease the solubility of GGG in the melt. Our investigations showed that to obtain films with a small FMR linewidth and thickness up to 10 μm, it is necessary to use melts with a lower content of boron oxide. However, decreasing the concentration of boron oxide in the melts has negative factors in addition to positive factors: The composition stability of the garnet phase becomes narrower and the volatility of lead oxide increases. The higher volatility of PbO results in substantial additional etching of the substrates and the YIG ESs
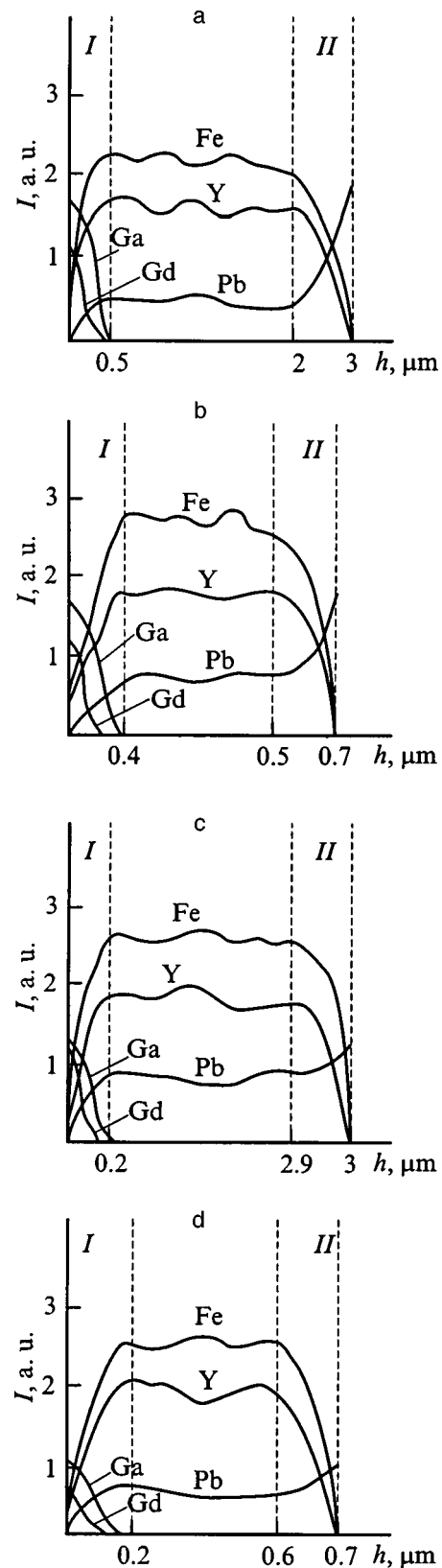

FIG. 1. Distribution of chemical elements which are constituents of the flux solution and substrate over the thickness of YIG films: I — film–substrate, II — film–air; a, b — films grown using the standard technology; c, d — with rotation of the substrate together with the mixer. There is no scale on the abscissa.

as they are lowered into the growth furnace and lifted out of it. To decrease the additional etching, a platinum screen must
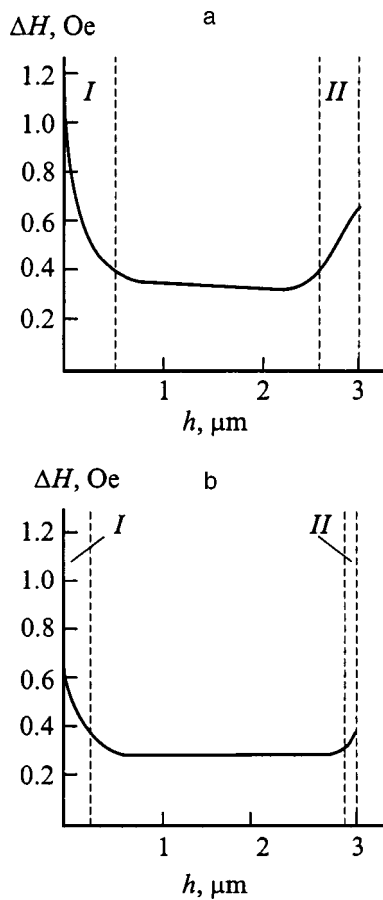
FIG. 2. Variation of the FMR linewidth ΔH over the thickness of the films. *I* — film–substrate, *II* — film–air. Films grown: a — by the standard technology; b — with the substrate rotating together with the mixer.

of 0.8 μm/min, the thickness of the surface layer enriched with Pb^{2+} ions will be only 0.04 μm. Investigations showed that the extraction of ESs from a melt with such a velocity reduces to a minimum the variation in the basic parameters — the film thickness and width of the FMR line with respect to prescribed values.

Figure 1 shows the results of microanalysis of the distribution of the chemical components Fe, Y, Pb, Gd, and Ga over the thickness of YIG films grown using the standard technology and with rotation of the substrate together with the mixer at the moments of immersion into and extraction from the melt. It is evident from Fig. 1 that the concentration of the controlled elements varies strongly over the thickness of the film, especially in the transitional F–S and F–A layers. In addition, in films grown with the substrate and the mixer rotating together, the content of Gd^{3+} and Ga^{3+} ions in the transitional F–S layers and Pb^{2+} ions in the F–A layers are much lower than in the transitional layers of the films grown using the conventional technology. A large decrease in the thickness of the transitional layers is also observed. For example, for a 3 μm thick YIG film the thickness of the F–S layer decreases by a factor of 2.5, and the thickness of the F–A layer decreases by a factor of 10!

Curves of the variation of the FMR parameter ΔH, which were obtained by layer-by-layer etching of the YIG films with a velocity of 0.1 μm/min, are displayed in Fig. 2. It is evident that the films obtained using our technology possess narrower FMR lines. This is especially noticeable in the regions of the F–S and F–A transitional layers.

In summary, technological growth regimes making it possible to decrease the thickness and variation of the composition of the transitional layers and thereby to decrease their influence on the magnetic characteristics of thin YIG films were found.

be secured to the substrate holder below the substrate. In our experiments, a platinum mixer served as a screen, and the mixer also was secured to the substrate holder.[10] The main function of the mixer is to trap, as it rotates, from inside the crucible fresh fluxed solution and direct it in the form of a twisted jet to the surface of the growing film, at the same time removing the spent melt, which is depleted of garnet-forming components. A flat diffusion layer is formed from this jet in centrifugal force field at the surface of the substrate. This is important for growing ferrite films which are uniform with respect to thickness and magnetic parameters.

We determined and investigated the dependence of the thickness of the transitional layers on the technological regimes of growth. Thus the thicknesses of the F–S and F–A layers decrease appreciably, if as the substrates are lowered into the melt and the ESs are extracted from the melt at the end of the growth process, the substrate holder together with the mixer rotates at 50 rpm. This can be explained by the removal of the Gd^{3+}, Ga^{3+}, and Pb^{2+} ions from the substrate surface by the ascending jet of fresh fluxed solution and delivery of the components of YIG to the surface.

The vertical mixing velocity of the substrate as it is lowered and then extracted from the melt after growth is also important. For example, if the ES rises at a velocity of 20 cm/min, then the structure moves to a position 1 cm above the melt surface in $\sim$3 s. In this time, with a film growth rate

[1] I. I. Adamenko, P. S. Kostyuk, L. M. Letyuk *et al.*, *Physical Electronics* (L'vov State University Press, 1982), No. 25, pp. 102–104.

[2] S. I. Yushchuk, S. A. Yur'ev, G. I. Voroshilo, and P. S. Kostyuk, in *Abstracts of Reports on New Magnetic Materials for Microelectronics* (*Magnetic Films*), Astrakhan', 1992, Part 1, pp. 220–221.

[3] S. I. Yushchuk and P. S. Kostyuk, Prib. Tekh. Éksp. **39**(6), 79 (1996).

[4] A. V. Rakov, *Spectroscopy of Thin-Film Semiconductor Structures* (Sov. radio, Moscow, 1975).

[5] A. G. Gurevich, *Magnetic Resonance in Ferrites and Antiferromagnets* (Nauka, Moscow, 1973).

[6] V. V. Pan'kov, L. A. Bashkirov, O. I. Pashkovskiĭ, and Yu. G. Saksonov, Dokl. Akad. Nauk SSSR **256**(2), 417 (1981).

[7] A. M. Balbashov and A. Ya. Chervonenkis, *Magnetic Materials for Microelectronics* (Énergiya, Moscow, 1979).

[8] P. Hansen, K. Witter, and W. Tolksdorf, Phys. Rev. B **27**, 6608 (1983).

[9] A. G. Gurevich and G. A. Melkov, *Magnetic Oscillations and Waves* (Nauka, Moscow, 1994).

[10] S. I. Yushchuk, S. O. Yur'ev, and P. S. Kostyuk, Visnik derzh. un-ta ''L'vivs'ka politekhnika,'' No. 289, 90 (1995).

Translated by M. E. Alferieff

Saturation of two-level systems under pulsed stochastic resonance conditions

S. A. Baruzdin

St. Petersburg State Electrical Engineering University, 197376 St. Petersburg, Russia

Pulsed stochastic excitation of a two-level system described by Bloch equations is studied. An equation for the average powers of the components of the state vector of the system is obtained on the basis of the theory of stochastic differential equations, and solved. The dynamical and nonlinear properties of the response of a system under pulsed stochastic resonance conditions are analyzed and the results are compared with the corresponding stationary state. The results obtained can be used in spectroscopy and for analysis of nonlinear filters based on the saturation effect and intended for processing rf and light range signals. © *1999 American Institute of Physics.* [S1063-7842(99)01312-4]

1. INTRODUCTION

A stationary stochastic resonance was first proposed in nuclear magnetic resonance spectroscopy by Ernst and Kaiser as alternatives to pulsed and slow-passage spectroscopy.[1–3] Initially, the theory developed disagreed with the experimental data, but these disagreements were later resolved in Refs. 4 and 5. Subsequently, stochastic resonance started to be used in optical spectroscopy also.[6]

In the investigation of stochastic resonance, a great deal of attention has been devoted to the nonlinear properties, due to saturation, of the systems under study. For the pulsed variant of stochastic resonance these questions have been examined in Refs. 7 and 8.

Together with spectroscopy, nuclear magnetic resonance, electron spin resonance, and their optical analog are the basis of the operation of rf and light range signal processing devices.[9–12] One of the basic problems of such devices is extraction of signals due to various types of noise and interference signals.

Linear and nonlinear filtering are distinguished. In the former, saturation effects are undesirable and limit the dynamical range of the devices and degrade the characteristics of filters.[13–15] Conversely, the operation of nonlinear filters is based on the saturation effect.[9,16–18] The characteristics of a frequency-selective limiter of the power of the harmonic components of the spectrum of a deterministic signal have been investigated in Ref. 9. The filter passes without distortions the spectral components of low-power signals and limits the power of intense components of the spectrum.

The statistical characteristics of the components of the magnetization vector of a nuclear spin system and its nonlinear properties under excitation by white Gaussian noise have been investigated in Refs. 4 and 5. Stationary excitation has been investigated in detail in Ref. 9 and in Refs. 4 and 5. At the same time, signal processors operating on the basis of spin and photon echoes operate not in the stationary but rather in a pulsed excitation regime and their nonlinear characteristics can differ substantially from the corresponding characteristics of the stationary regime.

The magnetic-dipole and electric-dipole interaction of an electromagnetic field with a two-level system is described by the Bloch equations or their optical analogs.[3,12] This makes it possible to examine from a general standpoint the saturation process in the rf and light ranges.

The objective of the present work is to determine the power characteristics of the state vector **X** of the system, by which is meant either the magnetization vector **M** or the pseudopolarization vector **P**, depending on the type of interaction.[7] The two-level system under study is excited by a pulse of light Gaussian noise with duration τ and power spectral density N_0.

2. STOCHASTIC BLOCH EQUATIONS

The behavior of the state vector **X** of a two-level system with the components x_1, x_2, and x_3 in an external magnetic or electric field is described by the Bloch equations, which can be represented in the matrix form[5]

$$\frac{d\mathbf{X}}{dt} = \mathbf{AX} + \mathbf{B}s(t)\mathbf{X} + \mathbf{a},$$

$$\mathbf{A} = \begin{pmatrix} -T_2^{-1} & \omega & 0 \\ -\omega & -T_2^{-1} & 0 \\ 0 & 0 & -T_1^{-1} \end{pmatrix};$$

$$\mathbf{B} = \begin{pmatrix} 0 & 0 & 0 \\ 0 & 0 & \sigma \\ 0 & -\sigma & 0 \end{pmatrix}; \quad \mathbf{a} = \begin{pmatrix} 0 \\ 0 \\ x_0/T_1 \end{pmatrix}, \quad (1)$$

where x_0 is the static magnitude of the state vector **X**, determining the initial conditions for its components $x_1 = 0$, $x_2 = 0$, and $x_3 = x_0$; T_1 and T_2 are the longitudinal and transverse relaxation times, respectively; ω is the resonance frequency; the function $\sigma s(t)$ describes the input action.

We shall assume that $s(t)$ is white Gaussian noise with zero mean and unit spectral power density. Then the spectral power density of the process $\sigma s(t)$ will be $N_0 = \sigma^2$.

Integrating Eq. (1) according to the rules of ordinary differential equations leads to incorrect results. This was pointed out in Refs. 4 and 5. To obtain the correct results it is necessary to use the theory of stochastic differential equations, the formalism of which for nuclear magnetic resonance was used in Ref. 4.

The equation (1) can be formally integrated in the form

$$\mathbf{X}(t) = \int_0^t [\mathbf{A}\mathbf{X}(t') + \mathbf{a}]dt' + \int_0^t \mathbf{B}\mathbf{X}(t')dW(t'),$$

$$dW(t) = s(t)dt, \tag{2}$$

where $W(t)$ is a Wiener process.

The stochastic integral

$$\mathbf{Y}(t) = \int \mathbf{G}(\mathbf{X}(t'),t')dW(t') \tag{3}$$

with the kernel $\mathbf{G}(\mathbf{X}(t'),t')$ can be interpreted in two ways. If the Ito interpretation is used when integrating Eq. (2), then incorrect results which contradict physical reality are obtained. The Stratonovich form of the stochastic integral is more suitable. This form is very convenient for interpreting stochastic differential equations originating from laws of deterministic motion, i.e., in the present case from the ordinary Bloch equations corresponding to deterministic excitation processes.

The computational rules for a stochastic integral in the Stratonovich interpretation are less convenient, but there exists a formula for transforming the Stratonovich integral into an equivalent Ito integral[4]

$$(\text{Str.})\mathbf{Y}(t) = \int_0^t \mathbf{G}(\mathbf{X}(t'),t')dW(t')$$

$$= (\text{Ito})\mathbf{Y}(t) = \int_0^t \mathbf{G}(\mathbf{X}(t'),t')dW(t')$$

$$+ \frac{1}{2}\sum_{k=1}^d \int_0^t \mathbf{G}_{x_k}(\mathbf{X}(t'),t')G_k(\mathbf{X}(t'),t')dt', \tag{4}$$

$\mathbf{G}_{x_k} = (\partial \mathbf{G}/\partial x_k)$ and G_k is the kth component of the d-dimensional vector $\mathbf{G}$.

In the case at hand, according to Eq. (2),

$$\mathbf{G}(\mathbf{X}(t'),t') = \mathbf{B}\mathbf{X}(t'). \tag{5}$$

On the basis of Eqs. (4) and (5) it is possible to switch to a stochastic differential equation in the Stratonovich sense

$$d\mathbf{X} = (\mathbf{A}'\mathbf{X} + \mathbf{a})dt + \mathbf{B}dW(t), \tag{6}$$

$$\mathbf{A}' = \begin{pmatrix} -T_2^{-1} & \omega & 0 \\ -\omega & -T_2^{-1} - \sigma^2/2 & 0 \\ 0 & 0 & -T_1^{-1} - \sigma^2/2 \end{pmatrix}. \tag{7}$$

The equation (6) together with the expression (7) corresponds to a system of stochastic Bloch differential equations. Averaging Eq. (6), we obtain a differential equation for the average values of the state vector

$$\frac{d\langle \mathbf{X} \rangle}{dt} = \mathbf{A}'\langle \mathbf{X} \rangle + \mathbf{a}. \tag{8}$$

3. COVARIATION EQUATION AND THE AVERAGE POWER OF THE COMPONENTS OF THE STATE VECTOR

The initial problem is to construct a differential equation for the covariation matrix $\mathbf{K}_x(t) = \langle \mathbf{X}(t)\mathbf{X}^T(t) \rangle$, where $\mathbf{X}^T$ is a transposed vector. For this we shall use Ito's theorem.[4]

If d random processes $x_i(t)$, each of which is given by the stochastic differential

$$dx_i = f_i dt + G_i dW$$

and, in addition, is generated by the same Wiener process $W(t)$, then the stochastic process $\mathbf{Y}(t) = \mathbf{u}(t, x_1(t), \ldots, x_d(t))$ possesses the stochastic differential

$$d\mathbf{Y}(t) = \left(\mathbf{u}_t + \sum_{i=1}^d \mathbf{u}_{x_i} f_i + \frac{1}{2}\sum_{i=1}^d \sum_{j=1}^d \mathbf{u}_{x_i x_j} G_i G_j \right) dt$$

$$+ \sum_{i=1}^d \mathbf{u}_{x_i} G_i dW(t), \tag{9}$$

where $\mathbf{u}_t = (\partial/\partial t)\mathbf{u}$, $\mathbf{u}_{x_j} = (\partial/\partial x_i)\mathbf{u}$, and $\mathbf{u}_{x_i x_j} = (\partial^2/\partial x_i \partial x_j)\mathbf{u}$.

In the case at hand $d = 3$, $\mathbf{u}(t, x_1(t), \ldots, x_d(t)) = \mathbf{X}(t)\mathbf{X}^T(t)$, and the stochastic processes $x_i(t)$ are given by the stochastic Bloch equations (6) and (7). As a result, using Eq. (9) and averaging the expression obtained, we obtain a system of differential equations for the components of the covariation matrix

$$(d/dt)\langle x_1^2 \rangle = -2\langle x_1^2 \rangle/T_2 + 2\omega\langle x_1 x_2 \rangle, \tag{10}$$

$$(d/dt)\langle x_2^2 \rangle = -2\omega\langle x_1 x_2 \rangle$$
$$-2[T_2^{-1} + (\sigma^2/2)]\langle x_2^2 \rangle + \sigma^2\langle x_3^2 \rangle, \tag{11}$$

$$(d/dt)\langle x_3^2 \rangle = -2[T_1^{-1} + (\sigma^2/2)]\langle x_3^2 \rangle$$
$$+ \sigma^2\langle x_2^2 \rangle + 2x_0\langle x_3(t) \rangle/T_1, \tag{12}$$

$$(d/dt)\langle x_1 x_2 \rangle = -\omega\langle x_1^2 \rangle$$
$$-[2T_2^{-1} + (\sigma^2/2)]\langle x_1 x_2 \rangle + \omega\langle x_2^2 \rangle, \tag{13}$$

$$(d/dt)\langle x_1 x_3 \rangle = \omega\langle x_2 x_3 \rangle - [T_1^{-1} + T_2^{-1}$$
$$+ (\sigma^2/2)]\langle x_1 x_3 \rangle + x_0\langle x_1(t) \rangle T_1^{-1}, \tag{14}$$

$$(d/dt)\langle x_2 x_3 \rangle = -\omega\langle x_1 x_3 \rangle - [T_1^{-1} + T_2^{-1}$$
$$+ 2\sigma^2]\langle x_2 x_3 \rangle + x_0\langle x_2(t) \rangle T_1^{-1}. \tag{15}$$

The system (10)–(15) is formed by two independent systems (10)–(13) and (14)–(15).

We introduce the complex transverse components of the state vector $\tilde{x} = x_1 - ix_2$ and $x^* = x_1 + ix_2$. The average power of the complex amplitude of the transverse component is

$$P_t = \langle \tilde{x}x^* \rangle = \langle x_1^2 \rangle + \langle x_2^2 \rangle. \tag{16}$$

We also note that if a rotating coordinate system, often used in the literature,[3,4,12] is introduced, then the components

of the state vector in this system x_1', x_2', and $x_3'=x_3$ will be related with the complex components of the stationary system by the relations

$$x_1 \mp i x_2 = (x_1' \mp i x_2')\exp(\pm i\omega t). \qquad (17)$$

The average power of the complex amplitude of the transverse component of the state vector in the rotating system will likewise be

$$(P_t)_R = \langle \tilde{x}x^* \rangle_R = \langle \tilde{x}x^* \rangle = \langle x_1^2 \rangle + \langle x_2^2 \rangle = P_t. \qquad (18)$$

On the basis of Eqs. (10)–(12) and (16)–(18) we obtain a system of differential equations for the powers of the complex and longitudinal components of the state vector, which is invariant with respect to the coordinate systems under study,

$$(dP_t/dt) = -[2T_2^{-1} + (\sigma^2/2)]P_t + \sigma^2 P_l, \qquad (19)$$

$$(dP_l/dt) = \sigma^2 P_t/2 - (2T_1^{-1} + \sigma^2)P_l + 2x_0\langle x_3(t)\rangle T_1^{-1}, \qquad (20)$$

where $P_l = \langle x_3^2 \rangle = \langle (x')^2 \rangle$ is the average power of the longitudinal component.

Let us solve the Cauchy problem with the initial conditions $P_t(t_0)$ and $P_l(t_0)$. To do so let a pulse of white Gaussian noise act on the symmetric interval $|t| \leqslant \tau/2$ and $t_0 = -\tau/2$. The solution of the system (19)–(20) can be represented in the form

$$\begin{pmatrix} P_t(t) \\ P_l(t) \end{pmatrix} = \mathbf{\Phi}(t,t_0)\begin{pmatrix} P_t(t_0) \\ P_l(t_0) \end{pmatrix} + \begin{pmatrix} P_t'(t) \\ P_l'(t) \end{pmatrix}; \qquad (21)$$

$$\mathbf{\Phi}(t,t_0) = \begin{pmatrix} \Phi_{11} & \Phi_{12} \\ \Phi_{21} & \Phi_{22} \end{pmatrix};$$

$$\begin{pmatrix} P_t'(t) \\ P_l'(t) \end{pmatrix} = \int_{t_0}^t \mathbf{\Phi}(t,\xi)\begin{pmatrix} 0 \\ 2\langle x_3(\xi)\rangle T_1^{-1} \end{pmatrix}d\xi; \qquad (22)$$

$$\Phi_{11}(t,t_0) = \frac{\lambda_2 \exp[r_2(t-t_0)] - \lambda_1 \exp[r_1(t-t_0)]}{\lambda_2 - \lambda_1};$$

$$\Phi_{12}(t,t_0) = \frac{\lambda_1\lambda_2\{\exp[r_1(t-t_0)] - \exp[r_2(t-t_0)]\}}{\lambda_2 - \lambda_1};$$

$$\Phi_{21}(t,t_0) = \frac{\exp[r_2(t-t_0)] - \exp[r_1(t-t_0)]}{\lambda_2 - \lambda_1};$$

$$\Phi_{22}(t,t_0) = \frac{\lambda_2 \exp[r_1(t-t_0)] - \lambda_1 \exp[r_2(t-t_0)]}{\lambda_2 - \lambda_1};$$

$$\lambda_1 = \frac{\sigma^2}{-T_1^{-1} + T_2^{-1} - (\sigma^2/4) + \beta};$$

$$\lambda_2 = \frac{\sigma^2}{-T_1^{-1} + T_2^{-1} - (\sigma^2/4) - \beta};$$

$$r_{1,2} = \alpha \pm \beta = \left(\frac{1}{T_1} + \frac{1}{T_2} + \frac{3\sigma^2}{4}\right)$$

$$\pm \sqrt{\left(\frac{1}{T_1} - \frac{1}{T_2}\right)^2 + \left(\frac{1}{T_1} - \frac{1}{T_2}\right)\frac{\sigma^2}{2} + \frac{9\sigma^4}{16}}. \qquad (23)$$

The first term in Eq. (21) describes the solution of the homogeneous system corresponding to Eqs. (19) and (20), while the second term takes account of its inhomogeneity.

The average value $\langle x_3(t)\rangle$ of the longitudinal component in Eq. (22), determining the solution of the inhomogeneous system, can be found from Eq. (8) as

$$\langle x_3(t)\rangle = \langle x_3(t_0)\rangle \exp\left[-\left(\frac{1}{T_1} + \frac{\sigma^2}{2}\right)(t - t_0)\right]$$

$$+ \frac{x_0\{1 - \exp[-(T_1^{-1} + (\sigma^2/2))(t - t_0)]\}}{1 + (\sigma^2 T_1/2)}. \qquad (24)$$

Substituting the expression (24) into Eq. (22) we obtain

$$P_t'(t) = \frac{2x_0\lambda_1\lambda_2}{T_1(\lambda_2 - \lambda_1)}\left\{\left[\langle x_3(t_0)\rangle - \frac{x_0}{1 + (\sigma^2 T_1/2)}\right]\right.$$

$$\left. \times [f_1(t) - f_2(t)] + \frac{x_0[q_1(t) - q_2(t)]}{1 + (\sigma^2 T_1/2)}\right\}, \qquad (25)$$

$$P_l'(t) = \frac{2x_0}{T_1(\lambda_2 - \lambda_1)}\left\{\left[\langle x_3(t_0)\rangle - \frac{x_0}{1 + (\sigma^2 T_1/2)}\right]\right.$$

$$\left. \times [\lambda_2 f_1(t) - \lambda_1 f_2(t)] + \frac{x_0[\lambda_2 q_1(t) - \lambda_1 q_2(t)]}{1 + (\sigma^2 T_1/2)}\right\},$$

$$f_1(t) = \frac{\exp[r_1(t-t_0)] - \exp[-(T_1^{-1} + (\sigma^2/2))(t - t_0)]}{r_1 + T_1^{-1} + (\sigma^2/2)},$$

$$f_2(t) = \frac{\exp[r_2(t-t_0)] - \exp[-(T_1^{-1} + (\sigma^2/2))(t - t_0)]}{r_2 + T_1^{-1} + (\sigma^2/2)},$$

$$q_1(t) = \frac{\exp[r_1(t-t_0)] - 1}{r_1},$$

$$q_2(t) = \frac{\exp[r_2(t-t_0)] - 1}{r_2}. \qquad (26)$$

4. DISCUSSION

To analyze the dynamic and nonlinear properties of the two-level systems under pulsed stochastic resonance conditions, we shall examine an example in which before the action of the excitation pulse at time $t_0 = -\tau/2$ the system is in thermodynamic equilibrium. The initial conditions for the state vector are the deterministic quantities

$$\langle x_1(-\tau/2)\rangle = x_1(-\tau/2) = 0,$$

$$\langle x_2(-\tau/2)\rangle = x_2(-\tau/2) = 0,$$

$$\langle x_3(-\tau/2)\rangle = x_3(-\tau/2) = x_0. \qquad (27)$$

Therefore

$$P_t(-\tau/2) = 0; \quad P_l(-\tau/2) = x_0^2. \qquad (28)$$

In accordance with Eqs. (21)–(28), for the moment at which the excitation pulse ends $t = \tau/2$ the power of the complex amplitude of the transverse component of the state vector determining the response of the system will be
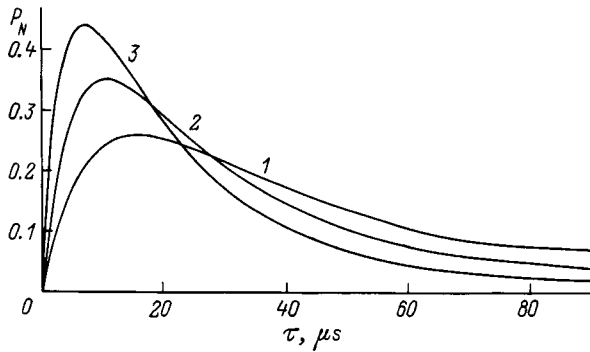
FIG. 1. Normalized power P_N of the transverse component of the state vector versus the duration τ of the excitation noise pulse.

$$P_t\left(\frac{\tau}{2}\right) = \frac{\sigma^2 x_0^2 [\exp(r_1\tau) - \exp(r_2\tau)]}{2\beta}$$

$$+ \frac{\sigma^2 x_0^2}{T_1\beta}\left\{\left[1 - \left(1 + \frac{\sigma^2 T_1}{2}\right)^{-1}\right][f_1(\tau) - f_2(\tau)]\right.$$

$$\left. + \left(1 + \frac{\sigma^2 T_1}{2}\right)^{-1}[q_1(\tau) - q_2(\tau)]\right\}. \quad (29)$$

Figure 1 shows the dependence of the normalized power of the transverse component $P_N = P_t(\tau/2)/x_0^2$ as a function of the excitation pulse duration τ. The power spectral density of white noise $N_0 = \sigma^2$ for the curves *1–3* is, respectively, 5×10^4, 10^5, and 2×10^5 rad^2/s, and the relaxation times $T_1 = 100$ μs and $T_2 = 25$ μs, which corresponds to the parameters of nuclear magnetic resonance of Co^{59} nuclei in thin magnetic films of cobalt.[12]

The initial sections of the curves are linear. As the pulse duration τ increases, the growth of power slows down, and the power reaches a maximum and then drops off monotonically, approaching a stationary value in the limit $\tau \to \infty$. We note that this value is

$$P_N = \frac{P_t(\infty)}{x_0^2} = \frac{T_2\sigma^2}{2[1 + (\sigma^2 T_1/2)][1 + (\sigma^2 T_2/4) + (\sigma^2 T_1/2)]},$$
$$(30)$$

which agrees with the total power of two transverse components in the stationary state in Ref. 5.

The plots presented in Fig. 1 essentially illustrate a transient process for the average power of the response of a two-level system. As one can see fromi Fig. 1, the larger the value of N_0, the larger the maximum power P_N and the smaller the corresponding pulse duration τ. However, in the steady state regime, larger values of N_0 correspond to lower power P_N. We note that an essentially steady stationary value is observed in the pulsed regime for $\tau \geq 3T_1$.

We also note that the maximum power P_N in the pulsed regime is more than an order of magnitude greater than the corresponding power of the response in the stationary regime. Thus, for $N_0 = 10^5$ rad^2/s the maximum power is reached with $\tau = 11$ μs and is 3.5×10^{-1}, while the stationary regime corresponds to a power of 3.14×10^{-2}. This could be important in spectroscopy for recording weak responses. Then, for pulsed stochastic resonance the excitation
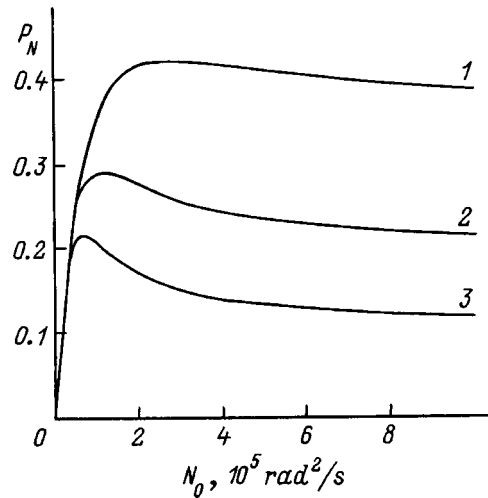

FIG. 2. Same as in Fig. 1 as a function of $N_0 = \sigma^2$. $T_1 = 100$ μs, $T_2 = 25$ μs.

of the system and detection of the response of the system are separated in time and the problem of detecting a weak response against the background of a strong exciting process, which happens when stationary methods are used, does not arise. In the latter case, various bridge schemes, requiring balancing, are used.[9] On this level, a quasistationary pulsed stochastic resonance regime, arising for $\tau \geq 3T_1$, is of interest.

When the excitation pulse ends, the power of the complex amplitude of the transverse component decays exponentially as a result of transverse relaxation

$$P_t(t) = P_t(\tau/2)\exp[(-2/T_2)(t - (\tau/2))], \quad t \geq \tau/2. \quad (31)$$

The dependence of P_N on the power spectral density of the exciting process $N_0 = \sigma^2$ with fixed pulse duration τ is presented in Fig. 2. The pulse duration τ for the curves *1–3* is 10, 20, and 30 μs, respectively. For comparison, in Fig. 3 the similar dependence is presented for the stationary state corresponding to Eq. (30). We call attention to the fact that this characteristic is different from the characteristic, presented in Ref. 9, of a power limiter for the harmonic components of the spectrum of a deterministic signal.

As one can see from Fig. 2, for low levels N_0 the system behaves as a linear system. As N_0 increases, the nonlinear properties of the system start to appear as a result of the
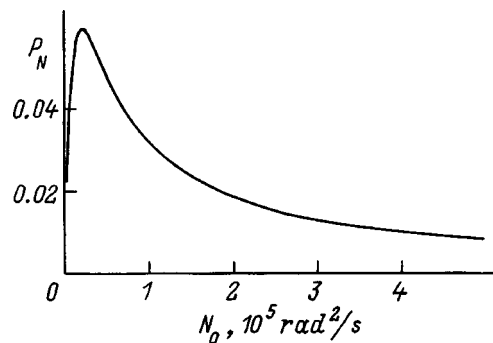

FIG. 3. Same as in Fig. 1 as a function of $N_0 = \sigma^2$ in the stationary regime. $T_1 = 100$ μs, $T_2 = 25$ μs.

saturation effect. The form of the characteristic is close to that of an ideal limiter in a quite wide range of values of N_0. In addition, this closeness is best seen for low values of the pulse duration τ. As τ increases, the form of the characteristic approaches the stationary form presented in Fig. 3. Lower values of τ correspond to a high degree of limiting (Fig. 2).

The results obtained can be used in pulsed stochastic spectroscopy and for the analysis and calculation of the characteristics of nonlinear filters and power limiters for noise and interference in the rf and light ranges.

[1] R. R. Ernst, J. Magn. Reson. **3**, 10 (1970).
[2] R. Kaiser, J. Magn. Reson. **3**, 28 (1970).
[3] R. R. Ernst, G. Bodenhausen, and A. Wokaun, *Nuclear Magnetic Resonance in One and Two Dimensions* [Clarendon Press, New York, 1987; Mir, Moscow, 1990].
[4] E. Bartholdi, A. Wokaun, and R. R. Ernst, Chem. Phys. **18**, 57 (1976).
[5] W. R. Knight and R. Kaiser, J. Magn. Reson. **48**, 293 (1982).

[6] S. Asaka, N. Nakatsuka, M. Fujiwara, and M. Matsuoka, Phys. Rev. A **29**, 2286 (1984).
[7] S. A. Baruzdin, Zh. Éksp. Teor. Fiz. **112**, 63 (1997) [JETP **85**, 34 (1997)].
[8] S. A. Baruzdin, Zh. Tekh. Fiz. **67**(10), 100 (1997) [Tech. Phys. **42**, 1201 (1997)].
[9] D. R. Jackson and W. Ort, TIIÉR **55**(1), 40 (1967).
[10] M. P. Petrov, A. P. Paugurt, A. V. Ivanov *et al.*, Pis'ma Zh. Tekh. Fiz. **12**(4), 833 (1986) [Sov. Tech. Phys. Lett. **12**, 344 (1986)].
[11] V. I. Dudkin, V. Yu. Petrun'kin, and V. I. Tarkhanov, Zh. Tekh. Fiz. **58**(9), 1738 (1988) [Sov. Phys. Tech. Phys. **33**, 1051 (1988)].
[12] S. A. Baruzdin, Yu. V. Egorov, B. A. Kalinikos *et al.*, *Functional Signal Processors* (*Theoretical Fundamentals and Algorithms*) (Radio i svyaz', Moscow, 1997).
[13] A. V. Ivanov, S. I. Goloshchapov, and A. P. Paugurt, Zh. Tekh. Fiz. **53**(11), 2171 (1983) [Sov. Phys. Tech. Phys. **28**, 1330 (1983)].
[14] S. I. Goloshchapov and A. P. Paugurt, Zh. Tekh. Fiz. **55**(12), 2361 (1985) [Sov. Phys. Tech. Phys. **30**, 1402 (1985)].
[15] S. A. Baruzdin, Izv. Vyssh. Uchebn. Zaved., Radiofiz. **41**(5), 9 (1998).
[16] V. P. Vakhrushev, A. A. Lipatov, A. N. Pogorelyĭ *et al.*, Izv. Vyssh. Uchebn. Zaved., Radiofiz. **29**(12), 36 (1986).
[17] L. A. Rassvetalov, Radiotekh. Élektron. (Moscow) **34**, 997 (1986).
[18] M. M. Kovalevskiĭ and L. A. Rassvetalov, Izv. Akad. Nauk SSSR, Ser. Fiz. **53**, 2322 (1989).

Translated by M. E. Alferieff

Methods for achieving high measurement sensitivity in holographic interferometry by rewriting holograms using incoherent light

A. M. Lyalikov

Ya. Kupal Grodno State University, 230023 Grodno, Belorus
(Submitted October 5, 1998)

Methods for increasing the measurement sensitivity in the rewriting of holograms by one beam of incoherent light are proposed. To achieve high measurement sensitivity it is suggested that an additional transmitting diffraction grating be used in optical rewrite systems. The linear and nonlinear forms of hologram rewriting are examined. The methods make it possible to lift the restrictions on the number of hologram rewrite cycles and to achieve maximum measurement sensitivity. The results of an experimental check are presented for the visualization of weak convection air flows near a heated body. © *1999 American Institute of Physics.* [S1063-7842(99)01412-9]

1. INTRODUCTION

Holographic methods for regulating the sensitivity of interference measurements are of great interest for the diagnostics of transparent media. Even though the sensitivity of interference measurements is high, diagnostics problems where the number or shift of interference fringes is inadequate for satisfactory analysis of interferograms are often encountered in practice. Then methods for increasing measurement sensitivity are ordinarily used.[1–3] Methods for increasing measurement sensitivity have been used to study gas flows near models in wind tunnels and on ballistic paths at low pressures, rarefied flows in shock tubes, for checking precise end measures and small deviations from planarity, and in interference spectroscopy.[2–4] Known methods for increasing measurement sensitivity with optical processing of holograms are based either on wavefront reconstruction in higher diffraction orders[5–7] or rewriting holograms with filtering of the spatial frequencies.[8–10] The latter methods make it possible to achieve higher measurement sensitivity. Hologram rewriting can be performed with one[8,9] or two[10] light beams. In the two-beam case[10] hologram rewriting can be done only in coherent light, whereas for single-beam rewriting the requirements on source coherence are substantially reduced and therefore the quality of the rewritten holograms improves because coherent noise is reduced.

A drawback of the method of increasing measurement sensitivity by hologram rewriting with a single beam is that the frequency of the carrier fringes in the rewritten holograms increases, which limits the number of rewrite cycles and, correspondingly, the possibility of achieving high coefficients of measurement sensitivity. The number of rewrite cycles in coherent light can be increased by simultaneously rewriting several reference holograms.[11] The limit on the number of rewrite cycles can be lifted completely combining hologram rewriting by a single beam of incoherent and by two beams of coherent light.[12] The optical rewrite system for implementing this method is very complicated, and the pres-

ence of a coherent light source degrades the quality of the final holograms because of coherent noise.

In the present paper methods for increasing measurement sensitivity in hologram rewriting with a single beam of incoherent light are examined. It is suggested that an additional transmitting diffraction grating with fringe period matched in a definite manner with the fringe period of the rewritten hologram should be employed in rewrite schemes.[13]

2. LINEAR REWRITING OF A HOLOGRAM

The optical scheme for linear rewriting of a hologram using a single beam of incoherent light is displayed in Fig. 1. We write the amplitude transmittance of a hologram written under linear writing condition conditions[4] as

$$\tau_0(x,y) \sim 1 + \cos\left[\frac{2\pi x}{T_0} + \varepsilon(x,y) + \varphi(x,y)\right], \quad (1)$$

where T_0 is the period of the carrier fringes, $\varepsilon(x,y)$ is the phase change caused by the experimental object, and $\varphi(x,y)$ are the phase distortions due to the aberrations of the system used to write the initial hologram.

The coordinate system XOY is chosen in the hologram plane so that the OY axis is parallel to the carrier holographic fringes. A distinguishing feature of a linear hologram of the form (1) and a nonlinear hologram is that under illumination it diffracts waves only in the $+1$ and -1 diffraction orders, arranged symmetrically with respect to the ze-
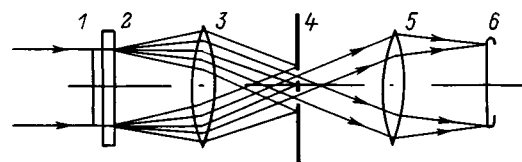

FIG. 1. Optical scheme for linear rewriting of holograms: *1* — hologram; *2* — transmitting diffraction grating; *3*, *5* — objectives; *4* — filtering diaphragm; *6* — hologram rewrite plane.

roth direct-transmission order. Let a transmitting grating *2* with fringes oriented parallel to the carrier fringes of the hologram be placed flush against the initial hologram *1* in the optical rewrite system (Fig. 1). The transmittance of such a grating is

$$\tau(x,y) = \sum_{n=-\infty}^{+\infty} c_n \exp\left[\frac{i2\pi nx}{T}\right], \tag{2}$$

where c_n are coefficients; $n = 0,1,2,\ldots$; and, T is the period of the fringes.

When a hologram superposed with a diffraction grating are illuminated in a direction along the normal, the distribution of the complex amplitudes $A(x,y)$ of the diffracted waves is directly proportional to the product $\tau_0(x,y)\tau(x,y)$. Using Eqs. (1) and (2), the distribution of the complex wave amplitudes at the exit of the combined hologram and diffraction grating can be represented in the more transparent form

$$A(x,y) \sim \left\{\frac{c_0}{2}\exp[i(2\pi\nu_0 x + \varepsilon(x,y) + \varphi(x,y))]\right.$$

$$+ \frac{c_0}{2}\exp[-i(2\pi\nu_0 x + \varepsilon(x,y) + \varphi(x,y))]\Big\}$$

$$+ \left\{\sum_{n=-\infty}^{+\infty} c_n \exp(i2\pi n\nu x)\right\}$$

$$+ \left\{\sum_{n=1}^{+\infty} \frac{c_n}{2}\exp[i(2\pi(\nu_0 - n\nu)x\right.$$

$$+ \varepsilon(x,y) + \varphi(x,y))]$$

$$+ \sum_{n=1}^{+\infty} \frac{c_n}{2}\exp[-i(2\pi(\nu_0 + n\nu)x$$

$$+ \varepsilon(x,y) + \varphi(x,y))]$$

$$+ \sum_{n=1}^{+\infty} \frac{c_n}{2}\exp[i(2\pi(\nu_0 + n\nu)x + \varepsilon(x,y) + \varphi(x,y))]$$

$$+ \sum_{n=1}^{+\infty} \frac{c_n}{2}\exp[-i(2\pi(\nu_0 + n\nu)x$$

$$\left.+ \varepsilon(x,y) + \varphi(x,y))]\right\}, \tag{3}$$

where ν_0 and ν are the spatial frequencies of the diffracted waves, related with the periods of the carrier fringes of the hologram and the diffraction grating as $\nu_0 = 1/T_0$ and $\nu = 1/T$.

Figure 2 shows the diffraction spectra of a linear hologram (a), the diffraction grating (b), and the superposed hologram and diffraction grating (c), observed in the back focal plane of the objective *3* (Fig. 1) on the filtering diaphragm *4*. In Fig. 2 the values of the spatial frequencies of the diffracted waves are marked, while the zeroth orders, corresponding to directly transmitted waves are left unmarked. The diffraction spectra presented in Figs. 2a–2c correspond to the case where the ratios of the periods of the carrier fringes of the hologram and the diffraction grating
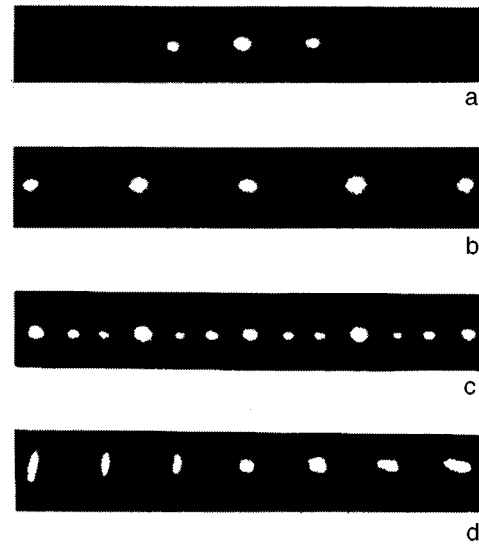
FIG. 2. Diffraction spectra.

$T_0 = 3/2T$ as the most favorable for implementing the rewrite method. The diffraction spectrum of the combined initial hologram and diffraction grating (Fig. 2c) contains components of waves diffracted exclusively by the hologram [first set of braces in Eq. (3)] and by the diffraction grating [second set of braces in Eq. (3)] as well as components which have undergone double diffraction (last set of braces in Eq. (3)). For for double-diffracted waves the first two sums describe the diffracted waves with difference spatial frequencies $\Delta\nu_n = \pm(\nu_0 - n\nu)$, and the other two sums describe diffracted waves with sum spatial frequencies $\pm(\nu_0 + n\nu)$. Diffracted waves with difference spatial frequencies $\pm\Delta\nu_1$ are of special interest for rewriting of the initial hologram. The complex amplitudes of these waves are

$$A_1(x,y) \sim c_1 \exp\{i[2\pi(\nu_0 - \nu)x + \varepsilon(x,y) + \varphi(x,y)]\},$$

$$A_1^*(x,y) \sim c_1 \exp\{-i[2\pi(\nu_0 - \nu)x + \varepsilon(x,y)$$

$$+ \varphi(x,y)]\}. \tag{4}$$

These waves are extracted by the filtering diaphragm *4* (Fig. 1) with the aid of two openings, and they form an interference pattern in the plane *6*, optically coupled by the objective *5* with the initial hologram *1*.

The amplitude transmittance of a hologram rewritten unde linear conditions is

$$\tau_1(x,y) \sim 1 + \cos\left[\frac{2\pi x}{T_1} + 2\varepsilon(x,y) + 2\varphi(x,y) + \psi(x,y)\right], \tag{5}$$

where $T_1 = 1/|2(\nu_0 - \nu)|$ and $\psi(x,y)$ are the aberrations of the rewrite system.

If the condition $T_0 = (3/2)T$ for the ratio of the periods of the carrier fringes of the initial hologram and diffraction grating is satisfied, which will correspond to the ratio of spatial frequencies $\nu = (3/2)\nu_0$, then the period of the carrier fringes of the rewritten hologram $T_1 = T_0$, i.e., it is the same as the period of the fringes of the initial hologram. It is

evident from Eq. (5) that the phase changes caused by the experimental object and the aberrations of the system writing the initial hologram are doubled.

In the second rewrite cycle the rewritten hologram is substituted for the initial hologram in the rewrite scheme (Fig. 1) and the entire process is repeated. After N rewrite cycles, where $N = 1,2,3, \ldots$, the amplitude transmittance of the rewritten hologram is

$$\tau_N(x,y) \sim 1 + \cos\left[\frac{2\pi x}{T_0} + 2^N \varepsilon(x,y) + 2^N \varphi(x,y) + \psi_N(x,y)\right],$$
(6)

where $\psi_N(x,y)$ are the aberrations of the rewrite system which have been accumulated over N cycles.

It is evident from Eqs. (6) and (1) that the phase changes due to the experimental object are increased by a factor of 2^N, and the period of the carrier fringes of the hologram has remained the same.

A reference hologram can be used to compensate the aberrations of the hologram writing system, which also are 2^N times greater than the aberrations of the initial hologram, and of the rewrite system which were accumulated over N rewrite cycles.[9] Such a hologram is written without the experimental object with the same period of the carrier fringes as the initial hologram (1). The amplitude transmitance of the reference hologram is

$$\tau'(x,y) \sim 1 + \cos\left[\frac{2\pi x}{T_0} + \varphi(x,y)\right].$$
(7)

After N rewrite cycles, performed by the method described above the amplitude transmittance of the final reference hologram is

$$\tau'_N(x,y) \sim 1 + \cos\left[\frac{2\pi x}{T_0} + 2\varphi^N(x,y) + \psi_N(x,y)\right].$$
(8)

It is evident from Eqs. (8) and (6) that the phase distortions caused by the aberrations of the write and rewrite system are the same for the final holograms. This makes it possible to exclude these aberrations completely at the stage where the interferogram is obtained.[9]

It should be noted that to implement the above-described method for increasing the measurement sensitivity, the initial and intermediate holograms should be recorded under linear conditions, which exclude the appearance of high orders of diffraction, which strongly distort the form of the diffraction spectrum. For the final rewritten holograms (6) and (8) the condition of linear writing is not required, since a holographic interferogram can be obtained by any method.[2–4] Figure 2d displays the diffraction spectrum of the final hologram rewritten four times ($N = 4$). The final hologram rewritten at the last stage was recorded even under nonlinear conditions, as is indicated by the appearance of higher orders with spatial frequencies which are multiples of ν_N. Comparing Figs. 2a and 2d we see that the periods of the carrier fringes of the initial hologram (a) and the hologram rewritten N times (d) are essentially the same.
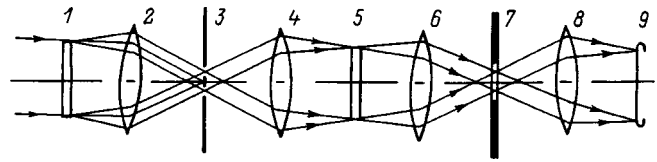

FIG. 3. Optical scheme for nonlinear rewriting of holograms: *1* — transmitting diffraction grating; *2, 4, 6, 8* — objectives; *3, 7* — filtering diaphragms; *5* — hologram; *9* — hologram rewrite plane.

3. NONLINEAR REWRITING OF A HOLOGRAM

If the initial hologram was written under nonlinear conditions, then its amplitude transmittance is[4]

$$\tau(x,y) \sim \left\{1 + \cos\left[\frac{2\pi x}{T_0} + \varepsilon(x,y) + \varphi(x,y)\right]\right\}^{-\gamma/2},$$
(9)

where γ is the gamma of the photoemulsion.

For holograms of the linear form (1) $\gamma = -2$. When such a hologram is illuminated, besides the ± 1 diffraction orders, higher orders are also present in the spectrum. If a nonlinear hologram is placed into the rewrite scheme (Fig. 1), then the diffraction spectrum of the combined hologram and diffraction grating in the back focal plane of the objective *3* on the diaphragm *4* will be even more complicated than for a linear hologram. The increased complexity of the pattern of the spectrum is due to the appearance of additional double-diffraction components on account of the high orders of the nonlinear hologram. The appearance of additional double-diffraction components with the difference $\pm(m\nu_0 - n\nu)$, where $m = 2,3, \ldots$, and sum $\pm(m\nu_0 - n\nu)$ spatial frequencies complicates the pattern of the diffraction spectrum to such an extent that it is virtually impossible to identify correctly the orders of diffraction required for rewriting.

Figure 3 shows an optical scheme for nonlinear rewriting of holograms by a single beam of incoherent light. This rewrite scheme differs from the preceding one (Fig. 1) by the presence of the system *2, 4* for optical conjugation of the diffraction grating *1* and the hologram *5*. Such a system makes it possible to perform in addition filtering of the spatial frequencies in the back focal plane of the objective *2* and thereby to simplify the diffraction spectrum of the waves which have undergone double diffraction.

In this hologram rewrite scheme (Fig. 3), it is proposed that a diffraction grating *1* and an optical filtering system *2–4* be used to form two beams of light illuminating the initial hologram *5* in a manner so that when the required waves are extracted, a hologram *9* with the same period of carrier fringes as the initial one *5* is rewritten in the filter plane *7*.

Let us assume that the fringes of the diffraction grating *1* make in the XOY plane certain angles with the OX and OY axes. Then the amplitude transmittance of the grating can be rewritten as

$$\tau(x,y) = \sum_{n=-\infty}^{+\infty} c_n \exp\left[i2\pi n\left(\frac{x}{T_x} + \frac{y}{T_y}\right)\right],$$
(10)

where T_x and T_y are, respectively, the distances between the carrier fringes of the diffraction grating which are measured along the OX and OY axes, respectively.

Since the initial hologram (9) is of a nonlinear form, we shall consider the more general case of the rewriting of a hologram in $\pm l$ diffraction orders.

If the enlargement of the optical conjugation system *2, 4* is 1, and the filtering diaphragm *3* separates the ± 1 diffraction orders, then the distribution of the complex amplitudes of the waves illuminating the hologram *5* in the plane of the initial hologram can be represented in the form

$$B(x,y) \sim c_1 \exp\{i2\pi(\nu_x x + \nu_y y)\},$$

$$B^*(x,y) \sim c_1 \exp\{-i2\pi(\nu_x x + \nu_y y)\}, \tag{11}$$

where the spatial frequencies are $\nu_x = 1/T_x$ and $\nu_y = 1/T_y$.

The distribution of the complex amplitudes of the diffracted waves on the initial hologram *5* is

$$A(x,y) = [B(x,y) + B^*(x,y)]\tau_0(x,y). \tag{12}$$

Waves diffracted by the initial hologram in the $\pm l$ diffraction order are of special interest,

$$A_l(x,y) \sim c_1 \exp\{i[2\pi((l\nu_0 + \nu_x)x + \nu_y y) + l\varepsilon(x,y) + l\varphi(x,y)]\},$$

$$A_l^*(x,y) \sim c_1 \exp\{-i[2\pi((l\nu_0 + \nu_x)x - \nu_y y) + l\varepsilon(x,y) + l\varphi(x,y)]\}. \tag{13}$$

It is obvious that if

$$\nu_x = -l\nu_0, \quad \nu_y = \frac{1}{2}\nu_0, \tag{14}$$

then the amplitude transmittance of the hologram rewritten in the plane *9* with separation of the waves $A_l(x,y)$ and $A_l^*(x,y)$ is

$$\tau_1(x,y) \sim \left\{ 1 + \cos\left[\frac{2\pi y}{T_0} + l\varepsilon(x,y) \right. \right.$$
$$\left. \left. + l\varphi(x,y) + \psi_l(x,y) \right] \right\}^{\gamma/2}, \tag{15}$$

where $\psi_l(x,y)$ are the aberrations of the rewrite system.

It is evident from Eq. (15) that the orientation of the carrier fringes of the rewritten hologram has changed by 90° with respect to the carrier fringes of the initial hologram (9), but the period of the fringes has not changed.

Figure 4 shows the diffraction spectra observed in the back focal plane of the objective *6* (Fig. 3) on the filtering diagram *7* with the initial hologram rewritten in the ± 1 (Fig. 4a) and ± 2 (Fig. 4b) diffraction orders. In Fig. 4 a rectangle marks the waves $A_1(x,y)$, $A_1^*(x,y)$ for $l=1$ (a) and $A_2(x,y)$, $A_2^*(x,y)$ for $l=2$ (b), which are separated by the filtering diaphragm *7* (Fig. 3).

A reference hologram rewritten the same number of times as the initial hologram can be used to compensate the aberrations of the write and rewrite systems.
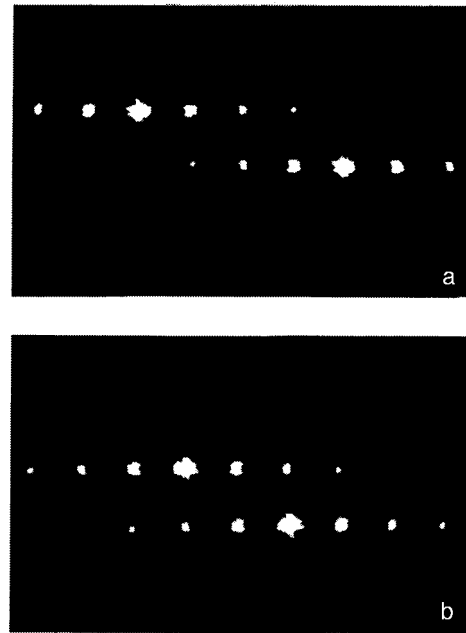

FIG. 4. Diffraction spectra observed on a filtering diaphragm *7* (Fig. 3) with rewriting of holograms in the ± 1 (a) and ± 2 (b) diffraction orders.

4. EXPERIMENTAL CHECK

The methods examined above for increasing the sensitivity in the rewriting of holograms by a single beam of incoherent light were used to visualize weak convection air flows near a heated body. The initial hologram was written using a holographic interferometer based on an IAB-451 shadow apparatus.[14] The period of the carrier fringes of the hologram was $T_0 = 0.04$ mm. The reference hologram was written in the absence of convection flows without changing the scheme.

Figures 5a and 5b show the reconstructed interferograms, obtained by superposing the initial and reference holograms, with adjustment to infinitely wide (a) and finite (b) fringes. For adjustment to finite fringes, the holograms were turned relative to one another by a small angle.[15] For adjustment to an infinitely wide fringe, virtually uniform illumination of both the light (a) and dark fields was observed in the field of the interferogram. The presence of a signal (curvature of an interference fringe) was observed only for adjustment to finite fringes by turning the holograms. However, when the holograms are turned relative to one another, aberrations comparable in magnitude to the useful signal can be introduced into the interferogram.

A method for increasing measurement sensitivity by using linear holograms was used to increase the measurement sensitivity in visualizing weak convection air flows. The initial and reference holograms were rewritten using the scheme presented in Fig. 1. A helium–neon laser was used as the light source. The spatial coherence of the laser radiation was destroyed by a rotating scatterer. The latter was placed in the defocused plane of a short-focal length collecting lens of a telescopic system forming a collimated beam. The diameter of the spot focused on the scatterer was 1–2 mm. Transmitting diffraction gratings were prepared on an FG-690 photo-
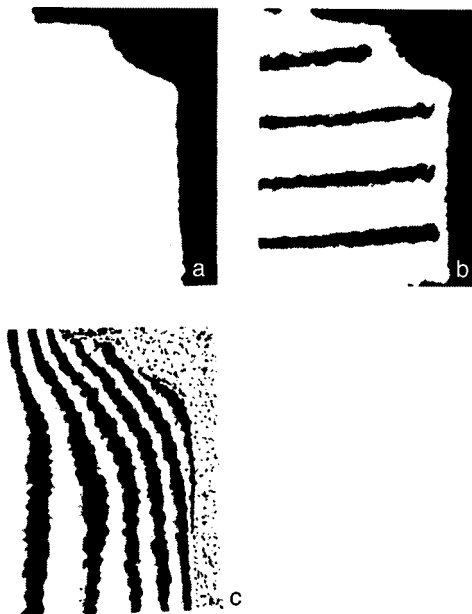
FIG. 5. Interferograms reconstructed by superposing the initial and reference holograms (a, b) and rewritten initial and reference holograms with 32 times higher sensitivity (c).

emulsion by an interference method. The method developed was tested using amplitude and phase gratings. The latter were made by bleaching amplitude diffraction gratings. The use of phase diffraction gratings in hologram rewrite schemes made it possible to increase substantially the transmittance of the optical schemes and thereby decrease the exposure time when rewriting holograms. However, the phase diffraction gratings obtained by bleaching contained much greater noise because of light scattering than amplitude gratings. This certainly affected the quality of the rewritten holograms.

Figure 5c shows the reconstructed interference pattern with adjustment to an infinitely wide band. This pattern was obtained by optical processing of the initial and reference holograms which were rewritten four times ($N=4$). The ho-

lograms were rewritten using the scheme presented in Fig. 1. The sensitivity of the rewritten holograms was increased by a factor of 16, and the interferograms were reconstructed in an optical superposed-hologram analyzer,[4] which made it possible to increase the measurement sensitivity in the final reconstructed interferogram by an additional factor of 2. Thus the measurement sensitivity in the interpretation of the final interferogram (Fig. 5c) was 32 times higher than the sensitivity of the interferogram (Figs. 5a and 5b). It should be noted that despite the large increase in measurement sensitivity, the fringe quality in the final interferogram is quite good, making it possible to read the fringe number with an error of not worse than 25%.

[1] C. Vest, *Holographic Interferometry* [Wiley, New York, 1979; Mir, Moscow, 1982].
[2] I. S. Zeĭlikovich and N. M. Spornik, *Holographic Diagnostics of Transparent Media* (University Press, Minsk, 1988).
[3] I. S. Zeĭlikovich and A. M. Lyalikov, Usp. Fiz. Nauk **161**, 143 (1991) [Sov. Phys. Usp. **34**, 74 (1991)].
[4] A. K. Beketova, A. F. Belozerov, A. N. Berezkin *et al.*, *Holographic Interferometry of Phase Objects* (Nauka, Leningrad, 1979).
[5] O. Bryngdahl and A. W. Lohmann, J. Opt. Soc. Am. **58**, 141 (1968).
[6] K. S. Mustafin, V. A. Seleznev, and E. I. Shtyrkov, Inventor's Certificate USSR No. 272602; Byull. Izorbr., No. 19 (1970).
[7] K. Matsumotto and M. Takashima, J. Opt. Soc. Am. **60**, 30 (1970).
[8] Zh. Shvider, in *Proceedings of the 3rd All-Union School on Holography*, Leningrad (1972), pp. 247–254.
[9] I. S. Zeĭlikovich, Opt. Specktrosk. **49**, 396 (1980) [Opt. Spectrosc. **49**, 215 (1980)].
[10] I. S. Zeĭlikovich and S. A. Pul'kin, Opt. Specktrosk. **53**, 588 (1982) [Opt. Spectrosc. **53**, 349 (1982)].
[11] I. S. Zeĭlikovich and A. M. Lyalikov, Opt. Mekh. Prom. **54**(9), 31 (1987).
[12] I. S. Zeĭlikovich, A. M. Lyalikov, and V. V. Sigov, Inventor's Certificate No. 1368624 USSR; Byull. Izobr., No. 3 (1988).
[13] A. M. Lyalikov, Pis'ma Zh. Tekh. Fiz. **24**(12), 72 (1998) [Tech. Phys. Lett. **24**, 487 (1998)].
[14] A. M. Spornik, Opt. Mekh. Prom., No. 2, 77 (1973).
[15] A. M. Spornik, A. F. Belozerov, and A. I. Byval'tsev, Inventor's Certificate No. 396540; Byull. Izobr., No. 36 (1973).

Translated by M. E. Alferieff

Control of the characteristics of a calcium molybdate collinear acousto-optic filter

V. N. Parygin, A. V. Vershubskiĭ, and K. A. Kholostov

M. V. Lomonosov Moscow State University, 119899 Moscow, Russia
(Submitted October 26, 1998)
Zh. Tekh. Fiz. **69**, 76–81 (December 1999)

The problem of controlling the characteristics of a calcium molybdate collinear acousto-optic
filter using acoustic trains of variable duration is investigated experimentally. It is shown
that electronic restructuring of not only the central transmission frequency but also the transmission
bandwidth of the filter as well as the form of the transmission curve is possible in collinear
acousto-optic filters. The frequency characteristics of the filter are measured by synchronous and
inertial methods. The experimental relative-transmission curves and the experimentally
measured side wings of the transmission bands of the acousto-optic cell are presented. © *1999
American Institute of Physics.* [S1063-7842(99)01512-3]

1. INTRODUCTION

In the last few years, tunable acousto-optic filters have
been finding more and more applications in laser technology,
spectroscopy, optoelectronics, and optical information pro-
cessing. These devices have a narrow (of the order of several
angstroms) transmission band, and the light wavelength λ
transmitted by the filter can be tuned electronically over an
entire octave (from λ_{min} to $\lambda_{max} \approx 2\lambda_{min}$) by a corresponding
change in the frequency of the acoustic wave.[1–3]

Two types of acousto-optic filters are described in the
literature: collinear and noncollinear.[4,5] Ordinarily, collinear
filters have a narrow transmission band, i.e., they are distin-
guished by high selectivity, which is very important in prob-
lems of the spectral analysis of optical radiation and prob-
lems of increasing the density of communication channels.
However, only a small number of crystals showing purely
collinear acousto-optic interaction are known at present.
These are quartz, lithium niobate, and calcium molybdate.
These materials are all of low acousto-optic quality. For this
reason, in practice, noncollinear filters, which have high ef-
ficiency but lower resolution, are also widely used together
with collinear filters.

Recent theoretical works[6–9] have shown that electronic
tuning of not only the central transmission frequency of a
filter but also the transmission bandwidth and the shape of
the transmission curve is possible in collinear acousto-optic
filters, if a pulsed signal is used instead of a continuous
acoustic signal controlling the filter. Then the duration of the
controlling pulse determines the transmission band of the
filter, and the form of the pulsed signal strongly influences
the form of the transmission function of a collinear filter. The
present work is devoted to an experimental investigation of
this problem.

2. THEORY OF COLLINEAR ACOUSTO-OPTIC INTERACTION

The propagation of an acoustic train in an anisotropic
medium can be described using the Christoffel equation for
the wave of elastic displacements $\mathbf{A}(x,y,z,t)$ in this
medium.[10] Collinear diffraction occurs only in anisotropic
media characterized by a complicated directional dependence

of the wave-vector surface. Such diffraction with a large in-
teraction length occurs only in the directions of sound propa-
gation, where the wave vector of the sound is perpendicular
to the tangential wave-vector surface.

If a sound beam propagates in the direction x without
energy drift, then one solution of the Christoffel equation in
an anisotropic medium is a weakly diverging Gaussian func-
tion describing the amplitude of this beam,

$$G_A(x,y,z) = \frac{1}{1-jDx}\exp\left\{-\frac{y^2+z^2}{R^2(1-jDx)}\right\}, \qquad (1)$$

where $D = 2/(KR^2)$ is the divergence of the train in trans-
verse directions y and z; R is the initial transverse size of the
train; the term $(1-jDx)$ describes the change in phase and
radius of the beam as the beam propagates in the medium.

An acoustic train propagating along the x axis in a me-
dium without energy drift can be represented as

$$A_0\mathbf{A}(x,y,z,t) = \mathbf{a} A_0 G_A(x,y,z)V(x,t)$$
$$\times \exp\{j(\Omega t - Kx)\} + \text{c.c.}, \qquad (2)$$

where $V(x,t)$ is the temporal envelope of the sound train,
i.e., a function describing the form of the train in the direc-
tion of propagation; $\mathbf{a}$ is a unit polarization vector; A_0 is the
input amplitude of the acoustic wave; Ω and K are, respec-
tively, the frequency and wave number of the train; the func-
tion $V(x,t)$ is slowly varying in both coordinates, so that in
the present theory we neglect its derivatives.

The propagation of an acoustic train (2) in a medium is
accompanied by a wave of elastic deformations, determined
by a tensor $\mathbf{S}_{lm}$ whose components in turn can be expressed
as

$$\mathbf{S}_{lm} = \frac{A_0}{2}\left\{\frac{\partial A_l}{\partial x_m} + \frac{\partial A_m}{\partial x_l}\right\}. \qquad (3)$$

The wave of elastic deformations changes the refractive
index of the medium. This is due to the elasto-optic effect,
described by the tensor $\mathbf{p}_{jklm}$.[10] The change in the permittiv-
ity tensor by the acoustic-deformation field has the form

$\Delta\varepsilon_{jk}=-N_j^2N_k^2\mathbf{p}_{jklm}\cdot\mathbf{S}_{lm}$, where N_j and N_k are the principal refractive indices of the medium and j,k,l, and m are coordinate indices.

The vector $\mathbf{E}$ of the light field in the pesence of sound propagating in the medium must satisfy the wave equation

$$\text{curl curl }\mathbf{E}+\frac{1}{c^2}\frac{\partial^2}{\partial t^2}\hat{\varepsilon}_0\mathbf{E}=-\frac{1}{c^2}\frac{\partial^2}{\partial t^2}\Delta\hat{\varepsilon}(\alpha\mathbf{E}),\qquad(4)$$

where $\alpha(x,y,z,t)$ is a scalar spatial and variable distribution of the deformations, $\hat{\varepsilon}$ is the permittivity of the medium in the absence of sound, and $\Delta\hat{\varepsilon}$ is the change in $\hat{\varepsilon}_0$ in the presence of sound and is proportional to the amplitude A_0 of the acoustic deformation.

It should be noted that curl curl $\mathbf{E}\neq-\nabla^2\mathbf{E}$ for light beams of finite size, since grad div $\mathbf{E}\neq0$ cannot be assumed to be zero even in an isotropic medium.

As is well known, for collinear diffraction the polarization of the diffracted light beam is orthogonal to the polarization of the light incident on the acousto-optic cell. For this reason, it is natural to represent the light beam in the region of interaction of the light and sound as a sum of the transmitted and diffracted beams with orthogonal polarizations, propagating in the same direction as the sound train (2),

$$\mathbf{E}=\mathbf{e}_tE_t(x,t)G_E(y,z)\exp[j(k_tx-\omega_tt)]$$
$$+\mathbf{e}_dE_d(x,t)G_E(y,z)\exp[j(k_dx-\omega_dt)],\qquad(5)$$

where $\mathbf{e}_t$ and $\mathbf{e}_d$ are unit polarization vectors; $E_t(x,t)$ and $E_d(x,t)$ are slowly varying amplitudes on the axis of the optical beams; ω, n, and $k=\omega n/c$ are the frequency, refractive index, and wave number of the light wave, respectively; and, $G_E(y,z)=\exp\{-(y^2+z^2)/r^2\}$. Here and below the index t refers to the transmitted light, and the index d refers to the diffracted light. The use of the function $G_E(y,z)$ in this form implicitly assumes that the divergence of the light beam in the region of acousto-optic interaction can be neglected.

We now substitute the vector $\mathbf{E}$ in the form (5) into the wave equation (4) and neglect $\partial^2E_t/\partial x^2$ and $\partial^2E_d/\partial x^2$. Using the diffraction condition $\omega_d=\omega_t+\Omega$, we equate to one another the terms multiplying $\exp\{j\omega_tt\}$ and $\exp\{j\omega_dt\}$ in both parts of the wave equation. Since the polarizations $\mathbf{e}_t$ and $\mathbf{e}_d$ are orthogonal to one another, we form the scalar products of the expression obtained and $\mathbf{e}_t$ and $\mathbf{e}_d$. As a result, we obtain from Eq. (4) two scalar equations relating the amplitudes E_t and E_d:

$$\frac{\partial E_t}{\partial x}+\frac{E_t}{2jk_t}\frac{\partial^2G_E}{\partial z^2}$$
$$=-jq_2e^{j\eta x}G_A^*(x,y,z)G_E(y,z)V(x,t)E_d(x,t),\qquad(6)$$

$$\frac{\partial E_d}{\partial x}+\frac{E_d}{2jk_d}\frac{\partial^2G_E}{\partial y^2}$$
$$=-jq_1e^{j\eta x}G_A(x,y,z)G_E(y,z)V(x,t)E_t(x,t).\qquad(7)$$

Here $\eta=k_t+K-k_d$, $q_1=k_d(\mathbf{e}_d\cdot\Delta\hat{\varepsilon}\mathbf{e}_t)/n_d^2$, $q_2=k_t(\mathbf{e}_t\cdot\Delta\hat{\varepsilon}\mathbf{e}_d)/n_t^2$. If $\lambda L\ll\pi r^2$, then the second derivatives on the left-hand side of Eqs. (6) and (7) can be neglected.

3. WEAK ACOUSTO-OPTIC INTERACTION APPROXIMATION

If the acousto-optic diffraction efficiency is low, then the transmitted light beam does not differ much from the incident beam. Then the known value $E_i=E_t(0)$ can be substituted into the right-hand side of Eq. (7) instead of the unknown function $E_t(x)$. In this situation the diffracted light at the exit of the acousto-optic cell is determined by the single equation (7), and if the divergence of the sound train is small $(D\to0)$, the problem can be solved analytically. Fourier transforming both parts of Eq. (7) in the yz plane we obtain

$$\frac{\partial E_d}{\partial x}\mathbf{F}\{G_E\}=-jq_1E_ie^{-j\eta x}V(x,t)\mathbf{F}\{G_AG_E\},\qquad(8)$$

where

$$\mathbf{F}\{G_E\}=\pi r^2\exp\{-(k_y^2+k_z^2)r^2/4\},$$

$$\mathbf{F}\{G_AG_E\}=\pi r^2(1+\rho^2)^{-1}\exp\{-(k_y^2+k_z^2)r^2/4(1+\rho^2)\},$$

$\rho=r/R$; and, k_y and k_z are the transverse components of the wave vector of the light.

If the radius of the sound train is large $(R\gg r)$, $\mathbf{F}(G_AG_E)\approx\mathbf{F}\{G_E\}$, and therefore we can cancel the terms on both sides of Eq. (8). As a result, we obtain the standard formula for the plane-wave theory.

In the subsequent analytic analysis of the problem, two different limiting cases are assumed: the region of acousto-optic interaction L is much larger than the length l of the acoustic train or the opposite situation holds. The latter case is close to the phenomenon of light diffraction by a continuous sound beam, so that we shall consider the first limiting case $(l\ll L)$. To find the amplitude $E_d(L,t)$ of the diffracted light at the exit of the cell, the expression (8) must be integrated over the coordinate x within the interaction length. If the temporal envelope of the sound train is chosen to be Gaussian $V(x,t)=\exp\{-(vt-x)^2/l^2\}$, then integration gives

$$E_d(L,t)=-jq_1l\frac{E_i}{\sqrt{1+\rho^2}}\left(\text{erf}\frac{vt}{l}-\text{erf}\frac{vt-L}{l}\right)$$
$$\times\exp\left\{-\frac{k_y^2+k_z^2}{4}r^2\frac{\rho^2}{1+\rho^2}-\frac{(\eta l)^2}{4}\right\},\qquad(9)$$

where $\text{erf}(x)=(2/\sqrt{\pi})\int_0^xe^{-\zeta^2}d\zeta$.

When the divergence of the sound train is substantial, the constant ρ becomes a function of x: $\rho^2(x)=r^2/R^2(1+D^2x^2)$. Then Eq. (8) can be integrated only numerically and a formula similar to Eq. (9) cannot be derived.

Using finite beams to describe diffraction of light by sound makes it possible to determine the diffraction efficiency not in terms of the ratio of the power densities of the incident and diffracted light, but rather in terms of the ratio of the power fluxes in the diffracted and incident light beams, as is always done experimentally. The power flux in a light beam can be calculated by means of an integral of the squared modulus of the distribution of the light field over the transverse section of the beam and by means of an integral of the squared modulus of the Fourier spectrum of the field over the angular coordinates k_y and k_z (Parseval's theorem).

The power flux of the light at the entrance into the acousto-optic cell is determined by the relation $P_0 = 0.5E_t^2 \int\int G_E^2 dy dz$, and the power flux at the exit of the cell can be calculated using the formula $P = 0.5\int\int E_d(L)E_d^*(L) \times (\mathbf{F}\{G_E\})^2 dk_y dk_z$, where $E_d(L)$ is determined by the expression (9). The ratio P/P_0 characterizes the acousto-optic diffraction efficiency. It has the form

$$\frac{P}{P_0} = \frac{(ql)^2}{1+2\rho^2}\left(\mathrm{erf}\,\frac{vt}{l} - \mathrm{erf}\,\frac{vt-L}{l}\right)^2 \exp\left\{-\frac{(\eta l)^2}{2}\right\}. \quad (10)$$

If successive sound trains follow continuously with interval $L/2 < S < L$, two trains can be located simultaneously inside the crystal. In this situation the phase difference between these trains has a large effect on the acousto-optic interaction efficiency. If, as in the preceding case, a Gaussian temporal envelope is chosen for two trains of identical length

$$V(x,t) = \exp\left\{-\frac{(vt-x)^2}{l^2}\right\}$$

$$+ \exp\left\{-\frac{(vt-x-S)^2}{l^2}\right\}\exp\{j\varphi(S)\}, \quad (11)$$

where $\varphi(S) = KS + \varphi_0$ is the phase difference between the two trains and φ_0 is the initial phase of the second train, then an expression describing the diffraction efficiency, similar to Eq. (10), is

$$\frac{P}{P_0} = \frac{(ql)^2}{1+2\rho^2}\exp\left\{-\frac{(\eta l)^2}{2}\right\}$$

$$\times [H_1^2 + H_2^2 + 2H_1 H_2 \cos(KS + \varphi_0)], \quad (12)$$

where

$$H_1 = \mathrm{erf}\,\frac{vt}{l} - \mathrm{erf}\,\frac{vt-L}{l},$$

$$H_2 = \mathrm{erf}\,\frac{vt-S}{l} - \mathrm{erf}\,\frac{vt-(L+S)}{l}.$$

Analysis of the relation (12) shows that by varying the phase difference between the trains the diffraction efficiency can be varied from $H_1^2 - H_2^2$ to $H_1^2 + H_2^2$. This is determined by the maximum change in the function $\cos(x)$. To achieve the maximum efficiency the phase φ_0 of the second train must differ from that of the first train by KS.

4. EXPERIMENT

A collinear acousto-optic filter based on a CaMoO$_4$ crystal of length $L = 3.5$ cm was used in the experimental investigations. A diagram of the acousto-optic cell is displayed in Fig. 1. When unpolarized oscillations are used, four rays are present at the exit of the acousto-optic cell. However, because the angle between the ordinary and extraordinary rays is small, three rays are observed: two diffracted and one transmitted, since the rays b and c merge. The optic axis of the crystal was orthogonal to the direction of the light and the sound. The refractive indices of a calcium molybdate crystal are $n_0 = 1.9720$ and $n_e = 1.9814$. The sound speed is
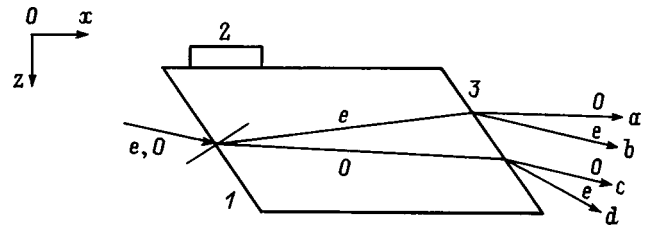

FIG. 1. Diagram of acousto-optic cell: *1* — entrance face; *2* — piezoelectric transducer; *3* — exit face; a, d — diffracted beams; b, c — transmitted beams.

$v = 2926$ m/s, and correspondingly the transmission time of an acoustic train through the crystal was $L/v = 11.9\ \mu$s.

A diagram of the experimental apparatus is presented in Fig. 2. The operation of the collinear filter *8* is controlled by a specially constructed generator *2* controlled by a computer *1*. The generator gives at the exit electric pulses of prescribed shape, frequency, and amplitude. A helium–neon laser *4*, generating radiation with wavelength $\lambda = 0.6328\ \mu$m with a light beam diameter of 3 mm was used as the light source. In certain experiments a diaphragm *6*, which decreases the size of the laser beam at the exit to 0.35 mm, was placed at the laser exit. The light is attenuated by the light filters *5*, which are necessary in order to decrease the intensity of the laser radiation, since an optimal light intensity must be used in measurements performed with a photomultiplier (FÉU) *10*. The laser generates unpolarized oscillations, so that three beams are observed at the exit of the acousto-optic cell *8*. To select and analyze one beam, crossed entrance and exit polarizers *7* and *9* are used.

The condition of collinear diffraction of light $\mathbf{k}_d = \mathbf{k}_t + \mathbf{K}$ with the indicated wavelength ($\lambda = 0.6328\ \mu$m) is satisfied with the acoustic frequency $\Omega/2\pi = 43.6$ MHz. Since the entrance and exit faces of the crystal are not perpendicular to the propagation direction of the light in the crystal, the diffracted light beam at the exit of the cell propagates at an angle of $0.53°$ with respect to the transmitted beam. This makes it possible to perform measurements of the diffracted light without noise from the transmitted laser beam.

In the experiments performed the diffraction efficiency reached 10%. This corresponds to a weak acousto-optic interaction. Measurements of the transmission band (with re-
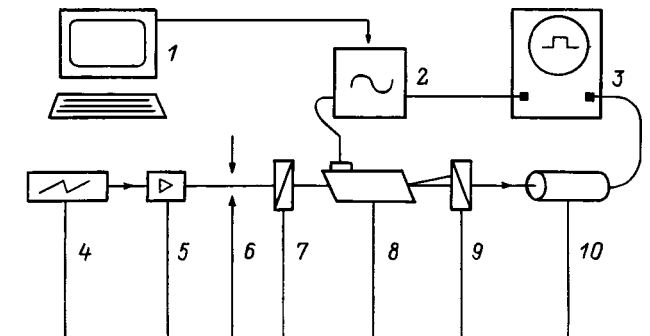

FIG. 2. Arrangement of the experimental apparatus: *1* — computer, *2* — generator, *3* — oscillograph, *4* — laser, *5* — light filters, *6* — diaphragm, *7* — entrance polarizer, *8* — acousto-optic cell, *9* — exit polarizer, *10* — photomultiplier.
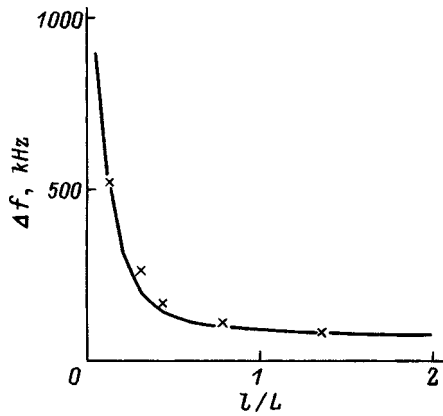
FIG. 3. Transmission band Δf versus the relative duration l/L of the sound train.

FIG. 5. Experimental curves of the relative transmittance of an acousto-optic cell versus the acoustic signal frequency f for various durations of the controlling pulse $\tau = l/v$, $\tau = 60$ and 17 (*1*), $6(2)$, $15\ \mu s$ (*3*).

spect to the 0.4 level) and the level of the first side lobes of the transmission function were performed for two cases: for square and Gaussian sound trains. Figure 3 shows the transmission band as a function of the sound train duration. The transmission bands for both types of trains are the same, if the length of the Gaussian train is measured with respect to the 0.4 level. The theoretical results are shown by a solid curve, and the experimental results are indicated by cross marks.

Figure 4 illustrates the dependence of the level of the side lobes measured in the experimental apparatus on the duration of the acoustic pulse. The magnitude of the side lobes for square pulses is constant (dashed line), while for Gaussian pulses it varies from zero for short duration to a level corresponding to the level of the side lobes of the square pulses (solid and dashed curves). Thus, the transmission characteristics of a collinear filter can be substantially changed by controlling the duration of the Gaussian train. This can be used in practice. As is evident from Fig. 4, for a Gaussian train with duration of the order of L/v the level of the side lobes drops substantially with no appreciable broadening of the transmission band.

Two different methods for measuring the transmission band and level of the side lobes of the filter characteristics were used in this work: synchronous and inertial methods.
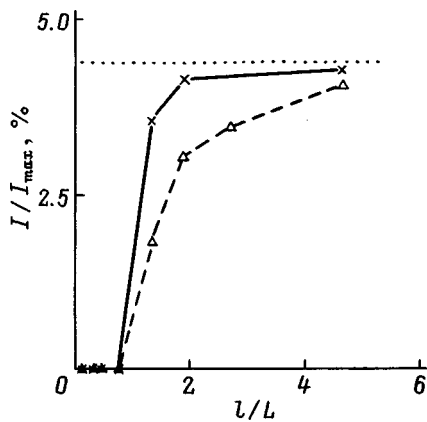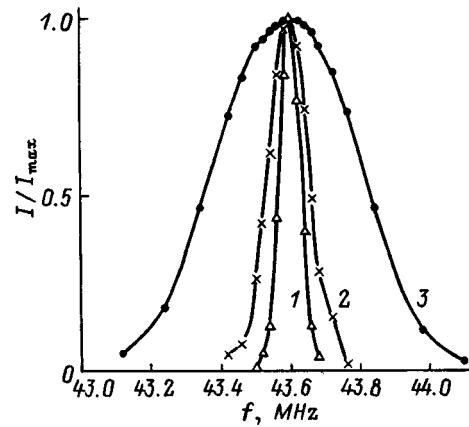

FIG. 4. Side lobe level I/I_{max} versus the relative duration l/L of a Gaussian sound train.

In the first case (dashed curve) the light intensity at the filter exit was measured at the moment when the center of the sound train was located at the center of the crystal. This means that the detector of the light radiation was switched on with the pulse repetition frequency of the controlling generator and with the corresponding phase. In the process, measurements in the transitional period, when the sound train enters and exits the crystal, were completely excluded. In principle, these transition processes increase somewhat the transmission band of the filter, since the length of the working part of the train during this time is shorter than its total length.

The second measurement method (solid curve) consisted in using the entire light flux corresponding to the diffracted beam. In this case, the voltage on the active load of the photomultiplier was measured with an inertial photodetector. Comparing the results in Fig. 4 shows that the side lobes of the transmission curve when using the inertial photodetector grow much more rapidly with increasing duration of the train than for measurements by the synchronous method.

Figure 5 shows the experimental dependences of the relative transmission of an acousto-optic cell on the frequency of the acoustic signal for various durations of the controlling pulse. The curve *1* corresponds to a pulse duration of $60\ \mu s$, which is 4.5 times greater than L/v. Points corresponding to a pulse with duration $17\ \mu s$, which is 25% greater than L/v, fall on the same curve. The curves *2* and *3* refer to short controlling signal pulses. The width of the transmission band in these cases increases as $1/\tau$ in accordance with Fig. 3.

Figure 6 shows the measured experimental wings of the transmission bands, shown in the preceding figure. The curves *1* and *2* correspond to durations of 60 and $17\ \mu s$. The curve *1* is described well by a function described of the form sinc $(\Omega - \Omega_0/2\pi)$, whereas the side lobes of the second curve are somewhat lower than the preceding case. The curve *3* no longer contains side lobes, and it gives a rapid and smooth dropoff of the intensity. A similar curve is observed in all cases when $\tau < L/v$. These results agree completely with the theoretical calculations of the transmission curves which we presented previously in Ref. 6.
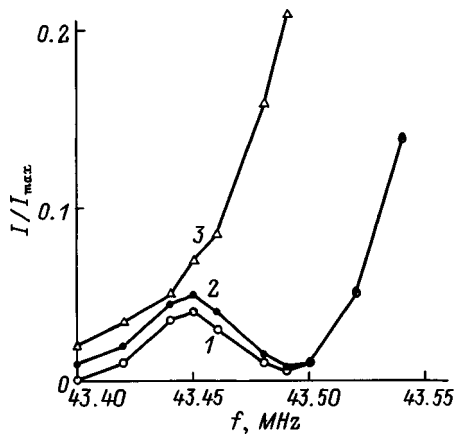
FIG. 6. Experimentally measured side wings of the transmission function for $\tau = l/v$, μs; *1* — 60, *2* — 17, *3* — 6.

FIG. 8. Theoretical curve of the relative light diffraction efficiency I/I_{max} of two successive sound trains versus the phase difference φ/π of the oscillations in these trains.

Figure 7 shows the theoretical dependence of the efficiency of diffraction of light by a sound train with duration l for the case where the amplitude of the acoustic wave is such that the light diffraction efficiency for a continuous train is close to the maximum level. For low efficiency this dependence is parabolic and then saturates. The crosses on the curve mark the experimentally obtained values of the diffraction efficiency for various pulse durations. Since the case of a weak acousto-optic interaction is realized in the experiment, the points fall well on the initial parabolic section of the curve. It follows from the figure that in order to maintain a constant diffraction efficiency as the pulse length decreases, the amplitude of the sound oscillations must be increased in proportion to $1/l^2$.

Figure 8 illustrates the efficiency of light diffraction by two successive trains versus the phase difference of the oscillations in these trains. The computed curve *1* corresponds to maximum efficiency not exceeding 20%. It is nearly sinusoidal, as follows from the theory for a weak acousto-optic interaction.[6] However, the form of the theoretical curve *2*, corresponding to a maximum efficiency of 50%, is strongly distorted compared with the preceding case. It contains a flat top due to nonlinear effects. The experimental cross marks, corresponding to a weak interaction, satisfactorily fall on the
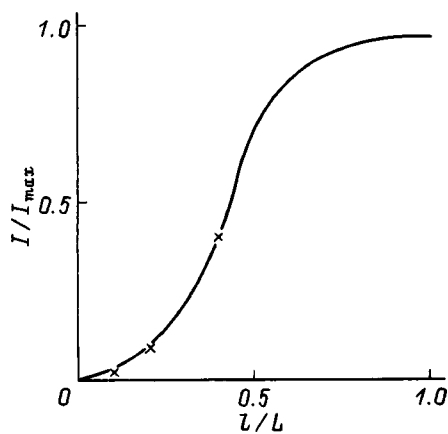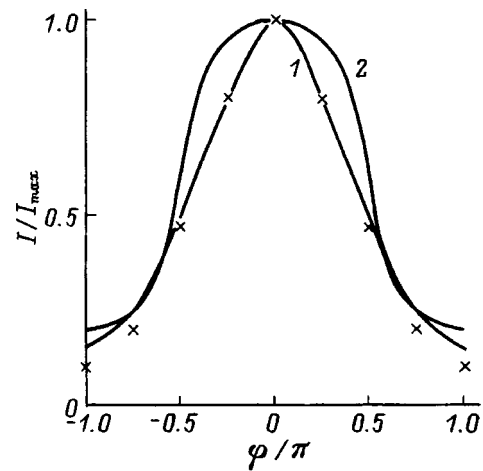
curve.[1] These points were measured by smoothly varying the carrying frequency, which is related linearly with the change in the phase difference between the pulses, while keeping distance between the trains constant.

5. CONCLUSIONS

As our investigations showed, the width and shape of the transmission function of a collinear acousto-optic filter can be controlled electronically over wide limits by using acoustic trains of finite length. The width of the frequency band of the acousto-optic cell can be increased smoothly more than tenfold by varying the duration of the acoustic train controlling the operation of the filter. Using trains with a smooth envelope decreases the level of the side lobes of the transmission function of the filter. The form of the transmission curve of the filter can be changed substantially and it can be made to be close to the form required for a given problem by adjusting the duration and form of the controlling pulse.

[1] L. N. Magdich and V. Ya. Molchanov, *Acousto-Optic Systems and Their Applications* (Sov. radio, Moscow, 1978).

[2] A. Harris, S. Nieh, and R. Fiegelson, Appl. Phys. Lett. **1**, 223 (1970).

[3] Xu Jieping and R. Stroud, *Acousto-Optic Devices* (Wiley, New York, 1992).

[4] A. Korpel, *Acousto-Optics* [M. Dekker, New York, 1988; Mir, Moscow, 1993].

[5] V. I. Balakshiĭ, V. N. Parygin, and L. E. Chirkov, *Physical Principals of Acousto-Optics* (Radio i svyaz', Moscow, 1985).

[6] V. N. Parygin and A. V. Vershubskiĭ, Vestn. MGU, Fiz. Astron. **39**(1), 28 (1998).

[7] V. N. Parygin, A. V. Vershubskiĭ, and Yu. G. Rezvov, Opt. Spektrosk. **84**, 1005 (1998) [Opt. Spectrosc. **84**, 911 (1998)].

[8] A. V. Vershubskiĭ and V. N. Parygin, Akust. Zh. **44**, 615 (1998).

[9] V. N. Parygin and A. V. Vershubskiĭ, Radiotekh Élektron **43**, No. 11 (1998).

[10] E. Dieulesaint and D. Royer, *Elastic Waves in Solids* [Wiley, New York, 1981; Nauka, Moscow, 1982].

FIG. 7. Theoretical curve of the relative light diffraction efficiency I/I_{max} versus the relative duration l/L of the sound train.

Translated by M. E. Alferieff

Bragg reflection during the propagation of magnetoelastic microwave pulses in a structure consisting of a ferrite thin film on a dielectric substrate

S. V. Meriakri

Institute of Radio Engineering, Russian Academy of Sciences, 141120 Fryazino, Moscow District, Russia
(Submitted April 7, 1997; resubmitted April 26, 1999)
Zh. Tekh. Fiz. **69**, 82–86 (December 1999)

The propagation of a microwave pulse in a ferrite thin film–substrate structure in a regime of re-reflections (''ringing'') of the acoustic component of the substrate is studied theoretically. It is shown that as a result of the interaction of microwave pulses with the boundaries of the substrate, propagation of a microwave excitation in this system can be regarded as a propagation of a wave packet in a periodic nonuniform medium. The basic characteristics of a propagating wave packet are obtained. © *1999 American Institute of Physics.*
[S1063-7842(99)01612-8]

The propagation of pulses of magnetoelastic waves (MEWs) is of interest, on the one hand, in connection with the study of the nature of magnetic waves and their interaction with acoustic waves in magnetic materials and, on the other, in connection with better understanding the pulsed propagation of microwave signals. An interesting object of investigation in this direction are pulses of fast magnetoelastic waves (MEWs).[1–4] Pulsed propagation of MEWs possesses a number of interesting features. For such waves the substrate is a dielectric waveguide where the purely elastic waves have a high dispersion and their phase velocity $v_P \gg v_S$ (v_S is the speed of sound in an infinite crystal). The velocity vector of fast elastic waves is almost perpendicular to the boundaries of the substrate, and they interact effectively with magnetostatic waves (MSWs), specifically, Damon–Eshbach waves. In Refs. 5 and 6 it was found experimentally that when a microwave pulse with duration τ_0 is applied to the entrance transducer, besides the transmitted signal, a series of delayed microwave pulses separated by the same delay times τ_d (''ringing'') was observed at the exit transducer. The first delayed pulse is separated from the initial pulse by the same time interval τ_d. The experiments were performed on structures consisting of a submicron yttrium iron garnet (YIG) film on a gallium–gadolinium garnet (GGG) substrate under conditions such that fast MEWs arise in the continuous regime. Investigation of the time delay showed that $\tau_d = 2\tilde{l}/v_S$, where $\tilde{l}$ is the substrate thickness, and studying a series of delayed pulses in a spectrum analyzer showed that their spectrum does not contain a series of frequencies corresponding to frequencies which are multiples of the frequencies of the Lamb modes of the substrate.[7] In Ref. 7 an approximate explanation was given for the suppression of frequencies which are multiples of the frequencies of the Lamb modes of the substrate on the basis of the spectral function of the magnetostatic echo, using the signal transfer coefficients which is not determined there.

In the present work a different method is proposed for describing the propagation of a microwave pulse with ''ringing.'' The method is based on an analogy between wave-guide propagation of pulses with reflections and the propagation of waves in periodic media. This analogy is due to the fact that when a microwave pulse interacts with the boundaries of a waveguide, a periodic temporal nonuniformity arises in the system. This makes it possible to obtain the basic characteristics of the propagating excitations by using the well-developed apparatus of wave propagation in periodic media for describing pulses in the ''ringing'' regime.

Let us examine the geometry of the problem. Let a film of thickness h lie in the half-space $y>0$ and the let the substrate lie in the half-space $y<0$. The external magnetic field $\mathbf{H}_0 \| 0z$ lies in the plane of the film and the microwave pulse propagates in the positive direction along the $\mathbf{0X}$ axis, perpendicular to the external magnetic field. A pulsed microwave signal

$$f(t) = \begin{cases} A_0 \cos \omega_0 t, & |t| \leqslant \dfrac{\tau_0}{2}, \\[2mm] 0, & |t| > \dfrac{\tau_0}{2}, \end{cases}$$

is excited in the structure. Here f is the amplitude of the excited signal and ω is its frequency. The amplitude f can be any of the components of the microwave fields (magnetic, electric, microwave current) depending on the method of excitation. The spectrum of this signal is

$$G(\omega) = \frac{1}{\sqrt{2\pi}} \int_{-\frac{\tau_2}{2}}^{\frac{\tau_0}{2}} A_0 e^{i\omega t} e^{i\omega_0 t} d\tau$$

$$= \frac{A_0}{\sqrt{2\pi}} \frac{\sin\left[(\omega - \omega_0)\dfrac{\tau_0}{2}\right]}{(\omega - \omega_0)\dfrac{\tau_0}{2}}. \tag{1}$$

The microwave magnetic fields of the pulse are found from the relation

$$\widetilde{\mathbf{H}}(\mathbf{r}, t) = \frac{1}{\sqrt{2\pi}} \int_{-\infty}^{\infty} \widetilde{\mathbf{H}}(\omega, \mathbf{r}) G(\omega) e^{i/\omega(\mathbf{q})^t} d\omega, \tag{1a}$$

where ω is the circular frequency; q is the wave number; $\tilde{\mathbf{H}}(\omega,\mathbf{r})$ are the Fourier components, at the point $\mathbf{r}$, of the microwave magnetic field of a pulse propagating in the ferrite; $\tilde{\mathbf{H}}(\omega,\mathbf{r})$ varies as the pulse propagates in the ferrite; the function $\tilde{\mathbf{H}}(\omega,\mathbf{r})$ will be determined below.

The system of equations for finding the microwave fields and the function $\omega(\mathbf{q})$ has the following form: a) in the ferrite

$$\frac{\partial \mathbf{M}}{\partial t} = -\gamma[\mathbf{M}\times\mathbf{H}_{\text{eff}}],$$

$$\mathbf{H}_{\text{eff}} = \mathbf{H}_0 + \mathbf{H}^{(m)} + b_{iklm}M_l u_{ik},$$

$$\operatorname{div}B = O; \quad \operatorname{curl}\mathbf{H}=0; \quad \mathbf{B}=\mathbf{H}+4\pi\mathbf{M},$$

$$\rho\ddot{u} = \frac{\partial}{\partial x_k}[c_{iklm}u_{lm}+b_{iklm}M_m M_l], \tag{2}$$

where H_{eff} is the effective internal magnetic field in the ferrite and is determined from the equation

$$\frac{\delta\mathcal{H}_{\text{eff}}}{\delta\mathbf{M}} = \mathbf{H}_{\text{eff}},$$

where $\mathcal{H}$ is the Hamiltonian of the system

$$\mathcal{H} = \int\left[\mathbf{M}\cdot\mathbf{H}_0 + \frac{(\mathbf{H}^{(m)})^2}{8\pi}+b_{iklm}M_l M_m u_{ik}+\frac{1}{2}\rho\dot{u}_i^2\right.$$
$$\left.+\frac{1}{2}c_{iklm}u_{ik}u_{lm}\right]dv$$

(the exchange interaction and anisotropy are immaterial in the present case and will not be considered); b) in vacuum

$$\operatorname{curl}\mathbf{H}=0, \quad \operatorname{div}\mathbf{H}=0, \tag{3}$$

where M is the magnetic moment vector of the ferrite, $H^{(m)}$ is the demagnetization field, b_{iklm} is the magnetoelastic constants tensor of the ferrite, u_{ik} is the deformation tensor, c_{iklm} is the elastic moduli tensor, u_i are the components of the displacement vector, $\gamma = 2.83$ MHz/Oe, and ρ is the density; c) in the substrate at time $t: (n-1)\tau_1 < t < (\tau_1-\tau_0)n$, $n=1,2,3,...;$ $\tau_0 = \tau_d/2$, the equation has the form

$$\rho\ddot{u}_i = \frac{\partial}{\partial x_k}c_{iklm}u_{lm}, \tag{4}$$

where at time $t: (\tau_1-\tau_0)n < t < n\tau_1$, the microwave pulse reaches the boundary of the substrate and interacts with it.

As a result of this interaction the velocity v_y in the direction of the y coordinate changes sign, i.e., the pulse is reflected from the boundary, acquiring a specific force impulse ΔF as a result of colliding with the boundary

$$\Delta F = \rho v_{\text{up}} = \rho v_{\text{down}} \approx 2\rho\dot{u},$$

v_{up} and v_{down} are the velocities of sound of the microwave pulse propagating in the positive and negative directions of the $0Y$ axis, respectively. Here the fact that $v_x \ll v_y$ for the fast magnetoelastic waves under study is taken into account.[1–5]

In summary, every time a microwave pulse approaches a boundary and interacts with it, the pulse experiences a force

that reverses its direction of propagation. The boundary itself becomes deformed locally during the interaction with the microwave pulse. Thus, the equation of motion in the substrate at time $t: (\tau_1-\tau_0)n < t < n\tau_1$ assumes the form

$$\rho\ddot{u}_i = \frac{\partial}{\partial x_k}[c_{iklm}u_{lm}] + \frac{2\rho\dot{u}_i}{\tau_0}. \tag{5}$$

It should be noted that in a ferrite film there is no need to take account of the interaction of the pulse with the film boundaries, since the travel time of both acoustic and magnetostatic waves over the thickness of the film and back $\tau_{pl} \ll \tau_0$, as a result of which a quasicontinuous wave propagation regime is realized in the film.[8] The components of the microwave fields of the system under study have been found in Refs. 4 and 5, where it was established that in the case under study a Lamb wave with a high mode number m ($m \approx 1000$), which has only one component u_z of the displacement vector, propagates in the substrate.

It follows from Eqs. (4) and (5) that in this situation the substrate can be treated as a medium with periodically time-varying coefficients. Since pulses move almost uniformly, with the exception of the moments when the collide with the substrate boundaries, and the collision time can be neglected, the temporal periodicity can be replaced by a spatial periodicity. Since an acoustic wave moves almost perpendicular to the substrate boundaries ($v_x \ll v_y$), neglecting the small displacement along the $0X$ axis, we shall assume that $y \approx v_s t$. Under these assumptions, from Eqs. (4) and (5) follows

$$\rho\frac{\partial^2 u_z}{\partial t^2} = c_{44}\nabla^2 u_z + \frac{2\rho}{\tau_0}\frac{\partial u_z}{\partial t}\Pi(y), \tag{6}$$

where

$$\Pi(y)=\begin{cases} 0, & n\tilde{l}<y<(n+1)\tilde{l}-v_S\tilde{l}, \\ -1, & (2n+1)\tilde{l}-v_S\tau_0<y<(2n+1)\tilde{l}, \\ 1, & (2n+1)\tilde{l}-v_S\tau_0<y<2\tilde{l}. \end{cases}$$

In summary, the substrate is replaced by an effective semi-infinite medium with periodically varying properties where an acoustic pulse propagates rectilinearly. It should be noted that this periodicity takes account of the conditions of reflection of a pulse from the substrate boundaries.

We seek the solution of Eq. (6) by the standard procedure of wave propagation in a periodic medium.[9] Substituting $u_z \sim u_z(x,y)e^{i\omega t}$ into Eq. (6) we have

$$\left[\frac{\rho\omega^2}{c_{44}}\left[1+\frac{2}{\omega\tau_0}\Pi(y)\right]+\nabla^2_{x,y}\right]u_z(x,y)=0. \tag{7}$$

The equation (7) is a differential equation with periodically varying coefficients. The normal modes of the undisturbed medium (without the term $\Pi(y)$) are known. We write them in the form

$$u_z(x,y) = u_{z,m}(x)e^{i(\beta_m y-\omega t)},$$

where $u_{z,m}$ are the normal modes of the unperturbed medium:[8] $u_{z,m}(x)\sim u_m e^{iqx}$.

Being normal modes, they satisfy the equation

$$\left(\frac{\rho\omega^2}{c_{44}}+\nabla_x^2-\beta_m^2\right)u_{z,m}=\left(\frac{\rho\omega^2}{c_4}-q_m^2-\beta_m^2\right)u_{z,m}=0. \quad (8)$$

Hence, since $v_x\ll v_y$, we have

$$\frac{\rho\omega^2}{c_{44}}=\beta_m^2(1+\xi_m^2),$$

$$\xi_m=\frac{q_m}{\beta_m}\ll1,$$

$$u_{z,m}=u_{ml}\exp[i(q_mx-\beta_my-\omega t)], \quad (8a)$$

and u_z is found from the normalization conditions taking account of the following considerations.

Let an arbitrary field with frequency ω be excited at $Y=0$. Then the field propagating in the understood medium can be represented as a linear combination of normal modes

$$u_z=\sum A_mu_m(x)e^{i(\beta_my-\omega t)}. \quad (9)$$

We choose the normalization as follows:

$$\int u_{zk}^*(x)u_{zl}(x)dx=\frac{2\rho}{c_{44}}\frac{\omega}{|\beta_k|}\delta_{kl}. \quad (9a)$$

The normalization is chosen so that a unit energy flux of the microwave pulse would flow per unit time through unit surface area. We shall seek the solution of the equations for a medium with periodically varying perturbations $u_z^{(b)}$ similarly to Ref. 9 by the method of variation of constants or coupled modes. For this, we assume the coefficients A_m in Eq. (9) to be y dependent. Substituting expression (9) with $A_m(y)$ into the equation of motion (7) and using Eq. (8) we obtain

$$\left[\sum\frac{d^2}{dy^2}A_k-2i\beta_k\frac{d}{dy}A_k\right]u_{zk}^{(b)}(x)e^{i\beta_ky}$$
$$=\frac{\rho\omega^2}{c_{44}}\frac{1}{\omega\tau_0}\left[\sum\Pi(y)A_lu_{zl}e^{i\beta_ly}\right]. \quad (10)$$

For $(\tilde{\omega}\tau_0)^{-1}\ll1$ the disturbance of the acoustic system will be small. Then the mode amplitudes A_k vary much more slowly than the exponential factors $e^{i\beta_ky}$, since the exponential factor corresponds to wave propagation of a pulse, and dA_k/dy corresponds to a periodic disturbance of the propagating pulse, so that $d^2A_k/dy^2\ll\beta_k(dA_k/dy)$. With these approximations we obtain the equations for coupled modes

$$\frac{d}{dy}A_k(y)-i\frac{\beta_k}{|\beta_k|}\sum_l\sum_m c_{kl}^{(m)}A_l$$
$$\times\exp\left[i\left(\beta_l-\beta_m-m\frac{\pi}{2}\right)y\right], \quad (10a)$$

$$c_{kl}^{(m)}=\frac{1}{4\pi\tau_0}\langle k|\Pi_m|l\rangle=\frac{\omega}{4}\int u_{zk}^*(x)\Pi_mu_{zl}(x)dx,$$

$$\Pi(y)=\sum_{m\neq0}\Pi_me^{im\frac{2\pi}{2l}y}. \quad (11)$$

The derivation of Eq. (10) took account of the normalization condition (9a), the orthogonality of the normal

modes, and the periodicity of the small perturbation of the wave propagation equations (7) and (10). Here Π_m are the Fourier coefficients for in Fourier series expansion of the function $\Pi(y)$. Resonance coupling of the modes occurs when

$$\beta_k-\beta_l=m\frac{2\pi}{\Lambda}. \quad (12)$$

In Eq. (10) the coupling between two modes for which the condition (12), where $\Lambda=2\tilde{l}$, holds plays the main role. Denoting these two main modes by the indices 1 and 2, we write the basic equations for the coupled modes as

$$\frac{d}{dy}A_1=-i\varkappa A_2e^{i\Delta\beta y},$$

$$\frac{d}{dy}A_2=-i\varkappa^*A_1e^{-i\Delta\beta y};$$

$$\Delta\beta=\beta_1-\beta_2-m\frac{2\pi}{\Lambda};\quad m=0,1,2;$$

$$\varkappa=c_{12}^{(m)}=c_{21}^{(-m)*}. \quad (13)$$

In the case at hand, a pulsed excitation propagates in the positive direction along the **0X** axis and a reflected wave propagating in the negative direction along the **0X** axis arises as a result of reflection from the periodic grating. Thus, it is necessary to examine the coupling between the waves propagating in opposite directions. In this case

$$\frac{\beta_1}{|\beta_1|}=1;\quad\frac{\beta_2}{|\beta_2|}=-1. \quad (13a)$$

To solve Eq. (13) for two waves propagating in opposite directions it is necessary to find $\varkappa=c_{12}^{(m)}$ and the Fourier expansion of $\Pi(y)$. Expanding $\Pi(y)$ in a Fourier series we obtain

$$\Pi(y)=\sum_{-\infty}^{\infty}\frac{i}{\pi m'}\left[\exp\left(i|m'|\frac{\pi a}{a+b}\right)+1\right]$$
$$\times\exp\left(im'\frac{\pi}{a+b}y\right);$$

$$m'=2k'+1,\quad a=l-v_S\tau_0,\quad b=v_s\tau_0, \quad (14)$$

With these relations and formula (10) we obtain an expression for $c_{kl}^{m'}$

$$c_{kl}^{(m')}=\frac{1}{4\pi\tau_0m'}\left[\exp\left(im'\frac{\pi a}{a+b}\right)+1\right]\frac{\rho}{c_{44}}\frac{2\omega}{\sqrt{|\beta_k||\beta_l|}}.$$

In the case at hand

$$\beta_1=\omega\sqrt{\frac{\rho}{c_{44}}}\left(1-\frac{\xi_1^2}{2}\right),$$

$$\varkappa=\sqrt{\frac{\rho}{c_{44}}}\left(1-\frac{\xi_1^2}{2}\right)\frac{1}{2\tau_0\pi m'}\left[\exp\left(i\frac{\pi m'a}{a+b}\right)+1\right],$$

$$|\varkappa| = \frac{\sqrt{1 + \cos\left|\dfrac{\pi m' a}{a+b}\right|}\left(1 + \dfrac{\xi_1^2}{2}\right)}{\sqrt{2}\,\pi m'\, v_S \tau_0}$$

$$= \frac{\sqrt{1 + \cos\dfrac{\pi m'(\tau_1 - \tau_0)}{\tau_1}}}{\sqrt{2}\,\pi m'\, v_S \tau_0}\left(1 + \frac{\xi_1^2}{2}\right).$$

Here $a + b = v_S \tau_1$ and $a = v_S(\tau_1 - \tau_0)$ were taken into account. The resonance coupling condition (12) is insufficient for strong coupling to occur between the two modes under study. The coupling condition for the dynamic coefficient must also be satisfied. Thus, for $\tau_0/\tau_1 \ll 1$, $m' = 0.2$ $(2n)$ the coefficient $\varkappa \approx 0$, and for other ratios τ_0/τ_1, such that $\pi m'(\tau_1 - \tau_0)/\tau_1 = \pi(2k'+1)$, there will be no coupling between the modes. However, there always exists a value of m for which $\varkappa \neq 0$. Let A_1 be the amplitude of the incident wave and A_2 the amplitude of the reflected wave. The initial conditions for the amplitudes are $A_1|_{\mathbf{r=0}} = 1$ and $A_2|_{\mathbf{r=2}} = 0$. Here L is the distance between the entrance and exit microwave signal transducers. Then we obtain from Eq. (13)

$$A_1(y) = \frac{e^{i\Delta\beta y/2}\left[s \cosh[s(L_y - y)] + i\dfrac{\Delta\beta}{2}\sinh[s(L_y - y)]\right]}{s \cosh(sL_y) + i\dfrac{\Delta\beta}{2}\sinh(sL_y)},$$

$$A_2(y) = e^{i\Delta\beta y/2}\frac{[-i\varkappa^* \sinh[s(L_y - y)]]}{s \cosh(sL_y) + i\dfrac{\Delta\beta}{2}\sinh(sL_y)}. \tag{15}$$

Here L_y is the projection of the distance on the $0Y$ axis in a coordinate system corresponding to a space with periodically varying coefficients that replaces the substrate $L_y^2 + L_x^2 = L_\Sigma^2 = L^2 \approx (2n\tilde{l})^2$, $n = 1,2,\ldots$, where L_Σ is the total path traversed after all reflections taking account of $L_x \ll L_y$, $L_y \approx 2n\tilde{l}$;

$$s^2 = \varkappa\varkappa^* - \left(\frac{\Delta\beta}{2}\right)^2; \quad \Delta\beta = \frac{2}{v_S}(1 - \xi_1^2)(\omega - \omega_n);$$

$$\omega_n = \frac{2\pi v_S}{(a+b)}2n,$$

where ω is the frequency corresponding to an even Lamb mode of the substrate.

The reflection coefficient R_n of the harmonics is determined by the expression

$$R_n = \frac{\varkappa\varkappa^* \sinh^2(sL_y)}{s^2 \cosh^2(sL_y) + \left(\dfrac{\Delta\beta}{2}\right)^2 \sinh^2(sL_y)} \tag{16}$$

and reaches its maximum value for with $\Delta\beta = 0$

$$R_{\max} = \tanh(|\varkappa|L_y),$$

$$R_{\max} \to 1 \quad \text{as} \quad |\varkappa|L_y \to \infty.$$

The reflection coefficient is an even function of $\Delta\beta$. The spectrum consists of a main peak with a distinct maximum and several side reflection peaks. We determined the width of the main peak from the condition that the reflection coefficient is maximum with the maximum deviation of $\Delta\beta$ from zero.

The maximum reflection coefficient R_0 for $|\Delta\beta| > 0$ is

$$R_0 \approx \frac{\varkappa\varkappa^* L_y^2}{1 + \varkappa\varkappa^* L_y^2}; \quad R_0 \to 1 \quad \text{as} \quad |\varkappa|L_y \to \infty.$$

This corresponds to $\Delta S = 0$. Hence we find the width of the main peak

$$\Delta\beta = 4|\varkappa|$$

or

$$\Delta\omega = \frac{\sqrt{2}}{\pi\tau_0}\left[\cos\frac{\pi(\tau_0 - \tau_1)}{\tau_1} + 1\right]\left[1 + \frac{3}{2}\xi_1^2\right]. \tag{16a}$$

The relative width of the nontransmission band is

$$\frac{\Delta\omega}{\omega} = \frac{\sqrt{2}}{\pi\omega}\frac{\cos\left[\dfrac{\pi(\tau_0 - \tau_1)}{\tau_1}\right]}{\tau_0}\left(1 + \frac{3}{2}\xi_1^2\right).$$

The side peaks occur if

$$sL_y = i\left(m + \frac{1}{2}\right)\pi;$$

$$\Delta\beta = \pm 2\left[|\varkappa|^2 + \left(m + \frac{1}{2}\right)\frac{\pi^2}{L_y^2}\right]^{1/2}. \tag{17}$$

The reflection coefficient R_b in them is

$$R_b = \frac{|\varkappa|^2 L_y^2}{\left(m + \dfrac{1}{2}\right)^2 \pi^2 + (\varkappa L_y)^2}. \tag{17a}$$

These reflection maxima become substantial for $|\varkappa L_y| > \pi/2$. In general, it is evident from Eqs. (16) and (17) that reflection in the side peaks is much weaker than reflection in the main peak, and the reflection decreases as the reflection number m increases. For

$$\Delta\beta = \pm\left[2\varkappa\varkappa^* + 2\left(\frac{l'\pi}{L_y}\right)^2\right]^{1/2}; \quad l' = 1,2$$

the reflection coefficient vanishes. For sufficiently large values of $s(L_y - y)$ the energy $E_1 \sim A_1^2$ of the incident mode decreases exponentially as the wave propagates, i.e., with increasing y. This phenomenon is due to not absorption but rather reflection of energy into the reflected mode, corresponding to amplitude A_2, i.e., in terms of the present model, for a pulse propagating in a nonuniform medium the individual Fourier components of the pulse are reflected from nonuniformities, as a result of which energy often moves in the opposite direction. The law of conservation of energy in this case will have the form

$$\frac{d}{d_y}\{|A_1|^2 - |A_2|^2\} = 0.$$

The fraction ΔE of the energy that will be reflected in the opposite direction during the propagation of the pulse in the forward direction is

$$\Delta E = \frac{|\varkappa|^2 \sinh^2(sL_y)}{s^2 \cosh^2(sL_y) + \left(\frac{\Delta\beta}{2}\right)^2 \sinh^2(sL_y)}, \tag{18}$$

where ΔE decreases with increasing $\Delta\beta$ and reaches its maximum value for $\Delta\beta = 0$, $L_y \rightarrow \infty$. Substituting expression (15) into Eq. (9), we obtain the component u_z of the displacement vector for a microwave pulse

$$u_z(x,y,\omega) = \sum A_n(y) u_m(x) e^{i(\beta_m y - \omega t)}$$

$$\approx A_1 u_1 \exp[i(\beta_1 y + qx - \omega t)] + A_2 u_2$$

$$\times \exp\left[i\left(\beta_1 y - \Delta\beta - m\frac{2\pi}{\Lambda} - q_1 x - \omega t\right)\right], \tag{19}$$

$$u_z(x,y,t) = \frac{1}{\sqrt{2\pi}} \int_{-\infty}^{\infty} u_z(x,y,\omega) G(\omega) e^{i\omega t} d\omega. \tag{20}$$

Similarly, using Eq. (2), and taking account of Eqs. (19), (15), and (9), we find the remaining microwave coefficients $\tilde{\mathbf{H}}(\omega,\mathbf{r})$. The propagation constant $\tilde{\varkappa}$ along the $0Y$ axis will have the form

$$\tilde{\varkappa} = \Delta\beta \pm is = \frac{\pi m}{\Lambda} \pm i\sqrt{\varkappa\varkappa^* - \left(\frac{\Delta\beta}{2}\right)^2}. \tag{21}$$

In the frequency range where $|\Delta\beta| < 2\tilde{\varkappa}|\varkappa|$ has an imaginary part, it corresponds to a ''forbidden band,'' where the forward wave decays. It is evident from Eq. (21) that the maximum value of the imaginary part of $\tilde{\varkappa}$ is equal to the coupling coefficient, i.e., the higher the dynamical coupling coefficient, the more strongly the forward wave decays in the reflection zones.

The displacement vector, and all other components of a microwave pulse propagating with reflections in a waveguide, will contain two components corresponding to two coupled modes. The first component propagates in the direction of the exit transducer and the second in the direction of the entrance transducer. At the exit transducer, the spectrum of the output signal (1), in which regions of signal transmission will be observed near the frequencies ω_n, will be ob-served in the spectrum. The width of these regions will be determined by Eq. (16a). It should be noted that for each ω_n there will be main nontransmission regions $\beta_1 - \beta_2 = 0$ and side nontransmission regions $\beta_1 - \beta_2 = (m\pi)/\Lambda$. However, the main nontransmission regions for other frequencies $\omega_n + k$ will merge with the side nontransmission regions for ω_n. A small decrease in the intensity of harmonics will be observed for frequencies at which side maxima of the reflection coefficient (17), which depend on L_y, will appear. However, these phenomena will play a negligible role, especially for cases of many reflections and when $\tau_0/\tau_1 < 1$. Transmission peaks will arise on the entrance transducer at frequencies corresponding to regions of nontransmission of a microwave signal.

In summary, in this work the propagation of a magnetoelastic pulse, propagating in a waveguide regime with reflections from the waveguide walls, was studied. It was established that part of the energy of a microwave pulse propagates in the direction of propagation and part propagates in the opposite direction as a result of Bragg reflection from a periodic nonuniformity, which could be the boundaries of the waveguide for the microwave pulse. Expressions were obtained for the amplitudes and the propagation constants of the waves moving forward and backward. The frequency ranges where there are nontransmission regions for the forward wave were found.

The complete picture of propagation of a microwave pulse in a waveguide in the presence of a large number of reflections can be obtained by the method of coupled waves.

[1] H. Mathews and H. van de Vaart, Appl. Phys. Lett. **15**, 373 (1969).
[2] J. P. Parekh, Electron. Lett. **6**(14), 430 (1970).
[3] A. S. Bugaev, Yu. A. Gulyaev, P. E. Zil'berman, and Yu. A. Filimonov, Fiz. Tverd. Tela (Leningrad) **23**(9), 2647 (1981) [Sov. Phys. Solid State **23**, 1552 (1981)].
[4] Yu. A. Filimonov, Candidate's Dissertation [in Russian], Moscow (1982), 168 pp.
[5] A. S. Andreev, P. E. Zil'berman, and V. B. Kravchenko, Radiotekh. Élektron. (Moscow) **30**(9), 1992 (1985).
[6] Yu. F. Ogrin and F. Yu. Ogrin, Pis'ma Zh. Tekh. Fiz. **19**(13), 65 (1993) [Tech. Phys. Lett. **19**(7), 425 (1993)].
[7] Yu. V. Gulyaev, Yu. F. Ogrin, and N. I. Polzikova, Dokl. Akad. Nauk SSSR **345**(1), 46 (1995) [Sov. Phys. Dokl. **40**, 582 (1995)].
[8] S. V. Meriakri, Radiotekh. Élektron. (Moscow) **42**(6), 668 (1997).
[9] A. Yariv and P. Yeh, *Optical Waves in Crystals: Propagation and Control of Laser Radiation* [Wiley, New York (1984); Mir, Moscow (1987), 616 pp.].

Translated by M. E. Alferieff

Heteroepitaxial growth of complex-oxide films from a self-organized system formed in a gas-discharge plasma

V. M. Mukhortov, Yu. I. Golovko, G. N. Tolmachev, and A. I. Mashchenko

Institute of General Physics, Russian Academy of Sciences, 117333 Moscow, Russia
(Submitted April 29, 1998; resubmitted October 1, 1998)
Zh. Tekh. Fiz. **69**, 87–91 (December 1999)

New experimental data on the characteristic features of the synthesis and crystallization of films of solid solutions of lead zirconate-titanate, deposited by means of rf diode sputtering of ceramic targets, are presented. Such a deposition system possesses threshold states, transition through which leads to a qualitative change in the processes occurring in the system and to the appearance of self-organization effects. The basic feature of this change is determined by the appearance of a new structured system, consisting of the sputtered particles and particles formed in the plasma, in the plasma of an rf discharge. © *1999 American Institute of Physics.* [S1063-7842(99)01712-2]

INTRODUCTION

Thin films of solid solutions of the lead zirconate–titanate (PZT) system have been attracting investigators for many years. This interest is due to the possibilities of producing fundamentally new devices for microelectronics on the basis of such solid solutions[1,2] and to the study the mechanisms of synthesis and crystallization of complex substances in a thin-film state. This compound, which is relatively simple with respect to composition and structure (perovskite type), contains two volatile components: lead and oxygen. The structure of PZT films is very sensitive to the deposition conditions and, irrespective of the preparation method, the films are virtually always multiphase,[3,4] as a result of which the electrophysical properties of films are degraded compared with bulk samples.

The system for obtaining films in a gas-discharge plasma is spatially limited by the target and substrate surfaces, while the lateral boundaries are set by the conditions for contraction of the discharge on account of the volume loss of electrons in the electronegative gas. Matter in the form of sputtered particles (atoms, ions, molecular complexes, clusters, and so on) and the energy of beam and slow electrons are constantly being transported through this system. Because of the high chemical activity and high density of the sputtered particles, spatial structuring of the deposition system occurs. This structuring is manifested in the appearance of characteristic zones which are characteristic of self-organized systems.[5]

CHOICE OF PARAMETERS DESCRIBING THE FUNCTIONING OF FILM-DEPOSITION SYSTEMS

In the present work the rf sputtering of polycrystalline stoichiometric lead zirconate titanate $PbTi_{0.44}Zr_{0.56}O_3$ targets in pure oxygen was used. We described the construction of the sputtering unit and the experimental apparatus in a previous work.[6]

We chose three types of parameters to describe the functioning of the film-deposition system: external parameters, describing the rf discharge; internal parameters, determining the transport mechanism and type of particles; and, target parameters, characterizing the final result of the operation of the entire film-deposition system and thereby determining the ranges of the internal and external parameters.

The discharge current, the incident and reflected powers, the voltage on the target, the substrate temperature, and the working-gas pressure were used as external parameters. The internal parameters were the electron density in the discharge and the spatial distribution of the intensity of the emission lines of the sputtered atoms and ions, which were determined by the methods of Refs. 6 and 7.

The characteristics of the structural perfection of the films obtained were chosen as the target parameters: the type of structure, the phase composition, the unit-cell parameters, the orientational relations between the crystallographic directions of the film and substrate, the angles of vertical (in the direction of the normal to the substrate plane) and azimuthal (in the substrate plane) disorientation of the crystallites in the film, the size of the regions of coherent scattering, and the magnitude of microdeformations. These characteristics were determined by x-ray diffraction analysis of the films in a DRON-4 diffractometer ($CuK\alpha$, β filter).

VARIABILITY OF EXTERNAL AND INTERNAL PARAMETERS ACCOMPANYING A PHASE TRANSITION OF THE TARGET PARAMETERS

Before examining the behavior of the external parameters, it should be noted that a certain ambiguity arises in measurements of the external parameters in rf sputtering systems. This is due to the presence of a bias current in parasitic capacitances and inductances in the sputtering unit and in the circuits for measuring the external parameters. In addition, in the near-electrode region of the discharge there is a capacitance due to the space charge with a nonlinear dependence on the gas pressure, the power introduced, the concentration and elemental composition of the sputtered components, and other parameters. It is impossible to take account of or com-
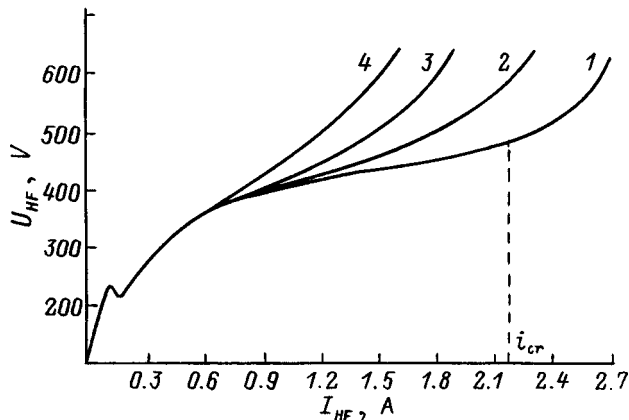
FIG. 1. Current–voltage characteristics of an HF discharge. The target–substrate distance is 8 mm. Oxygen pressure, Torr: *1* — 1.8, *2* — 0.7, *3* — 0.5, *4* — 0.3.

FIG. 2. Spatial distribution of the radiation intensity of the emission lines: *1* — Zr* ($\lambda = 3791$ Å), *2* — Pb* ($\lambda = 3639$ Å), *3* — O* ($\lambda = 3947$ Å), *4* — O^+ ($\lambda = 4414$ Å); $I_{HF} = 2.3$ A, $T_n = 550$ °C, I–III — discharge zones.

pensate for these capacitances and inductances in real sputtering systems. For this reason, the magnitudes of the measured currents and voltages, which fix the operation of the sputtering system, are only qualitative.

Depending on the state of the deposition system, PZT films differing by type of structure can be obtained: amorphous, films with pyrochlore structure, and polycrystalline and heteroepitaxial films with perovskite structure. The transition from one type of structure to another in the target parameters space corresponds to a phase transition.

Figure 1 shows a typical current–voltage characteristics of the sputtering system for various working-gas pressures. For 1.8 torr pressure, the threshold value of the current at which PZT film growth occurs in a perovskite structure is noted in this figure. It is evident from the dependence presented that the threshold current lies on the monotonic section of the current-voltage characteristic. Previously,[8] it was established that for every complex oxide there exists a unique critical oxygen pressure P_O at which the deposition of films with stoichiometric composition and prescribed structure similar to that of the target material becomes possible. For example, for $(Ba,Sr)TiO_3$ with deposition in a perovskite structure this pressure is greater than 0.3 Torr, and pressures $P_O > 0.7$ Torr are required for Y–Ba–Cu–O with deposition in an orthorhombic phase (a tetragonal phase–orthorhombic phase transition occurs in the target parameters). For PZT films the threshold oxygen pressure is greater than 1.7 Torr. We note that threshold pressure is a necessary but not sufficient condition for ensuring synthesis and crystallization of the initial phase during film growth.

In our view, the external parameters do not reflect the characteristic features of the functioning of the deposition system. This is why it is necessary to switch to internal parameters to analyze the operation of such systems. One of these parameters could be the electron density (n_e) in the discharge. The deposition of complex oxides $BaTiO_3$, $(Ba,Sr)TiO_3$ and Y–Ba–Cu–O[9,10] has shown that there exists a threshold value $n_e > 10^{12}$ cm^{-3}, above which during film growth the oxidation process predominates over the reduction process. This has also been confirmed in the dep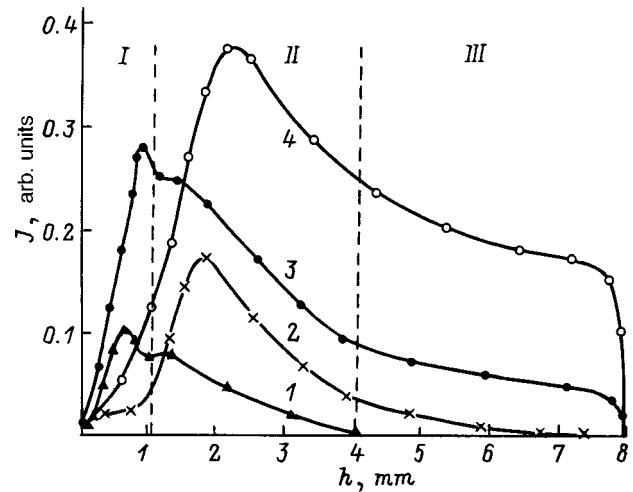osition of films of the PZT system. While performing measurements of the n_e distribution across the discharge, we found that contraction of the discharge is observed at oxygen pressures above 0.3 Torr. This is manifested as a sharp decrease of n_e at a distance equal to the target radius in the entire region of the negative emission of the discharge.

The spatial distribution of the intensity of the emission lines of sputtered atoms and ions was chosen as the second internal parameter. Figure 2 shows the characteristic distribution of the intensity of the emission lines at oxygen pressure 1.7 Torr. It is evident that the cathode–substrate space can be divided into three characteristic zones. The intensity of the lines in the first zone is determined by the completeness of the sputtering of the target surface.[8] The type of particles entering the gas medium can be judged according to the presence of emission lines of the sputtered material in this zone. Specifically, the oxygen component of the oxide sputters in the form of a neutral excited atom with excitation potential $\leqslant 12.7$ eV. Zirconium enters the gas medium as an ion and an excited atom, whereas lead enters only in an unexcited, atomic state. No titanium lines were observed in the discharge. However, titanium lines were clearly detected when a titanium target was sputtered in pure argon. The addition of several percent of oxygen to argon caused the titanium lines to vanish. The second zone of the discharge partially reflects the influence of the plasma mechanism of excitation of atoms and ions. In this zone the dominant process leading to the excitation of atoms and ions is inelastic impact by beam electrons entering from the cathode region. The third zone of the discharge reflects the characteristic features of the transport of the sputtered particles through the plasma of an rf discharge.

The spatial distribution of the intensity of the emission lines accompanying a change in the conditions of film deposition near a phase transition of the target parameters was investigated. As an example, the behavior of only the emission line $\lambda = 3639$ Å of lead at various substrate temperatures (T_n) ranging from 400 to 595 °C is shown in Fig. 3. The other components of the complex oxide did not show a
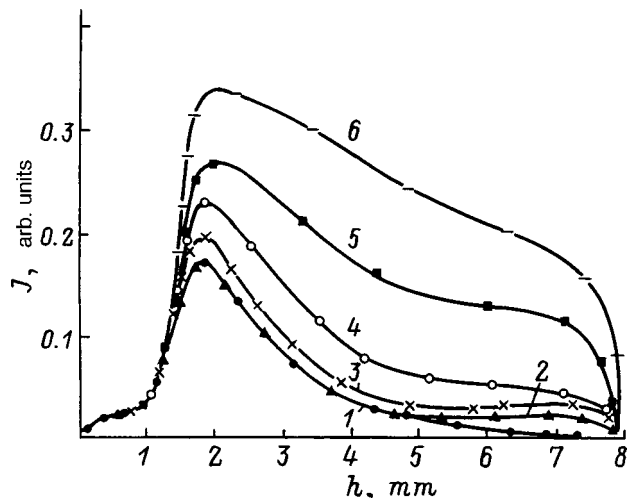
FIG. 3. Variation of the spatial distribution of the radiation in the emission lines of lead as a function of substrate temperature. T_n, °C: *1* — 560, *2* — 570, *3* — 575, *4* — 585, *5* — 590, *6* — 595; P_{O_2} = 1.8 Torr, I_{HF} = 2.4 A.

temperature dependence. At substrate temperatures from 400 to 500 °C the spatial distribution of the radiation of lead atoms did not change and corresponded to curve *1*. Growth of heteroepitaxial PZT films with perovskite structure was observed for intensities bounded by the curves *4* and *6*. The films were multiphase and possessed the following orientation relative to the substrate directions: the *c* (or *a*) axis of the tetragonal unit cell of the film was oriented perpendicular to the substrate surface, i.e., parallel to [001] MgO, and the two other axes of the tetragonal cell were oriented parallel to the [100] or [010] MgO directions. The vertical disorientation angle did not exceed 0.5°, and the azimuthal disorientation angle was less than 3°. The coherent scattering regions were greater than 1000 Å in size, and the microdeformations were less than 10^{-4}. The phase space bounded by the curves *2* and *4* (Fig. 3) corresponded to polycrystalline films with perovskite structure with an admixture of the pyrochlore phase. The structural perfection of the heteroepitaxial films of the pyrochlore phase with deposition under the conditions bounded by the curves *1* and *2* is quite high (the microdeformations are less than 5×10^{-3}).

Figure 4 shows the spatial variation of the intensity of the lead line for various target–substrate distances (curves *1–4* are for growth conditions of the pyrochlore phase, curves *5–9* are for the perovskite phase). It is evident from the curves presented that under the perovskite growth conditions with target–substrate distances ranging from 8 to 15 mm the lead line in the third zone of the discharge remains constant. The heteroepitaxial films obtained in this range of distances were virtually identical from the standpoint of structural perfection. Below the critical temperature the line "drops to zero" at the location of the substrate, irrespective of its position. The films deposited at these temperatures possessed pyrochlore structure.

CHARACTERISTIC FEATURES OF THE NEW SPATIAL STRUCTURE FORMED IN AN RF DISCHARGE

We shall now discuss certain experimental factors obtained in the course of this work. First, the emission lines of
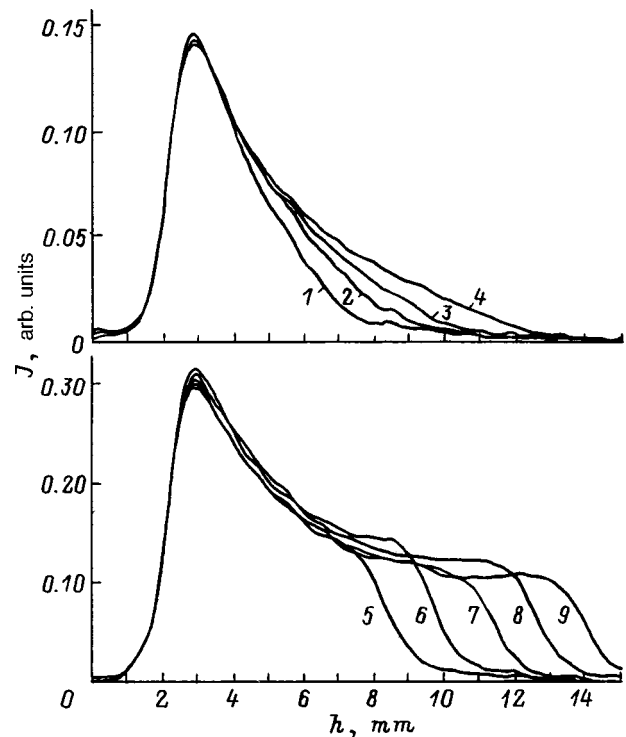

FIG. 4. Spatial distribution of the radiation of the emission lines of lead versus the target–substrate distance. P_{O_2} = 1.8 torr, I_{HF} = 2.4 A.

titanium are absent in the discharge in the entire interval from the target to the substrate. A characteristic feature of the negative emission of the gas discharge is the presence of beam electrons there with energies close to the cathode voltage drop.[11] For this reason, the excitation of atoms and ions by electron impact dominate here. If titanium atoms or simple molecular compounds based on titanium had been present in the gas, then we would have definitely observed their emission. Since the stoichiometry with respect to the metallic components is preserved in the condensate, it can be inferred that this component is in a bound state in a level higher than the molecular compound, i.e., as a minimum in a cluster. For such particles the beam-electron energies are inadequate to cause them to dissociate.

The second feature is the "dropping to zero" of the emission lines of the sputtered atoms at the location of the substrate irrespective of is position relative to the target (Fig. 4). In addition, this effect is observed only at pressures of the active gas above a threshold value. For atoms and ions of the main gas (oxygen) this effect is absent, which corresponds to the behavior of a gas-discharge plasma in the region of negative emission.

The third feature is the influence of the substrate temperature, beginning with a certain threshold value, on the spatial distribution of the intensity of the emission lines of the sputtered atoms.

Finally, the fourth feature is the intensity degeneracy of the lines of the lead atoms and the line of atomic oxygen relative to the spatial coordinate. The dissipation of the electron energy in negative emission is exponential (as is evident from the behavior of the ionic lines of oxygen) exponentially. Therefore the intensities of other spectral lines should

behave similarly. But, it is evident from Fig. 4 that starting at a certain distance from the target surface the intensity of the emission of the volatile component does not change. Moreover, the maxima of the radiation of the emission lines with the lower excitation potential lie closer to the cathode, which contradicts the well-known experimental data.[12]

The experimental facts noted above cannot be explained on the basis of the well-known and well-studied elementary processes in a gas-discharge plasma in the region of negative emission. In this connection, we suggest that, on the basis of a single film deposition process, we actually have two systems. The first one is an rf discharge in oxygen with all characteristic properties of negative emission (the behavior of the ionic lines of oxygen is the internal parameter characterizing it). The second system consists of the sputtered particles which enter the gas phase in atomic, ionic, and cluster form. Then the threshold state of the rf discharge is characterized by a density of sputtered particles that is sufficient for the formation of an independently functioning system from them. The values of the internal parameters should be greater than the critical values. At present there are no experimental data on the specific composition and size of the clusters entering from the target into the gas medium. However, it can be inferred that the clusters must include titanium and oxygen as well as all other metallic components. The cluster part of the sputtered particles is the center of condensation of components of a complex oxide in the gas phase, probably right up to the formation of macroparticles in the form of dust.[5] A characteristic feature of complex oxides is the presence of volatile components in them. In our case these are oxygen and lead. For this reason, the growth of a cluster is determined by the energetics of two processes: recombination accompanying condensation of atoms on the surface of a cluster and cooling accompanying evaporation of volatile components from the surface of a cluster. Because the oxygen pressure in the system is high, about 90% of the sputtered components of the oxide in the atomic state do not leave the region next to the target surface. A high concentration of the atomic component in this zone results in rapid growth of the cluster. As a result of being bombarded with beam electrons, the cluster becomes negatively charged and is removed from the cathode region of the discharge under the action of the cathodic voltage drop. The subsequent motion of a cluster toward the substrate can be of a Brownian motion character. However, condensation is accompanied by evaporation of volatile components in the excited state from the surface of a cluster. The evaporated components are reflected from the atoms of the main gas, as a result of which a region with high density of atoms forms near the cluster surface. It is from this region that the emission lines of the volatile components are emitted. Then the spatial distribution of the intensity of the atomic and ionic lines reflects the dynamics of evaporation and condensation of the oxide components on the cluster surface as the cluster moves away from the target toward the substrate, and the derivative of the intensity with respect to the spatial coordinate reflects the change in the cluster sizes. When the intensity of the lines of lead and atomic oxygen does not change with increasing distance from the target surface, it can be inferred that condensation and reevaporation become stationary and cluster size remains unchanged. Film growth occurs from clusters surrounding by a cloud of volatile components. The total concentration of the components in a cloud and a cluster corresponds to the stoichiometry of the initial sputtered complex oxide, which is what ensures stoichiometry in the growing film.

CONCLUSIONS

In summary, the rf sputtering system for complex-oxide synthesis and crystallization directly during the deposition process possesses threshold states. When a transition through these occurs, a qualitative change occurs in the processes in the system. The basic feature of this change is the appearance of a new structured system, consisting of sputtered particles and particles formed in the plasma, in the plasma of an rf discharge. Continuous flow of matter and energy, transported by the beam electrons, through this structure results in the appearance of self-organization. In the space of the target parameters the appearance of a new system is manifested as a nonperovskite–perovskite phase transition.

[1] S. L. Swarts and V. F. Wood, Condens. Matter News **1**, 4 (1992).

[2] I. Lee, R. Ramesh, V. G. Keramidas, and O. Anciello, Integrated Ferroelectrics **8**, 317 (1995).

[3] J. M. Rcaney, K. Brooks, and R. Klissurska, J. Am. Ceram. Soc. **77**, 1209 (1994).

[4] E. V. Vlasenko, I. L. Zhuravlev, A. A. Lavrenov *et al.*, Élektronnaya Promst. **8**, No. 125, 58 (1983).

[5] B. M. Smirnov, Usp. Fiz. Nauk **167**, 1169 (1997).

[6] V. M. Mukhortov, G. N. Tolmachev, A. I. Mashchenko *et al.*, Zh. Tekh. Fiz. **62**, 5 (1992) [Sov. Phys. Tech. Phys. **37**, 495 (1992)].

[7] O. V. Kozlov, *Electric Probes in Plasma* [in Russian], Atomizdat, Moscow, (1969), p. 93.

[8] V. M. Mukhortov, G. N. Tolmachev, Yu. I. Golovko *et al.*, Zh. Tekh. Fiz. **68**(9), 99 (1998) [Tech. Phys. **43**, 1097 (1998)].

[9] Z. Surowiak, Y. S. Nikitin, and S. V. Birykov, Thin Solid Films **208**, 76 (1992).

[10] V. M. Mukhortov, Yu. I. Golovko, S. V. Biryukov *et al.*, Metallofizika (Kiev) **10**(5), 97 (1988).

[11] V. I. Myshenkov and N. Ya. Yatsenko, Fiz. Plazmy **8**, 543 (1982) [Sov. J. Plasma Phys. **8**, 306 (1982)].

[12] Yu. P. Raĭzer, *Principles of the Modern Physics of Gas Discharge Processes* [in Russian], Nauka, Moscow (1980), p. 105.

Translated by M. E. Alferieff

BRIEF COMMUNICATIONS

Assessment of the thermal stability of a polymer liquid by the controlled pulsed heating method

P. V. Skripov, A. A. Starostin, and D. V. Volosnikov

Institute of Thermal Physics, Ural Branch of the Russian Academy of Sciences, 620219 Ekaterinburg, Russia
(Submitted January 28, 1999)
Zh. Tekh. Fiz. **69**, 92–94 (December 1999)

A method of controlled pulsed heating of a quick-response probe placed in the experimental material is developed. It is shown that the ''temperature plateau'' regime can be used to estimate the average lifetime of a polymer liquid before its ebullition. A correlation was found between the slope of the curve of the lifetime versus the temperature on the plateau and the thermal stability of the material. © *1999 American Institute of Physics.* [S1063-7842(99)01812-7]

The process of polymer destruction by an impulsive load has its own characteristic features[1–3] associated with the specifics of the relaxation of the high-molecular system under strongly nonequilibrium conditions. To study the response of a polymer it is important to know the change in its temperature during the pulse. For thermal action, this change can be modeled using quick-response heater-probes.

We used the method of pulsed heating of a thin wire probe[4] to study the response of a polymer liquid to intense heat release. A reproducible signal, concentrated in time and similar to the signal due to spontaneous ebullition of a superheated low-molecular liquid,[5,6] was observed on the heating curves $T(t)$ of the probe for heating rates $\dot{T} \geqslant 10^5$ K/s. We attribute its appearance to ebullition of the products of thermal decomposition that form in the heated layer over the duration of the pulse. The temperature of the signal was taken as the temperature of explosive ebullition of the polymer liquid T^* (Ref. 7). It increases with the average heating rate $\dot{T}$ (from 10^5 to 10^7 K/s in our experiments), i.e., with a decrease in the degree of decomposition of the polymer at the moment it boils up.

To clarify the nature of the ebullition of the polymer liquid and, specifically, the contribution of the thermal decomposition process to its preparation, it is important to know how to control the heating conditions $T(t)$ in the region of thermal instability of the material. A temperature-plateau type heating regime was chosen. It consists in a rapid increase of the probe temperature (~ 10 μs) to a selected value $T = T_{pl}$, holding this value for a certain time ($t_{pl} \sim 10^2 - 10^3$ μs), and determining the temperature-time characteristics required for the liquid to boil up. The liquid in contact with the probe will be under nearly isothermal conditions. The thickness of the heated layer is $\sqrt{a \cdot t} \approx 3$ and ≈ 10 μm with $t_{pl} = 0.1$ and 1.0 ms, respectively, and the thermal diffusivity $a = 1 \times 10^{-7}$ m^2/s. The size of the critical vapor bubble is three orders of magnitude smaller.[4,8] This circumstance makes it possible to examine the average lifetime of the material at $T = T_{pl}$.

Combining the classical method of pulsed heating of a probe with a rapid system for controlling the pulse amplitude made it possible to obtain various heating regimes. In the present paper we describe the ''temperature plateau'' method for estimating the average lifetime of a polymer liquid before it boils up.

EXPERIMENTAL PROCEDURE

A platinum probe, 20 μm in diameter and 1 cm long, was used in the experiments. The probe served simultaneously as a heater and a resistance thermometer. It was inserted into a bridge circuit and was heated with a square voltage pulse U. The imbalance voltage $\Delta U(U)$ of the bridge served as the recorded equivalent change of the average-mass temperature $\bar{T}$ of the probe. The bridge was adjusted so that the temperature $\bar{T} = T_{pl}$ would correspond to zero imbalance. For $\Delta U = 0$ the value of $\bar{T}$ is determined exactly and does not depend on the supply voltage for the bridge. This fact forms the basis of the operation of the control system, regulating $U(t)$ so as to minimize $\Delta U(t_{pl})$.

The probe heating function $U(t)$ contained three sections: a section of uncontrolled heating where temperatures near T_{pl} ($t_1 \approx 10$ μs) are rapidly reached, a section of smooth additional heating up to T_{pl} ($t_2 \approx 10$ μs, $U_2 < U_1$), and a section of controlled heating with $\bar{T} \simeq T_{pl}$. Because the thickness of the heated layer increases with time, the supply voltage on the third section is of a decreasing character (Fig. 1, curve *1*).

To increase the informativeness of the method the control system had a tunable ''stiffness'' of thermal stabilization of the probe, set by the gain using a feedback circuit. The curves *2* and *3* in Fig. 1 show the temperature change with various control parameters. Depending on the stabilization stiffness, the characteristic transition time to the control regime was $1 - 10$ μs, and the error in maintaining the temperature $(\bar{T} - T_{pl})/(\bar{T} - T_\infty)$ was $1 \times 10^{-3} - 3 \times 10^{-2}$, where T_∞ is the temperature in the liquid mass.
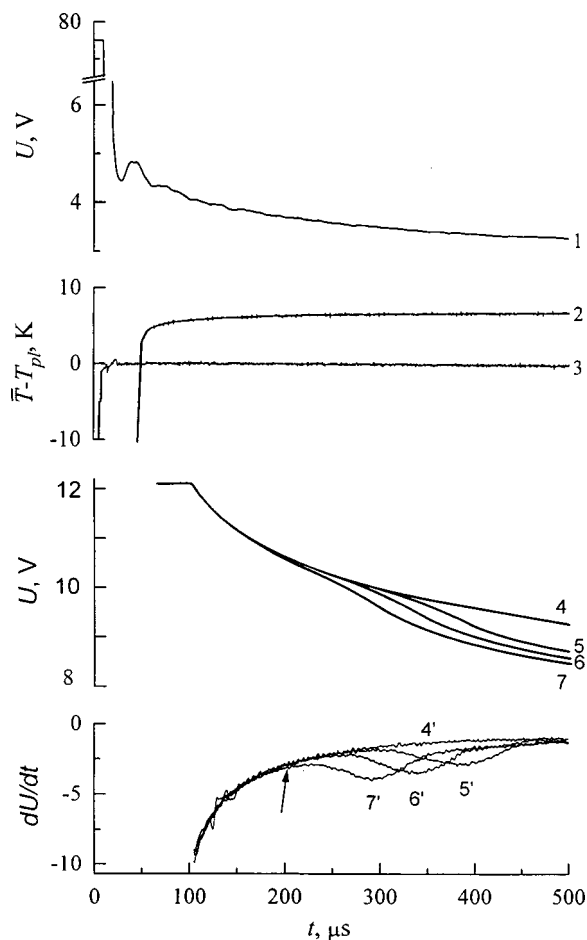
FIG. 1. Characteristic values of the amplitude of the warming pulse (*1*) and the probe temperature (*2*, *3*) with ''soft'' (*2*) and ''stiff'' (*3*) stabilization. Supply curves in experiments with PMS-1000 (*4–7*) and their time derivatives (*4′–7′*) at $T_{pl}=905$ (*4*), 917 (*5*), 921 (*6*), 925 K (*7*) and pressure 10 kPa. For the curve *7′* the arrow indicates the moment of ebullition.

FIG. 2. Average lifetime of PMS-1000 as a function of temperature on the plateau: $\bar{T}$ (filled symbols) and T^* (open symbols, *1′*) at pressures 10 (*1*), 20 (*2*), and 30 kPa (*3*).

EXPERIMENTAL RESULTS AND DISCUSSION

The key aspect of the method is a search for an ebullition on the supply curves $U(t;T_{pl})$. First, we determined by the classical method the temperature T^* of explosive ebullition of a polymer liquid with several rates of heating. Based on these data, having estimated the intensity of thermal decomposition, we choose a value of T_{pl} at which we expect to find ebullition. Next we choose acceptable values of U_1, t_1, and U_2. We display the functions $U(t)$ and $\Delta U(t)$ on an oscillograph screen and store them in a buffer memory of a computer. The moment of ebullition is noted by the perturbation of the curves $U(t)$ and $\partial U/\partial t$ relative to their form in a continuous liquid (curves *4–7* in Fig. 1). The appearance of vapor islands on the probe surface decreases the supply voltage required to maintain a prescribed temperature. Small disturbances are resolved by preliminary analog processing of the function $U(t)$, including removal of the so-called pedestal and amplification in the moving sampling window.

The average lifetime $\bar{t}(T_{pl})$ of the material up to the moment of its ebullition was determined in the experiments. The moment at which the probe temperature reached the pla-
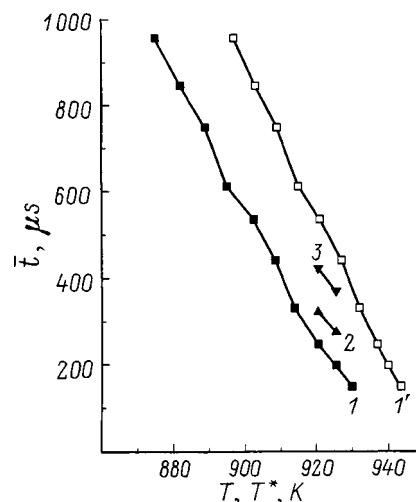
teau (the values of $\Delta U(t)$ crossed the zero level) was taken as the reference point. The object of study was PMS-1000 polydimethylsiloxane produced by the Aldrich Chemical Company. Its viscosity was 1014 cSt, and the average molecular mass was $\bar{M}_n \approx 14000$. The pressure p was 10–30 kPa.

The results of the measurements are presented in Fig. 2. Taking account of the temperature distribution along the probe, we infer that ebullition occurs at the center. In this connection, Fig. 2 also shows data on $\bar{t}(T^*)$, where T^* is the estimated temperature of the center of the probe at the moment of ebullition. The correction for end effects is introduced using the method of Ref. 4. An increase in the pressure in accordance with the general character of the dependence $T^*(p)$ for liquids[4,8] resulted in an increase in $\bar{t}(T_{pl})$ and a decrease in the amplitude of the ebullition signal. In the experiments a correlation was found between the slope of the characteristic $\bar{t}(T_{pl})$ and the thermal stability of the material. For dodecane and hexadecane, this slope was an order of magnitude larger than in Fig. 2, which agrees with the temperature-threshold character of the spontaneous ebullition of stable substances.[4,8] It is much lower for Laprol-5003 polyether, which is thermally less stable than siloxanes.

These results were obtained under conditions of ''soft'' stabilization. The temperature change on the plateau was ≈ 10 K/ms, and the plateau was reached at 50 μs. Such conditions were preferable for solving the problem posed. Substantial transient processes and a low stability of the control system with respect to self-excitation are characteristic of the ''stiff'' stabilization regime, at least at the present stage of this work. Our plan is to develop the method presented here and to perform measurements on a number of polymers with different thermal stability.

[1] V. V. Kostin, V. E. Fortov, I. K. Krasyuk *et al.*, Teplofiz. Vys. Temp. **35**, 962 (1997).

[2] A. V. Bushman, M. V. Zhernokletov, I. V. Lomonosov *et al.*, Dokl. Ross. Akad. Nauk **329**(5), 581 (1993) [Sov. Phys. Dokl. **38**, 165 (1993)].

[3] O. F. Shlenskiĭ, N. V. Afanas'ev, and A. G. Shashkov, *Thermal Destruction of Materials* [in Russian], Énergoatomizdat, Moscow (1996), 288 pp.

[4] P. A. Pavlov, *Dynamics of Ebullition of Strongly Superheated Liquids* [in Russian], Ural Branch of the USSR Academy of Sciences, Sverdlovsk (1988), 244 pp.

[5] P. V. Skripov and S. E. Puchinskis, J. Appl. Polym. Sci. **59**, 1659 (1996).

[6] S. E. Puchinskis, P. V. Skripov, and A. A. Starostin, High Temp.-High Press. **29**, 497 (1997).

[7] P. A. Pavlov and P. V. Skripov, Teplofiz. Vys. Temp. **36**(3), 448 (1998).

[8] P. V. Skripov, *Metastable Liquid* [in Russian], Nauka, Mosow (1972), 312 pp.

Translated by M. E. Alferieff

Nonstationary supersonic flow around a body

V. V. Svettsov

Institute of the Dynamics of Geospheres, Russian Academy of Sciences, 117334 Moscow, Russia

It is found that a nonstationary regime of supersonic flow around bodies that differs radically from the standard stationary flow can occur for high Mach numbers and low specific heat ratios of a gas. This regime is characterized by large-scale vortices in a shock-compressed region in front of the body, a curved shock-wave profile, and oscillation of all flow parameters. © *1999 American Institute of Physics.* [S1063-7842(99)01912-1]

It is generally believed that a stationary flow is established around bodies with simple shape moving at supersonic velocities in a uniform perfect gas. Flow nonuniformities can give rise to distortions of the front of the bow shock wave with formation of vortex motions,[1] but it is believed that if these nonuniformities vanish, then the flow once again will revert to a standard form. It turns out that this is not always so.

In the experiments of Ref. 2 with propane flowing around the end face of a cylinder with Mach number $M = 2.5$ the incident flow was perturbed by heating the gas at the surface of a molybdenum wire secured at the center of the end face perpendicular to it. The perturbation of the flow can be made to be bounded in time by using an exploding wire that produces a ''thermal wake'' in the incident gas. We shall assume that the track consists of a heated cylindrical region with a radius equal to 0.1 times the radius of the body, and the density of the gas in the wake is two times lower and the pressure the same as in the unperturbed flow. Calculations performed for $M = 2.5$ showed that for any length of the wake the flow reverts to the standard flow around a body a certain time after the perturbation ceases. But, as M increases, the results are found to be completely different: For a definite length of the thermal wake the flow never arrives at the standard stationary form that existed before the perturbation of the flow.

Let us examine the numerical solution of this problem for a perfect gas with specific heat ratio $\gamma = 1.08$,[2] $M = 5$, and long thermal wake equal in length to two times the diameter of the end face. The gas-dynamic equations were solved by several numerical methods: large particles, Godunov's, TVD and PPM, and on square grids with a step of 0.01 and 0.005 times the radius of the body. The qualitative behavior of the flow was the same in all calculations. Figure 1 illustrates the computational results obtained with the PPM method.[3] Distances are scaled to the radius R of the body and times are scaled to R/V, where V is the velocity of the incident flow. At the time $t = 0$ a standard flow around a body was established, and the thermal wake was located flush against the bow shock wave. The velocity of sound and the velocity of the shock wave in the thermal wake were higher than in the unperturbed gas; this leads to the formation and growth of a precursor — a conical shock wave with vortex motion of gas

and a system of shock waves and contact discontinuities behind the shock front.[1,2] At $t = 3.6$ the precursor reaches the end of the wake. As soon as the incident flow becomes uniform once again, the precursor decreases in size, but after the flow is restructured the precursor once again starts to grow, after which its dimensions fluctuate.

The velocity field is demonstrated in Fig. 2. The density of the gas behind the front of a strong shock wave is $\rho(\gamma+1)/(\gamma-1)$, where ρ is the density of the incident gas. The gas velocity behind an oblique shock wave is directed almost along the front and is approximately $V \sin \alpha$, where α is the slope angle of the wave front with respect to the surface of the body. A thin layer of gas behind the front of an oblique shock wave therefore possesses a high momentum flux density, and when this gas flow stops at the body, the pressure rises to a value approximately equal to the momentum flux,

$$P_m = \rho V^2 \frac{\gamma+1}{\gamma-1} \sin^2 \alpha.$$

This is much higher than the pressure behind the first stationary jump ρV^2 even for small α. The pressure gradient along the surface of the body ($\sim P_m/R$) accelerates gas along the surface toward the symmetry axis up to a maximum velocity equal to approximately $0.4V$. Then this flow stops at the symmetry axis, and the pressure at the axis on the bow surface of the body is higher than ρV^2. For this reason, the gas is once again accelerated, but now along the axis of symmetry and then once again stops near the front of the bow shock wave. An additional increase in pressure due to this stopping causes the bow shock wave to advance toward the incident flow. A powerful vortex motion develops in the region of shock-compressed gas.

When the bow shock wave moves far away from the body, the gas flow behind the oblique shock wave emerges close to the edge of the bow surface (Fig. 1d). Then the pressure on the edge of the end face decreases, the vortex motion slows down, and the bow shock wave starts to approach the body until the gas flow behind the front of the oblique wave once again increases the pressure at the edge of the body, which in turn results in the development of a vortex and a transition to a new cycle. Figure 3 shows oscillations of the distance of the shock wave away from the body
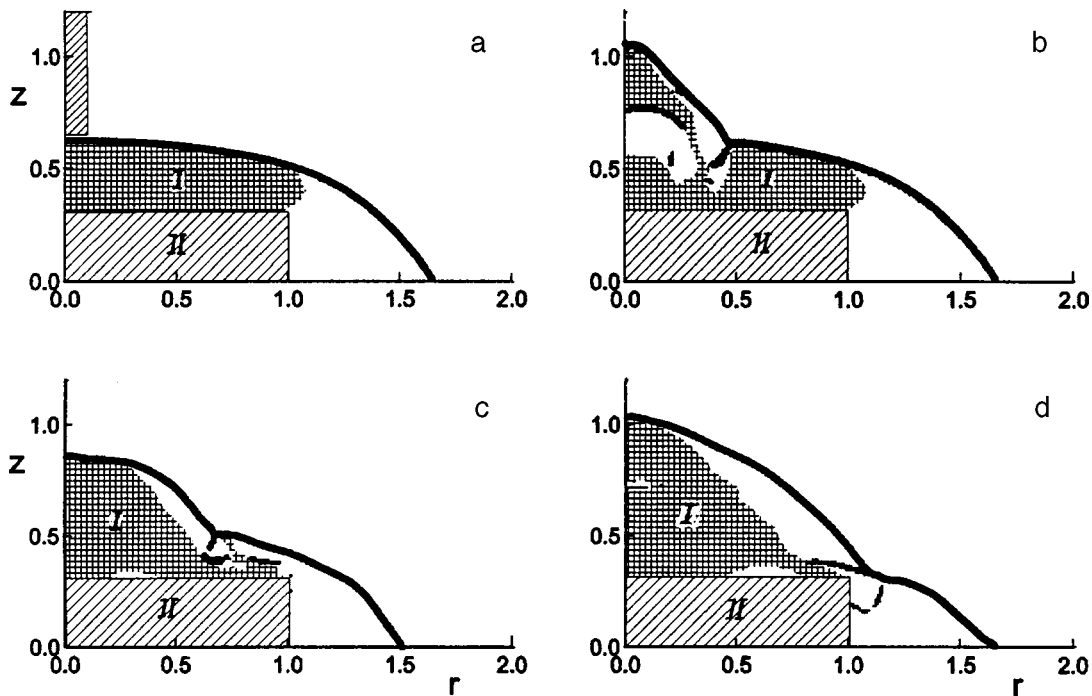
FIG. 1. Flow around a cylinder before and after perturbation of the flow by a thermal nonuniformity at times $t=0$ (a), 3.6 (b), 475 (c), 483 (d). The regions next to strong shock fronts are shown by thick lines; I — regions of subsonic flow, II — body and warm wake at $t=0$. The incident flow is directed from top to bottom along the symmetry axis z.

and the maximum pressure on the body. The process is not strictly periodic, but a characteristic oscillation time of about 15 dimensionless units can be extracted. No tendencies toward either the average circulation of the flow to decay in a cycle or the amplitude of the oscillations of the parameters to decrease were observed in the numerical solution. The calculations were performed in time up to 1000 dimensionless units.

For $M=60$ a series of calculations of flow around a cylinder and a step was performed for various values of γ. It was found that for γ greater than a certain limiting value γ_2, ranging from 1.15 to 1.2, any spatially bounded disturbances of the flow decay in time and the solution of the problem of the flow around the body reverts to a standard form. In a

certain region $\gamma_1 < \gamma < \gamma_2$ there exist two regimes of uniform flow around the body: the standard regime and a nonstationary vortex regime. The realization of either regime depends on the initial data. For very small $\gamma < \gamma_1 \approx 1.03 - 1.05$, vortices, distortions of the front of the bow shock wave, appear in the numerical calculations and the flow spontaneously transforms to a nonstationary regime even without perturbation of
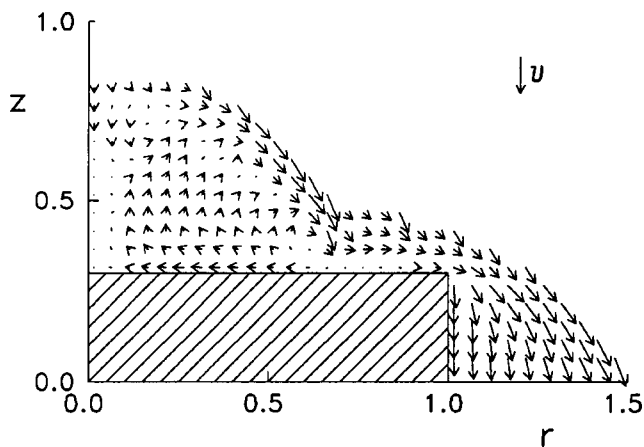

FIG. 2. Velocity field behind the front of the bow shock wave at $t=475$. The velocity of the incident flow was shown in the upper right-hand corner.
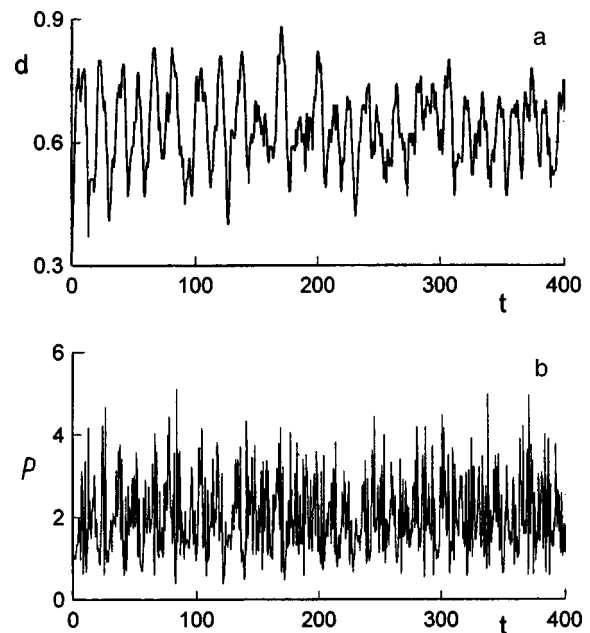
FIG. 3. Time dependences of the maximum distance from the front of the bow shock wave to the body (a) and the maximum pressure on the surface of the body in units of ρV^2 (b).

the incident flow. This could be a consequence of the fact that a definite level of perturbations, associated both with the computational errors and the propagation of weak waves in a shock-compressed layer during the setting process, is always present in the calculations.

Two-dimensional calculations of flow around a square of parallelepipeds were performed for $\gamma = 1.1$. Perturbations of the flow were produced by a warm layer of bounded length, located in the symmetry plane of the body, but the symmetry condition was not used in solving the problem. At a certain time after the flow became uniform, the symmetry of the flow was destroyed, but the flow regime nonetheless remained nonstationary with several vortices and distortions of the front of the bow shock wave in the form of two or three humps of varying size.

The computational results can be checked in experiments with a warm wake, but it should be kept in mind that small values of γ are always associated with nonequilibrium processes behind the shock front — excitation of the vibrational degrees of freedom, dissociation, and ionization. Strong distortions of the front of a bow shock wave have been observed in experiments[4] on freon flow around blunt bodies with Mach numbers ranging from 4 to 10. The appearance of perturbations was explained by a special kind of instability of a shock wave, associated with relaxational pro-cesses behind the shock front at the initial stage of dissociation.[5] In the light of the results obtained, large-scale disturbances of the shock-compressed layer in the experiments of Refs. 4 and 5 can be interpreted as a transition to a nonstationary vortex regime. We note that the dependence of the appearance of distortions of the front on the shape of the model and the rounding of its edges[4,5] shows that the instability is connected with the hydrodynamic flow. Aside from the relaxation instability, other factors could also lead to the appearance of a vortex regime. Dissociation decreases γ and increases the setting time of the flow. Just as in the calculations, a definite level of perturbations sufficient for changing the flow regime around a body can arise in experiments.

[1] N. N. Pilyugin, R. F. Talipov, and V. S. Khlebnikov, Teplofiz. Vys. Temp. **35**(2), 322 (1997).

[2] I. V. Artem'ev, V. I. Bergel'son, I. V. Nemchinov *et al.*, Izv. Akad. Nauk SSSR, Mekh. Zhidk. Gaza No. 5, 146 (1989).

[3] P. Colella and P. R. Woodward, J. Comput. Phys. **54**, 174 (1984).

[4] A. S. Baryshnikov, A. P. Bedin, V. G. Maslennikov, and G. I. Mishin, Pis'ma Zh. Tekh. Fiz. **5**(5), 281 (1979) [Sov. Tech. Phys. Lett. **5**, 113 (1979)].

[5] A. S. Baryshnikov, A. P. Bedin, G. I. Mishin, and G. E. Skvortsov, *Physical and Gas-Dynamic Ballistic Studies* [in Russian], Nauka, Leningrad (1980), pp. 34–42.

Translated by M. E. Alferieff

Effect of neutron irradiation on the IR absorption spectra of cupric oxide single crystals

N. N. Loshkareva, B. A. Gizhevskiĭ, Yu. P. Sukhorukov, A. E. Kar'kin, and S. V. Naumov

Institute of Metal Physics, Ural Branch of the Russian Academy of Sciences, 620219 Ekaterinburg, Russia
(Submitted October 19, 1998)
Zh. Tekh. Fiz. **69**, 98–99 (December 1999)

A strong increase of the absorption coefficient with photon energy increasing from 0.1 to 1.0 eV is observed in the spectra of CuO single crystals irradiated with neutrons to a fluence of 5×10^{18} cm^{-2}. The difference of the absorption coefficients before and after irradiation depends on the wavelength as λ^{-2}. The effect of neutron irradiation on CuO is qualitatively similar to that of neutrons on other semiconductors (for example, GaAs) and differs from that obtained by irradiating CuO with charged particles. © *1999 American Institute of Physics.*
[S1063-7842(99)02012-7]

The infrared optical spectra of CuO, just as the spectra of semiconductor compositions of copper–oxygen high-temperature superconductors (HTSCs), show a phase inhomogeneity in these materials and can be described on the basis of a cluster approach by the existence of nuclei of a phase of polar Jahn–Teller centers (hole $(CuO_4)^{5-}$ and electronic $(CuO_4)^{7-}$) in the main matrix consisting of $(CuO_4)^{6-}$ clusters.[1] As we have shown, irradiation of CuO with high-energy charged particles (electrons and He$^+$ ions[2,3]) results in substantial changes in the structure and in anisotropy of the optical absorption spectra. These changes are due to the specific nature of CuO as a phase-inhomogeneous compound.[1]

In the present work we have investigated the effect of irradiation with neutral particles (neutrons with a fluence of 5×10^8 cm^{-2}) on the infrared absorption spectra of CuO single crystals, cut along the (110) and (ac) planes. The temperature during irradiation was below 100 °C. It follows from the x-ray diffraction patterns that the parameters of the monoclinic lattice did not change and the linewidths increased. The electrical resistance of the samples was 10^2 Ω·m before annealing and two to three orders of magnitude higher after irradiation. No changes were observed in the resistivity anisotropy after irradiation.

The absorption spectra of CuO single crystals were investigated in the photon energy range 0.1–1.0 eV (in the region between the fundamental absorption edge $E_g = 1.46$ eV and the phonon spectrum). Irradiation did not degrade the quality of the optical surface.

An absorption band at 0.2 eV (Fig. 1), corresponding to the transitions in a hole Jahn–Teller center,[1] and a region of absorption increasing weakly toward high energies are present in the range investigated. After irradiation strong monotonic growth of absorption is observed starting at 0.1 eV. Such a change in the spectra is observed with light incident on the (ac) plane and in the case of (110) plane, for natural and polarized light. An appreciable increase in the intensity of the band at 0.2 eV against the background of structureless growth of absorption did not occur. In a monoclinic CuO crystal, the $[\bar{1}01]$ axis, relative to which we observed strong anisotropy of the absorption coefficient near the transition at 0.2 eV,[1] lies in the (ac) plane. The natural dichroism — the ratio of the difference of the absorption coefficients for polarizations parallel and perpendicular to
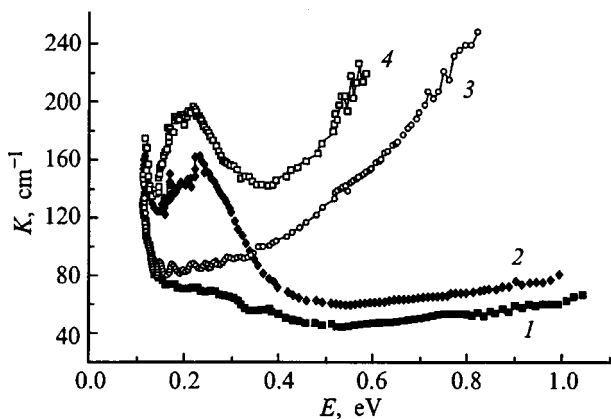

FIG. 1. Absorption spectra of a CuO single crystal, the (ac) plane, in polarized light before (*1, 2*) and after (*3, 4*) irradiation: *1, 3* — $E \perp [\bar{1}01]$; *2, 4* — $E \parallel [\bar{1}01]$.
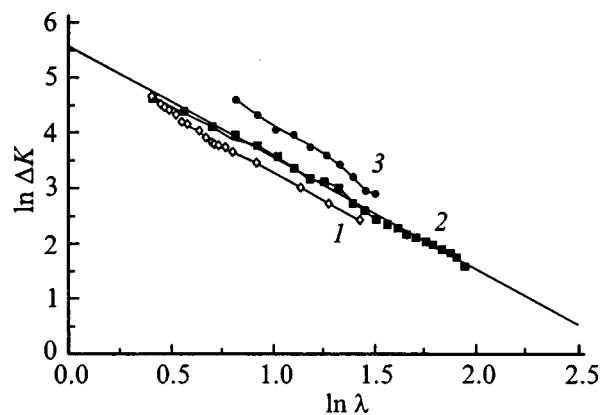

FIG. 2. Difference of the absorption coefficients of CuO before and after irradiation versus the wavelength: *1* — (110) plane, natural light; *2* and *3* — (ac) plane, polarized light, $E \perp [\bar{1}01]$ and $E \parallel [\bar{1}01]$.

the $[\bar{1}01]$ axis to their sum in the unirradiated crystal — is greater than 40%. When CuO was irradiated with charged particles (electrons and He$^+$ ions), the dichroism in the region of the band at 0.2 eV changed substantially (by a factor of 2). For neutron irradiation no substantial change of dichroism is observed, showing that the anisotropy of the hole centers does not change. In contrast to He$^+$ and electron irradiation, for neutron irradiation new bands did not appear in the spectra.

The difference ΔK of the absorption coefficients before and after irradiation, to a high degree of accuracy (2%), is inversely proportional to the squared wavelength (Fig. 2) for a sample cut in the (110) plane for measurements in natural light and for a sample cut in the (ac) plane for measurements in linearly polarized light with the vector **E** directed parallel and perpendicular to the $[\bar{1}01]$ axis. Additional absorption is a result of light scattering by defects produced by irradiation. The dependence $\Delta K \sim \lambda^{-2}$ was observed in ordinary semiconductors, for example, in GaAs, and was attributed to ''metal-like'' inclusions.[4] Neutrons are the most damaging particles. The atom knocked out first with energy substantially above threshold rapidly loses this energy in collisions with other atoms. The result of such an interaction are thermal wedges and regions of disordering. The high temperature in the region of a thermal wedge can cause local dissociation and precipitation of components in the form of colloidal inclusions. Such inclusions in a CuO matrix can be nuclei of an inhomogeneous phase, which as a result of neutron action form a finely dispersed structure (less than 0.01–0.1 μm in size), with electronic Jahn–Teller centers, in which optical transitions are forbidden, predominating in the nuclei. The appearance of electronic centers could be one reason for the increase in the resistivity as a result of compensation of acceptors in the initial p-type cupric oxide. Another reason for the increase in resistivity seems to be lattice disordering effects which lead to fluctuations of the potential. X-ray diffraction data confirm the appearance of disordering after irradiation.

In summary, irradiation of CuO with neutrons results in radiation-stimulated structureless absorption characteristic for binary semiconductors (for example, GaAs). The results of neutron irradiation differ substantially from irradiation of CuO with charged particles, where the specific nature of the phase-inhomogeneous state of cupric oxide is sharply manifested.

[1] A. S. Moskvin, N. N. Loshkareva, Yu. P. Sukhorukov *et al.*, Zh. Éksp. Teor. Fiz. **105**, 967 (1994) [JETP **88**, 518 (1994)].
[2] Yu. P. Sukhorukov, N. N. Loshkareva, A. S. Moskvin *et al.*, Fiz. Tverd. Tela **39**, 2141 (1997) (St. Petersburg) [Phys. Solid State **39**, 1916 (1997)].
[3] B. A. Gizhevskiĭ, T. A. Belykh, S. V. Naumov *et al.*, Fiz. Khim. Organ. Mater., No. 1, pp. 9–14 (1998).
[4] R. F. Konopleva, V. L. Litvinov, and N. A. Ukhin, *Characteristic Features of the Radiation Damage to Semiconductor by High-Energy Particles* [in Russian], Atomizdat, Moscow (1971), 176 pp.

Translated by M. E. Alferieff

Dependence of the ultrasound velocity on the acting stress during plastic flow of polycrystals

L. B. Zuev, B. S. Semukhov, and K. I. Bushmeleva

Institute of Strength Physics and Materials Science, Siberian Branch of the Russian Academy of Sciences, 634021 Tomsk, Russia

The dependence of the propagation velocity of ultrasound in polycrystalline materials on the magnitude of the stress acting during deformation is measured. It is established that the dependence has three stages, which are apparently due to the formation of dislocation ensembles of various characteristic sizes in the deformed material. © *1999 American Institute of Physics.* [S1063-7842(99)02112-1]

The conventional models of plastic deformation processes include, as rule, the idea that such deformation occurs in stages.[1] Although for single crystals, especially face-centered crystals, there is no difficulty in identifying the stages on the yield curve, for materials of other crystal classes and especially polycrystals this procedure remains complicated, since there are no sufficiently informative and reliable indications of a change in the deformation mechanisms. In a previous work[2] we have shown that in the course of plastic flow the propagation velocity of ultrasound in the material changes, the dependence $V(\varepsilon)$ having a complicated N shape. This made it possible, for example, to identify on the plastic flow curve of Al additional stages due to[3] differences in the dynamics of the rotations of blocks during deformation.

In the present paper we present data on the dependence of V on the magnitude of the stress σ acting during deformation. The ultrasound velocity (surface waves, frequency 2.5 MHz) was measured with the sample stretched in an Instron-1185 testing machine using an ISP-12 device,[4] operating according to the principle of autocirculation of pulses. The samples were shaped in the form of a double paddle with a 50 mm long working part. The measurements were performed on Al, the alloys Al+Li with a different Li con-

tent, Fe + 3%Si, Zr + 1.5%Nb, and 65G and 09G2S steels.

The typical dependences $V(\sigma)$ shown in Fig. 1 for Al and Fe + 3%Si have three stages. The linear character of the relation between V and σ at each stage is interesting. Similar three-stage dependences $V(\sigma)$ were obtained for the other materials studied in the course of the experiments described. It is important to keep in mind that the law of plastic flow of Al and other materials investigated in this range of strains has the form $\sigma \sim \varepsilon^{1/2}$, and no sudden changes are observed in the curves $\sigma(\varepsilon)$. It should be noted that the two descending sections of the dependence $V(\sigma)$ occur for all materials investigated, and the left-hand branch of the plot can have a positive (Al and alloys based on it, the alloys Zr + 1.5%Nb, Fe + 3%Si) or zero (steels) slope. The decrease of the deforming force at the end of the stretching process is well-known to be associated with the formation of a macroscopic neck and is usually associated with a small increase in the ultrasound velocity.

In discussing the nature of the regularities established it should be kept in mind, first and foremost, that a monotonic decrease of V with plastic deformation of Al single crystals as a result of the evolution of a dislocation structure has been reported previously.[5] In Ref. 6 a change of the resonance frequency, proportional to V, of aluminum single crystal
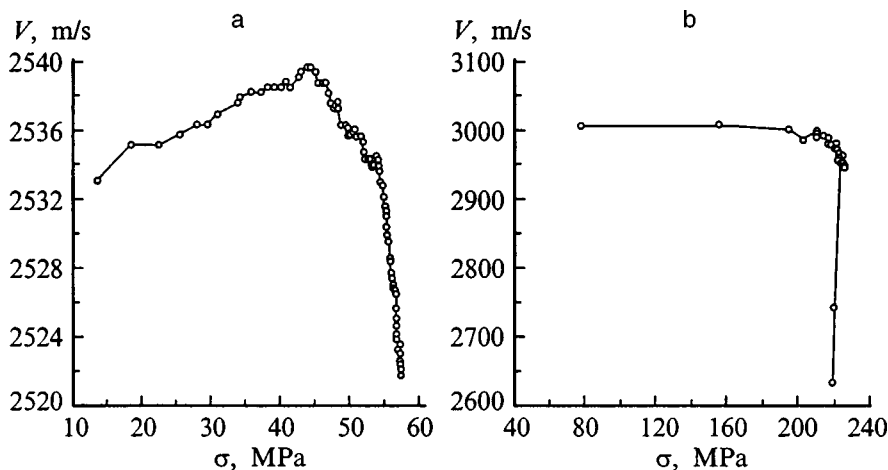

FIG. 1. Propagation velocity of ultrasound versus the acting stress: a — Al, b — Fe + 3%Si.
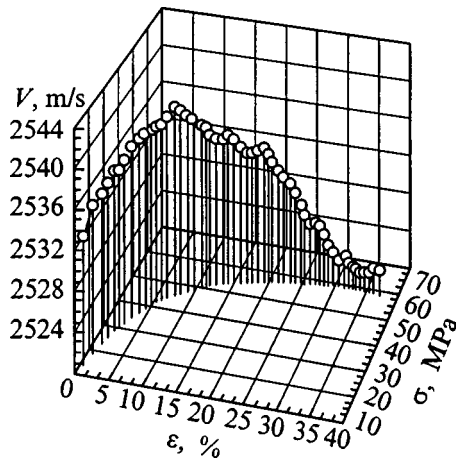
FIG. 2. Variation of the propagation velocity of ultrasound along the curve of plastic flow of Al.

samples was observed on bending, and it was attributed to a change in the damping with increasing dislocation density during plastic flow. However, it seems that the dependence $V(\sigma)$ makes it possible to identify more accurately the $\sigma \sim \varepsilon^{1/2}$ stage on the parabolic curve of plastic flow. Figure 2 demonstrates the complicated character of the variation of V along the curve $\sigma(\varepsilon)$. The equation relating V and σ evidently has the form

$$V = V_0 + \xi\sigma, \tag{1}$$

where the constants V_0 and ξ are different for different sections of the function $V(\sigma)$. The dimensions of the coefficient of proportionality ξ in Eq. (1) are, evidently, $[L]^2 \cdot [T] \cdot [M]^{-1}$. Since, as follows from the data presented, this coefficient can change sign in the course of plastic flow, it should contain a microscopic characteristic which can also change sign in this process. The set of such characteristics in the problem under study is limited. It is known that the density ρ_{md} of mobile defects has an extremal dependence on the strain,[7] and therefore its derivative with respect to time (or to strain, since under active loading $\varepsilon \sim t$) should change sign. Introducing the derivative $d/dt(1/\rho_{md}) = D^{(\varepsilon)}$, which has the dimension and meaning of a ''diffusion coefficient'' in the equation of an autowave of plastic deformation,[8,9] and taking account of the fact that the propagation velocity of elastic waves in the material is related with the density ρ_0 of the material, dimensional analysis allows us to write

$$\xi \sim L_i / \rho_0 D^{(\varepsilon)}. \tag{2}$$

Here L_i is the characteristic scale of the plastic deformation acting at this moment.[10] The appearance of the latter quantity

makes it possible to explain formally the discrete change in the coefficient ξ by a transition of the process to a different scale level,[10] and the behavior of $D^{(\varepsilon)}$ determines the variations of the sign of ξ during plastic deformation.

On the other hand, it is well known[11] that the propagation velocity of ultrasound ''feels'' the internal stresses in the medium. For this reason, the changes observed to occur in this quantity during plastic deformation could be related with a change in the sizes of the stressed regions and the level of internal stresses in them. It is completely clear that measurement of the propagation velocity of ultrasound in the course of stretching makes it possible to identify additional stages on the plastic flow curve, which are evidently due to the different character of the dislocation ensembles created in the deformed material (cells, fragments[12]). It can be assumed that in this case the interstage transition in the function $V(\sigma)$ is due to the formation of dislocation ensembles of different characteristic size L_i and different average internal stress level in the volume of the cell or fragment. This is what is reflected against the background of the dependence of the ultrasound velocity on the strain or stress. It is interesting that such changes of the dislocation microstructure are essentially not observed in the behavior of the strain hardening coefficient, but their contribution to the change in the ultrasound velocity is very noticeable. Therefore measurements of the ultrasound velocity directly during the mechanical tests on materials can give additional important information about the physics of deformation processes.

[1] A. Seeger, in *Dislocations and the Mechanical Properties of Crystals* [Russian translations of collected articles, edited by M. V. Klassen-Nekhlyudova and V. L. Indenbom], IL, Moscow (1960), pp. 179–268.

[2] L. B. Zuev, B. S. Semukhin, and K. I. Bushmeleva, Pis'ma Zh. Tekh. Fiz. **22**(14), 76 (1996) [Tech. Phys. Lett. **22**(7), 590 (1996)].

[3] L. B. Zuev, T. M. Poletkin, and B. S. Semukhin, Kristallografiya **40**(6), 1071 (1995) [Crystallogr. Rep. **40**, 996 (1995)].

[4] V. V. Murav'ev, L. B. Zuev, and K L. Komarov, *Velocity of Sound and the Structure of Steels and Alloys* [in Russian], Nauka, Novosibirsk (1996), 183 pp.

[5] A. Hikata, B. B. Chick, and C. Elbaum, Acta Metall. **10**, 423 (1962).

[6] A. B. Lebedev, S. B. Kustov, and B. K. Kardashev, Fiz. Tverd. Tela (Leningrad) **34**, 2915 (1992) [Sov. Phys. Solid State **34**, 1562 (1992)].

[7] J. D. Gilman, in *Microplasticity*, edited by V. N. Geminov and A. G. Rakhshtadt (Metallurgiya, Moscow, 1997), pp. 18–37.

[8] L. B. Zuev and V. I. Danilov, Int. J. Solids Struct. **34**, 3795 (1997).

[9] L. B. Zuev and V. I. Danilov, Fiz. Tverd. Tela (St. Petersburg) **39**, 1399 (1997) [Phys. Solid State **39**, 1241 (1997)].

[10] V. E. Panin, Izv. Vyssh. Uchebn. Zaved. Fiz. **41**, 7 (1998).

[11] A. N. Guz', *Elastic Waves in Prestressed Bodies* [in Russian], Naukova Dumka, Kiev (1986), Vol. 1, 376 pp., Vol. 2, 536 pp.

[12] F. R. N. Nabarro, Z. S. Bazinski, and D. B. Holt, Adv. Phys. **13**, 193 (1964) [Metallurgiya, Moscow, 1967].

Translated by M. E. Alferieff

Mechanoluminescence and submicrorelief of a copper surface

K. B. Abramova, V. I. Vettegren', I. P. Shcherbakov, S. Sh. Rakhimov, and V. N. Svetlov

A. F. Ioffe Physicotechnical Institute, Russian Academy of Sciences, 194021 St. Petersburg, Russia

Copper plates are irradiated with pulsed laser light on one side, and the opposite side is investigated with a scanning tunneling microscope. It is found that the submicrorelief of the back surface changes after irradiation. During irradiation it emits a light pulse. It is established that a relation exists between the luminescence intensity and the magnitude of the change in the surface submicrorelief. © *1999 American Institute of Physics.* [S1063-7842(99)02212-6]

It has been observed[1,2] that when a surface of metal plates is irradiated with pulsed laser light, the back side of the plates luminesces. In Refs. 3–5 this phenomenon was explained by a release of the energy stored in dislocation nuclei, as the dislocations emerge at the surface of the metal under the action of stress fields. According to the theory,[3–5] the intensity I_m (J/s·cm^2) of mechanoluminescence is related with the dislocation density N_d (cm^{-2}) in a surface layer of thickness S_t (cm) as follows:

$$I_m = \eta P_h N_d \frac{S_t}{at},\qquad(1)$$

where a (Å) is the lattice parameter of the metal, P_h is the probability of hole formation in the electronic subsystem of the metal accompanying deformation, η is the probability of radiative recombination, and t (s) is the luminescence time.

It is evident from Eq. (1) that the mechanoluminescence intensity is directly proportional to the dislocation density.

It is well known that the dislocation density in metals increases during deformation and decreases during high-temperature annealing. For this reason, the intensity of the mechanoluminescence of the surface layer of a deformed sample should be higher than that of an annealed surface. Indeed, in Ref. 1 it was shown that even for a light pulse with power $P_l \approx 0.2 P_{thr}$ (where P_{thr} is the power at which a plasma flame appears) luminescence of cold-rolled copper samples is observed and no luminescence is detected from the surface of an annealed sample.

It is known that when dislocations emerge at the surface of a metal, "steps," "protrusions," and other defects are formed.[6] Measuring the height of the "steps" and knowing the magnitude of Burgers vector, the number of dislocations which have emerged at the surface can be estimated. Further, the validity of expression (1) can be confirmed by comparing the density of such dislocations and the mechanoluminescence intensity. The goal of the present work is to check this assumption.

We studied the surface profiles of two batches of 0.1–0.5 mm thick copper plates (99.96% purity) with a surface area of 30×30 mm: One batch was sawed from cold-rolled ribbons and the second was obtained by annealing the ribbons in dry nitrogen gas at 700 K temperature for 1 h.

The changes in the surface relief were studied with an RTP-1 scanning tunneling profilometer, developed at the Scientific-Research Institute of Physics at Leningrad State University and built by the production cooperative "Éra."

A gallium arsenide diffraction grating, whose surface was coated with a gold layer, was used to monitor the resolution and the stability of the operation of the apparatus. The measuring tips were fabricated from tungsten wire by electrochemical etching. Their shape was estimated according to images of the smallest defects in the topograms.

In the profilometer the measuring tip could be moved perpendicular to the surface by no more than 1 μm. To remove microirregularities greater than 1 μm the samples were polished with GOI paste and then washed with acetone and alcohol.

The chemical structure of the surface of the samples before and after the investigations was checked by Auger spectroscopy using an LH-10 spectrometer. It was found that the surfaces investigated are coated with a $\sim 1.5-2$ nm thick oxide layer. To level the distortions that can arise because of the presence of such a layer, the shape and sizes of defects greater than 5 nm in depth were investigated.

An electrolyte forms on the investigated surface of the metals as a result of the condensation of the water vapor present in air, and an ionic current arises in this electrolyte. This current makes it impossible to obtain the surface profile. To suppress this phenomenon the sample was covered with a polyurethane cap through which dry nitrogen was blown.

To record the luminescence from the surface studied, the plates were placed at a distance $r_1 = 3$ cm from the entrance window (with radius $r_2 = 0.3$ cm) of an FÉU-136 photomultiplier which is sensitive to radiation in the wavelength range 300–800 nm and operates in an analog mode in combination with a digital storage oscillograph. Consideration of the experimental geometry showed that the light flux incident on the photocathode of the photomultiplier is 200 times weaker than the intensity of the luminescence of the sample surface.

The back side of the plates was irradiated with laser pulses with the following parameters: duration 1.5 ms, energy 24 J in the free lasing mode, transverse dimensions of the light beam ranging from 2 to 8 mm. The power of the light incident on the surface of a plate was varied using neutral light filters.
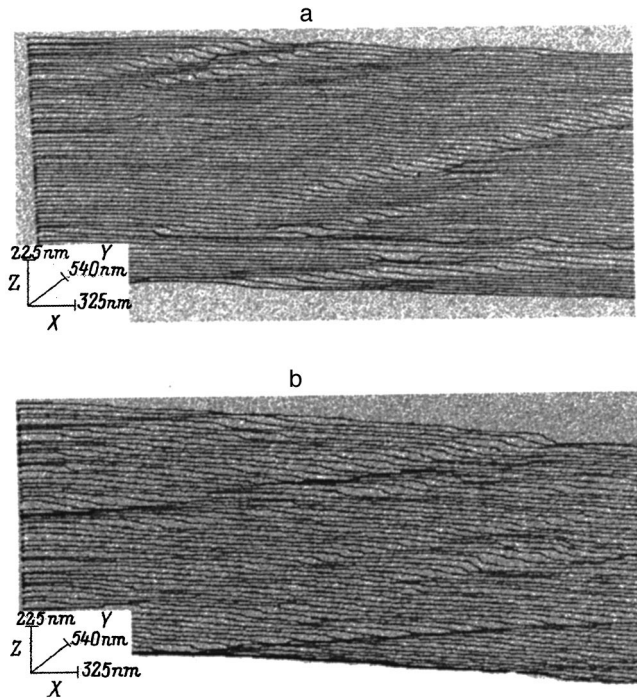
a

b

FIG. 1. Topograms of polished copper surfaces: a — annealed sample, b — deformed sample.

a

b

FIG. 2. Topograms of copper surfaces after the back-side irradiation with a laser pulse: a — annealed sample, b — deformed sample.

Topograms of the surface of annealed and deformed copper samples after the surface was polished with diamond pastes are shown in Fig. 1. Grooves ≈ 20 nm deep, 200–300 nm wide, and up to 8 μm long, and making an angle $\approx 30°$ with the roll axis X, can be seen in the topograms. As a rule, one wall of the defects is perpendicular to the surface, while the opposite wall makes an angle $\approx 30°$ with it. Such an orientation of the walls suggests that they were formed during mechanical polishing of the samples. Indeed, it is known[7–9] that during plastic deformation the planes of easy glide make angles of ≈ 30 and $90°$ with the surface plane of the sample. It is evident from the figure that the defect density at the surface of a deformed sample is higher for an annealed sample. This effect is probably due to the fact that the surface layer of deformed samples contains a larger number of dislocations than in the annealed sample. Emerging at the surface during polishing, they form a larger number of defects.

The grooves on the back side of the plates vanished after irradiation with a single laser pulse with $P_l \approx 0.2 P_{thr}$ (Fig. 2). A small number of defects, having the form of depressions and protrusions, remained on the surface of the annealed sample instead of the ''grooves.''

Comparing Figs. 1 and 2 shows that the orientation and form of the defects on the copper surfaces studied before and after irradiation with a laser pulse are different. Therefore the defects observed on the copper surfaces after irradiation with a light pulse were formed under the influence of this pulse. At the same time the defects which existed before irradiation with the laser pulse relaxed.

The depth (height) of defects on the surface of an annealed sample varies from 15 to 30 nm, and the transverse dimensions vary from 50 to 100 nm. The depth of defects on
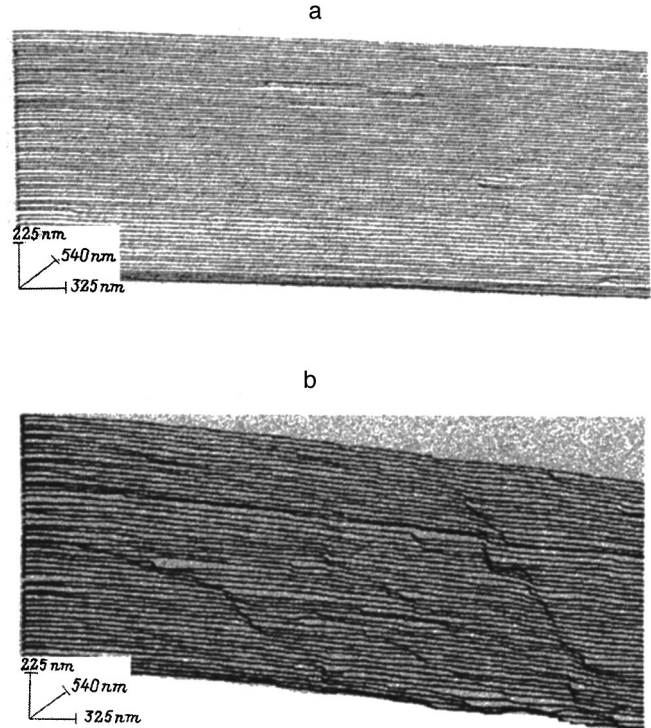
the surface of the deformed sample varies from 15 to 90 nm, and the transverse dimensions vary from 50 to 200 nm and the defect density is much higher. One of the defects is shown in an enlarged form in Fig. 3. It is evident that the left-hand and back walls of the defect are approximately perpendicular to the surface. Other defects also had the same orientation along at least one wall. Therefore it can be inferred that they were formed when dislocations emerged along the planes of easy glide (111) onto the copper surface. In this case, it follows from the data presented that the density of dislocations which have emerged at the copper surface under the action of the laser pulse is higher in the deformed sample than in the annealed sample.

It is shown in Ref. 2 that when a sample is irradiated with a laser pulse, compressive stresses arise on the opposite side and luminescence appears when stresses on the surface are close to the yield point. Apparently, these stresses forced some of the dislocations to emerge at the surface of the metal.

Figure 4 shows oscillograms of the photomultiplier signals when the back side of copper plates is irradiated by a laser pulse. It is evident that luminescence from the sample is
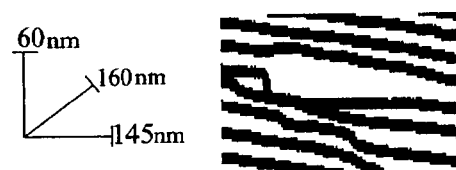

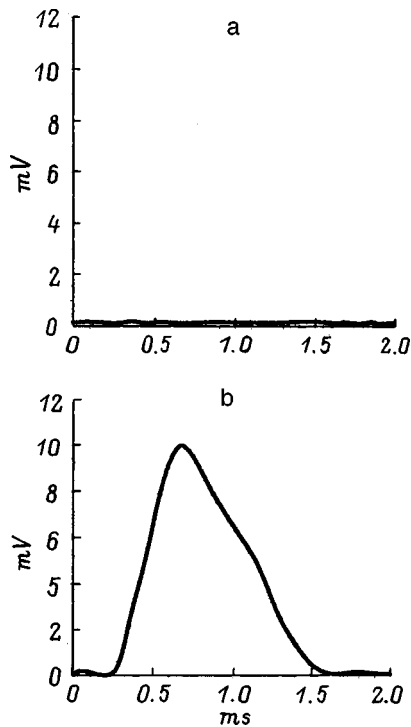FIG. 3. One of the defects of the topograms of copper surfaces in an enlarged form.

FIG. 4. Mechanoluminescence oscillograms recorded by a photomultiplier during back-side irradiation with a laser: a — annealed sample, b — deformed sample.

detected when a deformed sample is irradiated, whereas there is no luminescence when the annealed sample is irradiated. This result is in good agreement with the conclusion drawn above that the density of dislocations which have emerged at the surface in a deformed sample is higher than in the annealed sample.

Let us calculate the intensity of the mechanoluminescence, using expression (1). As is well known, for copper $\eta \approx 10^{-6}$, $P_h \approx 10^{-3}$, $S_t \approx 2.5 \times 10^{-2}$ cm, $a \approx 4.4$ Å [3,5] and in the experiments described $t \approx 1.5 \times 10^{-3}$ s. Substituting these values into Eq. (1) we obtain

$$I_m \approx 10^{-20} \cdot N_d \, \text{W/cm}^2. \tag{2}$$

Let us now estimate the change in the dislocation density on the investigated surface of the deformed sample when the back surface is irradiated with a laser pulse.

The total length L_1 of the defect walls on the investigated area $S = 9.4 \times 10^{-8}$ cm^{-2} before irradiation is $\approx 2.5 \times 10^5$ nm (Fig. 1b). After irradiation the total length of the defect walls is $L_2 \approx 0.6 \times 10^5$ nm (Fig. 2b). Since the magnitude of Burgers vector for copper is $|\mathbf{b}| \approx 0.3$ nm, the change in the dislocation density at the surface is

$$N_d = \frac{L_1 + L_2}{bS} \approx 1 \times 10^{13} \, \text{cm}^{-2}.$$

Substituting this value of N_d into Eq. (2), we find that the luminescence intensity $I_{md} \approx 1 \times 10^{-7}$ W/cm^2.

Taking account of the experimental geometry and the sensitivity of the photomultiplier, we found that the measured intensity of mechanoluminescence of the sample surface is $I_{mdf} \approx 2 \times 10^{-7}$ W/cm^2. As one can see, this value agrees well in order of magnitude with the mechanoluminescence intensity determined from the number of submicrodefects arising at the surface of the deformed sample.

For the annealed sample the change in the dislocation density at the surface after irradiation by a laser pulse was $N_d \approx 10^{10}$ cm^{-2}. Substituting this value of N_d into Eq. (2) and taking account of the experimental geometry and the area of the radiating surface ~ 0.1 cm^2, we obtain that the intensity of the radiation on the photocathode of the photomultiplier is $I_{mof} \approx 5 \times 10^{-13}$ W. This is below the noise level of the FÉU-136 photomultiplier. Therefore the photomultiplier did not record anything when the annealed sample was irradiated with a laser pulse.

In summary, our investigations have established that 1) the change in the submicrorelief of the surface and mechanoluminescence which arise as a result of irradiation by a laser pulse can be explained by the emergence of mobile dislocations onto the surface of the metal and 2) the mechanoluminescence intensity is determined by the initial microstructure of the sample and the defect density.

[1] K. B. Abramova, I. P. Shcherbakov, I. Ya. Pukhonto, and A. M. Kondyrev, Zh. Tekh. Fiz. **66**(5), 190 (1996) [Tech. Phys. **41**, 511 (1996)].
[2] K. B. Abramova, I. P. Shcherbakov, A. A. Semenov, and A. I. Rusakov, Fiz. Tverd. Tela (St. Petersburg) **40**, 957 (1998) [Phys. Solid State **40**, 877 (1998)].
[3] M. I. Molotskiĭ, Fiz. Tverd. Tela (Leningrad) **20**, 1651 (1978) [Sov. Phys. Solid State **20**, 956 (1978)].
[4] M. I. Molotskiĭ and B. P. Peregud, Zh. Tekh. Fiz. **51**, 618 (1981) [Sov. Phys. Tech. Phys. **26**, 369 (1981)].
[5] B. R. Chandra, M. S. Ryan, Seema R. Simon, and M. H. Ansari, Cryst. Res. Technol. **4**, 495 (1996).
[6] V. I. Vettegren', S. N. Rakhimov, and V. N. Svetlov, Fiz. Tverd. Tela (St. Petersburg) **37**, 3635 (1995) [Phys. Solid State **37**, 2001 (1995)].
[7] B. L. Averbakh, in *Fracture* [in Russian], Mir, Moscow (1973), pp. 471–504.
[8] V. I. Vettegren', S. N. Rakhimov, and E. A. Bakulin, Fiz. Tverd. Tela (St. Petersburg) **37**, 3630 (1995) [Phys. Solid State **37**, 1998 (1995)].
[9] V. I. Vettegren', V. L. Gilyarov, S. N. Rakhimov, and V. N. Svetlov, Fiz. Tverd. Tela (St. Petersburg) **40**, 668 (1998) [Phys. Solid State **40**, 614 (1998)].

Translated by M. E. Alferieff